Image Analysis for Contrast Enhanced Ultrasound Carotid Plaque Imaging

Z. Akkus

Colophon

Image Analysis for Contrast Enhanced Ultrasound Carotid Plaque Imaging
Z. Akkus

Printed by: Ridderprint, Ridderkerk, the Netherlands

Image Analysis for Contrast Enhanced Ultrasound Carotid Plaque Imaging

Beeldanalyse voor contrast-echografie van plaques in de halsslagaderen

Thesis

to obtain the degree of doctor from the
Erasmus University Rotterdam
by command of the Rector Magnificus

Prof.dr. H.A.P. Pols

and in accordance with the decision of the Doctoral Board.

The public defense shall be held on
Wednesday October 8, 2014 at 11.30 hours by

Zeynettin Akkus
born in Batman, Turkey

Doctoral Committee

Promotor:	Prof.dr.ir. A.F.W. van der Steen
Copromotors:	Assoc. Prof. J.G. Bosch Dr. A.F.L. Schinkel
Other members:	Prof.dr.ir. N. de Jong
	Prof.dr.ir. A. van der Lugt
	Assoc. Prof. M. Averkiou

This research was performed within the framework of **CTMM**, the Center for Translational Molecular Medicine (www.ctmm.nl), project **PARISk** (grant 01C-202), and supported by the Netherlands Heart Foundation.

Financial support for the printing of this thesis is provided by:

CARDIALYSIS
Clinical Trial Management - Core Laboratories

Table of Contents

Propositions accompanying the PhD thesis

Image analysis for contrast enhanced ultrasound carotid plaque imaging

1) Motion compensation is crucial for accurate quantification of intraplaque neovascularization (IPN). (this thesis)

2) Quantitative CEUS imaging parameters can replace qualitative visual scoring to measure the degree of IPN in an objective and reproducible manner. (this thesis)

3) Currently available commercial contrast quantification tools are not suitable for analysis of carotid IPN due to artifacts and intermittent perfusion of plaques. (this thesis)

4) Systematic comparison of different IPN analyses over patient datasets requires the use of identical patient-specific regions of interest for all analyses. (this thesis).

5) Simultaneous acquisition of BMUS and CEUS allows an accurate carotid plaque segmentation and IPN quantification in CEUS. (this thesis)

6) Even though it has been shown and published that IPN assessment in the far wall of the carotid artery using CEUS is unreliable due to the pseudo-enhancement artifact, this artifact is still neglected in many CEUS studies. (ref.: Atherosclerosis, 229:451-52)

7) It is better to have a simple method that doesn't work than a complex method that doesn't work. (S. Klein)

8) Confidence and hard-work is the best medicine to kill the disease called failure. (Abdul Kalaam)

9) If you judge a fish on its ability to climb a tree, it will live its whole life believing that it is stupid. (A. Einstein)

10) Wisdom begins in wonder. (Sokrates)

11) Do not be satisfied with the stories that come before you. Unfold your own myth. (Mevlana Rumi)

Chapter 1
Introduction

1. INTRODUCTION

1.1 Carotid Arteries

The carotid arteries are the large arteries which are located at both sides of the neck under the jaw (see Figure 1). Their pulse can be felt as they are quite superficial (about 1 to 3cm away from the skin). The right common carotid artery (CCA) starts from a branch of the aorta (brachiocephalic artery) and the left CCA starts directly from the aortic arch. Just below the jaw, they bifurcate into two branches which are called internal and external carotid arteries. The internal carotid arteries (ICA) supply blood to the face and the external carotid arteries (ECA) supply blood to the brain. The bifurcation is a frequent location for atherosclerosis.

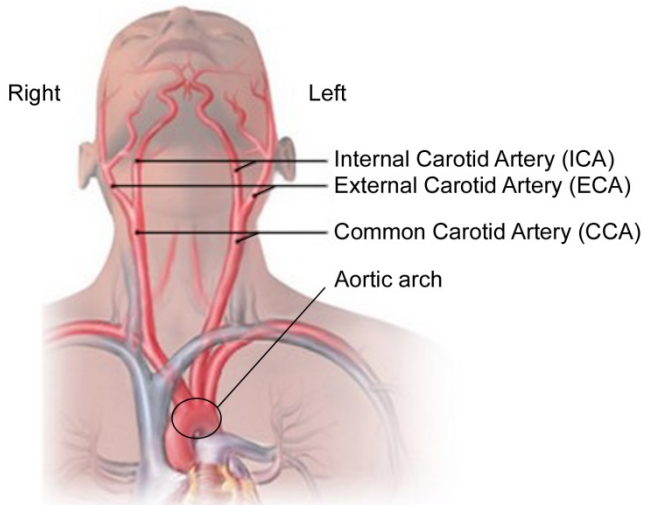

Figure 1: Anatomy of carotid artery (original available at www.vascularconcept.com).

1.1.1 Atherosclerosis and Intraplaque Neovascularization

Atherosclerosis is a disease of the arteries, which causes narrowing of an artery lumen due to accumulation of fatty substances and calcium within the wall of the artery. The depositions of these substances are called plaques. They narrow the artery lumen and obstruct the oxygen-rich blood flow to organs of the body (see Figure 2).

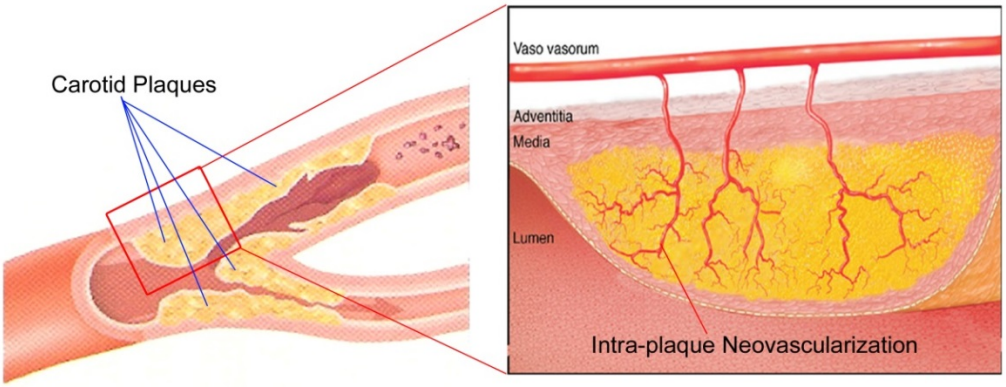

Figure 2: Depiction of carotid plaques and intraplaque neovascularization (original available at www.lucid-echo.com)

Patients with carotid plaques carry an increased risk of cardiovascular events such as stroke, transient ischemic attack, amaurosis fugax, and myocardial infarct [1]. If a plaque ruptures, pieces of the plaque or blood clots split from the site of injury travel through the blood stream and block a smaller artery in the brain or eye. This causes a stroke in the brain or loss of vision in the eye.

According to the World Health Organization, 15 million people suffer from stroke worldwide each year [2]. Five million of these people die and another 5 million are permanently disabled. In Europe, approximately 650,000 people die from stroke each year. In US, one American dies from a stroke every 4 minutes on average [3]. Therefore, early detection of plaques at risk of rupture (vulnerable plaques) may allow prevention of the stroke and save lives.

Large European and North American clinical trials have established the benefit of carotid endarterectomy in reducing the risk of recurrent stroke for symptomatic patients with severe stenosis. However, the difficulty in identifying vulnerable plaques means that many patients undergo needless operations. There is an increasing realization that the degree of stenosis is a poor predictor of individual stroke risk and that current risk stratification models should to be improved. Current clinical practice for selecting patients for carotid endarterectomy operation is heavily reliant on assessing the degree of arterial lumen narrowing. This is widely assessed using non-invasive ultrasound which provides anatomical images and measurements of blood flow velocity.

Alternatively, neovascularization within plaques (see Figure 2) has been examined in several histo-pathological studies [4-6]. It was demonstrated that intraplaque neovascularization (IPN) is associated with progressive atherosclerotic disease and plaque vulnerability. Neovascularization is the development of functional microvascular networks with red blood cell perfusion. As plaques are also a tissue developed within an artery wall, the body encourages development of blood vessels to feed this tissue. Recent developments in contrast enhanced ultrasound (CEUS) have shown that these small microvasculature networks with slow flow can be visualized by the use of ultrasound contrast agents. Quantification

of IPN by CEUS may allow early detection of vulnerable plaques and may be of clinical value for selecting patients for carotid endarterectomy.

So far, assessment of IPN relies mostly on subjective visual assessment as quantification tools for IPN are scarce. Recently, a review paper [7] presented the methods used to assess IPN so far and discussed the current status of CEUS in carotid atherosclerosis.

1.2 Diagnostic Ultrasonography

Diagnostic ultrasonography is an ultrasound-based imaging technique used for visualizing and diagnosing pathological changes of internal body structures such as muscles, vessels, heart or other organs. For example, vascular sonography has been widely used to examine vessels and pathological changes of the vessel wall. Ultrasound can also be used therapeutically (e.g. high intensity focused ultrasound is used to heat and destroy tumors).

Ultrasound is a sound pressure wave with a frequency higher than the human hearing range (20Hz-20kHz). An ultrasound transducer which consists of piezo-electric material is used to transmit and receive the sound wave. The sound wave is transmitted into the tissue and the reflected echo (wave) is recorded and used to construct an ultrasound image. As the average speed of sound through biological soft tissue is approximately 1540 m/s, the time of flight between the transmitted and received echo is used to localize an object and construct an acoustic image of the interrogated region. The propagation of an acoustic wave is characterized by its speed c and wavelength λ: $c = f\lambda$.

Ultrasound has several advantages compared to other medical imaging techniques. It is safe as it does not use harmful ionizing radiation like X-ray and CT. It is considerably lower in cost. Images are provided in real-time. It is portable, can be transported to a patient's bedside, and is useful for patient screening and follow-up. The disadvantages of ultrasound include its strong operator dependence, and inability to examine areas of the body containing gas and bones.

1.2.1 Modes of Ultrasound

Different types of images can be formed by using ultrasound. There are several modes of ultrasound that are used in diagnostic ultrasonography. The most common are:

B-mode: Brightness mode (B-mode) is the most well-known ultrasound mode. A 2D cross section of a tissue is displayed by scanning an ultrasound beam over the tissue.

M-mode: Movement mode (M-mode) displays movement of structures over time. First, a scan line is placed on a region of interest in a B-mode image. The M-mode displays how the structure crossed by that scan line move toward or away from the probe over time.

Doppler mode: In this mode, blood flow is measured and visualized by using the Doppler effect which is the shift in frequency of a wave for an observer moving relative to its source. In diagnostic ultrasound, an ultrasound wave is emitted with a particular frequency by using an ultrasound probe. Ultrasound waves reflected from red blood cells (moving objects) return to the probe with a Doppler shift. This shift in frequency is used to calculate the velocity of the blood flow. Velocity information is presented as a color-coded overlay on top of a B-mode image, which is called color Doppler.

Harmonic mode: In this mode, a wave with a fundamental frequency is emitted into the body and the second harmonic of the wave is detected. In this way, noise, clutter and artifacts (side lobes and reverberations) are greatly reduced. Harmonic imaging also improves resolution and signal-to-noise ratio.

Contrast Mode: Contrast mode imaging is used for visualization of the lumen of cardiac cavities and blood vessels. Secondly, it is used to quantify blood perfusion in organs by use of ultrasound contrast agents. This mode is useful in vascular, cancer, and cardiology research for detecting perfusion abnormalities of tissues.

1.3 Contrast Enhanced Ultrasound

Contrast enhanced ultrasound (CEUS) can provide information about blood perfusion of organs by use of ultrasound contrast agents (microbubbles). Contrast agents can penetrate into the microvasculature network and are confined to the microvasculature. This also allows detection of plaque neovascularization (IPN) by using CEUS. Compared to B-mode anatomical ultrasound images, the tissue information is suppressed and only contrast agents flowing within the blood are displayed. CEUS is widely used to diagnose perfusion abnormalities of organs such as liver, prostate and myocardium. Beside this, CEUS is used to assess perfusion of atherosclerotic plaques. This allows detecting of these small microvessels by using CEUS. There are two types of contrast enhanced ultrasound: 1) non-targeted CEUS using free-floating microbubbles 2) targeted CEUS using targeted microbubbles which bind to certain receptors on endothelial. In this thesis work, we only focused on non-targeted CEUS.

1.3.1 Ultrasound Contrast Agents

Ultrasound contrast agents are gas-filled microbubbles with a size distribution of 1 to 10μm, as small as red blood cells. They are intravenously injected and small enough to pass the lungs. Subsequently, they reach the left ventricle of the heart

and enter the systemic circulation. Later, they are mainly eliminated by the lungs. A microbubble consists of a shell and a gas core. The shell material affects mechanical elasticity and residence time of the microbubble in the systemic circulation [8]. Currently, the shell of the microbubble is made of lipid, albumin, or polymers [9]. The gas core of the microbubble provides an efficient scattering due to high compressibility. Microbubbles contain gasses such as air, sulphur-hexafloride (SF_6) or octofluoropropane (C_3F_8). The gases such as SF_6 and C_3F_8 have low solubility in blood and increase the residence time of microbubbles in the systemic circulation. In this thesis work, we only used SonoVue contrast agent, manufactured by Bracco Inc., which has phospholipid coating and contains SF_6 gas. SonoVue has shown to be safe, is not trapped in microvasculature networks, and not diffusing across vascular or microvessel walls. There has been no evidence of harmful effects of SonoVue. Microbubbles respond to ultrasound insonification nonlinearly due to their high compressibility and resonance, which is different than the linear response of a tissue. This difference between the tissue and microbubbles allows separating the tissue and microbubble responses. Several contrast imaging techniques have been developed so far based on nonlinear response of microbubbles.

1.4 Contrast Detection Techniques

Proper detection of ultrasound contrast agents is very important for their usability in diagnostic ultrasound. The strong scattering property of microbubbles can be used to change the response of the blood from echolucent (dark) to echogenic (bright) of the lumen of large arteries or the chambers of heart. However, when microbubbles are flowing within a microvasculature network surrounded by a tissue, their detection will be more difficult due to the combined response from tissue and microbubbles. To be able to detect microbubbles within the microvascular network, contrast-specific detection techniques are necessary. Pulse inversion and amplitude modulation techniques are the most common techniques that have been used to detect contrast agents. In addition, a technique called counter-propagation has been recently introduced by Renaud et al. [10] to detect microbubbles and suppress contrast-specific artifacts that are produced by the most common techniques.

1.4.1 Pulse Inversion

In pulse inversion technique, two pulses are transmitted, where the second pulse is a phase inverted copy of the first one. Their responses are added up. The tissue which is a linear target will reflect identical but inverted echoes back to the transducer as a response of these two pulses. Summing up these two responses will cancel out the linear response of the tissue. However, microbubbles will respond differently to these inverted pulses. When the received echoes for microbubbles are added, they do not cancel completely. The fundamental components and the odd harmonics (3rd, 5th, etc.) of the response signal cancel

each other but the even harmonics (2nd, 4th, 6th, etc.) produced by microbubbles are added.

1.4.2 Amplitude (Power) Modulation

This technique is also based on suppression of linear echoes and obtaining harmonic response. In this case, the scaling property of linearity is used to distinguish between the linear tissue and nonlinear microbubble responses. In power modulation, three pulses (two single-amplitude pulses and one double-amplitude pulse) of the same shape are transmitted. Summing up the response of the two single-amplitude pulses and subtracting from the response of the double-amplitude pulse will give no remaining signal for the linear tissue. However, microbubbles will respond differently to the two amplitudes. The generation of harmonics is dependent on the fundamental signal amplitude and therefore the double-amplitude pulse will generate stronger harmonics than the single-amplitude pulses. In this case, adding the responses of the two single-amplitude pulses and subtracting from the response of the double-amplitude pulse will result in a remaining harmonic signal that will allow distinguishing microbubbles from the tissue.

1.4.3 Counter-Propagation Technique

The techniques like pulse inversion and amplitude modulation require linear propagation along the tissue to detect nonlinear response of microbubbles. However, when a transmitted pulse crosses cavities with a high concentration of contrast agent, the waveform of the pulse is distorted due to nonlinear propagation medium. This will cause the tissue right behind these cavities to be misclassified as microbubbles, called pseudo-enhancement artifacts [11]. Renaud et al. [10] proposed a technique which distinguishes microbubbles from tissue based on the response of microbubbles to two acoustic waves propagating in opposite directions. In biological tissues, there will no effect observed when two waves pass over each other. However, microbubbles create an interaction between the two waves when they are passing over each other. This is used to detect microbubbles and create images free from nonlinear propagation artifacts (pseudo-enhancement artifacts). This technique has been recently developed but has not been used in clinical practice yet.

1.5 Ultrasound Image Analysis

Ultrasound is an operator dependent imaging modality. Therefore, ultrasound image acquisition and interpretation includes variability between operators or physicians. Furthermore, visual interpretation of ultrasound image sequences is a tedious task for physicians. In ultrasound image analysis, much effort has been put into the cardiovascular applications (e.g. the analysis of heart, carotid arteries, or

coronary arteries) to reduce the variability between physicians and to assist interpretation of images. Main challenges in ultrasound image analysis are suppressing noise and artifacts, compensating for motion, and registration and segmentation of anatomical structures.

1.5.1 Noise Filtering

Ultrasound images are generally contaminated with speckle noise which is produced by scatterers smaller than the wavelength of a transmitted ultrasound pulse. A reliable speckle reduction is a challenge in ultrasound imaging. Noise reduction is often applied as a pre-processing step for further analysis. The most commonly used filters to reduce noise are neighbourhood-based filters such as average, median, and Gaussian filtering. These filters will partly suppress the noise but they may also cause blurring of edges of anatomical structures. Therefore, anisotropic filters are used instead of neighbourhood-based filters to prevent smoothing sharp boundaries [12]. For further speckle reduction methods that have been developed so far, we refer to the literature [13].

1.5.2 Motion Analysis

Ultrasound imaging for the cardiovascular applications contains considerable motion such as heart movement, pulsation, body movement and probe motion. To be able to follow a region of interest, motion analysis is necessary. So far, block matching (also known as speckle tracking) [14], multidimensional dynamic programming (MDP) combined with block matching [15], optical flow [16], and Kalman-filter based techniques [17] have been used to analyse motion in ultrasound images. Block matching is the most commonly used technique. In this technique, a template of a structure is defined and scanned over a search field. For each position in the search field a measure of similarity to the template is calculated (e.g. sum of absolute differences, or normalized cross correlation). The similarity maxima are followed over time for motion analysis. MDP can be used to find an optimal connective displacement path over time.

1.5.3 Image Registration

Image registration has been widely used in medical imaging field to find the best spatial correspondence of anatomical structures between the same or different imaging modalities. This allows comparing images for different cardiac phases or images obtained at different times. Medical image registration can also be used for monitoring disease progression. Image registration approaches can be classified as landmark-based [18], intensity-based [19], and combination of landmark and intensity based [20] approaches. In landmark-based approaches, anatomical or geometrical landmarks (e.g. contours of objects) are extracted from images. Geometrical measures such as Euclidian distance are used to find the similarity between these landmarks in images. In intensity-based approaches, a

measure of correspondence (e.g. sum of absolute differences, normalized cross correlation, or mutual information) between intensities of images is used. Intensity-based approaches are the most widely used registration techniques in medical imaging.

Registration is an iterative optimization framework for finding spatial correspondence between intensities or landmarks of a fixed and moving image. In each of iteration, a spatial transform is estimated and applied to the moving image. After that, the similarity between the fixed and moving image is calculated. The resulting similarity matrix is given as an input to an optimizer based on the computation of gradients (e.g. gradient descent or ascent). This process is repeated until alignment converges to a steady state or a maximum number of iterations is reached.

1.5.4 Image Segmentation

Image segmentation is the process of partitioning of an image into multiple segments which have different visual characteristics. The segmentation process locates objects and boundaries in the image. Several segmentation approaches for ultrasound images have been presented in the literature. These methods have been reviewed in several recent surveys [21-23]. Noble et al. stated that a good ultrasound image segmentation method needs to make use of all constraints (e.g. imaging physics, anatomical shape, and temporal constraints) and concluded that more segmentation validations are necessary to better understand the strengths and limitations of available methods. Naik et al. [15] presented a survey for carotid artery segmentation in ultrasound images. They concluded that none of the existing techniques were very good in all aspects (e.g. automation, robustness to noise, computation time, or being suitable for clinical applications), and that performance of semi-automatic segmentation techniques is better than that of fully-automatic techniques.

Segmentation methods can be divided into two groups which are region-based and edge-based approaches. Region-based segmentation approaches include methods such as thresholding, region growing, watershed approach, classification-based and morphological methods. Edge-based segmentation approaches include methods such as level-set, active contours, active shape models, classification-based, and graph-based methods. In this thesis work, we only focus on regional classification-based and graph-based approaches.

In classification-based approaches, segmentation is formulated as a probability estimation problem for given prior information such as image intensity distributions. Probabilities of each image pixel belonging to a given class are calculated by using a maximum-likelihood or Bayesian maximum a posteriori criterion. This results in a fuzzy segmentation of the image. The most commonly

used method is Expectation-Maximization [24] which iteratively maximizes the a posteriori likelihood.

In graph-based segmentation approaches, an optimal connective path is searched by finding a minimal cost path, e.g. using dynamic programming. In this case, the image is considered as a graph of nodes (image pixels). Every node has a cost value (e.g. pixel intensity). The optimal connective path is searched from left to right or vice versa in a 2D image by calculating cumulative cost. In the last column of the image, the lowest cumulative cost is found and the optimal path is found by backtracking.

1.6 Scope and Outline

1.6.1 Aim of Thesis

We aim at development of novel, robust, accurate and objective quantification tools for intraplaque neovascularization (IPN) to replace tedious, subjective, and qualitative visual IPN scoring that has been used for assessment of IPN so far. In this work, we developed several IPN quantification tools and derived several quantitative imaging parameters. We also aim at selection of the best quantitative IPN imaging parameters among the derived IPN parameters. Furthermore, we aim at accurate segmentation of the lumen and wall of carotid artery in patients with atherosclerotic plaques to fully automate plaque segmentation and IPN quantification. In addition, all developed tools were implemented in a software package that we developed as a platform for carotid IPN quantification. Our software package was developed for clinical research use and has been used as such. This thesis work was performed in the context of a large consortium project, CTMM-ParisK (Plaque At Risk), which investigates molecular, morphological, biomechanical and imaging biomarkers of carotid artery atherosclerotic plaque to detect plaque at risk of rupture.

1.6.2 Thesis Outline

Motion analysis

Chapter 2 describes an essential pre-processing step for IPN quantification, which is motion compensation for carotid plaques. Multidimensional dynamic programming combined with block matching is used to obtain the motion pattern of plaques over time.

Quantification Methods

Chapter 3 describes a quantification tool that was developed to detect and track contrast spots within the region of interest (ROI) of plaques. In this method, contrast spots and stationary artefact spots are discriminated based on their

displacement. The method gives the number of microvessel paths detected within the plaque ROI as an imaging biomarker for IPN.

Chapter 4 describes motion compensated perfusion quantification tools (i.e. time intensity curve and maximum intensity projection analyses) for plaques. The imaging parameters derived from motion compensated perfusion analysis and those in *Chapter 3* are compared to visual IPN scoring to select the best IPN imaging parameters.

Chapter 5 describes a method that statistically segments contrast spots. In this method, intensities within the plaque ROI are classified into background, contrast spots, and artifacts. The method is quite insensitive to artifacts compared to the methods in *Chapters 3* and *4*.

Software development

Chapter 6 describes the concept, design and capabilities of a software package which is developed as a platform for IPN quantification. The parameters derived in *Chapter 5* are compared to the parameters in *Chapters 3* and *4*, and to visual IPN scoring.

Image registration and segmentation

Chapter 7 describes a nonrigid motion compensation method for combined B-mode and contrast enhanced ultrasound images and a fully automatic method for segmentation of the lumen of the carotid artery. The method also allows studying the lumen geometry over time (e.g. for distensibility measurements).

Chapter 8 describes a fully automatic carotid plaque segmentation method in combined B-mode and contrast enhanced ultrasound images.

Clinical application

Chapter 9 describes assessment of IPN in patients with familial hypercholesterolemia, using the software described in *Chapter 6* and quantification tools described in *Chapters 3-5*.

Discussion and conclusion

Chapter 10 discusses the merits of the developed IPN analysis tools and provides the future perspectives and conclusion of this study.

References:

[1] M. Naghavi, P. Libby, E. Falk*, et al.*, "From vulnerable plaque to vulnerable patient - A call for new definitions and risk assessment strategies: Part I," *Circulation,* vol. 108, pp. 1664-1672, Oct 7 2003.

[2] W. H. Organization, "World Health Report," 2002.

[3] A. S. Go, D. Mozaffarian, V. L. Roger*, et al.*, "Heart Disease and Stroke Statistics—2013 Update: A Report From the American Heart Association," *Circulation,* vol. 127, pp. e6-e245, January 1, 2013 2013.

[4] D. Staub, M. B. Patel, A. Tibrewala*, et al.*, "Vasa Vasorum and Plaque Neovascularization on Contrast-Enhanced Carotid Ultrasound Imaging Correlates With Cardiovascular Disease and Past Cardiovascular Events," *Stroke,* vol. 41, pp. 41-47, Jan 2010.

[5] F. Shah, P. Balan, M. Weinberg*, et al.*, "Contrast-enhanced ultrasound imaging of atherosclerotic carotid plaque neovascularization: a new surrogate marker of atherosclerosis?," *Vascular Medicine,* vol. 12, pp. 291-297, 2007 2007.

[6] S. Coli, M. Magnoni, G. Sangiorgi*, et al.*, "Contrast-Enhanced Ultrasound Imaging of Intraplaque Neovascularization in Carotid ArteriesCorrelation With Histology and Plaque Echogenicity," *Journal of the American College of Cardiology,* vol. 52, pp. 223-230, 2008.

[7] G. L. ten Kate, S. C. H. van den Oord, E. J. G. Sijbrands*, et al.*, "Current status and future developments of contrast-enhanced ultrasound of carotid atherosclerosis," *Journal of Vascular Surgery,* vol. 57, pp. 539-546, 2013.

[8] M. McCulloch, C. Gresser, S. Moos*, et al.*, "Ultrasound contrast physics: a series on contrast echocardiography, article 3," *Journal of the American Society of Echocardiography : official publication of the American Society of Echocardiography,* vol. 13, pp. 959-967, 2000.

[9] J. R. Lindner, "Microbubbles in medical imaging: current applications and future directions," *Nat Rev Drug Discov,* vol. 3, pp. 527-533, 2004.

[10] G. Renaud, J. G. Bosch, G. L. ten Kate*, et al.*, "Counter-propagating wave interaction for contrast-enhanced ultrasound imaging," *Physics in Medicine and Biology,* vol. 57, pp. L9-L18, Nov 7 2012.

[11] G. L. ten Kate, G. G. J. Renaud, Z. Akkus*, et al.*, "Far-Wall Pseudoenhancement during Contrast-Enhanced Ultrasound of the Carotid Arteries: Clinical Description and in Vitro Reproduction," *Ultrasound in Medicine and Biology,* vol. 38, pp. 593-600, Apr 2012.

[12] P. Perona and J. Malik, "Scale-space and edge detection using anisotropic diffusion," *Pattern Analysis and Machine Intelligence, IEEE Transactions on,* vol. 12, pp. 629-639, 1990.

[13] P. C. Tay, S. T. Acton, and J. A. Hossack, "Ultrasound Despeckling Using an Adaptive Window Stochastic Approach," in *Image Processing, 2006 IEEE International Conference on*, 2006, pp. 2549-2552.

[14] S. Golemati, A. Sassano, M. J. Lever*, et al.*, "Carotid artery wall motion estimated from B-mode ultrasound using region tracking and block matching," *Ultrasound in Medicine and Biology,* vol. 29, pp. 387-399, 2003 2003.

[15] S. T. Nevo, M. Van Stralen, A. M. Vossepoel*, et al.*, "Automated tracking of the mitral valve annulus motion in apical echocardiographic images using multidimensional dynamic programming," *Ultrasound in Medicine and Biology,* vol. 33, pp. 1389-1399, Sep 2007.

[16] B. D. Lucas and T. Kanade, "An iterative image registration technique with an application to stereo vision," presented at the Proceedings of the 7th international joint conference on Artificial intelligence - Volume 2, Vancouver, BC, Canada, 1981.

[17] A. Gastounioti, S. Golemati, J. Stoitsis*, et al.*, "Comparison of Kalman-filter-based approaches for block matching in arterial wall motion analysis from B-mode ultrasound," *Measurement Science & Technology,* vol. 22, Nov 2011.

[18] J.-P. Thirion, "New feature points based on geometric invariants for 3D image registration," *International Journal of Computer Vision,* vol. 18, pp. 121-137, 1996/05/01 1996.

[19] C. T. Metz, S. Klein, M. Schaap*, et al.*, "Nonrigid registration of dynamic medical imaging data using nD+t B-splines and a groupwise optimization approach," *Medical Image Analysis,* vol. 15, pp. 238-249, 2011.

[20] D. B. Carvalho, S. Klein, Z. Akkus*, et al.*, "Registration of Free-Hand Ultrasound and MRI of Carotid Arteries through Combination of Point-Based and Intensity-Based Algorithms," in *Biomedical Image Registration*. vol. 7359, B. Dawant*, et al.*, Eds., ed: Springer Berlin Heidelberg, 2012, pp. 131-140.

[21] J. A. Noble and D. Boukerroui, "Ultrasound image segmentation: a survey," *Medical Imaging, IEEE Transactions on,* vol. 25, pp. 987-1010, 2006.

[22] F. Molinari, G. Zeng, and J. S. Suri, "A state of the art review on intima–media thickness (IMT) measurement and wall segmentation techniques for carotid ultrasound," *Computer Methods and Programs in Biomedicine,* vol. 100, pp. 201-221, 2010.

[23] V. Naik, R. S. Gamad, and P. P. Bansod, "Carotid Artery Segmentation in Ultrasound Images and Measurement of Intima-Media Thickness," *BioMed Research International,* vol. 2013, p. 10, 2013.

[24] A. P. Dempster, N. M. Laird, and D. B. Rubin, "Maximum Likelihood from Incomplete Data via the EM Algorithm," *Journal of the Royal Statistical Society. Series B (Methodological),* vol. 39, pp. 1-38, 1977.

Chapter 2

Motion Compensation Method using Dynamic Programming for Quantification of Neovascularization in Carotid Atherosclerotic Plaques with Contrast Enhanced Ultrasound (CEUS)

Intraplaque neovascularization (IPN) has been linked with progressive atherosclerotic disease and plaque instability in several studies. Quantification of IPN may allow early detection of vulnerable plaques. A dedicated motion compensation method with normalized-cross-correlation (NCC) block matching combined with multidimensional (2D+time) dynamic programming (MDP) was developed for quantification of IPN in small plaques (<30% diameter stenosis). The method was compared to NCC block matching without MDP (forward tracking (FT)) and showed to improve motion tracking. Side-by-side CEUS and B-mode ultrasound images of carotid arteries were acquired by a Philips iU22 system with a L9-3 linear array probe. The motion pattern for the plaque region was obtained from the B-mode images with MDP. MDP results were evaluated in-vitro by a phantom and in-vivo by comparing to manual tracking of three experts for multibeat-image-sequences (MIS) of 11 plaques. In the in-vivo images, the absolute error was 72±55μm (mean±SD) for X (longitudinal) and 34±23μm for Y (radial). The method's success rate was visually assessed on 67 MIS. The tracking was considered failed if it deviated >2 pixels (~200μm) from true motion in any frame. Tracking was scored as fully successful in 63 MIS (94%) for MDP vs. 52(78%) for FT. The range of displacement over these 63 was 1045±471μm (X) and 395±216μm (Y). The tracking sporadically failed in 4 MIS (6%) due to poor image quality, jugular vein proximity and out-of-plane motion. Motion compensation showed improved lumen-plaque contrast separation. In conclusion, the proposed method is sufficiently accurate and successful for in vivo application.

Z. Akkus, A. Hoogi, G. Renaud, G.L. ten Kate, S. van den Oord,A. Schinkel, N. de Jong, A.F.W. van der Steen, J.G Bosch. **Motion Compensation Method using Dynamic Programming for Quantification of Neovascularization in Carotid Atherosclerotic Plaques with Contrast Enhanced Ultrasound (CEUS).** Proc. SPIE medical imaging 2012, 8320, 83200C.

1. INTRODUCTION

Many studies have shown that patients with carotid plaques carry an increased risk of sudden cardiovascular events, such as stroke, transient ischemic attack, myocardial infarction and even death. The benefit of carotid endarterectomy has been established in reducing the risk of recurrent stroke for symptomatic patients with severe stenosis by large European and North American clinical trials [16-17]. For a carotid endarterectomy operation, current clinical practice for selecting patients is heavily based on assessing the degree of arterial lumen narrowing. However, there is an increasing consciousness that not the size of the plaque, but its composition and risk of rupturing is related to these acute cardiovascular events. Therefore, the degree of stenosis is actually a poor predictor of individual stroke risk and improved risk stratification models should focus on plaque vulnerability rather than size.

Some studies suggested some other parameters to be included in plaque analysis. Plaque echogenicity was assessed by taking its gray scale median (GSM) after normalizion of image gray values to those of blood and adventitia [1]. Furthermore, echolucency of plaques was examined and it was hypothesized that it may represent an increased risk of cerebrovascular events [2]. Analysis of plaque image texture in addition to quantification of GSM has also been investigated in efforts to improve reliability and demonstrate the clinical value of greyscale image analysis [3].

Alternatively, the neovascularization within the plaque was examined and several pathological studies demonstrated that intraplaque neovascularization (IPN) is associated with progressive atherosclerotic disease and plaque vulnerability [4-5]. Recent developments in contrast enhanced ultrasound (CEUS) have shown that small microvessels with slow flow can be visualized by the use of ultrasound contrast agents. Therefore our research aims at an accurate quantification of IPN by CEUS, which may allow early detection of vulnerable plaques and may be of clinical value for selecting patients for carotid endarterectomy. Since the carotid artery shows considerable motion due to the pulsating blood pressure, breathing and swallowing motion compensation of the plaque is a prerequisite step for analysis of identical regions of interest (ROI) for an accurate quantification of IPN. A dedicated method of motion compensation for this purpose is explored in this study.

In a previous study, Chan [7] presented two approaches to carotid plaque and tissue motion. A number of points was selected and tracked based on salient features such as high contrast edges or corners to estimate tissue motion. Besides, the boundary of plaque in each frame was extracted based on gray-level histogram thresholding and motion of the boundary was used to estimate the plaque motion. Golemati et al. [6] introduced region tracking and quantification of the carotid wall motion by block matching using normalized-cross-correlation (NCC) with 3.2x2.5mm (49x41 pixels) templates on ultrasound B-mode images. Bang et al. [8]

demonstrated a block matching technique using NCC with 21x21 templates for multiple points over a region to track intraplaque motion and quantified various plaque motion parameters. Akkus and Ramnarine [9] assessed dynamic plaque motion and intraplaque deformation in carotid artery at high frame rate with a forward tracking block matching technique using NCC with a fixed 3x3 mm template. Dave and Forsberg [10] introduced a motion compensation method based on sum of absolute differences to improve the quantification of breast lesion with contrast enhanced ultrasound. Akkus et al.[12] presented a motion compensation method with forward tracking block matching technique using NCC with a fixed ~5x5 mm (49x49 pixels) template and subpixel detection for quantification of IPN in CEUS images . The main drawbacks of forward tracking with block matching are the sensitivity to temporary disturbances (artifacts, out-of-plane motion, reduced or noisy NCC values, peak hopping) resulting in a temporary or permanent loss of tracking. These limitations may be overcome by more advanced robust tracking approaches.

Gastounioti et al. [11] presented a comparison of Kalman filter-based approaches for block matching in carotid wall motion analysis. They concluded that the combination of adaptive block matching and Kalman filtering yielded average displacement error reduction of 24% with respect to block matching without Kalman filtering. Kalman filtering based approaches are more robust to noise than block matching and thereby they will result in considerable improvement in the quality of motion estimation.

Üzümcü et al [13] presented time continuous tracking and segmentation of cardiovascular magnetic resonance images using multidimensional dynamic programming (MDP). Nevo et al.[14]presented an automated tracking of the mitral valve motion in echocardiographic images using MDP combined with apodized block matching. Hoogi et al. [15] presented an algorithm for tracking contrast spots using MDP combined with apodized block matching for quantification of IPN.

In this study, we propose a dedicated motion compensation method using multidimensional dynamic programming combined with apodized block matching to overcome forward tracking limitations and for accurate quantification of IPN. We make use of the observation that the plaque itself is generally a unique landmark in the B-mode image, in contrary to healthy carotid wall sections. The plaque region itself is a suitable template for motion tracking. Therefore, side by side simultaneous contrast and B-mode images were acquired and the local motion pattern of the plaque region was extracted from the B-mode image with multidimensional (2D+t) dynamic programming and the extracted motion pattern was used to correct the plaque motion to quantify neovascularization accurately in the contrast image.

2. DATA ACQUISITION

Simultaneous side-by-side standard B-mode ultrasound and CEUS were acquired using a Philips iU22 system with a L9-3 linear array probe to achieve visualization of the plaque morphology and vascularization. The mechanical index for CEUS was adjusted to 0.06-0.08 for maximum contrast signal visualization. SonoVue contrast agent (Bracco S.p.A., Milan, Italy) was used to perform contrast enhanced ultrasound (CEUS). The ultrasound contrast agent was injected in the antecubital vein using an 18 Gauge intravenous cannula. The cannula was flushed with a 5.0 ml NaCl 0.9% solution bolus injection before the first injection of the ultrasound contrast agent. The ultrasound contrast agent was injected in boluses of 0.5-1.0 ml. Each contrast agent bolus was followed by a saline flush using 2.0 ml NaCl 0.9% solution. The arrival and appearance of contrast enhancement in the carotid lumen was observed within 10-30 seconds after the contrast injection. After administration of contrast agent, high-quality contrast images could be obtained and stored for approximately 1 minute. Contrast administration was repeated when required up to a maximum total dose of 10.0 ml. Both right and left carotid arteries were examined using a standard acquisition protocol. Cine clips and still frames were digitally stored as a DICOM (Digital Imaging and Communications in Medicine) format for offline analysis. The study was approved by the ethical committee and all patients gave written informed consent.

3. METHOD

The carotid artery wall shows considerable motion due to the pulsating blood pressure, breathing and swallowing. For an accurate quantification of small microvessels within the carotid plaques motion compensation is a prerequisite step. The contrast spots associated with these microvessels have sizes of a few pixels, while the plaque motion can amount to tens of pixels. The motion compensation method should be accurate and reliable enough for this purpose. In CEUS images, only ultrasound contrast agent is seen and tissue is suppressed so that it is quite difficult to extract plaque motion from CEUS images. Therefore we acquired simultaneous side-by-side B-mode images and CEUS images and the motion pattern of plaque was extracted from B-mode images and applied to the contrast images to follow identical plaque region. Plaque itself in B-mode images is quite a unique landmark in both directions, in contrary to healthy carotid wall sections, which are highly similar when moving along the vessel direction. For determining motion in image sequences, several techniques are commonly applied, such as image registration, optical flow, or block matching. Image registration approaches, employing either rigid or nonrigid deformations from frame to frame, determine a continuous field of deformations that transform the previous image into the next. Optical flow determines local direction of movement from the relation between spatial and temporal intensity gradients. Block matching approaches take a small local sample and search the most similar sample in the next frame. Our task does not match well with registration or optical flow. Motion is highly discontinuous near the plaque, because of the flowing blood and close-by tissues like jugular vein and muscle moving in different directions. Furthermore, image intensities are non-constant; there is a high level of (speckle) noise and

artifacts like saturation and shadowing. All these factors violate the assumptions underlying registration and optical flow. Therefore, a block matching technique is preferred. Blockmatching has been most popular for tracking in ultrasound images in general, and the discontinuity issues for small carotid plaques further strengthen this choice. Given this choice for blockmatching, we further need to focus on a reliable similarity measure and a robust tracking approach to tackle the noise/artifact issues. We considered MDP combined with apodized block matching using NCC similarity a good choice. In block matching NCC was preferred instead of sum of absolute difference (SAD) or sum of square differences (SSD) because NCC is insensitive to brightness and contrast changes of the image and template.

3.1 Block Matching using Normalized Cross Correlation

In case of a plaque motion tracking plaque displacement is assessed through an ultrasound image sequence by tracking the positions of small regions of speckle pattern through consecutive frames. A small rectangular region of the first image containing the speckle pattern (the template) is scanned around a defined search field in the second image to find the position where they best match. This determines the shift in location of the template from the first ultrasound image and all subsequent images in the sequence, as shown in figure 1 and figure 2. The similarity of the template to the image, at each point in the search field, is assessed by calculating their normalized cross correlation (NCC). NCC is commonly used in ultrasound tissue motion tracking since it is not affected by changes in the brightness and contrast of the image and template. The NCC is defined in equation 1 [14]. Here, f(x,y) are the pixels values in the image. The position (x_1,y_1) is the user-indicated position in or near the plaque in the first frame that should be tracked. The rectangular template t_1 around position (x1,y1) of size 2M+1 by 2N+1 pixels contains the tracked structure. $I_1(x, y, 1)$ are the pixel values within this template in the first frame. The template is compared to match blocks $I_t(u, v, t)$ of the same size in other frames, that are displaced by u in the x direction and v in the y direction with respect to (x1,y1). All offset combinations (u,v) within a search region around (x1,y1) are tested and for each one, the correlation value NCC(u,v,t) between template and match block is calculated according to eq.(1). $I_t(x+u, y+v, t)$ is the matching block at frame t where the template $I_1(x, y, 1)$ is scanned through each position in the search region by displacing u pixels in the x direction and v pixels in the y direction. Pixel values of the template $I_1(x, y, 1)$ and the region under the template $I_t(x+u, y+v, t)$ are normalized at each position (u, v) by subtracting their mean values ($\overline{I_1}$, $\overline{I_t}$) and dividing by their standard deviation. $\hat{I}_1(x, y)$ and $\hat{I}_t(x, y, u, v)$ are the normalized template and the region under the template (matching block) respectively. The coefficients can range in value from –1.0 to +1.0. The correlation results in 1 when an identical pattern is found. In the case of noisy images and deformable tissue this will not happen: the best correlation will be the value closest to 1. The correlation coefficients for each position u,v are stored in a matrix. The highest NCC value in the matrix defines the

most likely position, where the template best matches the speckle in the search field.

The template and the match block in the image are apodized by multiplication with a 2D Gaussian kernel (W) which gives higher weight to central pixels and decreases the contribution of peripheral pixels during the calculation of cost value for each pixel in the search field. The size of the 2D Gaussian kernel is the same as the template size.

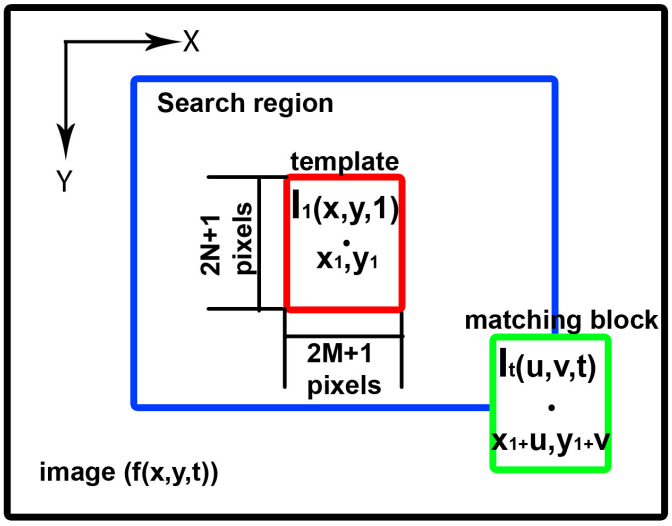

Figure 1: Block matching diagram

$$NCC(u,v,t) = \frac{\sum_{y=y_1-N}^{y_1+N}\sum_{x=x_1-M}^{x_1+M} \hat{I}_1(x,y) \bullet \hat{I}_t(x,y,u,v)}{\sqrt{\sum_{y=y_1-N}^{y_1+N}\sum_{x=x_1-M}^{x_1+M} \hat{I}_1(x,y)^2 \bullet \sum_{y=y_1-N}^{y_1+N}\sum_{x=x_1-M}^{x_1+M} \hat{I}_t(x,y,u,v)^2}},$$

$$\hat{I}_1(x,y) = \left(I_1(x,y,1) - \overline{I_1}\right) \bullet W(i,j)$$

$$\hat{I}_t(x,y,u,v) = \left(I_t(x+u,y+v,t) - \overline{I_t}\right) \bullet W(i,j) \qquad (1)$$

In this study, we chose the parameters of our tracking to match our problem. We are tracking relatively small carotid artery plaques that are located between the carotid lumen and the adventitial wall, close to independently moving blood and tissue like muscle and jugular vein. The motion is relatively small, in the order of few pixels per frame and 5-15 pixels maximum displacement over several

heartbeats. We try to track over prolonged periods spanning several seconds and hundreds of images. We chose to use a fixed template, ~6 x 4 mm (61 x 41 pixels (x,y)), derived from the first image of sequence. To prevent drift in the tracking or loss of tracking, this template is not updated (updating means taking a new template at the detected 'best position'). The image scene is expected to remain stable during the whole sequence, except for transient periods of swallowing etc., so updating is unnecessary and potentially dangerous.

The size of chosen template should be big enough to enclose a distinctive plaque region with uniform motion. When the template size is decreased, the uniqueness of the template pattern decreases; the probability of encountering another similar pattern will increase and false positioning may occur. If template size is increased, other structures with different motion may be included and interfere with the positioning. After several experimental trials the chosen size of the fixed template of 6 x 4 mm proved to be a good compromise. The normalized cross correlation was used to obtain the cost value for each pixel position. The basic cost function was constructed as 1-NCC, which is optimal when it is minimal.

The template was scanned over the following frames to obtain cost values in a 6x2mm search region and cost values are stored in a three dimensional (u,v,t) matrix for using as an input to MDP.

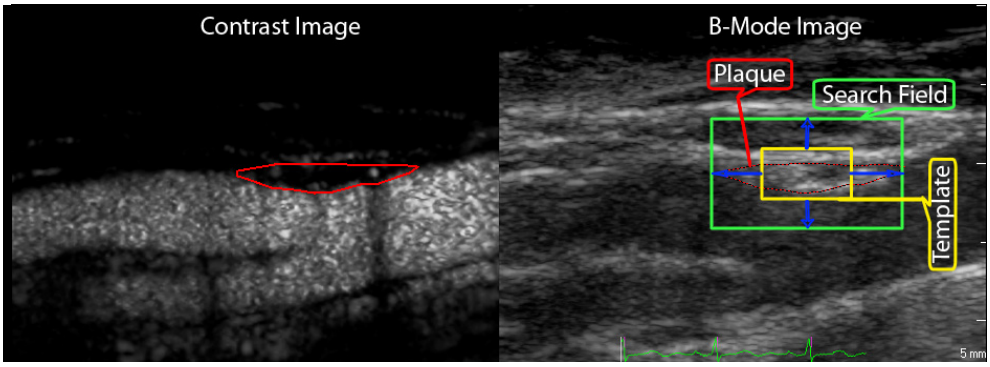

Figure 2: Block matching. The plaque region is outlined manually in the contrast image (left) and shown in the b-mode image (right). A representative tissue point within or near the plaque is indicated manually in the b-mode. A template around this point is extracted and compared to all positions within the search field in consecutive B-mode frames to obtain cost value (1-NCC) for each pixel.

3.2 Multidimensional dynamic programming (2D + t)

Dynamic programming (DP) is a method for solving variational problems by finding locally optimal solutions successively. DP algorithms enable to find an

optimal connective path through a graph of nodes. In image processing, the graph is generally a matrix of cost values related to an image. Each node has a cost and the optimal path is searched through the graph of nodes - the path for which the sum of the costs is minimal. The step size which is the maximum distance between two nodes in consecutive columns is selected based on desired connectivity. An example of DP search for a 1D path is shown in figure 3. On the left (fig. 3a) we see the nodes of the cost matrix, and the connectivity between the nodes when going from left to right. Each node has maximum 3 predecessors in the previous column. Each node has a cost which is derived from an image related cost function. In fig. 3b the cumulative cost for each node is calculated from left to right. In the leftmost column, the cumulative cost is the cost of the node itself. In the next column, for each node the predecessors are compared and the one with lowest cumulative cost is chosen. The cost of the node itself is added to this lowest one to get the cumulative cost for the current node. From left to right, all columns of cumulative costs are filled. In the cost matrix on the right side (fig 3c), the optimal path is found by taking the node in the last column with the lowest cumulative cost and going from right to left using back propagation. The minimal cumulative costs are shown in color and the optimal path connects minimal cumulative costs. This results in a globally optimal path. Note that a simple forward search for the neighbor with lowest cost would not find the optimal path with lowest cost 9, but a suboptimal path with cost 10.

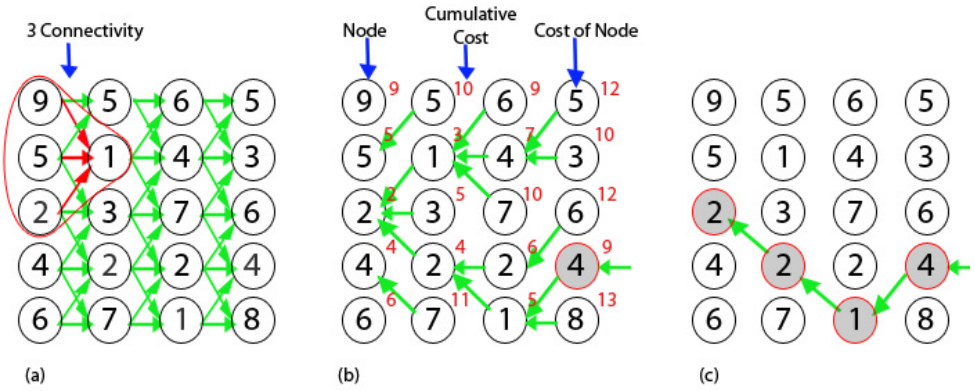

Figure 3: Example of DP search for a 1D path. a: original cost matrix with its connectivity graph b: Cost matrix with cumulative cost c: The optimal path found by backtracking

DP has been widely used in medical image segmentation and tracking. It provides robust solutions and enforces spatial or temporal continuity. In our case we use multidimensional DP for an optimal path search for motion tracking of carotid plaques while enforcing temporal continuity. In this case, we used two dimensional dynamic programming to find the optimum path through a stack of 2D cost function over time (a 3D (2D+t) data set) since the motion is two

dimensional, horizontal and vertical as it is illustrated in figure 4. 2D cost function is obtained from block matching as it explained in section 3.1. The method is based on Nevo et al [14] where it was used for mitral valve tracking. We adapted the method for carotid plaque tracking. Hoogi et al. [15] used a similar approach for motion tracking of contrast spots. Constraints on temporal continuity are imposed by setting limits to the allowed displacement changes between two consecutive frames. Generally, horizontal or vertical displacement is in the order of few pixels from frame to frame. The step size for horizontal displacement from frame to frame was chosen as 5 pixels and 3 pixels for vertical motion, which are considered the maximum displacements that can be seen in two consecutive frames. A side step penalty was applied in both x and y direction during the calculation of cumulative cost in order to penalize fast movements. Then the optimal (minimum cost) path was searched along the time dimension with MDP. To refine the tracking results, a 1:10 subpixel detection was performed in a second iteration of MDP by 1:10 cubic spline interpolation of NCC in neighborhoods of the detected point in each frame.

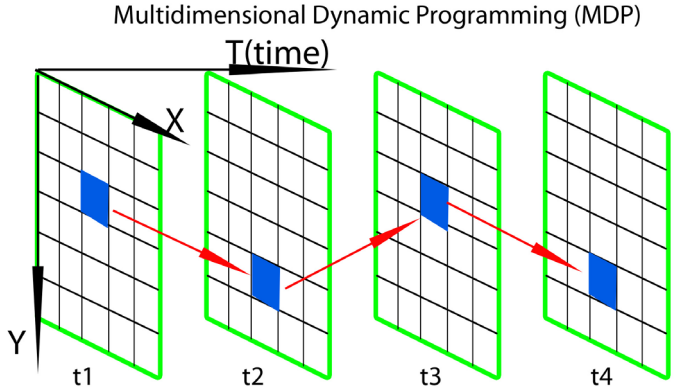

Figure 4: An illustration of multidimensional dynamic programming.

$$pathCost(i+\Delta x, j+\Delta y, k) = \underset{-5\le\Delta x\le+5,\,-3\le\Delta y\le+3}{} CumCost(i+\Delta x, j+\Delta y, k-1) + Cost(i,j,k) * [1+(1/fx)]^{|\Delta x|} * [1+(1/fy)]^{|\Delta y|} \quad (2)$$

$$CumCost(i,j,k) = \min[pathCost(i+\Delta x, j+\Delta y, k)] \quad (3)$$

In equation 2, CumCost is the cumulative cost which is calculated for each node. Cost is the basic cost which is the 1-NCC for each position. k is the frame number. Δx and Δy are side steps from the current pixel. fx and fy are the amount of side step penalty applied in horizontal and vertical directions respectively. The magnitude of these side step penalties were decided after several experimental trials. fx was selected 10 and fy was selected 20 to penalize fast movements. After applying side step penalization, the minimum of the cumulative pathcosts for the neighborhood of predecessors of the current position is taken to assign the cumulative cost for the current position in equation 3. This procedure is repeated

for each position in the column and subsequently for the next column, until all cumulative costs have been found. The position in the last column with minimal cumulative cost is the end of the optimal path, which is found by backtracking (fig 3c).

4. VALIDATION

The MDP was validated in-vitro with a phantom, mimicking carotid lumen and wall, that was moved by a computerized XYZ positioning system with 1mm steps in X and Y directions over 7mm with an accuracy of 5 micron (figure 5a). A b-mode image with the tracked position is shown in fig.5b. The tracked translation is shown in fig 6. The mean error and standard deviation between true motion and measured motion was calculated by taking into account all measured points except for the transition points between the steps (total number of frames N=368 for X, N=372 for Y), shown in table 1.

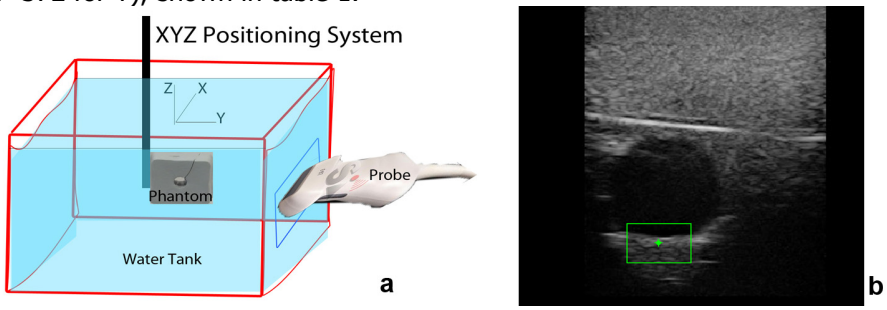

Figure 5: In vitro validation: a: Illustration of in-vitro setup. b: B-mode image of phantom

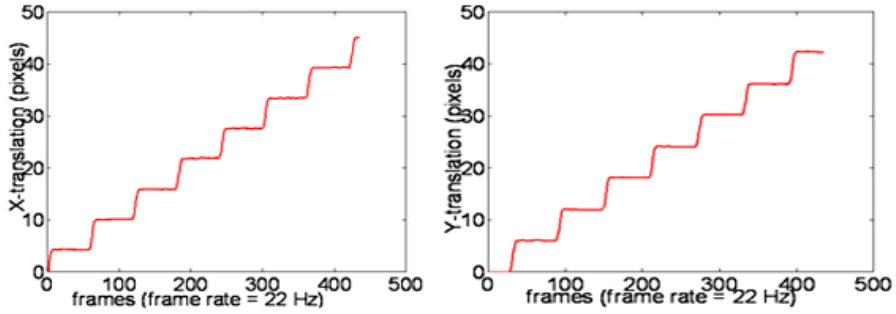

Figure 6: Longitudinal(x) displacement (left) and radial (Y) displacement (right)

In-vivo validation was done by comparing MDP to manual tracking of plaque by three experts for multibeat image sequences (MIS) of 11 plaques (N=1650 frames). Independently, three experts manually tracked the motion of a preferred plaque point in 150 frames of each 11 plaques. The first manual tracking point of each expert was used to initialize an automated tracking. All trackings were expressed as displacements from their respective start positions i.e. displacement for the start frame was 0. This allows direct comparison of the displacement pattern between trackings, irrespective of the absolute start position. The average

of three manual trackings was used as the best estimate of ground truth. Therefore, the standard deviation (SD) of the three from ground truth was considered a measure for the observer variability. The SD of the three automated (MDP) tracking patterns from average of the three was considered a measure for the MDP reproducibility. Mean and standard deviation of these differences (within experts, within MDP and between each MDP and ground truth) were calculated. The results were averaged for 11 plaques and shown in table 2. For comparison, the mean and standard deviation of the ground truth displacement is 384 ± 372 μm for X and 75 ± 95 μm for Y (averaged for 11 plaques).

Furthermore, the MDP success rate was visually assessed on 67 atherosclerotic wall plaque MIS (N=7964 frames). The tracking was considered failed if the MDP visually deviated more than 2 pixels from true motion in any frame.

5. RESULTS

In the phantom validation, the error was 18 ± 19 μm (mean ± standard deviation) for X (longitudinal) and 92 ± 57 μm for Y (radial). This is the error between true motion and measured motion by MDP over 7 mm.

Table 1: Statistics of MDP tracking results in the in vitro validation. All results expressed as mean ± standard deviation in μm.

	Error (mean ± SD)	Range of Displacement
X-translation	18 ± 19 μm	7000 μm
Y-translation	92 ± 57 μm	7000 μm

This shows that there is hardly any bias in X and standard deviation is in the order of 0.1 pixel, so the subpixel accuracy is indeed achieved. For Y, there is a half of a pixel bias and standard deviation is about one third of a pixel. From the linear regression on the data, strong correlation was found between measured and true motion (regression line, $y = 1.0077\,x - 0.0056$, $R^2 = 0.999968$ for X and $y = 0.9739x + 0.0036$, $R^2 = 0.999988$ for Y).

Tracking was visually scored as fully successful in 63 of 67 MIS (94%). The range of displacement over these 63 in X (longitudinal) and Y (radial) was respectively 1045±471μm (mean ± standard deviation) and 395±216μm. The tracking sporadically failed in 4 (6%) MIS due to jugular vein proximity, poor image quality, and out-of-plane motion. In the quantitative evaluation against manual tracking by three experts, absolute error was 72 ± 55 μm for X and 34 ± 23 μm for Y.

Motion compensation showed improved lumen-plaque contrast separation as shown in figure 7. Dynamic programming (MDP) improvement on tracking can be seen on several cases where the forward tracking method fails, such as in figure

10. Success rate with forward tracking was 78% (52 plaques) among 67 plaques. With MDP the success rate increased to 94% (63 plaques). Failure rate was reduced by factor of 4.

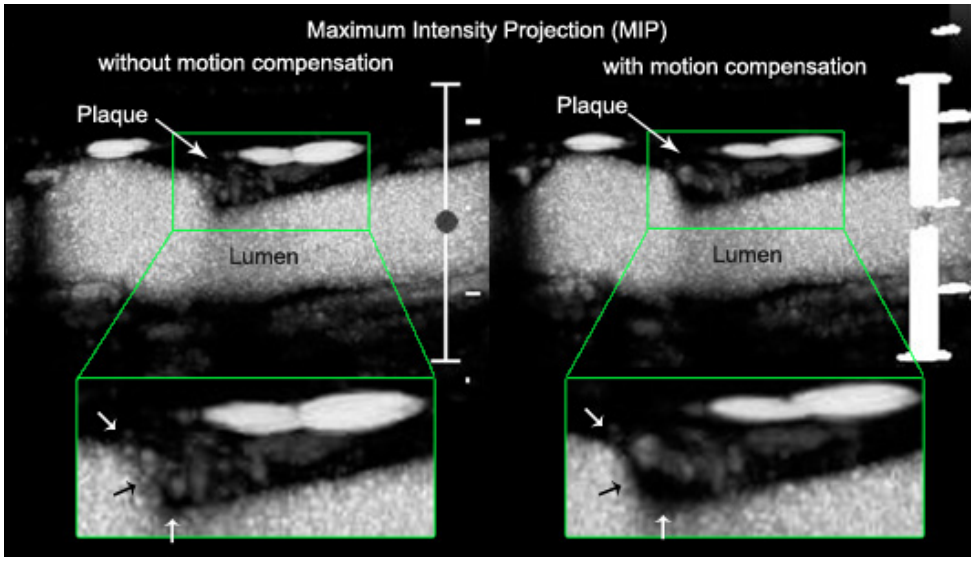

Figure 7: Maximum intensity projection of image sequence of 130 frames without & with motion compensation.

Motion correction showed improved lumen-plaque contrast separation in the maximum intensity projection (MIP) of a contrast image sequence. In a MIP, the maximum intensity over all frames is determined for each pixel. In the case of a moving bubble, the MIP should show the path of the bubble. As can be seen in figure 7, the microvessel path is much clearer with motion compensation than in the MIP image without motion compensation and there is no contrast filling in plaque region from lumen. It is clear that for future analysis of plaque neovasculature, the motion compensation is indispensable.

A typical example of manual and automated tracking is shown in figure 8. Strong correlation was found (R^2 =0.96 for X and R^2 =0.83 for Y) between the displacement obtained by the MDP automated tracking and manual tracking. Linear regression result for longitudinal displacement is shown in figure 9.

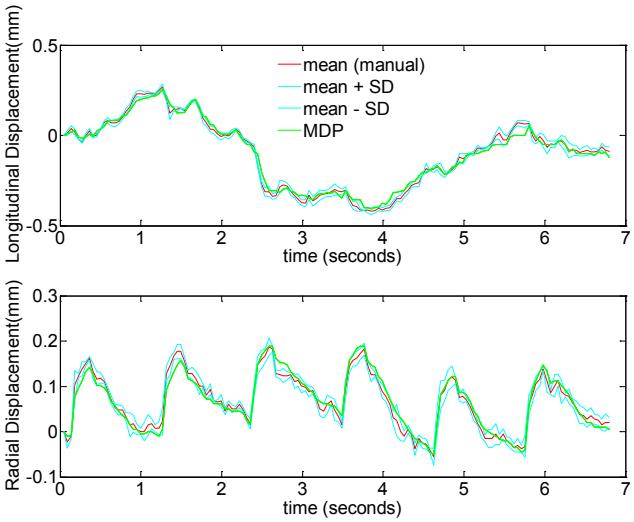

Figure 8: Manual tracking (mean of three experts, red), mean manual tracking ± SD (cyan), and mean of 3 MDP (green) of a plaque in longitudinal and radial direction. (1 pixel = 0.1056 mm).

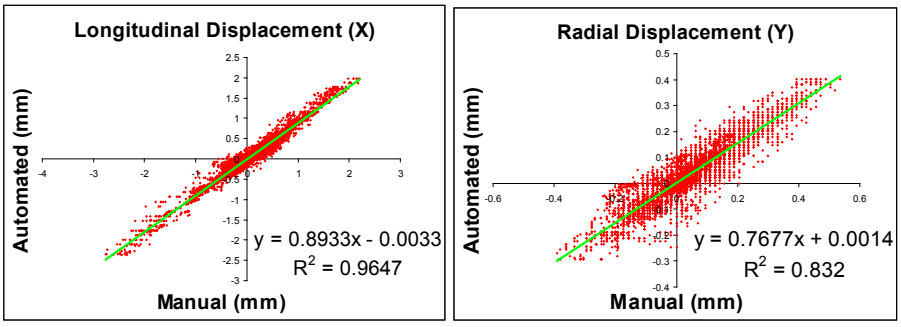

Figure 9: Results of linear regression of longitudinal and radial displacement of plaque region obtained by manual and automated tracking.

Table 2: Statistics of manual (three experts) tracking and automated tracking (MDP) results.
All results expressed as mean ± standard deviation in µm.

Absolute Error	Manual tracking (interobserver variability)	Automated (MDP) tracking (automated reproducibility)	Ground truth(mean manual) vs. Automated tracking(MDP)
Longitudinal(X)	75 ± 45	13 ± 12	72 ± 55
Radial(Y)	32 ± 21	3 ± 3	34 ± 23

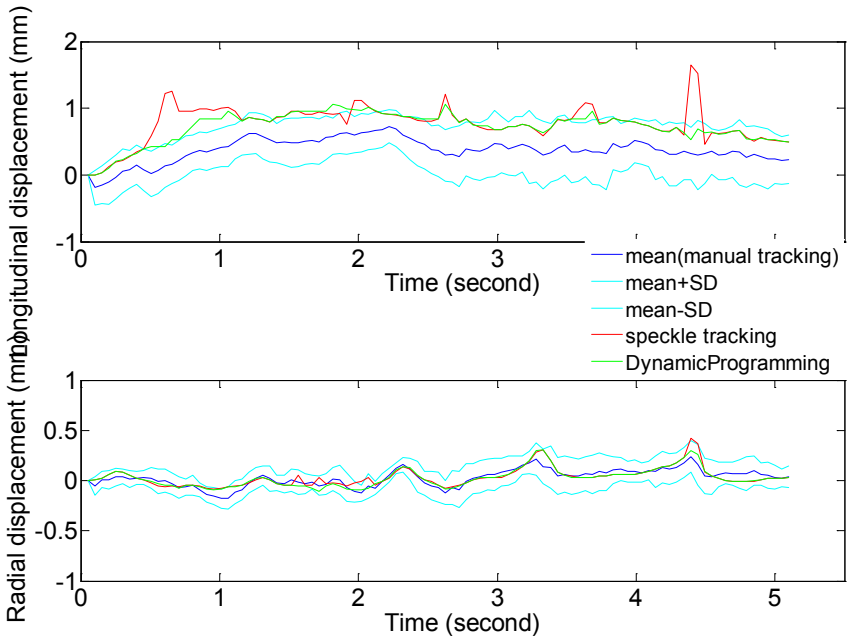

Figure 10: Manual tracking (mean of three experts, blue), mean manual tracking ± SD (cyan), forward tracking (red), and MDP (green) of a plaque in longitudinal and radial direction. (1 pixel = 0.1056 mm).

6. DISCUSSION

We introduced a dedicated motion tracking method with MDP combined with apodized block matching. The proposed method gives detailed motion tracking with 1:10 subpixel detection, which prevents quantization distortion with respect to integer pixel detection. A template size of 6 x 4 mm was chosen, which is wider than the one that was used by Golemati et al. [6] for wall lumen interface. Having a wider template in longitudinal direction experimentally proved to be less subject to tracking loss. Bang et al. [8] used a smaller template but this was used for multiple grid points over a region and averaged to obtain regional motion. In our case we focused on one point tracking to obtain local motion pattern, and thereby the template size should be big enough. Then the optimum motion path is searched with MDP.

In MDP, the maximum allowed step size from frame to frame in X and Y was selected based on the fastest motion that can be seen in our dataset. Generally the motion from frame to frame is not bigger than a few pixels. During the calculation of cumulative cost an additional side step penalty was applied to penalize fast movements. The side step penalty should be selected carefully. If it is too high, it

can cause an over-smoothed path. In the case of a very small penalty, it might not help to improve tracking results. The chosen values represent a reasonable compromise.

Accuracy of the method was evaluated in vitro and in vivo. In phantom validation, the mean error is about half of a pixel for Y directional movements and is about one tenth of a pixel for X direction. It shows there is a systematic error in Y direction, which may be caused by deviation in the speed of sound which depends on the water temperature in the experiment. This seemingly higher error is fully attributable to a small scaling error. This shows that there was a 3% scaling error in Y direction, probably due to a small speed-of-sound difference due to temperature. In X direction, this error is absent for a linear array probe. From the regression coefficient, it can be seen that the random errors in the y direction are smaller than for the X direction, as can be expected in this type of ultrasound image, since the axial resolution is better than the lateral resolution. In the in-vivo validation, in the comparison of three manual trackings against the ground truth, there is a systematic error smaller than a pixel for X and less than half of a pixel for Y, and standard deviation is about half of a pixel for X and smaller than half of a pixel for Y due to variability of manual point selection and interpretation difference of three experts while following true motion. The error between automated tracking and one expert is in the same range as the error of three experts. In the comparison of three automated tracking for the selected points of three experts in table 1, it can be seen that the systematic error is one tenth of a pixel for X and almost 0 for Y and its standard deviation is much lower than the standard deviation of three experts. It means that automated tracking is as good as expert tracking but more reproducible.

The visual assessment of 67 plaques shows that the method is fully successful in a large part (96%) of the cases. However, it failed in some frames of other cases, due to jugular vein proximity, wall saturation, poor image quality, or out of plane motion. The failure rate was reduced by a factor of 4 with MDP when compared to forward tracking. The main drawbacks of forward tracking with block matching are the sensitivity to sudden disturbances and tendency to loss of tracking when there are artifacts, out-of-plane motion, reduced or noisy NCC values, or peak hopping. If gain setting on the machine is not optimized well for the B-mode image, wall or plaque echo might be saturated. When the tissue is moving this saturation can shift with respect to the tissue, causing unreliable tracking. Detection or suppression of such artifacts may prevent such problems. Poor image quality and out of plane motion can cause the loss of tracking due to poor correlation. Proximity of the jugular vein to the carotid artery is another reason for tracking to fail since this induces opposing motion patterns close together. In this case a smaller or vertically shifted template might help to exclude jugular vein to improve tracking. To be able to deal with the sporadical failure of tracking in the cases of bad image quality, out of plane motion, or wall saturation, MDP will help and improve the tracking results. For some severe cases, other

solutions would be needed, but for the large majority of cases the method is robust enough in practice.

7. CONCLUSION

Multidimensional dynamic programming provided improved tracking. When the correlation is good the dynamic programming will give the same results as forward tracking of the best correlation. In the case of transient loss of correlation MDP provides an overall optimal continuous path for tracking and thereby MDP is less subject to tracking loss. The MDP combined with apodized block matching method is more robust to noise than forward tracking. In the in-vivo comparison, the automated method performed within the range of interobserver variability. In conclusion, the proposed motion tracking method is sufficiently accurate and successful for in vivo application. Our method will allow improved quantification of IPN.

ACKNOWLEDGMENT

This research was supported by the Center for Translational Molecular Medicine and the Netherlands Heart Foundation (PARISk).

REFERENCES

[1] Sabetai M.M., Tegos T.J., Nicolaides A.N. "Reproducibility of computer-quantified carotid plaque echogenicity: Can we overcome the subjectivity?" Stroke 31, 2189–2196 (2000).
[2] Mathiesen E.B., Bonaa K.H., Joakimsen O., "Echolucent plaques are associated with high risk of ischemic cerebrovascular events in carotid stenosis: the Tromso study," Circulation 103, 2171–5 (2001).
[3] Griffin M., Nicolaides A., Kyriacou E., "Normalisation of ultrasonic images of atherosclerotic plaques and reproducibility of grey scale median using dedicated software," Int Angiol 26, 372–7 (2007).
[4] Feinstein S.B., "Contrast ultrasound imaging of the carotid artery vasa vasorum and atherosclerotic plaque neovascularization," J Am Coll Cardiol 48, 236-43 (2006).
[5] Staub D., Patel M.B., "Tibrewala A., et al. Vasa vasorum and plaque neovascularization on contrast-enhanced carotid ultrasound imaging correlates with cardiovascular disease and past cardiovascular events," Stroke 41, 41-7 (2010).
[6] Golemati S., Sassano A., Lever M.J., Bharath A.A., Dhanjil S., Nicolaides A.N., "Carotid artery wall motion estimated from B-mode ultrasound using region tracking and block matching," Ultrasound Med Biol. 29, 387–399 (2003)
[7] Chan K.L., "Two approaches to motion analysis of the ultrasound image sequence of carotid atheromatous plaque," Ultrasonics 31(2), 117–123 (1993)
[8] Bang, T.D., Bruinsma A., Kaspersen J.H.,Hernes T.A.N., Myhre H.O., "A new method for analysis of motion of carotid plaques from rf ultrasound images," Ultrasound Med Biol, 29(7), 967-976 (2003).
[9] Akkus Z, Ramnarine V.K., "Dynamic assessment of carotid plaque motion," Ultrasound 18(3), 140 – 147 (2010)
[10] Dave J.K., Forsberg F., "Novel automated motion compensation technique for producing cumulative maximum intensity subharmonic images," Ultrasound in Med. & Biol., 35(9), 1555–1563 (2009).
[11] Gastounioti A., Golimati S., Stoitsis J., Nikita K.S., "Comparison of Kalman filter based approaches for block matching in arterial wall mtion analysis from B-mode ultrasound," Meas. Sci. Tech. 22(9), 114008(9pp) (2011).
[12] Akkus Z., Bosch J.G., Renaud G., Hoogi A., ten Kate G.L., van den Oord S., Schinkel A., de Jong N., van der Steen A.F.W., "Motion Compensation Method for Quantification of Neovascularization in Carotid Atherosclerotic Plaques with Contrast Enhanced Ultrasound (CEUS)," Proc. of IEEE International Ultrasonics Symposium, Orlando, in press (2011).
[13] Üzümcü M., Van der Geest R.J., Swingen C., Reiber J.H.C., Lelieveldt B.P.F., "Time continuous tracking and segmentation of cardiovascular magnetic resonance images using multidimensional dynamic programming," *Invest Radiol* 41, 52– 62 (2006).
[14] Nevo S.T., Van Stralen M., Vossepoel A.M., Reiber J.H.C., De Jong N., Van der Steen A.F.W., Bosch J.G., "Automated tracking of the mitral valve annulus motion in apical echocardiographic images using multidimensional dynamic programming", Ultrasound in medicine & biology, 33(9), 1389-99 (2007).
[15] Hoogi A., Bosch J.G., Akkus Z., Renaud G., ten Kate G.L., van den Ord S., Schinkel A., de Jong N., Dan A., van der Steen A.F.W., "Quantitative analysis of flow behavior of carotid plaque neovasculature," Proc. IEEE Int Ultrasonics symposium, Orlando, (in press) (2011).
[16] Ferguson G.G., Eliasziw M., Barr H.W.K., Clagett G.P., Barnes R.W., Wallace M.C, Taylor D.W., Haynes R.B., Finan J.W., Hachinski V.C., Barnett H.J.M., "The North American Symptomatic Carotid Endarterectomy Trial," Stroke 30, 1751-1758 (1999).
[17] Rothwell P.M., Gutnikov S.A., Warlow C.P., "Reanalysis of the Final Results of the European Carotid Surgery Trial," Stroke 34, 514-523 (2003).

Chapter 3

Quantitative analysis of ultrasound contrast flow behavior in Carotid Plaque Neovasculature

Intraplaque neovascularization is considered as an important indication for plaque vulnerability. We propose a semiautomatic algorithm for quantification of neovasculature, thus, enabling assessment of plaque vulnerability. The algorithm detects and tracks contrast spots using multidimensional dynamic programming. Classification of contrast tracks into blood vessels and artifacts was performed. The results were compared with manual tracking, visual classification and maximal intensity projection. In 28 plaques, 97% of the contrast spots were detected. In 89% of the objects, the automatic tracking determined the contrast motion with an average distance of less than 0.5 mm from the manual marking. Furthermore, 75% were correctly classified into artifacts and vessels. The automated neovascularization grading agreed within 1 grade with visual analysis in 91% of the cases, which was comparable to the interobserver variability of visual grading. These results show that the method can successfully quantify features that are linked to vulnerability of the carotid plaque.

A. Hoogi, Z. Akkus, S. van den Oord, G.L. ten Kate, A. Schinkel, J.G Bosch, N. de Jong, A. Dan, A.F.W. van der Steen**. Quantitative analysis of ultrasound contrast flow behavior in Carotid Plaque Neovasculature.** Ultrasound Med. Biol., 38(12):2072-2083, 2012.

INTRODUCTION

Atherosclerosis, a systemic disease of the arterial wall, may be considered at some stages as a form of cardiovascular inflammatory disease (Amini et al. 1990; Ogata et al. 2005). The important contribution of carotid atherosclerosis to the pathogenesis of cerebral events has been recognized (Gomez 1990). Atherosclerosis-related stroke or myocardial infarction have been linked to the presence of neovascularization and inflammation in the atheromatous plaque, which are considered reliable markers of vulnerability of the plaque and predictors of its rupture (Huang et al. 2008). Moreover, the study of (Barger et al. 1984) indicated that in most cases, atherosclerotic plaques and the neovascularization process come together. The role of the neovascularization in the plaque vulnerability is as following: The first stage in the formation of atherosclerotic plaques is vessel wall thickening as a result of endothelial damage. Vessel wall thickening is caused by infiltration of low-density lipoproteins (LDL) into the intima complex of the vessel wall. Consequently, monocytes are triggered to migrate through the vessel wall and differentiate to macrophages. The macrophages take up the modified LDL and form the so called macrophage foam cells. This leads to a more complex inflammatory response in the affected vessel wall (Libby et al. 2011). As this process progresses, more advanced atherosclerotic plaques are formed. During the formation of these plaques, the vessel wall thickness will exceed the oxygen diffusion threshold. This will lead to a release of a number of angiogenic growth factors such as hypoxia inducible transcription factor (HIF). These factors will trigger the physiologic vasa vasorum to proliferate into the atherosclerotic plaque (Falk 2006; Sluimer and Daemen 2009; Sluimer et al. 2008). The immature neovessels may promote the formation and destabilization of this atherosclerotic plaque and these vessels are associated with future cardiovascular events (Hellings et al. 2010).

Hence, the indication for carotid endarterectomy, which is commonly based on the degree of diameter stenosis may be insufficient, while risk evaluation based on the plaque composition would be valuable in the treatment decision process (Nandalur et al. 2005; Barnett et al. 2002). Therefore, developing a non-invasive imaging method based on quantification of plaque vascularization to assess plaque vulnerability is highly desirable. In addition, monitoring neovascularization response to drug treatment, as an expression of the inflammation process, may be obtained (Lin and Alessio 2009; Parker et al. 1988; Rissanen et al. 2008). In our study, the plaque is monitored by 2D ultrasound (US) imaging which is a noninvasive, reliable, accessible, and cheap image acquisition modality (Molinari et al. 2007). The spatial resolution of carotid ultrasound imaging is approximately 0.1 mm which is better than with MR, CT or X-ray angiography imaging of the carotids (Lin and Alessio 2009). This resolution refers to a 4 cm depth and a fundamental frequency of at least 7MHz (Stein et al. 2008). Moreover, contrast-enhanced ultrasound imaging (CEUS) allows detection of contrast microbubbles in very small vessels with high sensitivity. Since CEUS can detect single microbubbles due to their strong reflectivity, blood flow within vessels of sizes less than 50 microns can

be detected (Hsu and Chen 2008; Willmann et al. March 2010). Several researches utilized the advantage of CEUS imaging in detecting neovascularization (Lin and Alessio 2009; Hoogi et al. 2011; Giannarelli et al. 2010).

Several semi-quantitative visual approaches to quantify contrast enhancement of intra-plaque neovascularization on contrast-enhanced ultrasound images have been reported (Fleiner et al. 2004; Giannoni et al. 2009; Coli et al. 2008), usually by using a discrete limited grading system. Those authors categorized the echogenicity as low if no bubbles were detected and as high if extensive contrast enhancement was depicted (Shah et al. 2007) used a semi-quantitative grading system based on visual interpretation alone, from the absence of neovascularization (grade 0) to high echogenicity (grade 3) caused by a high amount of contrast agent enhancement.

Several studies used maximum intensity projection (MIP) to reconstruct an arterial tree (Hoogi et al. 2011; van Ooijen et al. 2003; Suri et al. 2002). Maximum intensity projection (MIP) is a 2D projection image obtained from a time sequence of 2D data by searching for every pixel the highest intensity value over time. In un-enhanced ultrasound imaging, MIP can be used to evaluate the general morphology of relevant objects, such as the carotid plaques. However, in contrast-enhanced ultrasound (CEUS) it has additional contribution in detection of the vessel trajectories. A major drawback of MIP is its high sensitivity to noise and to the quality of the applied motion compensation, thus a MIP analysis can produce an over-estimated arterial tree. Therefore, using MIP enforces a preliminary high quality filtering (Anderson et al. 1990). Another drawback of MIP is its absence of any temporal information on the examined objects. Therefore, it encounters difficulties in differentiation between artifacts and blood vessels and produces over-estimated results of the neovascularization inside the plaque. To our knowledge, there are no other studies published in the literature quantifying the intra-plaque neovascularization by demonstrating the 2D behavior of a contrast spot over time. We utilize the importance of the temporal behavior as described in the following pages.

In the present study, a semi-automatic algorithm is developed. A multidimensional dynamic programming (MDP) method is implemented to reconstruct the neovascularization tree in a CEUS image of the carotid plaque. The main advantage of this method is its ability to take discrete contrast blobs and generate continuous routes, demonstrating the temporal behavior of bubbles' flow. It was tested on a large set of clinical cases, and required minimal intervention of the operator. In comparison to common methods such as forward tracking, the algorithm is robust to noise and allows differentiation between blood vessels and artifacts. Therefore, it provides much more accurate results than other methods which do not have any temporal information, such as the MIP described above.

MATERIALS AND METHODS

Patients' population and imaging acquisition

Seventy six patients without established atherosclerotic disease were recruited if they had at least one clinical risk factor for the development of atherosclerosis (i.e. Hypercholesterolemia, Diabetes, Smoking, Hypertension, positive family history). The study was approved by the institutional review board (Dutch NTR2239) and a written informed consent was obtained from each participant. Standard carotid ultrasound and CEUS were performed with a Philips iU-22 ultrasound system (Philips Medical Systems, Bothell, USA), equipped with an L9-3 probe. Image acquisition was performed by a trained sonography technician using a standard scanning protocol according to the American Society of Echocardiography consensus statement (Stein et al. 2008). The left and the right common carotid artery (CCA), carotid bifurcation, internal carotid artery (ICA), external carotid artery (ECA), and vertebral arteries were imaged by B-mode ultrasound, color Doppler and pulse-wave Doppler. Each side was extensively evaluated for the presence of carotid plaques. The degree of stenosis of the CCA, ICA and ECA was assessed according to current guidelines on the basis of spectral Doppler velocities. After standard carotid ultrasound, CEUS was performed using intravenous administration of SonoVue contrast agent (Bracco S.p.A., Milan, Italy). The ultrasound system settings were optimized for CEUS, using a dual display mode for simultaneous standard B-mode ultrasound and CEUS. The mechanical index for CEUS was lowered to 0.06-0.08 and the frame rate was adjusted to 20Hz. Before injection of the ultrasound contrast agent the intravenous access was flushed with a 5.0 ml saline (NaCl 0.9%) solution bolus injection. The ultrasound contrast agent was injected in boluses of 0.5 ml. Each contrast agent bolus was followed by a 2.0 ml saline flush. After administration of contrast agent, high-quality contrast images could be obtained for approximately 1 minute. Contrast administration was repeated when required up to a maximum total dose of 10.0 ml. Still frames and cine clips were digitally stored for offline analysis. Loops were acquired of longitudinal cross-sections that best visualized the plaque. Since we dealt with two dimensional planes, they were recorded from different angles, to fully characterize the atherosclerotic plaques. Cine loops were recorded, starting from the time the contrast agent was seen in the carotid lumen (after the flash) till most of it had disappeared. From the total set of acquisitions, cine loops were selected for analysis based on plaque size, plaque location and presence of artifacts. Plaques of thickness below 1.5 mm, or obscured by heavy shadowing or saturation in the plaque were excluded from analysis. Plaques smaller than 1.5 mm are hard to analyze reliably. The effect of out-of-plane motion caused by every heartbeat is more obvious in these small plaques than in the bigger plaques. Small plaques can completely disappear out of plane, making motion compensation and bubble tracking impossible.

Plaques in the distal wall and proximal plaques below significant contrast in the jugular vein were excluded because of the significant contrast-induced artifacts reported for such locations (ten Kate et al. 2012). Therefore, we only analyzed plaques that were located at the proximal wall of the artery (CCA, ICA or ECA) near the bifurcation of the carotid.

From the remaining sequences, a subset was drawn randomly. In total, cine loops of 28 different plaques (of 27 different patients) were selected for analysis. The characteristic length of the analyzed sets was 118 ± 49 frames (about 6 seconds). The high prevalence of atherosclerotic plaques in this asymptomatic population with an increased risk is similar to that found in other studies (Chahal et al. 2011)

Data analysis

The cine loops that were acquired during each clinical examination were transferred as DICOM files to a computer workstation for off-line post-processing and were analyzed by an algorithm especially developed for this purpose, using Matlab software (The Mathworks Inc., Natick, Massachusetts,US). Figure 1 presents the various steps of the algorithm.

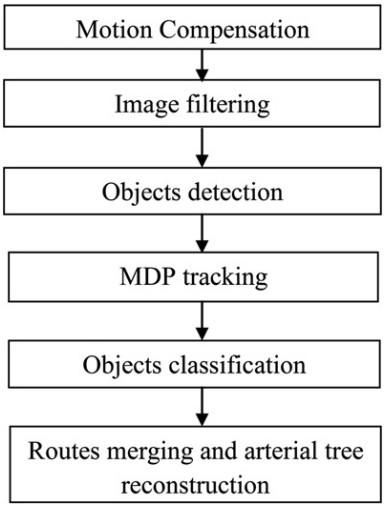

Fig. 1: The main steps of the developed algorithm for quantification of the neovascularization inside the plaque.

Motion compensation

The first step of the algorithm is motion compensation that is performed by applying a forward-tracking block matching (BM) method as described in (Akkus et al. 2011). The local motion pattern of the plaque region is extracted from the B-mode image with BM and applied to the corresponding region in the contrast image. First, the user selects the point to be tracked in the first image of a given sequence. A fixed template of 49 x 49 pixels around this point is derived from the first image of the sequence. Then the plaque displacement is assessed through the sequence by tracking the template's speckle pattern with BM through consecutive frames. The template's center position is scanned over all positions within a defined search field in each image to find the position where they best match. This determines the shift in location of the template from the first ultrasound image and

all subsequent images in the sequence, as shown in figure 2. The search field extends 10 pixels in each direction from the best position found in the previous frame. This is big enough to handle the maximum motion from frame to frame, which is in the order of a few pixels. The similarity of the template to the image, at each point in the search field, is assessed by normalized cross correlation (NCC). This similarity measure is commonly used since NCC is insensitive to local variations. . The local plaque motion pattern is obtained by following the highest correlation values through the image sequence. The contrast images are aligned to the first contrast image based on detected plaque displacement in X and Y direction for motion correction.

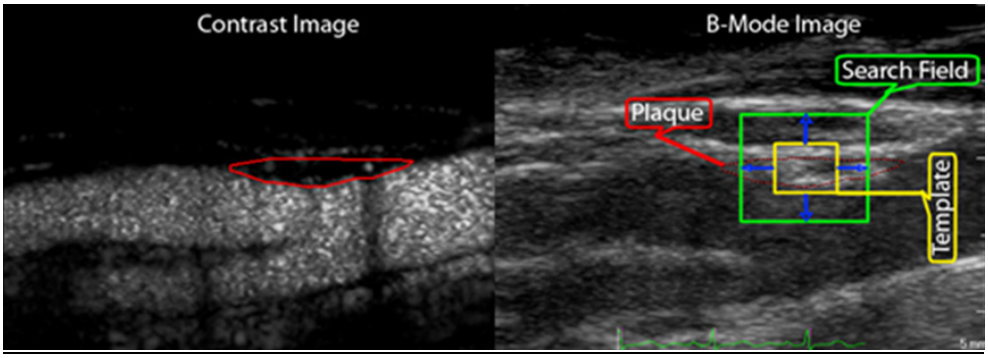

Fig. 2: Block matching method. The plaque region is manually outlined in the contrast image (left) and shown in the bmode image (right). A representative tissue point within the plaque is indicated manually in the B-mode. A template around this point is extracted and compared with all positions within the search field in consecutive B-mode frames. The obtained motion pattern for the plaque region is applied to the contrast images.

Noise reduction

Noise reduction is performed by using a 2D Gaussian filter of 5*5 pixels with $\sigma = 1$. The width of the window is carefully chosen in order to prevent smoothing and blurring of the contrast accumulations, thus it should be smaller than the characteristic size of a contrast accumulation. Those accumulations have characteristic size bigger than 7*7 pixels. In addition to the Gaussian filter that is applied over all frames, an adaptive threshold is calculated as an additional way to eliminate noise. This threshold is calculated in a region of interest (ROI) which is manually chosen by the user. The ROI should be close enough to the borders of the plaque without taking into account the lumen or the arterial wall, thus preventing artifacts. The threshold is independently calculated in the first frame for each patient by using the 10^{th} percentile of the gray values in this ROI. All values below the threshold are set to zero and the rest are left intact. The 10^{th} percentile is a safe choice for the threshold since we assume that most of the plaque area is background (non-contrast).

This low threshold will minimize false negative cases, at the cost of more false positives (that can be eliminated in a later stage).

After applying the noise reduction, the US sequence is divided into overlapping groups of 10 frames each. Time duration of 10 frames is supposed to be sufficient to see continuous presence of an object (as opposed to noise) and to detect a reasonable amount of motion of the object (as opposed to artifacts). In the first frame of the group, candidate objects are detected whose motion is followed over the group. An eight frames overlap (80%) between subsequent groups is chosen to minimize false negative cases. The following object detection is implemented only on the first frame of each group.

Contrast spot detection

An artificial 'bubble' template is used for the detection of contrast-like objects. It exploits the geometrical characteristic and the gray levels distribution of a typical contrast spot. An artificial template is constructed resembling a typical pattern of real bubbles (Fig 3a). The template takes into account parameters as reasonable 'radius' and varying gray levels. Maximal intensity is determined at the center point and constant linear decrease of gray levels is applied in correspondence with the distance from that point.

The artificial template is correlated with different areas in the chosen ROI using normalized cross correlation. A correlation coefficient matrix is calculated (Fig 3c) and the maximal correlation is located. Then, the correlation values in a 5*5 neighborhood around this location are set to zero. The detection of the maximal correlation, as well as the deletion of its close neighborhood, are performed iteratively till the maximal correlation value is below 0.6, which we take as the threshold for a contrast spot to be considered as a bubble (Fig 3d). Several radii of 3,5,7 and 9 pixels are examined for the artificial bubble template. The sets of found points are united to obtain a complete detection of the objects.

After detecting the contrast spots in the first frame of each group, tracking is performed by dynamic programming between the first frame of each group and its last frame.

Bubble tracking by dynamic programming

Dynamic Programming (DP) is an optimal approach for solving variational problems by finding locally optimal solutions consecutively. The idea is to track the two-dimensional displacement of a bubble in the plaque over time. This corresponds to finding a connective path in the time direction through a three-dimensional (X,Y,T) matrix with minimal total cost by multidimensional DP (Fig.4) (Nevo S . T . et al. 2007). After the tracking process has detected the 'optimal path' over 10 frames, the gray values of the object along the path are evaluated. By removing all path points where the gray level is below a predefined threshold (the detailed 10^{th} percentile threshold) one can decide when a bubble is gone.

The resulting optimal path is determined by the following parameters described below: costs (correlation values) and path smoothness (allowed step size and side step penalty)

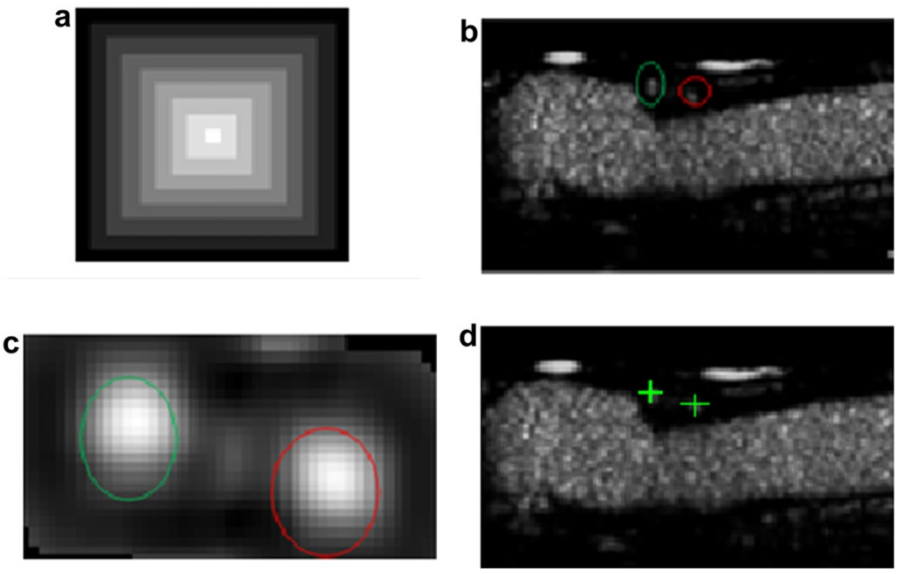

Fig. 3: Objects detection by an artificial template. (a) An artificial bubble with a 9-pixel "radius." (b) Original image with two intra-plaque objects and their corresponding locations in the correlation matrix. (c) The correlation matrix. (d) The final detection.

Correlation values

For each object a template of 13*13 pixels around its center is taken from the first frame of each group. Similar to the motion compensation process, each template is correlated for the other 9 frames in the group within a search area of 41*41 pixels around the location of the detected object in the first frame. The size of the search area is large enough to accommodate a maximal displacement of 20 pixels over 10 frames. Before the correlation process takes place, both templates are apodized similar to (Nevo S . T . et al. 2007) with a 2D Gaussian weighting characterized by σ=3. This weighting is applied to reduce the relative contribution of the background to the NCC. NCC is optimal when it is close to its maximal value of 1. To use NCC properly in the MDP minimization process we use for the basic cost function: $(1 - NCC)^{1/3}$ (equation 1, part A).

Step size

The connectivity of the graph should fit the maximum distance that a bubble accumulation can pass in two sequential frames. The allowed step size is taken as 3 pixels, corresponding to 6mm/s, large enough to handle the possible motion of bubbles in small vessels. Furthermore, temporal smoothness of the motion is controlled by the side step penalty which is presented in (equation 1, part B) (Nevo S . T . et al. 2007).

$$F(x,y) = \underbrace{(1-NCC)^{1/3}}_{A} \cdot \underbrace{\left\{(1+1/f_x)^{|\Delta x|} \cdot (1+1/f_y)^{|\Delta y|}\right\}}_{B} \quad (1)$$

where Δx and Δy are the distances that a specific pixel can go through in sequential frames. These distances can be in the allowed range of [-3, 3], in x and y direction respectively. f_x and f_y are the weights corresponding to those distances. Their value was chosen to be 10 to penalize fast movements.

Relative to forward tracking, our method has several advantages for evaluating the contrast spots motion. First, it exploits the MDP advantages: relatively insensitive to noise and small disturbances, efficient and producing a time continuous motion (Rabben et al. 2000). When the correlation is good the dynamic programming will give the same results as forward tracking of the best correlation. However, in the case of transient loss of correlation or excessive noise, MDP provides an overall optimal continuous path for tracking and thereby is less subject to tracking loss. Another benefit from the MDP search is the 2D path derived from it. In this way, our technique is capable of evaluating the spatial displacement of the intra-plaque objects in both the horizontal and the vertical direction. Third, it takes the advantages of block matching using normalized cross correlation (NCC): robust against linear changes, fast and proven (Nevo S . T . et al. 2007).

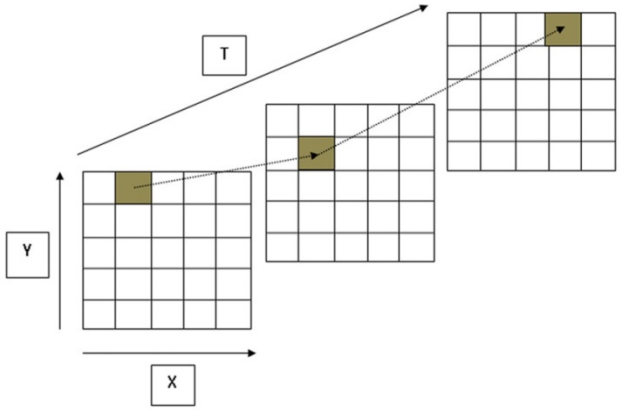

Fig. 4: Example of 2-D dynamic programming. Each slice represents the cost function at a certain frame. The optimal path is shown with arrows.

Contrast spot classification and routes merging

After detecting the objects' routes by using the MDP, the following steps are applied. First, a classification of the objects into two categories is performed: actual blood vessels and artifacts. The classification is necessary to remove artifacts from further processing and exclude them from plaque vulnerability estimates. The classification is based on a minimum expected displacement for moving bubbles as opposed to stationary artifacts. We apply a threshold of 8 pixels

(~0.8mm) for the XY displacement (eqn. 2) of an object over a group of 10 frames. Below this threshold, the object is classified as artifact. This threshold corresponds to a bubble velocity of 2mm/s, which is low for blood flow even in capillaries.

$$\text{XY displacement} = \sqrt{\{(X_{max} - X_{min})^2 + (Y_{max} - Y_{min})^2\}} \qquad (2)$$

Second, a merging of reconstructed routes which are supposed to be of the same vessel is performed. . Merging means that different routes which probably represent the temporal behavior of the same object should be handled as following: the shorter one is deleted while the longer route remains to represent both of them. For the merging process two parameters should be measured. The first one is the mean distance between two examined routes. Three pixels (~0.3mm) distance threshold was predefined due to experimental trials, taking into account the characteristic size of a bubble (bigger than 7*7 pixels). The second is the overlapping percentage between two routes. Above 60% pixels overlapping is needed for one route deletion (60% of the short route is located in a distance smaller than 3 pixels from the longer one).

Algorithm validation

Manual marking of contrast routes, maximal intensity projection (MIP) and visual grading were performed and compared to the algorithm results for its validation. To evaluate the accuracy of the tracking, two independent observers manually marked the location of each object over time. An object was visually detected based on its area and gray level. For every plaque with contrast spots inside, the observers manually tracked each object (artifact or vessel) from the frame it appeared till it disappeared. Plaques without any contrast spots inside were visually classified as neovascularization grading 0, and had no manual contrast tracking. For each object, the mean distance between routes that were manually marked by the 2 observers was measured, as well as standard deviation (SD) values. An average route between those 2 routes was calculated. The total XY displacement along this route and its total length were calculated. This average route was compared to the algorithm results. Mean and SD values of the distances between the automatically reconstructed route and the average manual route were calculated. Mean distance smaller than 5 pixels (0.525 mm) was considered as a high accuracy of the algorithm analysis, since characteristic size of a contrast spot is above 0.8 mm. Interobserver variation was around 0.2 mm.

The equivalent XY displacement and total length of the automatically reconstructed route was also measured.

The XY displacement results were also compared to the Maximal Intensity Projection (MIP) results to show the advantage of our method over commonly used methods such as the MIP.

The MIP was implemented on the plaque area after motion compensation and after applying the same 10^{th} percentile threshold which is used in the 'noise reduction' section of the presented algorithm. The MIP image was examined and analyzed only if discrete routes could be seen inside. If not, the MIP image of the specific plaque was ignored. For plaques of which the MIP image could be analyzed, a skeleton was implemented to extract the blood vessels centerlines. Thresholding followed by a thinning procedure is a common method which is presented in several papers (Parker et al. 1988; Poli and Valli 1997; Tozaki et al. 1994). The XY displacement of each reconstructed centerline route was calculated and compared to the results obtained by our method. Due to lack of temporal information and the stringent requirements of optimal noise reduction and motion compensation while using MIP (Anderson et al. 1990), the detection of blood vessels can be inaccurate. As a result, the neovascularization grading will be inaccurate.

The visual classification of objects into actual blood vessels and artifacts, was based on their visually assessed motion pattern and gray value appearance over time.

The decision process of the automated neovascularization grading is performed analogous to the physician's decision using the number of detected blood vessels: 0 for no vessels, 1for 1 vessel, 2 for 2 vessels and 3 for 3 or more vessels.

RESULTS

One hundred and four objects were visually detected in 28 movies. One hundred and one objects were automatically detected and only three objects were missed. The automated detection additionally found 4 false positive objects.

Figure 5 presents the detection of an object inside a plaque and its whole reconstructed route over time, obtained by the MDP method.

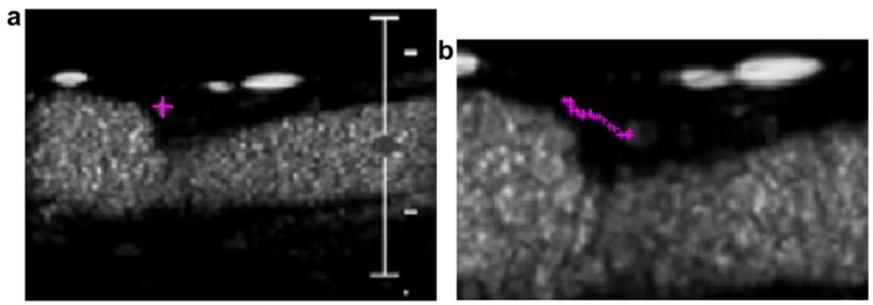

Fig. 5: Detecting and tracking an intra-plaque object. (a) The intra-plaque detected object. (b) Its reconstructed route over time.

In figure 6, a comparison between the automatic and the manual reconstructed routes of the same object is presented. They show a very similar motion pattern with a small bias of 1-2 pixels.

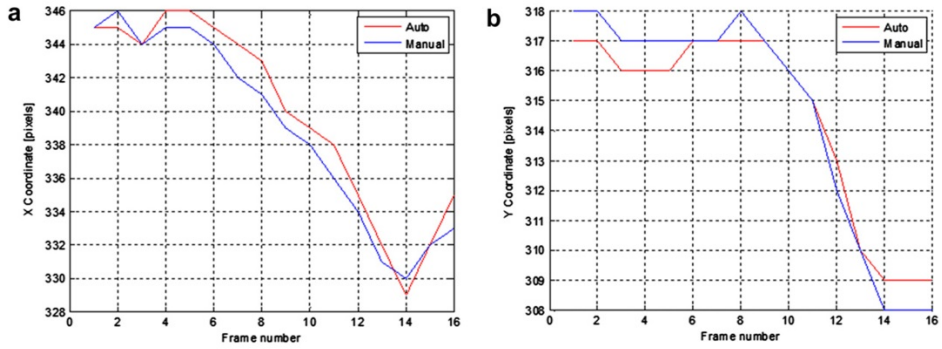

Fig. 6: Comparison between a reconstructed route using the presented method and the manual result. (a) X position over time. (b) Y position over time.

Ninety objects were accurately tracked, following the constraint that was presented in the methods section. In the other 11 objects tracking was lost over time due to noisy images or very blurry objects inside the plaque.

The 104 objects were classified visually into 40 actual blood vessels and 64 artifacts. The mean and SD values of the XY displacements of objects visually classified as blood vessels and artifacts were $1.14 \pm 0.36\ mm$ and $0.53 \pm 0.31\ mm$ respectively. The difference between those populations was significant ($p<0.001$). Therefore, a 0.8mm threshold to differentiate between those populations was chosen. Applying this threshold, one can see in Table 1 that 76 of the 90 well tracked contrast spots were correctly classified in comparison to the visual classification.

Table 1: Classification of 90 objects into blood vessels and artifacts according to visual analysis and automated analysis

Visual Algorithm	Blood vessels	Artifacts
Blood vessels	35	12
Artifacts	2	41

Figure 7 presents an example of 3 identified spots in a carotid plaque and their classification.

Figure 8 presents the merging process over two examples of plaques. Figure 8(a-b) presents the all detected blood vessels over the whole cine and before the merging process. Figure8 (c-d) shows the final neovascularization tree after the routes were merged. In Fig.8a and 8c, 2 separate routes of different contrast spots were reconstructed. In Fig.8b and 8d, 2 routes which split from a common 'trunk' of the arterial tree are shown (the flow is from the right side of the image to the left side).

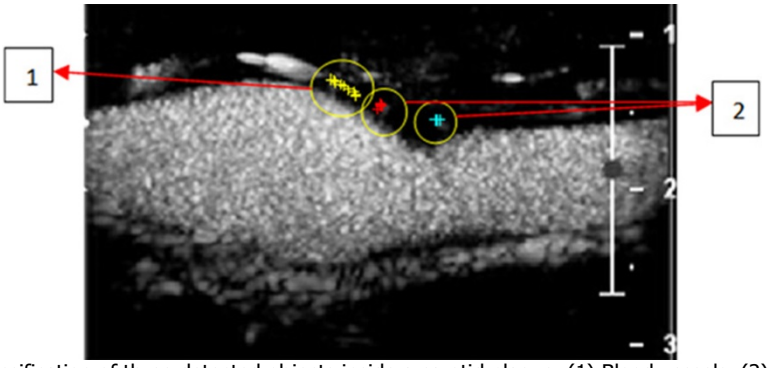

Fig. 7: Classification of three detected objects inside a carotid plaque. (1) Blood vessels. (2) Artifacts.

Table 2 compares the automatic and the manual results. It presents the average and the SD results that were calculated over 31 classified vessels from the 28 plaques (the vessels that are mentioned in table 1).

Comparison to the maximal intensity projection (MIP) method was performed. In twenty-two plaques discrete routes could be seen, thus could be analyzed. In other 6 plaques the MIP image didn't include any clear routes inside but large undefined areas, thus have not been analyzed. Figure 9 presents a typical example of blood vessels routes that were detected by manual marking (green), the automatic (red) and the MIP algorithms. The presented image is already the MIP image inside the plaque and its skeleton is yellow colored. The cyan marking represents the ROI that was chosen in the first frame of the US cine. It is clearly seen that the MIP generates an inaccurate reconstructed tree, while the manual and the automated reconstructions are similar to each other. This inaccuracy is expressed by the purple and the orange circled areas. Figure 9 shows an overestimated grading due to intra-plaque artifacts (orange) and non-optimal preliminary noise reduction and motion compensation (purple colored).

The characteristic XY displacement of the defined blood vessels was $2.73 \pm 1.24\ mm$, which is in average 130% bigger than the manual and the automated measured XY displacement for the same vessels.

The last step of the presented method is to determine the neovascularization grading inside the plaques. As one can see in table 3, the two physicians had consensus on 68% of the cases (19 out of 28 plaques, dark gray), their scores differed 1 grade in 25% (7 cases, mid gray) and 2 grades in 7% (2 cases, light gray). In table 4, comparison of the automated scoring against the physicians' visual scoring can be seen. Scores of both physicians were treated as independent scores, so there were 56 pairs of scores in total. The automated score was identical to the physicians' visual scoring in 64% of the cases (36 out of 56 cases, dark gray), 1 grade difference in 27%(15 cases, mid gray), and 2 grades

difference in 9% (5 cases, light gray). Obviously, the differences between the automated and the visual scores are very comparable to the differences between two independent observers.

Table 2: Comparison of the automatically reconstructed blood vessels routes and the manually reconstructed routes by measuring XY displacement and length of blood vessels. The comparison includes 31 vessel paths from 28 different plaques.

Interobserver variability of manual tracking	0.21 ± 0.14 mm
Distance between the average manual route and the automated reconstructions	0.23 ± 0.15 mm
XY displacement of the manually reconstructed blood vessels	1.19 ± 0.54 mm
XY Displacement of the automatically reconstructed blood vessels	1.14 ± 0.36 mm
Mean length of the blood vessels routes—manually reconstructed	1.93 ± 0.66 mm
Mean length of the blood vessels routes—automatically reconstructed	1.84 ± 0.69 mm

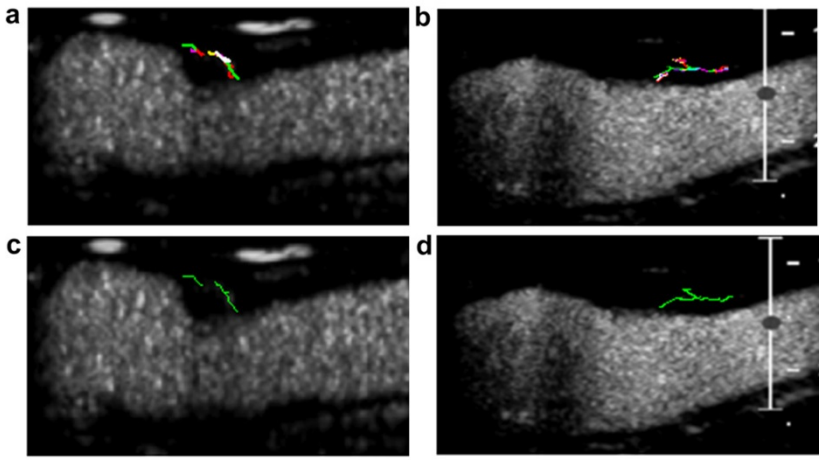

Fig. 8: Routes merging. Two different cases of reconstructed arterial tree before and after routes merging: (a) routes which belong to two different vessels before the merging process (over the whole cine); (b) split of two routes from a common "trunk" before the merging process. (c) The plaque which presents in 8 (a) , after the merging process. (d) The arterial tree which presents in 8 (b), after the merging process.

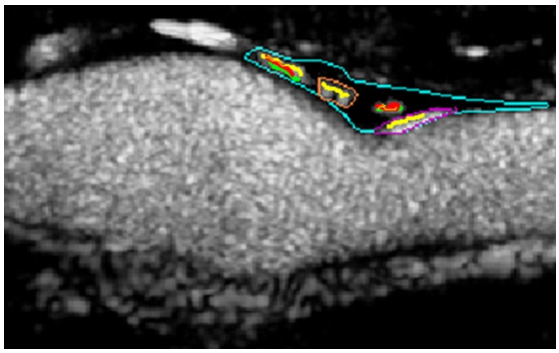

Fig. 9: Overestimation neovascularization grading using the MIP. Comparison between the manual marking (green), our method (red) and the MIP (yellow colored skeleton).The ROI is cyan marked. False detection (non-vessels detection) by the MIP is purple and orange colored.

Table 3: Comparison of intraplaque neovasularization visual scores of physician 1 against physician 2. 28 plaques were examined. Consensus (dark gray), 1 grade off (mid gray), 2 grades off (light gray)

		Physician 2 (Visual Scoring)			
Physician 1 (Visual Scoring)		*Grade 0*	*Grade 1*	*Grade 2*	*Grade 3*
	Grade 0	**3**	**0**	**2**	**0**
	Grade 1	**0**	**6**	**2**	**0**
	Grade 2	**0**	**4**	**10**	**0**
	Grade 3	**0**	**0**	**1**	**0**

Table 4: Comparison of intraplaque neovasularization algorithm scoring against visual scores of physician 1 & 2. 28 plaques were examined (56 visual scorings for 2 physicians). Consensus (dark gray), 1 grade off (mid gray), 2 grades off (light gray)

		Visual Scoring (Physician 1 & 2)			
Algorithm		*Grade 0*	*Grade 1*	*Grade 2*	*Grade 3*
	Grade 0	**6**	**2**	**0**	**0**
	Grade 1	**0**	**9**	**1**	**0**
	Grade 2	**2**	**6**	**21**	**1**
	Grade 3	**0**	**3**	**5**	**0**

DISCUSSION

In our research, we developed a semiautomatic technique for detecting and tracking the contrast spots motion using MDP combined with block matching, and morphological artificial templates. Based on that analysis, the reconstruction of the neovascularization arterial tree inside the plaque was performed. Our method deals

with a chain of 4 independent steps: detection of the intra-plaque objects, tracking those objects, classification into artifacts and actual blood vessels and overall grading of the neovascularization inside each plaque. Each step can be independently improved, so in this paper we report each step's success. We applied this method on clinical recorded data from 27 patients. There was quite some variability in the data. Movies differ by various criteria as movie quality and the extent of change in the shape of the contrast spots over the time. This enforced us to examine various combinations of the following parameters: the threshold for noise removal, the allowed step size and its penalty for tracking process. Those parameters were chosen experimentally (see details in the Methods section). The 10^{th} percentile threshold for noise removal and the 0.6 threshold for template correlation were chosen because it allows the detection of almost all (97%) relevant objects at the cost of 3.8% of false positive cases. The maximum allowed step size was selected based on the fastest motion seen in the movies - not larger than 3 pixels over 2 sequential frames. A side step penalty is applied to penalize large movements. MDP provides an overall optimal continuous path for tracking, less subject to transient loss of correlation and more robust to noise than forward tracking. The side step penalty was carefully selected: if it is too high, it can cause an over-smoothed path and if it is too small, it might not help to improve tracking results.

Detecting the contrast spots inside the plaque using artificial templates exploits the geometrical characteristic and the gray level distribution of the contrast spots. All visually identifiable contrast spots (one hundred and four different contrast spots) in 28 plaques were manually marked. Of those, 101 (97%) were also automatically detected. Tracking the intra-plaque contrast spots based on manual annotation is a cumbersome and tedious procedure with poor repeatability. To overcome this limitation, we propose a semiautomatic method based on MDP that requires minimal user interaction. In 90 of those 101 detected objects the automatic tracking determined the contrast motion correctly (89%). We validated the algorithm by using manual and visual interpretations of those cases. The reconstruction of the blood vessels routes was validated by comparing to a manual tracking of the contrast spots. As shown in the example of figure 8, in most of the cases, the automatically reconstructed route is smoother than the manual due to the detailed advantages of the MDP method.

The mean and the SD values of the distance between the automatically and the manually reconstructed routes are close to the equivalent values that were calculated between the routes manually marked by the 2 observers. Therefore, one can conclude that the algorithm results are accurate, within the range that human observers cover. The automatic tracking is a bit smoother than the manual tracking, as is expected because of its smoothness constraint. Moreover, the automated results are objective, since no human interaction is involved. The observers manually selected the brightest location inside the contrast spot, while the algorithm sometimes detected another location inside the object as its representative. A characteristic size of a contrast spot is above 7 pixels and a mean distance threshold of 5 pixels (0.525 mm) was chosen. Therefore, if the mean

distance between the manual marking and the automated one was smaller than this threshold, it can be considered as a tracking after different locations inside the same object.

The minor difference between the XY displacement results of manual and automatically found tracks can occur due to the stop term of the algorithm and the manual tracking. The algorithm stops tracking when a contrast spot has gray level below 10. However, the manual tracking stops when the observer can no longer distinguish the contrast spot.

Seventy-six of the 90 well tracked contrast spots were correctly classified in comparison to the visual classification (84%). When considering the whole population (104 identified objects), 73% was eventually correctly classified. Twelve objects which were visually classified as artifacts were automatically classified as blood vessels due to their large displacements over the time. These displacements were caused because of noisy images or inaccurate motion compensation.

The validation of the automated neovascularization grading was performed by comparing it to the physicians' grading. The physicians were blind to each other and analyzed all clips related to plaque of each patient. The two physicians had consensus on 68% of the cases. Variability can be caused by taking into account the adventitial vasa vasorum. It can be considered as relevant neovascularizttion by one observer, while the other one will ignore that. In addition, an artifact may be considered by an observer as a blood vessel due to a significant XY displacement, that the second observer will ignore.

It is clear that even with well-defined criteria, the visual scores can differ considerably between independent observers. This stresses the need for an objective, automated analysis. The automated score was identical to the physicians' visual scoring in 64% of the cases, 1 grade difference in 27%, and 2 grades difference in 9%. Therefore, the automated neovascularization grading agreed within 1 grade with visual analysis in 91% of the cases. Obviously, the differences between the automated and the visual scores are very comparable to the differences between two independent observers.

We also compared the results to the maximum intensity projection (MIP) analysis. The XY displacement of the blood vessels reconstructed by the MIP was 130% bigger than the manual analysis of the same parameter. This deviation of the MIP analysis is caused by suboptimal predefined filtering and motion compensation, resulting in overestimated routes. Moreover, due to the absence of temporal behavior of the examined objects, static artifacts are also included in the reconstructed arterial tree. Those MIP inaccuracies can affect the analysis of the blood vessel characteristics and the neovascularization grading.

The proposed algorithm was developed on 2D echocardiography images. Currently no high-frame rate 3D contrast images of carotid arteries are available. Such images would be ideal for analyzing the complete neovasculature in 3D over the whole plaque, rather than in a single slice. The same analysis method may be applied in 3D with straightforward extensions.

A limitation of the current study is the fact that there was no strict separation of test and training data. Several of the parameters of the algorithm were determined empirically from a few sequences in the test set. This paper concentrates on the

description of the methods and proof of its principles, the reported results are a preliminary estimate of the capabilities of the method. Considerable improvements can still be expected by more elaborate choice of parameters, but given the large variability of the gold standard (visual classification) we consider this very promising. In future work the algorithm will be evaluated on a larger, independent set of data to establish its overall clinical performance in a blinded way.

CONCLUSIONS

We developed a number of tools for preliminary quantification of neovascularization in carotid plaques. This includes a technique for detection of contrast spots in the plaque, tracking of such spots over time by MDP, classifying them into artifacts and vessels and reconstructing the arterial tree. This study showed that the technique is feasible and valuable in evaluating accurate intra-plaque neovascularization grading. The method provides efficient analysis with minimal user interaction and agrees well with manual and visual validations.

ACKNOWLEDGMENT

This research was supported by the Center for Translational Molecular Medicine and the Netherlands Heart Foundation (PARISk)

REFERENCES:

Akkus Z, Bosch J.G, Renaud G, Hoogi A, ten Kate G.L, van den Oord S, Schinkel A, de Jong N, van der Steen A.F.W. Motion Compensation Method for Quantification of Neovascularization in Carotid Atherosclerotic Plaques with Contrast Enhanced Ultrasound (CEUS). Proc. of IEEE International Ultrasonics Symposium, Orlando, 2011

Amini AA, Weymouth TE, Jain RC. Using Dynamic Programming for Solving Variational Problems in Vision. IEEE Trans Pattern Anal Mach Intell 1990;12:855-67.

Anderson CM, Saloner D, Tsuruda JS, Shapeero LG, Lee RE. Artifacts in maximum-intensity-projection display of MR angiograms. American Journal of Roentgenology 1990;154:623-9.

Barger AC, Beeuwkes R, Lainey LL, Silverman KJ. Hypothesis: Vasa Vasorum and Neovascularization of Human Coronary Arteries. N Engl J Med 1984;310:175-7.

Barnett HJM, Meldrum HE, Eliasziw M. The appropriate use of carotid endarterectomy. CMAJ 2002; 166:1169-79.

Chahal NS, Lim TK, Jain P, Chambers JC, Kooner JS, Senior R. Does subclinical atherosclerosis burden identify the increased risk of cardiovascular disease mortality among United Kingdom Indian Asians? A population study. Am Heart J 2011;162:460-6.

Coli S, Magnoni M, Sangiorgi G, Marrocco-Trischitta MM, Melisurgo G, Mauriello A, Spagnoli L, Chiesa R, Cianflone D, Maseri A. Contrast-Enhanced Ultrasound Imaging of Intraplaque Neovascularization in Carotid Arteries: Correlation With Histology and Plaque Echogenicity. J Am Coll Cardiol 2008;52:223-30.

Falk E. Pathogenesis of Atherosclerosis. J Am Coll Cardiol 2006;47:C7-C12.

Fleiner M, Kummer M, Mirlacher M, Sauter G, Cathomas G, Krapf R, Biedermann BC. Arterial Neovascularization and Inflammation in Vulnerable Patients: Early and Late Signs of Symptomatic Atherosclerosis. Circulation 2004;110:2843-50.

Giannarelli C, Ibanez B, Cimmino G, Garcia Ruiz JM, Faita F, Bianchini E, Zafar MU, Fuster V, Garcia MJ, Badimon JJ. Contrast-Enhanced Ultrasound Imaging Detects Intraplaque Neovascularization in an Experimental Model of Atherosclerosis. J Am Coll Cardiol Img 2010;3:1256-64.

Giannoni MF, Vicenzini E, Citone M, Ricciardi MC, Irace L, Laurito A, Scucchi LF, Di Piero V, Gossetti B, Mauriello A, Spagnoli LG, Lenzi GL, Valentini FB. Contrast Carotid Ultrasound for the Detection of Unstable Plaques with Neoangiogenesis: A Pilot Study. European Journal of Vascular and Endovascular Surgery 2009;37:722-7.

Gomez C. Carotid plaque morphology and risk for stroke. Stroke 1990;21:148-51.

Hellings WE, Peeters W, Moll FL, Piers SRD, van Setten J, Van der Spek PJ, de Vries JPM, Seldenrijk KA, De Bruin PC, Vink A, Velema E, de Kleijn DPV, Pasterkamp G. Composition of Carotid Atherosclerotic Plaque Is Associated With Cardiovascular Outcome. Circulation 2010;121:1941-50.

Hoogi A, Adam D, Hoffman A, Kerner H, Reisner S, Gaitini D. Carotid Plaque Vulnerability: Quantification of Neovascularization on Contrast-Enhanced Ultrasound With Histopathologic Correlation. Am J Roentgenol 2011;196:431-6.

Hsu AR, Chen X. Advances in Anatomic, Functional, and Molecular Imaging of Angiogenesis. J Nucl Med 2008;49:511-4.

Huang P, Huang F, Zou C, Sun H, Tian X, Yang Y, Tang J, Yang P, Wang X. Contrast-enhanced sonographic characteristics of neovascularization in carotid atherosclerotic plaques. Journal of Clinical Ultrasound 2008;36:346-51.

Libby P, Ridker PM, Hansson GK. Progress and challenges in translating the biology of atherosclerosis. Nature. 2011; 473(7347):317–325.

Lin E, Alessio A. What are the basic concepts of temporal, contrast, and spatial resolution in cardiac CT?. Journal of Cardiovascular Computed Tomography 2009;3:403-8.

Molinari F, Liboni W, Pavanelli E, Giustetto P, Badalamenti S, Suri JS. Accurate and Automatic Carotid Plaque Characterization in Contrast Enhanced 2-D Ultrasound Images. Engineering in Medicine and Biology Society, 2007. EMBS 2007. 29th Annual International Conference of the IEEE, 2007:335-8.

Nandalur KR, Baskurt E, Hagspiel KD, Phillips CD, Kramer CM. Calcified Carotid Atherosclerotic Plaque Is Associated Less with Ischemic Symptoms Than Is Noncalcified Plaque on MDCT. Am J Roentgenol 2005;184:295-8.

Nevo S . T ., van Stralen M ., Vossepoel A . M ., Reiber J . H . C ., de Jong N ., van der Steen A . F . W ., Bosch J . G . Automated tracking of the mitral valve annulus motion in apical echocardiographic images using multidimensional dynamic programming. Ultrasound in Medicine and Biology 2007;33:1389-1399.

Ogata T, Yasaka M, Yamagishi M, Seguchi O, Nagatsuka K, Minematsu K. Atherosclerosis Found on Carotid Ultrasonography Is Associated With Atherosclerosis on Coronary Intravascular Ultrasonography. J Ultrasound Med 2005;24:469-74.

Parker DL, Wu J, van Bree RE. Three-dimensional vascular reconstruction from projections: a theoretical review. Engineering in Medicine and Biology Society, 1988. Proceedings of the Annual International Conference of the IEEE, 1988:399,400 vol.1.

Poli R, Valli G. An algorithm for real-time vessel enhancement and detection. Comput Methods Programs Biomed 1997;52:1-22.

Rabben SI, Torp AH, Støylen A, Slørdahl S, Bjørnstad K, Haugen BO, Angelsen B. Semiautomatic contour detection in ultrasound M-mode images. Ultrasound Med Biol 2000;26:287-96.

Rissanen TT, Korpisalo P, Karvinen H, Liimatainen T, Laidinen S, Grohn OH, Yla-Herttuala S. High-Resolution Ultrasound Perfusion Imaging of Therapeutic Angiogenesis. J Am Coll Cardiol Img 2008;1:83-91.

Shah F, Balan P, Weinberg M, Reddy V, Neems R, Feinstein M, Dainauskas J, Meyer P, Goldin M, Feinstein SB. Contrast-enhanced ultrasound imaging of atherosclerotic carotid plaque neovascularization: a new surrogate marker of atherosclerosis?. Vascular Medicine 2007;12:291-7.

Sluimer JC, Daemen MJ. Novel concepts in atherogenesis: angiogenesis and hypoxia in atherosclerosis. J Pathol 2009;218:7-29.

Sluimer JC, Gasc J, van Wanroij JL, Kisters N, Groeneweg M, Sollewijn Gelpke MD, Cleutjens JP, van den Akker LH, Corvol P, Wouters BG, Daemen MJ, Bijnens AJ. Hypoxia, Hypoxia-Inducible Transcription Factor, and Macrophages in Human Atherosclerotic Plaques Are Correlated With Intraplaque Angiogenesis. J Am Coll Cardiol 2008;51:1258-65.

Stein JH, Korcarz CE, Hurst RT, Lonn E, Kendall CB, Mohler ER, Najjar SS, Rembold CM, Post WS. Use of Carotid Ultrasound to Identify Subclinical Vascular Disease and Evaluate Cardiovascular Disease Risk: A Consensus Statement from the American Society of Echocardiography Carotid Intima-Media Thickness Task Force Endorsed by the Society for Vascular Medicine. Journal of the American Society of Echocardiography 2008;21:93-111.

Suri JS, Kecheng Liu, Reden L, Laxminarayan S. A review on MR vascular image processing: skeleton versus nonskeleton approaches: part II. Information Technology in Biomedicine, IEEE Transactions on 2002;6:338-50.

ten Kate GL, Renaud GGJ, Akkus Z, van den Oord SCH, ten Cate FJ, Shamdasani V, Entrekin RR, Sijbrands EJG, de Jong N, Bosch JG, Schinkel AFL, van der Steen AFW. Far-Wall Pseudoenhancement During Contrast-Enhanced Ultrasound of the Carotid Arteries: Clinical Description and In Vitro Reproduction. Ultrasound Med Biol 2012;38:593-600.

Tozaki T, Kawata Y, Niki N, Ohmatsu H, Moriyama N. 3-D visualization of blood vessels and tumor using thin slice CT images. Nuclear Science Symposium and Medical Imaging Conference, 1994., 1994 IEEE Conference Record, 1994:1470,1474 vol.3.

van Ooijen PMA, Ho KY, Dorgelo J, Oudkerk M. Coronary Artery Imaging with Multidetector CT: Visualization Issues1. Radiographics 2003;23:e16-.

Willmann JK, Kimura RH, Deshpande N, Lutz AM, Cochran JR, Gambhir SS. Targeted Contrast-Enhanced Ultrasound Imaging of Tumor Angiogenesis with Contrast Microbubbles Conjugated to Integrin-Binding Knottin Peptides. Journal of Nuclear Medicine March 2010;51:433-40.

Chapter 4

New Quantification Methods for Carotid Intraplaque Neovascularization using Contrast Enhanced Ultrasound

As carotid intraplaque neovascularization (IPN) is linked to progressive atherosclerotic disease and plaque vulnerability, its accurate quantification might allow early detection of plaque vulnerability. We therefore developed several new quantitative methods for analyzing IPN perfusion and structure. From our analyses, we derived six quantitative parameters – IPN surface area (IPNSA), IPN surface ratio (IPNSR), plaque mean intensity, plaque-to-lumen enhancement ratio, mean plaque contrast percentage, and number of microvessels (MVN) – and compared them to visual grading of IPN by two independent physicians. A total of 45 carotid arteries with symptomatic stenosis of 23 patients were analyzed. IPNSA (correlation r=0.719), IPNSR (r=0.538) and MVN (r=0.484) were found to be significantly correlated to visual scoring ($p<0.01$). The IPNSA parameter matched the best to visual scoring. These results show that IPNSA, IPNSR and MVN may thus have the potential to replace qualitative visual scoring and to measure the degree of carotid IPN.

Z. Akkus, A. Hoogi, G. Renaud, S. C.H. van den Oord, G. L. ten Kate, A. F.L. Schinkel, D. Adam, N. de Jong, A. F.W. van der Steen, J. G. Bosch. **New Quantification Methods for Carotid Intraplaque Neovascularization using Contrast Enhanced Ultrasound.** Ultrasound Medicine and Biology, 40(1):25-36, 2013

INTRODUCTION

Several studies have shown that patients with carotid plaques carry an increased risk of sudden cardiovascular events, such as stroke, transient ischemic attack (TIA), myocardial infarction and even death (Naghavi et al. 2003; Spagnoli et al. 2004). The benefit of carotid endarterectomy in reducing the risk of recurrent stroke for symptomatic patients with severe stenosis has been established by large European and North American clinical trials (Ferguson et al. 1999; Rothwell et al. 2003). For a carotid endarterectomy operation, current clinical practice for selecting patients is heavily based on assessing the degree of arterial lumen narrowing. However, there is an increasing consciousness that not the size of the plaque, but its composition and risk of rupturing is related to these acute cardiovascular events (Schaar et al. 2004; Feinstein 2006; Hellings et al. 2010; Staub et al. 2010). Therefore, the degree of stenosis is actually a poor predictor of individual stroke risk and improved risk stratification models should focus on plaque vulnerability rather than size. Early identification of atherosclerotic plaques at risk for instability and rupture may improve treatment strategies for the prevention of cardiovascular events. Several pathological studies demonstrated that intraplaque neovascularization (IPN, also called plaque vasa vasorum) is associated with progressive atherosclerotic disease and plaque vulnerability (Fleiner et al. 2004; Hellings et al. 2010; Michel et al. 2011). Recent developments in contrast enhanced ultrasound (CEUS) enable detection of atherosclerosis and small microvessels with slow flow within the plaque by the use of ultrasound contrast agents (Feinstein 2006; Coli et al. 2008).

Mostly, visual scoring of IPN has been used to assess degree of IPN (Feinstein 2006; Shah et al. 2007; Coli et al. 2008; Staub et al. 2010). A good correlation between the visual scoring of IPN and the number of intraplaque neovessels in histological samples was reported in several validation studies (Magnoni et al. 2009; Schinkel et al. 2010). However, assessing IPN visually is observer dependent and different studies use different grading scales (Shah et al. 2007; Staub et al. 2010; Staub et al. 2011). Staub et al. (2010) reported substantial intra-observer agreement and moderate inter-observer agreement for visual IPN scoring. A review paper for assessment of carotid IPN with CEUS was presented by (ten Kate et al. 2013). However, quantification methods for IPN are scarce.

Huang et al. (2008) presented dynamic evaluation of the plaque enhancement. Plaque contrast enhancement was greater in soft plaques than in mixed plaques. Xiong et al. (2009) reported that stroke and TIA patients had significantly more intraplaque contrast enhancement than asymptomatic patients. Papaioannou et al. (2009) presented a case of far wall carotid atherosclerotic plaque imaged by CEUS for the evaluation of IPN. An increase in gray level after injection of contrast was reported. All these studies were based on analysis of Time Intensity Curves (TIC). Hoogi et al. (2011) presented the first method which segments the contrast spots within the plaque in the individual images and calculates IPN surface area. They reported a good correlation between contrast based and histology based IPN to plaque surface area ratio ($R^2 = 0.7905$).

Limitations of previous quantification methods

The enhancement of plaques after injection of contrast material was generally analyzed quantitatively by use of a TIC analysis in the previous studies (Huang et al. 2008; Xiong et al. 2009). However, it may be questioned whether common TIC analysis as applied in large well-perfused organs like the liver, prostate or heart is applicable to quantification of microvessels in plaques. The plaques are very small and weakly perfused. The flow within the plaques is not continuous but characterized by occasional appearance of a faint and moving contrast spot. In addition, the high intensity contrast in the carotid lumen is directly adjacent to the plaque, and the plaque is moving due to arterial pulsation and breathing. This complicates the generation of a valid non-contaminated plaque region of interest (ROI) for the TIC derivation. For these reasons, it is hard to obtain bolus kinetic parameters from time intensity curves for plaque.

Huang et al. (2008), Xiong (2009) and Papaioannou et al. (2009) analyzed far wall carotid plaques but it is not possible to reliably analyze atherosclerotic plaques that are located on the far wall of the carotid artery (ten Kate et al. 2012; Thapar et al. 2012) due to the pseudo-enhancement artifact in the far wall plaques. Due to this artifact, the contrast enhancement in the far wall plaques will show a similar perfusion pattern as the lumen and will be overestimated.

The method presented by Hoogi et al. (2012) applied ECG gating to limit motion and only one CEUS image per cardiac cycle was used. Therefore, continuity of microvessel paths after time integration may be lost. Some additional motion compensation was performed, but this was done on the CEUS image itself where the tissue is not visualized. Therefore it is quite difficult to extract plaque motion from CEUS images.

In our study, we avoided the known limitations of automated quantification methods in the previous studies. All images of the plaque within the selected frame interval in the image sequence were used. Side by side images, contrast and B-mode, were acquired simultaneously to obtain the motion pattern of plaque from the B-mode image sequence. Our motion compensation prevented the plaque ROI from including parts of saturation artifacts and lumen, and minimized the risk of false peak intensities that could have contaminated the TICs. Perfusion and structure analyses of IPN with accurate motion compensation were performed and several quantification parameters were derived to estimate neovascularization degree of carotid plaques. The proposed IPN analyses were tested on a patient dataset. The derived parameters were compared to visual scores of IPN. The purpose of our study is finding the parameters which match significantly to the visual consensus scores, to replace subjective visual scoring and provide a quantitative IPN assessment in CEUS.

METHODS

Simultaneous side-by-side, contrast mode and B-mode, images were acquired at 20-23Hz frame rate using a Philips iU22 system (Philips Medical Systems, Bothell, USA) with a L9-3 linear probe. This probe has a slice thickness of about

2mm for 3cm depth (Hudson 2011). The cine loops that were acquired during each clinical examination were transferred as DICOM files (JPEG compressed) to a computer workstation for off-line analysis.

User-friendly and well-structured carotid intraplaque neovascularization quantification software (CINQS) was developed in MevisLab, a development environment for medical image processing and visualization (MeVis Medical Solutions AG and Fraunhofer MEVIS, Bremen, Germany) The IPN quantification algorithms were implemented in MATLAB (The Mathworks Inc., Natick, Massachusetts, US), and run through a MeVisLab-MATLAB interface module. Communication between MevisLab modules and graphic user interface (GUI) is controlled via Python scripts.

Within CINQS, three regions of interest (ROI) were manually defined. After motion compensation, perfusion and structure analyses of plaque were performed to derive several quantitative parameters.

Motion compensation

Due to the pulsating blood pressure, breathing and swallowing, the carotid artery wall shows considerable motion. To quantify small microvessels accurately within the carotid plaques, motion compensation is a prerequisite step. The contrast spots associated with these microvessels have sizes of a few pixels (1 pixel ~ 0.1 mm), while the plaque motion can amount to tens of pixels. The motion compensation method should be accurate and reliable enough for this purpose. In CEUS images, only ultrasound contrast agent is seen and tissue is suppressed so that it is quite difficult to extract plaque motion from CEUS images. We therefore acquired simultaneous side-by-side B-mode images and CEUS images and extracted the motion pattern of plaque from B-mode images, applying it to the contrast images to follow the identical plaque region, as is illustrated in figure 1. Plaque itself in B-mode images is quite a unique landmark in longitudinal and transversal directions, unlike healthy carotid wall sections, which are highly similar when moving along the vessel direction.

The motion pattern is performed by using multidimensional dynamic programming (MDP) combined with apodized block matching (BM) as described in (Akkus et al. 2012). First, the user chooses a point on the plaque in a B-Mode image of the sequence. A fixed template of 61 x 41 pixels (6x4 mm) around this point is derived from the chosen image of the sequence. To find the similarity of the template to image pattern in any image, normalized cross correlation (NCC) is used. The center position of the template is scanned over all positions within a defined search field (61 x 21 pixels (6x2 mm)) in each image. The results of NCC for all positions are used as a 3D matrix input to MDP. The optimal plaque displacement was obtained with MDP as described in detail in (Akkus et al. 2012) and the contrast images are aligned to the reference contrast image based on the detected plaque displacement in X and Y direction.

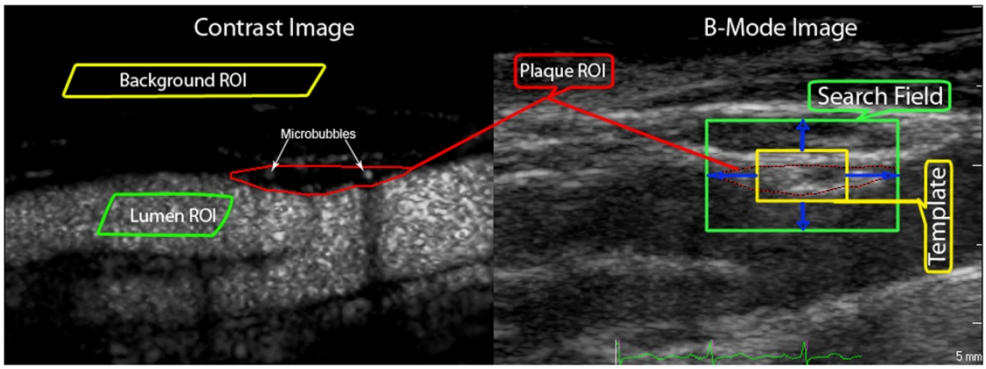

Fig. 1: An example of a side-by-side contrast image (on the left side) and B-mode image (on the right side), and illustration of motion compensation.

Plaque Perfusion Analysis

In this analysis, contrast perfusion of the plaque is analyzed over time. First, three ROIs are manually drawn on the contrast image for plaque, lumen and background. The background ROI is used to measure the noise level in the tissue part in the contrast image. Motion compensation is applied to the plaque ROI as explained in the previous section. After this, time intensity curve (TIC, Fig. 2) and maximum intensity projection (MIP, Fig. 3) of plaque over time are calculated. The term 'intensity' in this paper refers to contrast image intensity, which is the log compressed signal power (gray scale values). In MIP, the maximum intensity of each pixel over time is projected onto a 2D image as illustrated in Fig. 4. In TIC analysis, the intensity within the ROI at each time point is represented as sum, mean, median, or standard deviation of intensities of all pixels within the ROI.From TIC, plaque mean intensity (PMI), lumen mean intensity (LMI), plaque to lumen enhancement ratio (PLER) and mean plaque contrast percentage (MPCP) parameters are derived. In PMI, the time average of plaque intensity is calculated. In LMI, the time average of lumen intensity is calculated. In PLER, the ratio of PMI and LMI is taken as a percentage. In MPCP, a fixed threshold (on a scale of 0 to 255) is applied to separate contrast from background and the time average of the percentage of plaque filled with contrast is calculated. The gray scale level of 2 (BTh) was chosen based on the maximum level of mean background noise in our data set. From the perfusion MIP image, the IPN surface area (IPNSA) and IPN surface area to plaque area ratio (IPNSR) with adaptive threshold (ATh) are derived. We calculated IPN surface area score (IPNSAS) as Log(IPNSA+1).

The adaptive threshold (equation 1) is calculated by taking into account background ROI, lumen ROI, and a visual limitation.

$$ATh = \max(VL, BGMI + 4 \times BGMSD) + (LM\ I - V\ L) \times 10\% \quad (1)$$

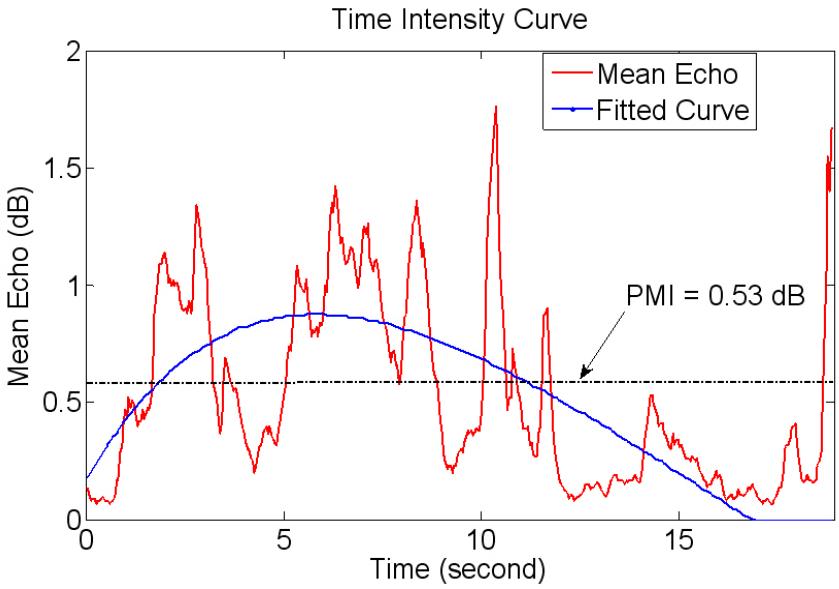

Fig. 2: Time intensity curve of a plaque. PMI: Plaque mean intensity.

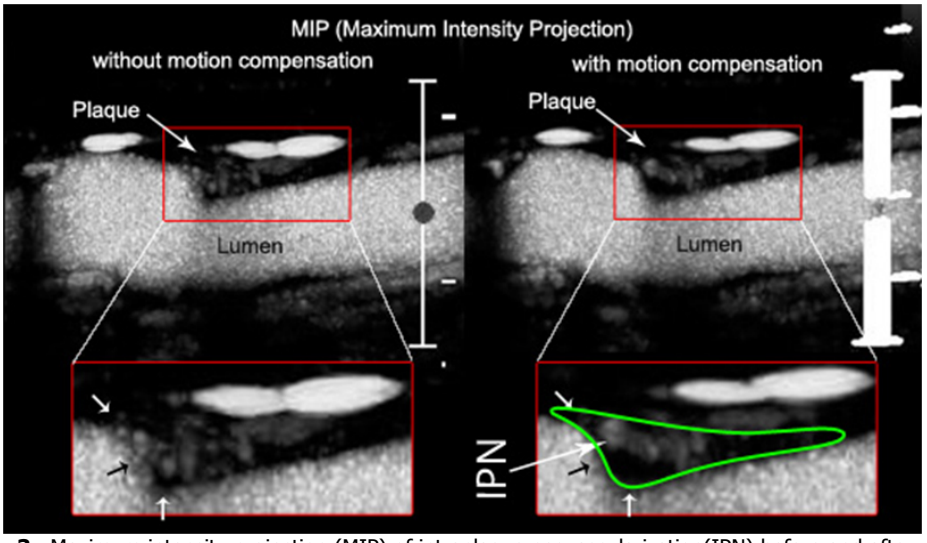

Fig. 3: Maximum intensity projection (MIP) of intraplaque neovascularization(IPN) before and after motion compensation.

Since we found that gray scale level below 10 (on a scale of 0 to 255) could not visually be detected, we employed a visual limitation (VL = 10). The background ROI was used to estimate background noise mean and standard deviation. We obtained the maximum of VL and time average of background ROI mean intensity (BGMI) plus four times the time average of background ROI standard deviation (BGMSD) for threshold. Threshold was also corrected for concentration of contrast

within the lumen by adding 10% of the LMI after subtraction of visual limitation. The formulations of IPN quantification parameters can be seen in Table 1.

To show the improvement of IPNSA with motion compensation, we analyzed our plaques twice with and without motion compensation.

Table 1: Formulations of IPN quantification parameters

$$\text{IPNSA}\ (mm^2) = \text{pa} \times \sum_{\text{i=1}}^{\text{n}} \text{p(i, ATh)} \ \text{ where } \begin{cases} 1, \text{if } Ic(i) > ATh \\ 0, \text{otherwise} \end{cases}$$

$$PMI = \frac{\sum_{i=1}^{F}\{(\sum_{j=1}^{n} Ic)/n\}}{F}$$

$$IPNSR\ (\%) = \frac{\sum_{\text{i=1}}^{\text{n}} \text{p(i, ATh)}}{n} \times 100\%$$

$$LMI = \frac{\sum_{i=1}^{F}\{(\sum_{j=1}^{m} Ic)/m\}}{F}$$

$$MPCP(\%) = \frac{\sum_{j=1}^{F} \frac{\sum_{\text{i=1}}^{\text{n}} \text{p(i, BTh)}}{n}}{F} \times 100\%$$

$$PLER(\%) = \frac{PMI}{LMI} \times 100\%$$

ATh = adaptive threshold; BTh = background noise threshold; F = number of frames; Ic(i) = contrast intensity of pixel i; IPNSA = intra-plaque neovascularization surface area; IPNSR=intra-plaque neovascularization surface ratio; LMI=lumen mean intensity; m= number of pixels for lumen region of interest; MPCP = mean plaque contrast percentage; n = number of pixels for plaque region of interest; pa = pixel area (mm2); PLER = plaque-to-lumen enhancement ratio; PMI = plaque mean intensity.

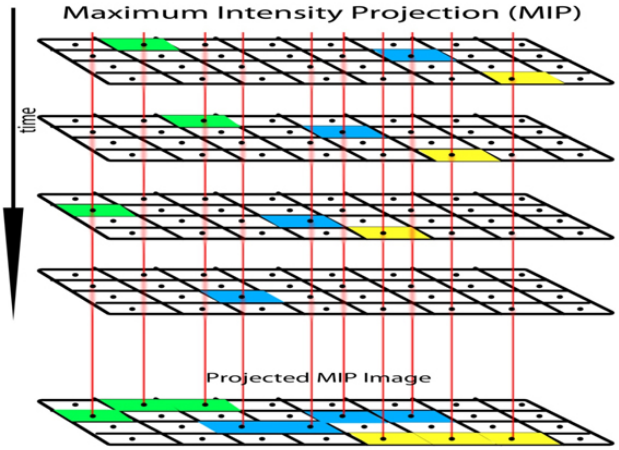

Fig. 4: Maximum intensity projection (MIP) illustration. Blue, yellow, and green objects moving over time in different direction and resulting projected image.

To compare our findings to previous studies, we reproduced a common parameter for plaque IPN (plaque contrast enhancement, PE) derived from TIC (Huang et al. 2008; Xiong et al. 2009). For this, we used the QLAB ROI quantification tool (Philips Medical Systems, Bothell, USA). We redrew the plaque ROIs as similar as possible to our analysis. A gamma-variate curve was fitted to the

resulting TIC. The fit was considered invalid only if the peak occurred at the first or last frame of the interval. From the fitted curve, we recorded peak intensity and baseline intensity (intensity within the plaque ROI right after the flash frame). PE was calculated by subtracting baseline intensity from peak intensity.

Vascular Structure Analysis

In vascular structure analysis (VSA), the structure of IPN was analyzed by a microbubble tracking algorithm as described in Hoogi et al. (2012). This contains several steps for detecting vessel paths.

First, the plaque ROI is manually drawn or is adopted from perfusion analysis. Second, motion compensation is applied as described in the motion compensation section. Noise reduction is performed using a 2D Gaussian filter of 5*5 pixels with sigma = 1 and beside this an additional adaptive threshold which is 10 percentile of intensity distribution within the plaque ROI is used to eliminate noise. The image sequence is divided into 10-frame groups with 80% overlap. The algorithm detects contrast spots by using different radii of artificial bubbles in the first frame of each group; it then tracks them using MDP combined with apodized BM for each group. After that, contrast tracks are classified into blood vessels and artifacts. This classification, which is necessary to remove artifacts from further processing and discard them from plaque vulnerability estimates, is based on a minimum expected displacement for moving bubbles in contrast to stationary artifacts. A threshold of 8 pixels (0.8 mm) is applied for the Euclidian distance of an object over a group of 10 frames. If displacement is below the threshold (corresponding to a velocity of about 1.5mm/s), the object is classified as an artifact. This implies that vessels that run almost perpendicular to the image plane will also be classified as artifacts. If the vessel directions are spatially distributed uniformly, less than 10% of vessels should be missed with this threshold.

In the final step of the algorithm, reconstructed routes which are supposed to be of the same vessel are merged. Different routes which probably represent the temporal behavior of the same object are combined. The number of detected vessels (MVN) is counted to estimate IPN degree.

Acoustic Shadow Detection

Acoustic shadowing of plaque (mostly associated with plaque calcification or heavy fibrosis) is a clinically interesting parameter but may also obscure the detection of IPN (both visually and automatically). Shadowing was assessed automatically by looking at the amount of shadowing below the plaque 0.5s after the flash frame when the lumen is filled with contrast again. The percentage of shadowing was estimated by calculating the shadow width below the plaque region relative to the atherosclerotic plaque width (see Fig. 5). The mean lumen intensity profile over a zone of 1cm below the plaque border including a neighborhood of 30 pixels left and right of the plaque is calculated. After that, a linear curve is fitted to the mean lumen intensity profile of both 30 pixels border neighborhood of the plaque to estimate local lumen mean intensity. A linear interpolation is applied

between the intensity values of the two corner points of the plaque to estimate original lumen mean intensity without presence of shadowing. For every plaque position, if lumen mean intensity is less than 30% of the estimated original lumen mean intensity, the plaque position was classified as shadowed. The 30% cut-off was decided based on the observed signal level in shadowed regions in our dataset. The presence of >50% of shadowing was considered to be substantial shadowing. Because shadowing in atherosclerotic plaques may have influence on both visual scoring and automated scoring of IPN, statistical analyses were performed both on plaques with and without substantially shadowed plaques.

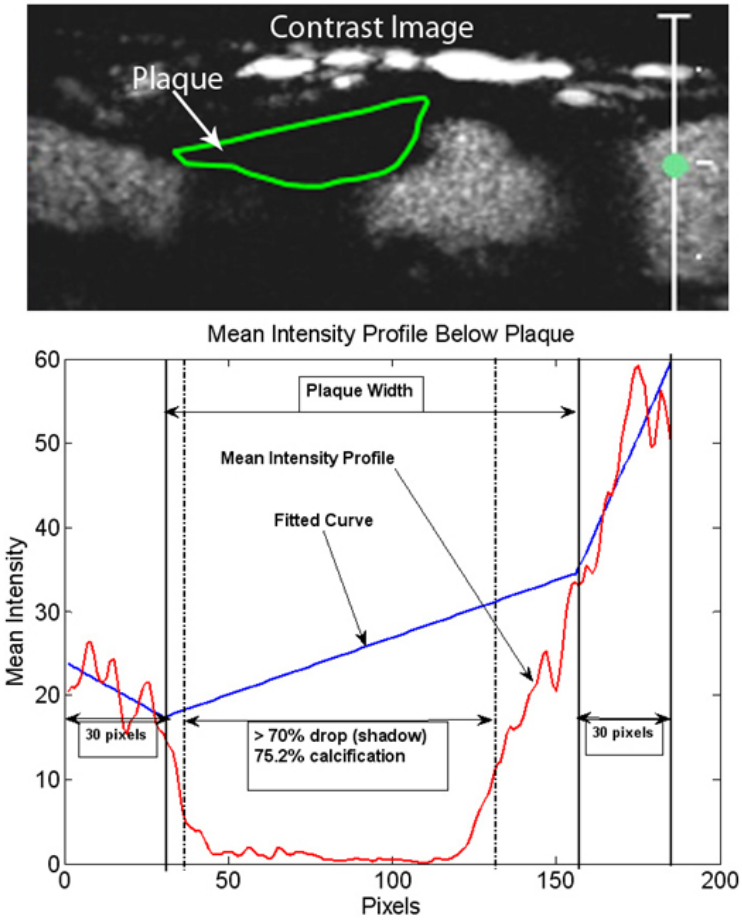

Fig. 5: Acoustic shadow detection: Mean intensity profile below the plaque width ± 30 pixels.

Patient population and study protocol

We included 25 patients with carotid atherosclerotic disease who suffered from stroke, transient ischemic attack, or ischemic ocular event. Patients had moderate to severe carotid stenosis (≥70%) as determined on CT-angiography or carotid

duplex ultrasonography. A total of 45 plaques of 23 patients (one per carotid artery, near wall) were included in the final analysis. Five carotid arteries were excluded from analysis. One carotid artery was excluded due to a prior surgical intervention. In one patient, the ultrasound clips of both arteries were excluded due to poor quality. In another patient, no atherosclerotic plaques were detected in the near wall of the carotid arteries. In these cases the carotid arteries were excluded from further analysis due to possible pseudo-enhancement in the far wall of the carotid artery. The study protocol was approved by the ethical committee at Erasmus Medical Center and all study participants provided informed consent.

Carotid ultrasound acquisition

The standard carotid ultrasound examination and the CEUS examination of the carotid arteries was performed using a Philips iU22 ultrasound system with a L9-3 linear array probe. A standardized image acquisition protocol was followed. The protocol was based on the American Society of Echocardiography consensus statement (Stein et al. 2008). CEUS was performed using intravenous administration of 0.5mL bolus of SonoVue ultrasound contrast agent (Bracco S.p.A., Milan, Italy). The bolus was injected in a consistent manner (0.5mL of SonoVue followed by a 2mL saline flush, consistent timing). For the CEUS examination, power modulation technique and a mechanical index of 0.06-0.08 was used for optimal contrast enhanced ultrasound images. The image log compression was always set to the same value (C50). For optimal coordination of the ultrasound examination, we used side-by-side display mode with a simultaneous B-mode and CEUS image. After arrival of the bolus, we recorded one or more 20 seconds cine clips starting with a flash and showing the replenishment. For both standard carotid ultrasound and CEUS of the carotid arteries, cineclips were digitally stored and reviewed offline.

Visual carotid ultrasound analysis

Two independent readers who were blinded from patient specific data reviewed the standard carotid ultrasound clips and CEUS clips. The clips were analyzed in a predefined sequence. The size of the atherosclerotic plaque was defined as the maximum plaque thickness measured perpendicular to the luminal flow. The atherosclerotic plaques were scored for the presence of IPN by using the CEUS clips. Contrast-enhancement in the atherosclerotic plaque was considered to represent IPN. For each carotid artery, the presence of IPN was graded in the CEUS clip with maximum enhancement using a previously published grading scale. No IPN was scored as 0, limited or moderate IPN as 1, and severe IPN as 2 (Staub et al. 2011). In case of a discrepancy in the scores of the independent readers, consensus was reached afterwards. The visual IPN score was only used for atherosclerotic plaques visible at the near wall of the carotid artery. Plaques at the far wall were excluded from analysis. Contrast enhancement in atherosclerotic plaques on the far wall is not reliable because of the far-wall pseudo-enhancement artifact (ten Kate et al. 2012; Thapar et al. 2012).

Automated IPN analysis

Automated analysis was applied on the same clips as used in visual analysis. All analyses were performed according to a structured protocol by two independent readers. After selecting the time frame interval for the analysis, three regions of interest (ROI) were drawn in the CEUS image: the atherosclerotic plaque, part of the carotid lumen and part of the background. Saturation artifacts in or around the atherosclerotic plaque were manually avoided during the drawing of the plaque ROI to prevent overestimation of IPN. In the B-mode image, a point of the atherosclerotic plaque was manually selected for motion compensation of the atherosclerotic plaque ROI. After the plaque ROI was aligned over time with motion compensation, perfusion and structure analyses of plaque were performed to derive several quantitative parameters. The results of parameters were saved in an excel file. The performed analyses and ROI objects were saved as XML file to retrieve them back later.

Statistical analysis

The results were statistically analyzed using SPSS PASW software for Windows (Version 17.0.2, SPSS Inc., Chicago, IL, USA). Categorical variables were expressed as counts and percentages. Continuous data was expressed as mean ± standard deviation. Before statistical analysis, all parameters were log-transformed. To test the association between the visual IPN score and the automated score derived from individual parameters, Spearman rank correlation was used. To test differences between the automated scores in the visual IPN score groups, Kruskall Wallis test was used. Since our data is not normally distributed, we used the Kruskall Wallis test which does not assume a normal distribution. The Intra-observer (n=45 plaques) and inter-observer (n=15 plaques) variability were measured using Bland-Altman plots and intraclass correlation coefficients (ICC) to assess the reproducibility of IPN parameters.

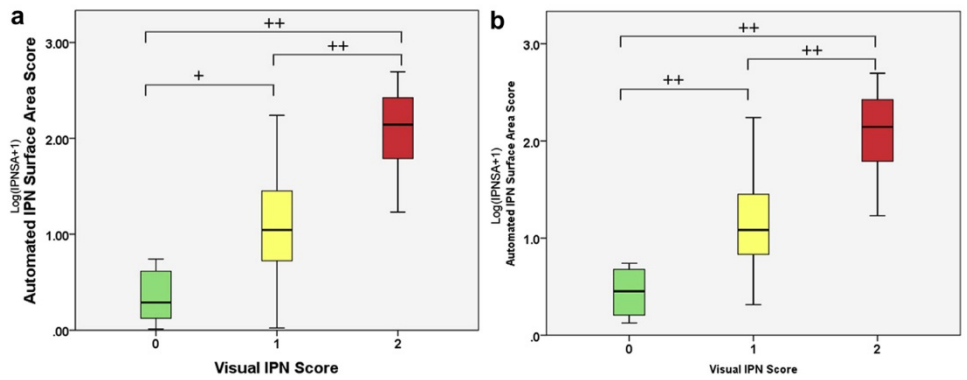

Fig. 6 (a) Association of automated IPN surface area score with visual IPN scoring groups (n=45). (b) Association of automated IPN surface area score with visual IPN scoring groups after exclusion of plaques with substantial shadowing (n=37). + = p <0.01, ++ = p <0.005.

RESULTS

The mean number of frames and standard deviation in the time-frame intervals selected for analysis was 307 ± 97. The average maximum plaque thickness was 6.82 ± 1.24 mm. In 45 analyzable plaques, 11 % (5 plaques) had IPN score 0, 64% (29 plaques) had IPN score 1 and 24% (11 plaques) had IPN score 2. Visual IPN score was 1.13 ± 0.59 (mean ± standard deviation). All 45 carotid arteries were evaluated using CINQS. Mean atherosclerotic plaque surface area was 11.6 ± 8.6 mm^2. The output of derived IPN parameters can be seen in Table 2. The correlations between output parameters and visual scoring groups were calculated. IPNSA, IPNSR and MVN were found to be significantly associated with visual scoring (Table 2). The MPCP, PMI and PLER were not associated with the visual IPN score (Table 2). The associations between the different visual IPN scoring groups and the IPN surface area are seen in Figure 6a. A total of 8 plaques (18%) were considered to have substantial shadowing. The correlations of all IPN parameters (Table 2) improved after exclusion of these plaques. The associations between the different visual IPN scoring groups and the IPN surface area after exclusion of plaques with substantial shadowing can be seen in Figure 6b. As it can be seen from Table 3 and Fig. 7, Inter-observer variability was low and inter-observer agreement was good to excellent (ICC: 0.68-0.94, $p<0.01$). Intra-observer variability was low and intra-observer agreement was excellent (ICC: 0.84-0.98, $p<0.001$).

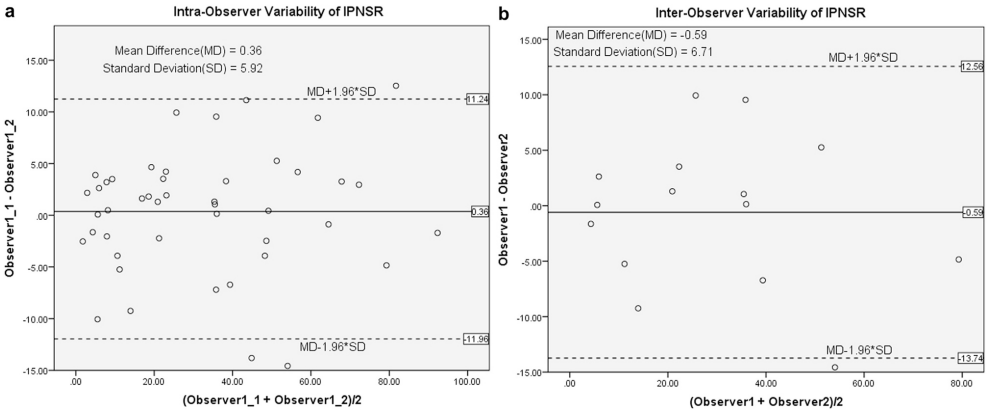

Fig. 7: (a) Bland-Altman plot of intra-observer variability of automated IPN surface ratio (IPNSR). (b) Bland-Altman plot of inter-observer variability of IPNSR.

In the comparison of PE as in (Xiong et al. 2009) and visual IPN scores, no valid gamma-variate curve fit could be found in 10 plaques out of 45. For the remaining fits, the correlation between the PE and visual IPN scores was very low ($r=0.105$). The PE parameter was therefore not further included in comparisons.

In absence of motion compensation, the found IPN surface area was considerably overestimated (>50% for some cases) due to the lumen or artifact infiltration (fig. 8). The correlation of visual IPN scores and IPNSA was decreased when motion compensation was left out (0.697 vs. 0.719).

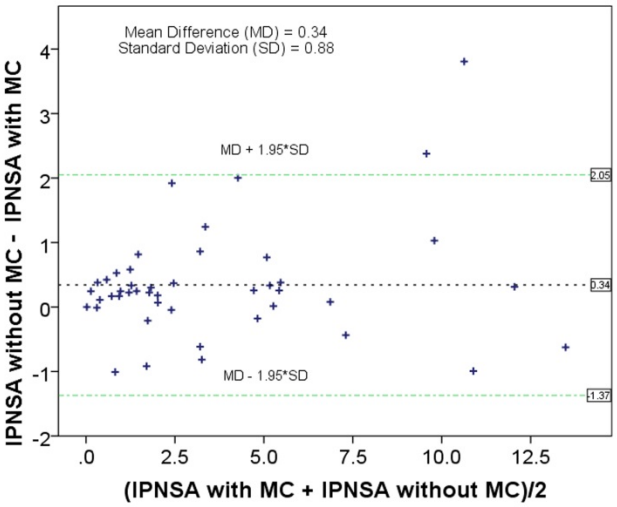

Fig. 8: Bland-Altman plot of intra-plaque neovascularization surface area (IPNSA) with and without motion compensation (MC)

DISCUSSION

Several pathological studies have recently linked IPN to atherosclerotic plaque progression, vulnerability, and rupture (Feinstein 2006; Coli et al. 2008; Hellings et al. 2010; Staub et al. 2010). As methods for IPN quantification are limited, we developed new quantification methods in our study. It is clear that qualitative assessment (visual scoring) of IPN presented in previous studies might include subjectivity. Although some studies have quantitatively evaluated IPN in CEUS images (Huang et al. 2008; Papaioannou et al. 2009; Xiong et al. 2009; Hoogi et al. 2011) they suffer from some limitations in their quantification methods.

As described in the introduction, one reported approach for IPN quantification is calculating plaque enhancement from TIC. Plaque contrast enhancement (PE) is calculated from peak intensity (PI) after fitting a curve to TIC (Huang et al. 2008; Xiong et al. 2009). Based on observations in our dataset, it is not reliable to obtain bolus kinetic parameters from TIC because flow within plaque is not continuous and not all microvessels will be perfused. An example of TIC of a plaque (Fig. 2) shows several peaks when the plaque is perfused over time and the peak of the fitted curve will not represent the true peak enhancement within the plaque. In our study, we derived PMI and PLER from TIC, but both of them were not associated with visual IPN score as can be seen in table 1. The classical PE showed even lower correlation with visual IPN in our dataset.

In addition, motion within the carotid images (i.e. pulsation, breathing, and body or probe motion) is generally ignored in the previous studies. However, motion compensation is essential for following identical ROI and to avoid contrast from lumen and saturation artifact around the plaque. In absence of motion compensation, PI might be influenced by outlier measurements and this will cause errors in detection of PI and in calculation of PE. In our study, our motion compensation prevented the plaque ROI from including parts of saturation artifacts

and lumen, and minimized the risk of contamination of the TICs.

Another reported IPN quantification approach is calculating IPN surface area (Hoogi et al. 2011). As stated before, using ECG gating and one image per cardiac cycle might not give an accurate time integration of contrast spots. This will cause contrast appearance in all intermediate frames to be missed and continuity of microvessel paths after time integration will be lost. Furthermore, ECG gating will not remove breathing and other motion artifacts. As explained, extracting plaque motion from CEUS images is less reliable than extracting from B-mode images. In our study, we therefore used a more reliable motion compensation method extracting plaque motion from simultaneous B-mode images, and analyzed contrast appearance in all time frames to improve the calculation of IPN surface area.

The calculation of IPNSA of 45 plaques without motion compensation showed substantial influence on the outcome (fig. 8). It caused on average 10% of overestimation. The overestimation seems mainly caused by contrast from lumen or intensity from saturation artifacts that infiltrates the plaque ROI. As seen in figure 8, there are also some underestimated IPNSA. This seems to be caused by contrast spots that move out of the plaque ROI when no motion compensation is applied. Motion compensation will be crucial especially in case of small plaques, plaques surrounded with saturation artifacts, and adjacency of contrast from the jugular vein.

Comparing automated quantification to visual scoring, we had some debatable cases. Although two cases of 45 analyzed plaques were visually scored as 1, MIP of contrast provided IPN surface area close to zero for those cases. In these cases the plaques had very faint spots and visual assessment may also have been influenced by spots close to the plaque ROI. In two cases of visual score 0, some contrast spots were detected with MIP. The contrast appears in only few images of those two sequences and thereby they might have been missed during the visual assessment.

The automated quantification software that we developed will allow an objective, reproducible assessment of IPN and comparison of CEUS studies. We show a clear improvement with respect to the subjectivity of visual IPN scoring as reported in previous studies (Staub et al. 2010). To the best of our knowledge, this is the first study to extensively describe automated quantification methods of carotid IPN using an accurate motion compensated analysis tools for contrast-enhanced ultrasound. This automated quantification software may also allow to detect changes in IPN and assess the effectiveness of medical therapies on IPN progression.

The relatively small study population is a limitation in this study. Another limitation is the use of visual scoring as the ground truth for automated quantification of IPN, which might be a suboptimal reference. To confirm the present findings, future studies including histological assessment of IPN are necessary. This was beyond the scope of the present study.

As a third limitation, the automatically derived IPN from ultrasound will overestimate the actual size of IPN (as determined from histology) due to the point spread function (psf) of the ultrasound signal. The axial resolution in the

ultrasound contrast is about ~ 700 μm for a 3.5 MHz 3-cycle pulse used for contrast detection. Microvessels with diameters of 10-400 μm within the plaque will be displayed as about 7 pixels (~700 μm) diameter in the contrast image. Still a good correlation between histological IPN and CEUS IPN is expected. Consistently, Hoogi et al. (2011) reported a good correlation between IPN detected in CEUS and the IPN from histology.

Fourth limitation is the pseudo-enhancement artifact in the far wall plaques (ten Kate et al. 2012; Thapar et al. 2012). This limitation of CEUS might be overcome by development of new pulse sequences (Renaud et al. 2012).

A further limitation is the possibility of out of plane motion due to 2D imaging. This should be small for accurate compensation of inplane motion. Finally, microvessels within the plaque that are running in a direction almost perpendicular to the imaging plane are considered as artifact in VSA, but this should not result in errors above 10%.

CONCLUSIONS

IPN quantification methods were described in this paper and several IPN parameters were derived to evaluate IPN degree. Our automated IPN quantification tools will provide simpler and more standardized quantification/grading methods than those used in previous studies. Three of the derived parameters (IPNSA, IPNSR and MVN) are correlated significantly with visual scoring of IPN. IPNSA showed the best distinction between the visual IPN scoring groups. These results show that the proposed quantitative parameters have the potential to replace qualitative visual scoring and to measure IPN degree in an objective and reproducible manner. Future studies are needed to confirm that these quantitative parameters outperform visual scoring in the prediction of cardiovascular events or the presence of IPN in histology.

Table 3: Intra-observer (n=45 plaques) and Inter-observer (n=15) agreement of different IPN parameters assessed using automated quantification software on all atherosclerotic plaques. ICC = intra class correlation, MD = Mean difference between observations, SD = standard deviation.

	Intra-observer		**Inter-observer**	
Parameter	**ICC**	**MD±SD**	**ICC**	**MD±SD**
IPNSA (mm^2)	0.984 (p<0.001)	-0.12 ±0.63	0.960 (p<0.001)	-0.08 ±0.63
IPNSR (%)	0.971 (p<0.001)	0.36 ±5.92	0.968 (p<0.001)	-0.59 ±6.71
PMI	0.905 (p<0.001)	-0.05 ±0.58	0.833 (p<0.001)	-0.15 ±0.42
PLER (%)	0.887 (p<0.001)	-0.03 ±0.58	0.921 (p<0.001)	0.11 ± 0.28
MPCP (%)	0.916 (p<0.001)	-0.74 ±4.89	0.825 (p<0.001)	-2.14 ±3.98
MVN	0.835 (p<0.001)	-0.44 ±1.87	0.682 (p=0.002)	0.11 ±0.70

Table 2: Output and correlation of different IPN parameters assessed using automated quantification software using ultrasound data of all atherosclerotic plaques (n=45)*.

Parameter	Mean ± SD	Visual IPN score			Visual Score Groups Comparison (Kruskal-Wallis Test)†			*Correlation with visual IPN scores	
		2	1	0	1 vs. 2	0 vs. 2	0 vs. 1	SSP Excluded (n=37)	All Plaques (n=45)
IPNSA (mm^2)	3.49 ± 3.44	7.62 ± 3.71	2.45±2.05	0.49 ± 0.47	p < 0.01	p < 0.01	p < 0.01	0.757 (p<0.001)	0.719 (p<0.001)
IPNSR (%)	32.69 ± 24.7	54.67±18.01	27.48±22.8	14.55±18.1	p < 0.01	p < 0.01	NS	0.574 (p<0.001)	0.538 (p<0.001)
PMI	1.62 ± 1.32	2.57 ± 1.46	1.29 ± 1.20	1.43 ± 0.67	p < 0.01	NS	NS	0.343 (p=0.040)	0.277 (p=0.063)
PLER (%)	1.63 ± 1.22	2.47 ± 1.21	1.36 ± 1.18	1.35 ± 0.68	p < 0.01	NS	NS	0.415 (p=0.011)	0.356 (p=0.017)
MPCP (%)	15.6 ± 11.8	20.9 ± 11.2	12.8 ± 11.2	19.7 ± 11.1	NS	NS	NS	0.219 (p=0.195)	0.151 (p=0.322)
MVN	3.33 ± 3.12	5.82 ± 3.54	2.66 ± 2.64	1.80 ± 1.92	p < 0.01	p < 0.05	NS	0.578 (p<0.001)	0.474 (p=0.001)

IPNSA = intra-plaque neovascularization surface area; IPNSR = intra-plaque neovascularization surface ratio; LMI = lumen mean intensity;

MPCP=mean plaque contrast percentage;MVN=number of micro-vessels; PLER=plaque-to-lumen enhancement ratio; PMI=plaque mean intensity;

SD = standard deviation; SSP = substantially shadowed plaques.

* Correlation coefficients were calculated using Spearman's Rank (rho) correlation.

† In visual score groups comparisons (Kruskal-Wallis Test), natural logarithms of parameters were used.

Acknowledgements

This research was supported by the Center for Translational Molecular Medicine (CTMM) and the Netherlands Heart Foundation.

References:

Akkus Z, Hoogi A, Renaud G, ten Kate GL, van den Oord SCH, Schinkel AFL, de Jong N, van der Steen AFW, Bosch JG. Motion Compensation Method using Dynamic Programming for Quantification of Neovascularization in Carotid Atherosclerotic Plaques with Contrast Enhanced Ultrasound (CEUS). Proc Spie 2012, 8320;83200C:1-12.

Coli S, Magnoni M, Sangiorgi G, Marrocco-Trischitta MM, Melisurgo G, Mauriello A, Spagnoli L, Chiesa R, Cianflone D, Maseri A. Contrast-Enhanced Ultrasound Imaging of Intraplaque Neovascularization in Carotid ArteriesCorrelation With Histology and Plaque Echogenicity. Journal of the American College of Cardiology 2008;52:223-30.

Feinstein SB. Contrast ultrasound imaging of the carotid artery vasa vasorum and atherosclerotic plaque neovascularization. Journal of the American College of Cardiology 2006;48:236-43.

Ferguson GG, Eliasziw M, Barr HWK, Clagett GP, Barnes RW, Wallace MC, Taylor DW, Haynes RB, Finan JW, Hachinski VC, Barnett HJM, Trial NASCE. The North American Symptomatic Carotid Endarterectomy Trial - Surgical results in 1415 patients. Stroke 1999;30:1751-8.

Fleiner M, Kummer M, Mirlacher M, Sauter G, Cathomas G, Krapf R, Biedermann BC. Arterial neovascularization and inflammation in vulnerable patients - Early and late signs of symptomatic atherosclerosis. Circulation 2004;110:2843-50.

Hellings WE, Peeters W, Moll FL, Piers SRD, van Setten J, Van der Spek PJ, de Vries JPPM, Seldenrijk KA, De Bruin PC, Vink A, Velema E, de Kleijn DPV, Pasterkamp G. Composition of Carotid Atherosclerotic Plaque Is Associated With Cardiovascular Outcome A Prognostic Study. Circulation 2010;121(17):1941-50.

Hoogi A, Adam D, Hoffman A, Kerner H, Reisner S, Gaitini D. Carotid Plaque Vulnerability: Quantification of Neovascularization on Contrast-Enhanced Ultrasound With Histopathologic Correlation. American Journal of Roentgenology 2011;196:431-6.

Hoogi A, Akkus Z, van den Oord SCH, ten Kate GL, Schinkel AFL, Bosch JG, de Jong N, Adam D, van der Steen AFW. Quantitative Analysis of Ultrasound Contrast Flow Behavior in Carotid Plaque Neovasculature. Ultrasound Med Biol 2012;38:2072-83.

Huang PT, Huang FG, Zou CP, Sun HY, Tian XQ, Yang Y, Tang JF, Yang PL, Wang XT. Contrast-enhanced sonographic characteristics of neovascularization in carotid atherosclerotic plaques. J Clin Ultrasound 2008;36:346-51.

Hudson, J. M. Quantification of Blood Flow using Ultrasound. PhD Thesis, Department of Medical Physics, University of Toronto, 2011; Chapter 3, pp 64-65.

Magnoni M, Coli S, Marrocco-Trischitta MM, Melisurgo G, De Dominicis D, Cianflone D, Chiesa R, Feinstein SB, Maseri A. Contrast-enhanced ultrasound imaging of periadventitial vasa vasorum in human carotid arteries. Eur J Echocardiogr 2009;10:260-4.

Michel JB, Virmani R, Arbustini E, Pasterkamp G. Intraplaque haemorrhages as the trigger of plaque vulnerability. Eur Heart J 2011;32:1977-85.

Naghavi M, Libby P, Falk E, Casscells SW, Litovsky S, Rumberger J, Badimon JJ et al. From vulnerable plaque to vulnerable patient - A call for new definitions and risk assessment strategies: Part I. Circulation 2003;108:1664-72.

Papaioannou TG, Vavuranakis M, Androulakis A, Lazaros G, Kakadiaris I, Vlaseros I, Naghavi M, Kallikazaros I, Stefanadis C. In-vivo imaging of carotid plaque neoangiogenesis with contrast-enhanced harmonic ultrasound. Int J Cardiol 2009;134:e110-e2.

Renaud G, Bosch JG, ten Kate GL, Shamdasani V, Entrekin R, de Jong N, van der Steen AFW. Counter-propagating wave interaction for contrast-enhanced ultrasound imaging. Phys Med Biol 2012;57:L9-18.

Rothwell PM, Gutnikov SA, Warlow CP, European Carotid Surgery T. Reanalysis of the final results of the European Carotid Surgery Trial. Stroke 2003;34:514-23.

Schaar JA, Muller JE, Falk E, Virmani R, Fuster V, Serruys PW, Colombo A, Stefanadis C, Cassells SW, Moreno PR, Maseri A, van der Steen AFW. Terminology for high-risk and vulnerable coronary artery plaques - Report of a meeting on the vulnerable plaque, June 17 and 18, 2003, Santorini, Greece. Eur Heart J 2004;25:1077-82.

Schinkel AFL, Krueger CG, Tellez A, Granada JF, Reed JD, Hall A, Zang W, Owens C, Kaluza GL, Staub D, Coll B, Ten Cate FJ, Feinstein SB. Contrast-enhanced ultrasound for imaging vasa vasorum: comparison with histopathology in a swine model of atherosclerosis. Eur J Echocardiogr 2010;11:659-64.

Shah F, Balan P, Weinberg M, Reddy V, Neems R, Feinstein M, Dainauskas J, Meyer P, Goldin M, Feinstein SB. Contrast-enhanced ultrasound imaging of atherosclerotic carotid plaque neovascularization: a new surrogate marker of atherosclerosis? Vascular Medicine 2007;12:291-7.

Spagnoli LG, Mauriello A, Sangiorgi G, Fratoni S, Bonanno E, Schwartz RS, Piepgras DG, Pistolese R, Ippoliti A, Holmes DR. Extracranial thrombotically active carotid plaque as a risk factor for ischemic stroke. Jama-J Am Med Assoc 2004;292:1845-52.

Staub D, Partovi S, Schinkel AFL, Coll B, Uthoff H, Aschwanden M, Jaeger KA, Feinstein SB. Correlation of Carotid Artery Atherosclerotic Lesion Echogenicity and Severity at Standard US with Intraplaque Neovascularization Detected at Contrast-enhanced US. Radiology 2011;258:618-26.

Staub D, Patel MB, Tibrewala A, Ludden D, Johnson M, Espinosa P, Coll B, Jaeger KA, Feinstein SB. Vasa Vasorum and Plaque Neovascularization on Contrast-Enhanced Carotid Ultrasound Imaging Correlates With Cardiovascular Disease and Past Cardiovascular Events. Stroke 2010;41:41-7.

Stein JH, Korcarz CE, Hurst RT, Lonn E, Kendall CB, Mohler ER, Najjar SS, Rembold CM, Post WS. Use of Carotid Ultrasound to Identify Subclinical Vascular Disease and Evaluate Cardiovascular Disease Risk: A Consensus Statement from the American Society of Echocardiography Carotid Intima-Media Thickness Task Force Endorsed by the Society for Vascular Medicine. Journal of the American Society of Echocardiography 2008;21:93-111.

ten Kate GL, Renaud GGJ, Akkus Z, van den Oord SCH, ten Cate FJ, Shamdasani V, Entrekin RR, Sijbrands EJG, de Jong N, Bosch JG, Schinkel AFL, van der Steen AFW. Far-Wall Pseudoenhancement during Contrast-Enhanced Ultrasound of the Carotid Arteries: Clinical Description and in Vitro Reproduction. Ultrasound Med Biol 2012;38:593-600.

ten Kate GL, van den Oord SCH, Sijbrands EJG, van der Lugt A, de Jong N, Bosch JG, van der Steen AFW, Schinkel AFL. Current status and future developments of contrast-enhanced ultrasound of carotid atherosclerosis. Journal of Vascular Surgery 2013;57:539-46.

Thapar A, Shalhoub J, Averkiou M, Mannaris C, Davies AH, Leen ELS. Dose-Dependent Artifact in the Far Wall of the Carotid Artery at Dynamic Contrast-enhanced US. Radiology 2012;262:672-9.

Xiong L, Deng YB, Zhu Y, Liu YN, Bi XJ. Correlation of Carotid Plaque Neovascularization Detected by Using Contrast-enhanced US with Clinical Symptoms. Radiology 2009;251:583-9.

Chapter 5

Statistical Segmentation of Carotid Plaque Neovascularization

In several studies, intraplaque neovascularization (IPN) has been linked with plaque vulnerability. The recent development of contrast enhanced ultrasound enables IPN detection, but an accurate quantification of IPN is a big challenge due to noise, motion, subtle contrast response, blooming of contrast and artifacts. We present an algorithm that automatically estimates the location and amount of contrast within the plaque over time. Plaque pixels are initially labeled through an iterative expectation-maximization (EM) algorithm. The used algorithm avoids several drawbacks of standard EM. It is capable of selecting the best number of components in an unsupervised way, based on a minimum message length criterion. Next, neighborhood information using a 5x5 kernel and spatiotemporal behavior are combined with the known characteristics of contrast spots in order to group components, identify artifacts and finalize the classification. Image sequences are divided into 3-seconds subgroups. A pixel is relabeled as an artifact if it is labeled as contrast for more than 1.5 seconds in at least two subgroups. For 10 plaques, automated segmentation results were validated with manual segmentation of contrast in 10 frames per clip. Average Dice index and area ratio were 0.73±0.1 (mean±SD) and 98.5±29.6 (%) respectively. Next, 45 atherosclerotic plaques were analyzed. Time integrated IPN surface area was calculated. Average area of IPN was 3.73±3.51 mm^2. Average area of 45 plaques was 11.6±8.6 mm^2. This method based on EM contrast segmentation provides a new way of IPN quantification.

Z. Akkus, J. G. Bosch, G.V. S. Ferrero, Diego D. B. Carvalho, G. Renaud, S. C. H. van den Oord, G. L. ten Kate, A. F. L. Schinkel, N. Jong, A. F. W. van der Steen. **Statistical segmentation of carotid plaque neovascularization.** Proc. SPIE medical imaging 2013, 8675, 867506.

1. INTRODUCTION

Patients with carotid plaques carry an increased risk of sudden cardiovascular events, such as stroke, transient ischemic attack (TIA), myocardial infarction and even death [1, 2]. The benefit of carotid endarterectomy in reducing the risk of recurrent stroke for symptomatic patients with severe stenosis has been established by large European and North American clinical trials [3, 4]. Current clinical practice for choosing patients for a carotid endarterectomy operation is mainly based on assessing the degree of arterial lumen narrowing. However, there is an increasing awareness that not the size of the plaque, but its composition and risk of rupturing is related to these acute cardiovascular events [5-8]. Thus, the degree of stenosis is actually a poor predictor of individual stroke risk and improved risk stratification models should focus on plaque vulnerability rather than size. Early identification of atherosclerotic plaques at risk for instability and rupture may improve treatment strategies for the prevention of cardiovascular events. Several pathological studies demonstrated that intraplaque neovascularization (IPN) is associated with progressive atherosclerotic disease and plaque vulnerability [7]. Recent developments in contrast enhanced ultrasound (CEUS) enable detection of atherosclerosis and small microvessels with slow flow within the plaque by the use of ultrasound contrast agents [6].

In validation studies, a good correlation was found between the visual scoring of IPN and the number of intraplaque neovessels in histological samples [10-11]. Staub et al. [8] investigated 147 patients using CEUS. The degree of adventitial and plaque vasa vasorum was visually assessed (Grade 1: absent; Grade 2: present). The presence and degree of adventitial vasa vasorum and IPN were directly associated with established cardiovascular disease. These findings support that IPN is a sign of plaque vulnerability. Huang et al. presented dynamic evaluation of the plaque enhancement by using time intensity curve (TIC) of plaque. Vascularization was observed in 94% of the plaques qualified as soft based on the ultrasound characteristics and in 73% of plaques qualified as mixed. No vascularization was observed in the hard and calcified plaques [21]. Xiong et al. reported that the stroke and TIA patients had significantly more intraplaque contrast enhancement obtained from TIC than asymptomatic patients [22]. However, it may be questioned whether common TIC analysis as applied in large well-perfused organs like the liver or heart is applicable to quantification of microvessels in plaques. The plaques are very small and weakly perfused. The flow within the plaques is not continuous but characterized by occasional appearance of a faint moving contrast spot. Furthermore, the high intensity contrast in the carotid lumen is directly adjacent to the plaque, and the plaque is moving due to arterial pulsation and breathing. This complicates the generation of a valid non-contaminated plaque region of interest (ROI) for the TIC derivation. For these reasons, it is hard to obtain bolus kinetic parameters from time intensity curves for plaque. Hoogi et al. [12] presented an alternative approach: a quantitative method which segments the contrast spots within the plaque by using a Chan-Vese active contour algorithm [17] to calculate an IPN surface area. They reported a good correlation between IPN to plaque surface area ratio and histological IPN to plaque

surface area ratio (R^2 = 0.7905). However, the presented method also suffers from some limitations: ECG gating was applied to limit motion and only one CEUS image per cardiac cycle was used. Therefore, contrast appearance in other frames is missed and continuity of microvessel paths after time integration may be lost. Some additional motion compensation was performed, but this was done on the CEUS image itself. In CEUS images, only ultrasound contrast agent is visualized and tissue is suppressed. Therefore it is quite difficult to extract plaque motion from CEUS images.

The current contrast detection methods (i.e. amplitude modulation, pulse inversion) which are available in clinical ultrasound systems provide also artifacts, i.e. saturation artifacts and far wall pseudo-enhancement artifacts [20]. Especially calcified carotid plaques or heavily fibrotic carotid wall may produce high and low intensity saturation artifacts in CEUS images. In addition, the point spread function of the ultrasound system will provide blooming of contrast and artifacts. Furthermore, the persistence setting (temporal averaging) used in ultrasound systems may cause reduction of the signal of moving contrast spots. Therefore, a simple segmentation by (adaptive) thresholding will not suffice and a more elaborate classification of the observed intensities within the plaques in CEUS images is crucial for an accurate quantification of IPN. We investigated statistical distribution of gray level intensities of contrast within the plaque combined with neighborhood relations for an accurate quantification of IPN.

In statistical modeling of observed data, finite mixtures are a powerful probabilistic modeling tool. One of the most common methods used to fit finite mixture models to the observed data is the expectation and maximization (EM) algorithm which converges to a maximum likelihood (ML) estimate of mixture parameters [16]. Linguraru et al. [18] presented a statistical segmentation of surgical instruments in 3D ultrasound images by using an EM algorithm. The results compared well to expert-annotated images. However, the EM algorithm has several drawbacks such as sensitivity to initialization or the possibility of convergence to a singular estimate at the boundary of the parameter space. Figueiredo and Jain (2002) presented an unsupervised EM algorithm for learning a finite mixture model from multivariate data. The algorithm is capable of selecting the number of components, does not require a careful initialization and avoids the boundaries of the parameter space [15].

In this study, we present an algorithm that automatically classifies all pixels within the plaque into background, contrast and artifacts for all time frames by using an unsupervised EM algorithm. A time integrated total IPN surface area is calculated. We avoid the known limitations of quantification methods in the previous studies. For the analysis of the selected plaque, all images of the ultrasound sequence are used. Proper motion compensation is performed by deriving the plaque motion from the simultaneously acquired B-mode images. The algorithm was implemented as a tool in the CINQS software package that we previously developed for quantification of IPN. In the *in vivo* validation, we analyzed 45 carotid plaques and the IPN surface area calculated from statistical segmentation of contrast spots was compared to IPN surface area calculated from

a maximum intensity projection (MIP) image. The methodology of the intraplaque contrast segmentation with EM is described in the following sections.

2. METHODS

Our analysis methods require CEUS images that have simultaneously acquired contrast mode and B-mode, stored as DICOM files. An example can be seen in figure 1. In this study we have been using the Philips iU22 system (Philips Medical Systems, Bothell, USA) with L9-3 probe. The contrast mode is using a power modulation technique and a mechanical index of 0.06-0.08 is chosen for optimal contrast enhanced ultrasound images. CEUS was performed using intravenous administration of SonoVue ultrasound contrast agent (Bracco S.p.A., Milan, Italy).

The cine loops acquired during clinical examination are transferred as DICOM files to a computer workstation for off-line post-processing. A custom developed, user-friendly and well-structured, carotid intraplaque neovascularization quantification software (CINQS) is used to analyze data. The CINQS is developed in MevisLab, a development environment for medical image processing and visualization (MeVis Medical Solutions AG and Fraunhofer MEVIS, Bremen, Germany) The IPN quantification algorithms are implemented in MATLAB (The Mathworks Inc., Natick, Massachusetts, US), and run through a MeVisLab-MATLAB interface module. The communication between MevisLab modules and graphical user interface (GUI) is controlled via Python scripts.

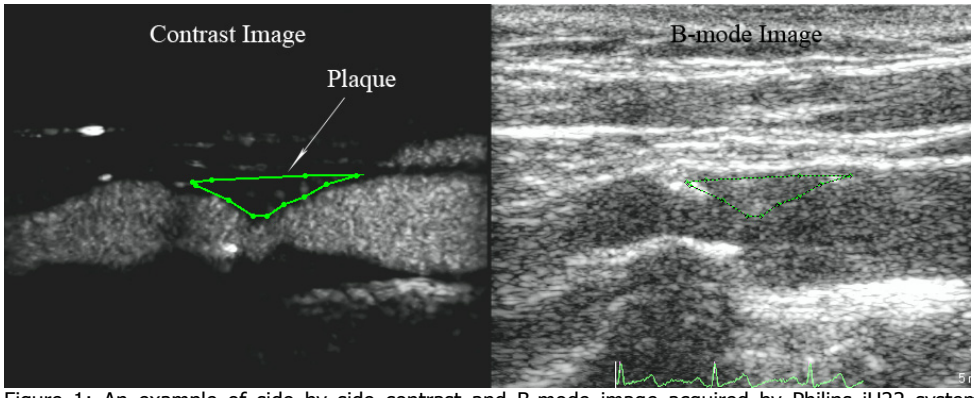

Figure 1: An example of side by side contrast and B-mode image acquired by Philips iU22 system. Contrast spots can be seen within the plaque region in the contrast image

The general analysis procedure is as follows. First, the time frame interval for the analysis is selected. The plaque region of interest is manually drawn in the CEUS image. In the B-mode image, a point of the atherosclerotic plaque is manually selected for motion compensation of the atherosclerotic plaque ROI. After motion compensation, the unsupervised EM algorithm [15] first selects the best number of components within the plaque based on gray level distribution and then the probability of each pixel belonging to each component is computed through an iterative EM algorithm using information from the neighboring pixels through a

Gaussian smoothing kernel with sigma=0.5. The resulting components are grouped by using a priori information obtained from expert-segmented contrast spots within a collection of plaques. Then neighboring and spatiotemporal information are used to distinguish artifacts and true contrast spots and to finalize classification. This is repeated for each frame and contrast spots are integrated over time using a logical OR operation to calculate the total IPN surface area. The different parts of the analysis procedure are detailed in the following sections.

2.1 Motion compensation

The carotid artery wall shows considerable motion due to the pulsating blood pressure, breathing and swallowing. Motion compensation is a prerequisite step for an accurate quantification of small microvessels within the carotid plaques. The contrast spots associated with these microvessels have sizes of a few pixels, while the plaque motion can amount to tens of pixels. The motion compensation method should be accurate and reliable enough for this purpose. In CEUS images, only ultrasound contrast agent is seen and tissue is suppressed so that it is quite difficult to extract plaque motion from CEUS images. Therefore we acquire simultaneous side-by-side B-mode images and CEUS images and the motion pattern of plaque is extracted from B-mode images and is applied to the plaque ROI in the contrast images to follow the identical plaque region. Plaque itself in B-mode images is quite a unique landmark in longitudinal and transversal directions, in contrary to healthy carotid wall sections, which are highly similar when moving along the vessel direction. In the first step of IPN analysis, motion compensation is performed by using multidimensional dynamic programming (MDP) combined with apodized block matching (BM) as was described in [13]. First, the user chooses a point on the plaque in a B-Mode image of the sequence. A fixed template of 61 x 41 pixels (6x4 mm) around this point is derived from the chosen image of the sequence. Then, the similarity of speckle pattern of template and speckle patterns in the consecutive images is calculated by using normalized cross correlation (NCC). The center position of the template is scanned over all positions within a defined search field (61 x 21 pixels (6x2 mm)) to find NCC coefficients. After this, the results of NCC are used as an input to MDP. The optimal plaque displacement is obtained with MDP as described in detail in [13] and the contrast images are aligned to the chosen contrast image based on detected plaque displacement in X and Y direction for motion correction.

2.2 Expectation-maximization

EM is an iterative procedure which finds local maxima of the maximum likelihood. The maximum likelihood parameters are computed iteratively starting with initial estimation. The algorithm converges to a steady state when a local maximum is reached [15, 16]. We use EM algorithm to solve a mixture estimation problem and separate background, blooming of contrast, contrast spots and artifact. We approximated the probability density function (pdf) of contrast by Gaussian distribution as seen in figure 8. The EM algorithm tries to determine the

probability of a pixel belonging to one of the defined classes (c). We describe the distribution function as a sum of four Gaussians ($p(y|\mu,\sigma)$):

$$p(y \mid \theta) = \sum_{c=1}^{4} \omega_c p(y|\, \mu_c, \sigma_c) \qquad (1)$$

The parameters of the Gaussian mixture model are:

$$\sum_{c=1}^{4} \omega_c = 1 \qquad \mu_c = \frac{1}{N} \sum_{i=1}^{N} y_i \qquad \sigma_c^2 = \frac{1}{N} \sum_{i=1}^{N} (y_i - \mu_c)^2 \qquad (2)$$

There are two steps at each iteration:

1. Expectation step: The parameters of the four distributions are calculated in this step.
   Let Y = ($y_1, y_2, \ldots\ldots y_N$) be the observations from the mixture of four Gaussians $\theta = \{\omega, \mu, \sigma\}$, $\omega = (\omega_1, \omega_2, \omega_3, \omega_4)$, $\mu = (\mu_1, \mu_2, \mu_3, \mu_4)$, $\sigma = (\sigma_1, \sigma_2, \sigma_3, \sigma_4)$ must be estimated from Y.
   Then the probability of each pixel belonging to one of the four defined classes Ψ_1, Ψ_2, Ψ_3, and Ψ_4 is computed by using the parameters θ and Bayes's law. In equation 3, ω_j is the a priori probability that a pixel belongs to that class Ψ_j. $P(y_i \in \Psi_j)$ is the posterior probability of that pixel.

$$p(y_i \in \Psi_j) = \frac{\omega_j \cdot\, p(y_i|\, \mu_j, \sigma_j)}{\sum_c^4 \omega_c \cdot\, p(y_i|\, \mu_c, \sigma_c)} \qquad (3)$$

   The expectation of log-likelihood will be computed for given parameters θ

$$\ln p(Y|\theta) = \sum_{i=1}^{N} \ln p(y_i|\theta) \qquad (4)$$

2. Maximization Step: The parameters $\theta = \{\omega, \mu, \sigma\}$, will be updated with each iteration until the algorithm converges to a steady state.

$$\omega_j = \frac{\sum_i p(y_i \in \Psi_j)}{\sum_{i,c} p(y_i \in \Psi_c)} \quad \mu_j = \frac{\sum_i p(y_i \in \Psi_j) \cdot y_i}{\sum_i p(y_i \in \Psi_j)} \quad \sigma_j^2 = \frac{\sum_i p(y_i \in \Psi_j) \cdot (y_i - \mu_j)^2}{\sum_i p(y_i \in \Psi_j)} \qquad (5)$$

The used EM algorithm adopted from Figueiredo and Jain [15] avoids several drawbacks of standard EM such as sensitivity to initialization and possible convergence to the boundary of the parameter space. It is capable of selecting the number of components in an unsupervised way. The method used for selecting the number of components is based on a minimum message length (MML) criterion

which is directly implemented by a modified EM algorithm. The important feature of this EM algorithm is the integration of estimation and model selection in a single algorithm instead of using MML as a model selection criterion to choose the best one among candidates. The MML criterion was used as a cost function and it was minimized through EM. The M-step of EM was used as a component annihilator. When one of the components becomes too weak, which means that it is not represented by data anymore, it is simply annihilated. The algorithm starts with a larger number of components than the true number of mixture components all over the space and the unnecessary ones are removed.

The best number of components within the plaque is selected in an unsupervised way. Then, the probability of each pixel belonging to each component is computed through an iterative EM algorithm using information from the neighboring pixels through a Gaussian smoothing kernel with sigma 0.5. Based on our observations of in vivo images, there are four meaningful classes to consider within the plaque. However, each class can contain more than one of the detected components. Therefore, the detected Gaussian distribution components are grouped into 4 classes, being a background class (background), intermediate class (blooming of contrast), contrast spot class and artifact class. The grouping is based on the mean of the Gaussian distribution components. The Gaussians which have mean between 0-5, 6-15, 16-150, 151-255 are assigned to background class, intermediate class, contrast spot class, and artifact class respectively, as an initial grouping of the found components. This a priori information was obtained from 3 representative plaques which includes the four classes. Each class was segmented by an expert in several frames of the 3 plaques (10 frames in total). The normalized histograms of expert segmentation of those four classes are seen in figure 7 and normalized fitted Gaussian probability distribution functions are seen in figure 8. The mean, standard deviation and mean error between Gaussian fit and histogram data is seen in table 1. As can be seen in figure 7-8, the overlap between blooming of contrast and contrast spot class and the overlap between artifact class and contrast spot are the main uncertainty in the EM algorithm.

2.3 Neighboring information

After this rough grouping into 4 classes, a 5-by-5 (pixels) kernel is scanned over the plaque region and intermediate class labels are reassigned to contrast spot class or background class.

- First, the central pixel of the 5-by-5 kernel has to be the intermediate class

The criteria for assigning a contrast spot class label to an intermediate class label:

- The amount of contrast spot labels have to be higher than the amount of background class labels in the kernel and at least 4 pixels have to belong to contrast spot class.

The criteria for assigning background class label to an intermediate class label:

- The amount of background class labels have to be higher than the amount of contrast spot class labels and at least 4 pixels have to belong to background class in the kernel.

In both cases, if less than 4 pixels (contrast spot or background) are found the intermediate class label remains unchanged.

2.4 Spatiotemporal behavior of contrast

Contrast spots within the plaque are moving with a slow velocity between 1mm/s and 6mm/s, which is obtained from tracking of spots in [14]. There are two types of artifacts within or around the plaque: low intensity stationary artifacts and high intensity saturation artifacts. These artifacts can move and change shape slowly over time, but they are relatively stationary in comparison to contrast motion. This property is exploited to distinguish between true contrast spots and artifacts. The image sequence is divided into 3 seconds subgroups of images. For each pixel in the plaque, the number of frames within the subgroup in which it was labeled as contrast is counted. If a pixel was labeled as contrast spot for more than 50% of frames in at least two 3-seconds subgroups, it was considered as an artifact and relabeled to the artifact class. After this a 9-by-9 pixels kernel is scanned over the plaque region to refine neighborhood of artifacts class. An example of classification of the plaque into artifact, contrast spot, blooming of contrast and background can be seen in figure 4.
The criteria for assigning intermediate class or spot class to artifact class:

- The central pixel of 9-by-9 kernel has to be the intermediate class or contrast spot class
- If the number of pixels belonging to artifact class is the highest, the pixel is assigned to artifact

2.5 *In Vivo* Classification Validation

All analyses were performed according to a structured protocol by one physician. For 10 atherosclerotic plaques, automated segmentation results were validated with manual segmentation of contrast by an expert in 10 frames per clip. The frames for manual segmentation were selected as every 10th frame right after the flash frame. Average Dice index and area ratio were calculated.

2.6 Comparison to visual scoring: Patient population and study protocol

A total of 45 plaques of 23 patients were included for analysis. Patients were scheduled for elective carotid endarterectomy (CEA). The indication for CEA was made in consensus by the treating neurologist and vascular surgeon. All patients were known to have a >70% stenosis of the internal carotid artery as determined on CT-angiography. Mean age of the patients was 65 ± 9 years. Mean body-mass index (BMI) of the patients was 29 ± 6 kg/m2. Fourteen patients (56%) were known to have hypertension, 6 patients (24%) were known to have diabetes and 11 patients (44%) were current smokers. The majority of the patients (92%) had ipsilateral cerebrovascular symptoms (i.e. stroke, TIA, ischemic ocular event). All patients underwent a bilateral standard carotid ultrasound examination and a CEUS examination of the carotid arteries on the day prior to CEA. The study protocol was approved by the ethical committee of the Erasmus Medical Center and all study participants provided informed consent.

One clip per carotid artery was chosen for automated analysis. Median number of frames in the selected time-frame intervals for analysis was 315 ± 97.

2.7 Visual carotid ultrasound analysis

All standard carotid ultrasound clips and CEUS clips were reviewed offline by two independent observers. Both observers were blinded from patient specific data. The analysis of the clips was performed in a predefined sequence. Standard carotid ultrasound clips were evaluated before the CEUS clips. The atherosclerotic plaques were scored for the presence of IPN by using the CEUS clips. Contrast enhancement in the atherosclerotic plaque was considered to represent IPN. For each carotid artery the presence of IPN was graded using a previously published grading scale: (0) no IPN, (1) limited or moderate IPN, or (2) severe IPN [19]. If there was a discrepancy in the scores of the independent readers, a consensus was reached afterwards. The visual IPN score was only used for atherosclerotic plaques visible at the near wall of the carotid artery. Plaques at the far wall were excluded from analysis because of a recently discovered artifact [20]. Contrast enhancement in atherosclerotic plaques on the far wall is not reliable because of this far-wall pseudo-enhancement artifact. The plaques selected for analysis were visually characterized. The average maximum plaque thickness was 6.82 ± 1.24 mm and the median Gray-Weale score of the atherosclerotic plaques was 3.

2.8 Automated IPN analysis

Forty-five (45) atherosclerotic plaques right after the flash frame were analyzed. Contrast spots are statistically segmented in each frame and total surface area of IPN was calculated after logical OR operation of contrast spot class over time. The natural logarithm of calculated IPN surface area was taken to compare with visual IPN scores as seen in figure 5. An example of IPN surface area is seen in figure 2, 4. The obtained results were compared to IPN surface area calculated from MIP image using an adaptive threshold which takes into account lumen intensity, background noise from tissue, and visual limitation. In our data set, we excluded saturation artifacts from nearby plaque ROI during the drawing of plaque ROI for comparison of MIP and statistical segmentation results. An example of saturation artifacts within the plaque ROI and results of MIP and statistical segmentation can be seen in figure 4.

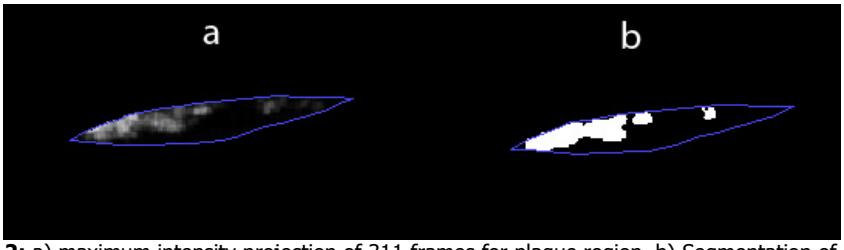

Figure 2: a) maximum intensity projection of 311 frames for plaque region. b) Segmentation of IPN over 311 frames after logical OR operation of contrast spot classification

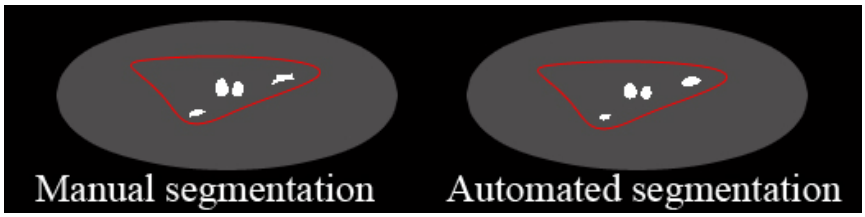

Figure 3: An example of manual and automated segmentation of contrast spots within the plaque

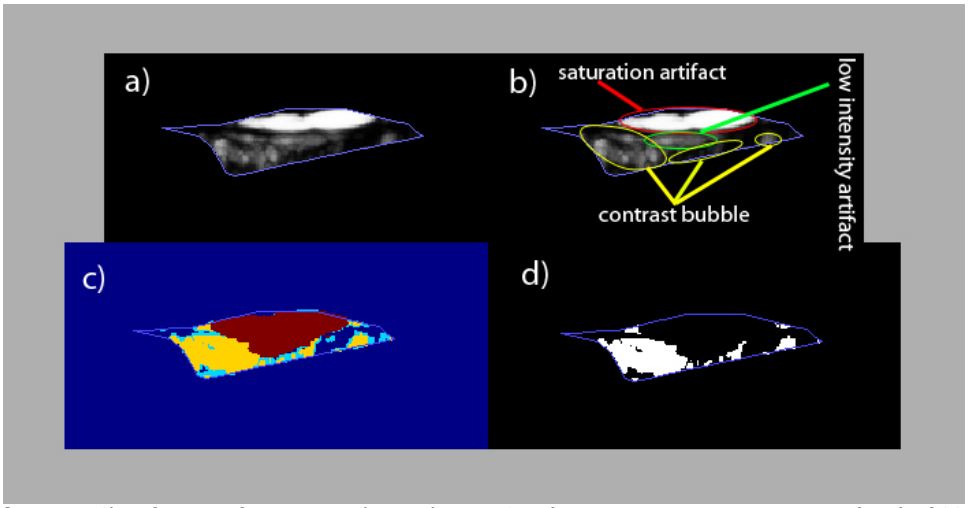

Figure 4: Classification of contrast within a plaque ROI. a) Maximum intensity projection (MIP) of 328 frames. b) Regions of different classes indicated in MIP image c) Labeled image after classification and OR operation over time. Red labels (artifacts). Yellow labels (contrast spot). Cyan labels (blooming of contrast). Blue labels are background. d) Only contrast spot class

3. RESULTS

In the *in-vivo* validation, average Dice index and area ratio of contrast spots were found to be 0.73±0.1 (mean±SD) and 98.5±29.6 (%) respectively. For 33% of the 100 chosen plaque images, both algorithm and expert detected contrast. Both algorithm and expert detected nothing in 57% of chosen plaque images. Algorithm gave false positive response in 4% of images and false negative in 5% of images. An example of manual and automated segmentation of contrast in the plaque can be seen in figure 3.

Average surface area of IPN calculated after time integration of segmented contrast spots with logical OR operation for 45 atherosclerotic plaques was 3.73±3.51 mm^2. Average surface area of IPN calculated after MIP image was 3.49±3.44 mm^2. Average area of the 45 plaques was 11.6±8.6 mm^2. The difference between IPN surface area derived from statistical contrast segmentation and IPN surface area derived from MIP image was 0.24±0.84 mm^2. An example of segmentation and time integration of contrast spots after logical OR operation and maximum intensity projection image over 311 images can be seen in figure 2. In

figure 6, an example of the probability map within a plaque obtained by EM is shown as an RGB image. It shows the probabilities of each pixel belonging to each of three classes (background, blooming of contrast and contrast spot) in the blue, green and red channel, respectively.

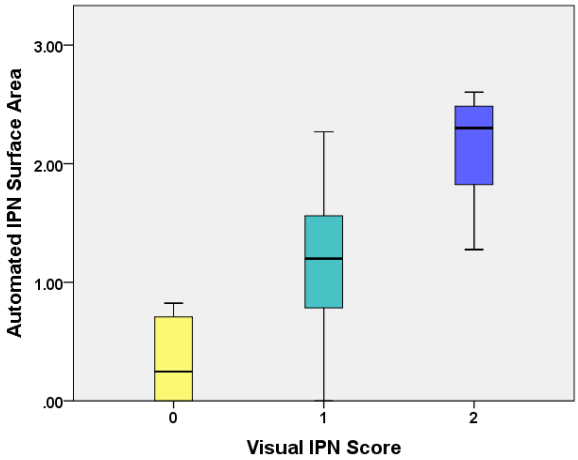

Figure 5: The association between visual IPN scores and automated IPN surface area score (Ln (IPN surface area (mm^2) +1)) obtained from statistical segmentation of contrast.

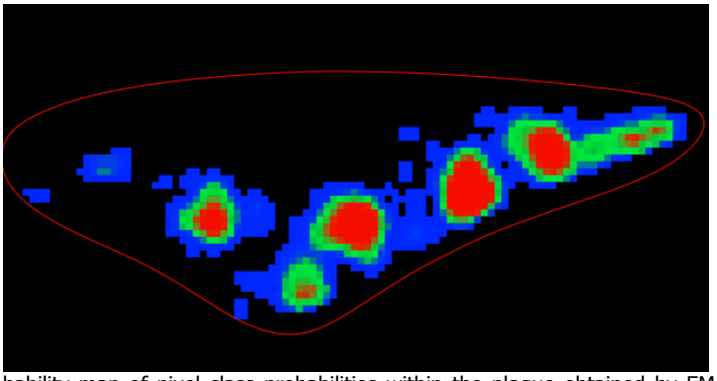

Figure 6: Probability map of pixel class probabilities within the plaque obtained by EM shown as an RGB image. Blue channel (probability of background class), green channel (blooming of contrast), Red channel (contrast spots) . All black pixels (0) are background as well. There is no artifact class in this image.

4. DISCUSSION

The presence and severity of IPN in atherosclerotic plaques has been linked to plaque vulnerability in several studies [6, 7, and 8]. In many of them, a visual grading scale was used for the assessment of IPN using CEUS. Although some studies have quantitatively evaluated IPN in CEUS images, they suffer for some limitations in their quantification methods [12, 21, and 22] as explained in the introduction. In our study, we overcome the known limitations of automated quantification methods in the previous studies. We used an accurate motion

compensation to avoid plaque ROI to hit lumen and analyzed the whole image sequence which is selected for analysis.

Classification of contrast within the plaque into background, contrast spot and artifact will allow an accurate quantification of IPN. This will avoid inclusion of artifacts in calculation of time integrated IPN surface area. MIP however will consider artifacts as contrast spots within the plaque. Therefore, our statistical segmentation of contrast spots is expected to provide more reliable and accurate results than MIP if there is an artifact within the plaque ROI. In this study, plaque ROIs were used that excluded the main artifacts; therefore the results of MIP and EM-based method are not very different. It would be worth comparing the results for ROIs including artifacts. There is a small bias (24 pixels) in the difference of the results of the two methods and standard deviation is around 89 pixels. When examining our data set, we found that in some cases, faint bubbles are suppressed due to the hard threshold used in MIP. However, the neighboring information applied in the EM-based method allows detecting them. The EM-based method also suppressed some individual contrast pixels and penetration of lumen at the edges of the plaque ROI that MIP preserved.

In the *in vivo* validation, the detection of presence/absence of contrast by the EM algorithm was identical to manual segmentation in 90% of the cases. There was false positive detection in 4% of the cases and false negative detection in 5% of the cases. The spots in those cases were small and faint and thereby it was hard to determine whether they were indeed contrast spots or noise. The surface area ratio between manual and automated segmentation, was on average almost 100%. There was a 30% standard deviation. This relatively large standard deviation can be attributed to the small size of the contrast spots. A few pixels variation in segmentation of those small contrast spots will already cause this.

One of the limitations in our study is that visual analysis was used as the reference or ground truth for automated quantification of IPN. Visual analysis may be a suboptimal reference, and future studies including histological assessment of IPN are needed to confirm the relation of our present findings to histology. In two cases of 45 analyzed plaques, although they were visually scored 1, our method did not detect any contrast. That is why the lowest bound of score 1 box plot stretched to 0 in figure 5. MIP of contrast also provided IPN surface area close to zero for those cases. Either the plaques had faint spots or visual assessment was influenced by spots close to the plaque ROI. In two cases of visual score 0, some contrast spots were detected with both our method and MIP. The contrast appears hardly ever in those two sequences and thereby they might be missed during the visual assessment. Second, due to the pseudo-enhancement artifact in the far wall plaques it is not possible to reliably analyze atherosclerotic plaques that are located on the far wall of the carotid artery [20]. Therefore, plaques in the far wall were excluded from analysis. Development of new pulse-sequences that overcome this artifact will probably provide a solution for this limitation of CEUS [23].

5. CONCLUSIONS

Our algorithm enables to automatically estimate the location and amount of contrast within the plaque over time.

The proposed method for segmentation of neovascularization is capable of classifying the plaque into four classes as background, blooming of contrast, contrast spot, and artifact. Artifacts within plaques can be detected and discarded after classification. The validation results show a correct segmentation and positioning of contrast spots. Automated IPN surface area shows a good distinction between different visual IPN scoring groups as seen in figure 5. Our EM-based method provides a new and potentially more accurate quantification of IPN to identify vulnerable plaques.

ACKNOWLEDGMENT

This research was supported by the Center for Translational Molecular Medicine and the Netherlands Heart Foundation (PARISk).

Table 1: The gray value mean and standard deviation of the distribution of background, blooming of contrast, contrast spot, and saturation artifacts class estimated from 10 expert segmented images of 3 plaques. Root mean square (RMS) error is determined between actual distributions and Gaussian distributions for the same mean and standard deviation.

	mean	standard deviation	RMS error
Background	2.3	1.8	0.0691
Blooming of contrast	10.4	4.9	0.055
Contrast spot	41.4	21.8	0.2847
Saturation artifact	168.53	59.3	0.4952

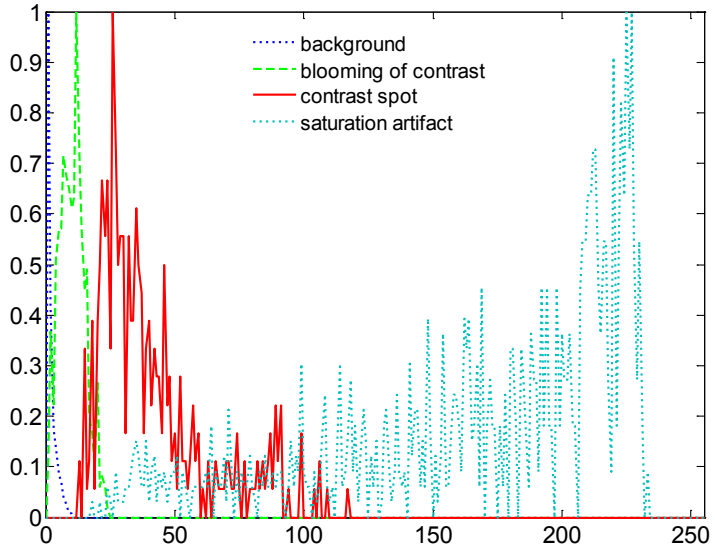

Figure 7: The normalized histograms of background, blooming of contrast, contrast spot and saturation artifact, which were obtained from manual segmentation in 10 frames of 3 plaques.

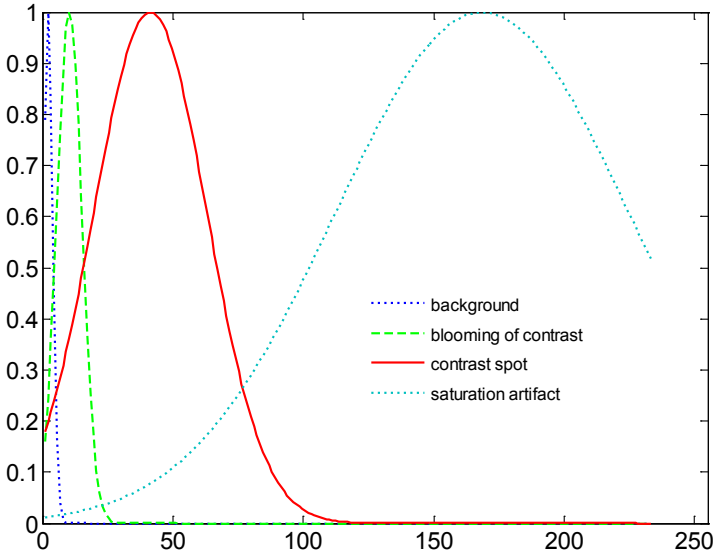

Figure 8: The normalized approximate Gaussian distribution of background, blooming of contrast, contrast spot and saturation artifact, which were obtained from manual segmentation in 10 frames of 3 plaques.

References:

[1] Naghavi, M. et al., "From vulnerable plaque to vulnerable patient - A call for new definitions and risk assessment strategies: Part I," Circulation, vol. 108, pp. 1664-1672, Oct 7 (2003).
[2] Spagnoli, L. G., et al., "Extracranial thrombotically active carotid plaque as a risk factor for ischemic stroke," Jama-Journal of the American Medical Association, vol. 292, pp. 1845-1852, Oct 20 (2004).
[3] Ferguson, G. G. et al., "The North American Symptomatic Carotid Endarterectomy Trial - Surgical results in 1415 patients," Stroke, vol. 30, pp. 1751-1758, Sep (1999).
[4] Rothwell, P. M. et al., "Reanalysis of the final results of the European Carotid Surgery Trial," Stroke, vol. 34, pp. 514-523, Feb (2003).
[5] Schaar, J. A. et al., "Terminology for high-risk and vulnerable coronary artery plaques - Report of a meeting on the vulnerable plaque, June 17 and 18, (2003), Santorini, Greece," European Heart Journal, vol. 25, pp. 1077-1082, Jun (2004).
[6] Feinstein, S. B. "Contrast ultrasound imaging of the carotid artery vasa vasorum and atherosclerotic plaque neovascularization," Journal of the American College of Cardiology, vol. 48, pp. 236-243, Jul 18 (2006).
[7] Hellings, W. E. et al., "Composition of Carotid Atherosclerotic Plaque Is Associated With Cardiovascular Outcome A Prognostic Study," Circulation, vol. 121, pp. 1941-U111, May 4 (2010).
[8] Staub, D., Patel, M.B., Tibrewala, A., et al. "Vasa vasorum and plaque neovascularization on contrast-enhanced carotid ultrasound imaging correlates with cardiovascular disease and past cardiovascular events" Stroke, 41:41-7 (2010).
[9] Fleiner, M. et al., "Arterial neovascularization and inflammation in vulnerable patients - Early and late signs of symptomatic atherosclerosis," Circulation, vol. 110, pp. 2843-2850, Nov 2 (2004).
[10] Magnoni, M. et al., "Contrast-enhanced ultrasound imaging of periadventitial vasa vasorum in human carotid arteries," European Journal of Echocardiography, vol. 10, pp. 260-264, Mar (2009).
[11] Schinkel, A. F. L. et al., "Contrast-enhanced ultrasound for imaging vasa vasorum: comparison with histopathology in a swine model of atherosclerosis," European Journal of Echocardiography, vol. 11, pp. 659-664, Sep (2010).
[12] Hoogi, A. et al., "Carotid Plaque Vulnerability: Quantification of Neovascularization on Contrast-Enhanced Ultrasound With Histopathologic Correlation," American Journal of Roentgenology, vol. 196, pp. 431-436, Feb (2011).
[13] Akkus, Z., Hoogi, A., Renaud, G., ten Kate, G.L., van den Oord, S.C.H., Schinkel A.F.L., de Jong, N., van der Steen A.F.W., Bosch, J.G. "Motion Compensation Method using Dynamic Programming for Quantification of Neovascularization in Carotid Atherosclerotic Plaques with Contrast Enhanced Ultrasound (CEUS) " Proc. SPIE 8320, 83200C (2012)
[14] Hoogi, A. Akkus, Z. et al., "Quantitative Analysis of Ultrasound Contrast Flow Behavior in Carotid Plaque Neovasculature, " Ultrasound in Medicine and Biology, vol. 38, pp. 2072-2083, Dec (2012).
[15] Mario, A.T.F., Anil K.J. "Unsupervised learning of finite mixture models" *IEEE Transactions on Pattern Analysis and Machine Intelligence* 24(3): 381–396, (2002).
[16] Couvreur, C. "The EM Algorithm: A Guided Tour." IEEE European Workshop on Computationally Intensive Methods in Control and Signal Processing, 115–120, (1996).
[17] Chan, T.F., Vese, L.A. "Active contour without edges", IEEE Trans Image Process, 10:266–277, (2001)
[18] Linguraru, M. G. et al., "Statistical segmentation of surgical instruments in 3-d ultrasound images," Ultrasound in Medicine and Biology, vol. 33, pp. 1428-1437, Sep (2007).
[19] Staub, D. *et al.*, "Correlation of Carotid Artery Atherosclerotic Lesion Echogenicity and Severity at Standard US with Intraplaque Neovascularization Detected at Contrast-enhanced US," *Radiology,* vol. 258, pp. 618-626, Feb (2011).
[20] ten Kate, G. L. *et al.*, "Far-Wall Pseudoenhancement during Contrast-Enhanced Ultrasound of the Carotid Arteries: Clinical Description and in Vitro Reproduction," *Ultrasound in Medicine and Biology,* vol. 38, pp. 593-600, Apr (2012).
[21] Huang, P. T. *et al.*, "Contrast-enhanced sonographic characteristics of neovascularization in carotid atherosclerotic plaques," *Journal of Clinical Ultrasound,* vol. 36, pp. 346-351, Jul-Aug (2008).
[22] Xiong, L. *et al.*, "Correlation of Carotid Plaque Neovascularization Detected by Using Contrast-enhanced US with Clinical Symptoms," *Radiology,* vol. 251, pp. 583-589, May (2009).
[23] Renaud, G. *et al.*, "Counter-propagating wave interaction for contrast-enhanced ultrasound imaging," *Physics in Medicine and Biology,* vol. 57, pp. L9-L18, Nov 7 (2012).

Chapter 6

Carotid Intraplaque Neovascularization Quantification Software (CINQS)

Intraplaque neovascularization (IPN) is an important biomarker of atherosclerotic plaque vulnerability. As IPN can be detected by contrast enhanced ultrasound (CEUS), imaging-biomarkers derived from CEUS may allow early prediction of plaque vulnerability. To select the best quantitative imaging-biomarkers for prediction of plaque vulnerability, a systematic analysis of IPN with existing and new analysis algorithms is necessary. Currently available commercial contrast quantification tools are not applicable for quantitative analysis of carotid IPN due to substantial motion of the carotid artery, artifacts, and intermittent perfusion of plaques. We therefore developed a specialized software package called Carotid Intraplaque Neovascularization Quantification Software (CINQS). It was designed for effective and systematic comparison of sets of quantitative imaging-biomarkers. CINQS includes several analysis algorithms for carotid IPN quantification and overcomes the limitations of current contrast quantification tools and existing carotid IPN quantification approaches. CINQS has a modular design which allows integrating new analysis tools. Wizard-like analysis tools and its graphical-user-interface facilitate its usage. In this paper, we describe the concept, analysis tools, and performance of CINQS, and present analysis results of 45 plaques of 23 patients. The results in 45 plaques showed excellent agreement with visual IPN scores for two quantitative imaging-biomarkers (The area under the receiver operating characteristic curve was 0.92 and 0.93).

Z. Akkus, G. van Burken, S. C.H. van den Oord, A. F.L. Schinkel, N. de Jong, A. F.W. van der Steen, J. G. Bosch. **Carotid Intraplaque Neovascularization Software (CINQS).** IEEE Journal of Biomedical and Health Informatics, 99,1-7, 2014

I. INTRODUCTION

Several pathological studies have presented intraplaque neovascularization (IPN) as an important biomarker for plaque instability and rupture [1-3]. These small microvessels within arterial atherosclerotic plaques can be visualized using contrast enhanced ultrasound (CEUS). Therefore, quantitative imaging biomarkers based on CEUS may allow early prediction of plaque vulnerability. To select the best quantitative imaging biomarkers, a systematic evaluation and optimization of existing and new IPN analysis algorithms, and an effective and systematic comparison of sets of multiple imaging biomarkers need to be done on patient populations.

IPN is seen in a CEUS image sequence as the subtle intermittent appearance of small moving contrast spots within the dark plaque. Currently available commercial tools for contrast quantification, e.g. QLAB ROI quantification tool (Philips Medical Systems, Bothell, USA) and VueBox (Bracco Suisse SA, Geneva, Switzerland), are not suitable for quantitative analysis of IPN. These quantification tools have been developed mainly for large organs such as heart, liver and prostate, not for plaques. Plaques are relatively small and weakly perfused structures, and directly adjacent to the bright artery lumen. Saturation and shadowing artifacts are common. Plaques are also moving substantially due to pulsation of the artery, breathing, or patient motion. Therefore, accurate tracking of the motion of the plaque is essential for intensity analysis to prevent contamination of the ROI by contrast from the lumen and high intensity artifacts. Currently available contrast quantification tools are based on time intensity curves (TIC). TICs of atherosclerotic plaques are characterized by a number of short peaks corresponding to the passage of single (or clusters of) contrast bubbles (see fig.1) and do not resemble the typical massive bolus passage or flash/replenishment curves seen in the lumen of an artery or in the perfusion pattern of large organs or tumors. As can be seen in fig.1, fitting a curve model for bolus perfusion (such as Gamma-Variate [4] or local density random walk (LDRW) [5]) to the TIC of IPN does not capture the true perfusion characteristics of IPN. In some studies [6-7], such bolus passage parameters such as plaque enhancement (PE) (PE=Peak intensity (PI) – Baseline intensity (BI, intensity at time 0)) and PE to lumen enhancement ratio parameters were used to assess IPN. They were derived from TIC curve fitting in the same way as for large organs. In our opinion, this is not a suitable approach. Therefore, there is a considerable demand for specialized IPN quantification tools.

So far, assessment of IPN relies mostly on subjective visual assessment as quantification tools for IPN are scarce. Recently, a review paper [9] presented the methods used so far to assess IPN and discussed the current status of CEUS in carotid atherosclerosis. There are some reported quantitative approaches [6-8] but they suffer from a number of limitations as described in [10].

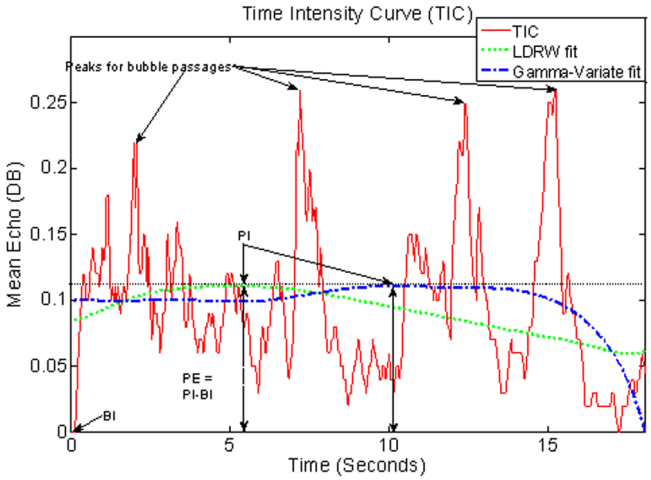

Figure 1: Time intensity curve (TIC) of a plaque and local density random walk (LDRW) and gamma-variate curve fits obtained with QLAB ROI quantification tool. PE = plaque enhancement. PI = peak enhancement. BI = baseline intensity, intensity at time 0.

In our study, we focus on carotid artery plaques at risk of rupture by using non-invasive CEUS imaging. Our work is performed in the context of a large consortium project, CTMM-ParisK (Plaque At Risk), which investigates molecular, biological, morphological, biomechanical and imaging biomarkers of carotid artery atherosclerotic plaque to detect plaque at risk of rupture. Our purpose is to compare existing and new IPN parameters derived from CEUS and to select suitable IPN parameters for prediction of plaque vulnerability. For this purpose, we need a platform which allows evaluation and optimization of IPN quantification tools for CEUS images. Requirements for such a platform include:

1. Development and optimization of new and existing IPN analysis algorithms
2. Testing existing and new IPN analysis algorithms systematically on patient datasets
3. Measuring intra-observer and inter-observer variability for reproducibility of results
4. Open to integration of new analysis tools for comparison
5. Reproducible and repeatable usage of analysis tools and platform
6. Tools should be usable by clinicians without programming knowledge

We therefore developed a software package called Carotid Intraplaque Neovascularization Quantification Software (CINQS). CINQS was developed for internal use within the CTMM-ParisK project. It contains a collection of different IPN analysis tools for carotid artery CEUS image sequences that can overcome the limitations of currently available contrast quantification tools and reported IPN quantification approaches. It enables systematic analysis of IPN with different analysis tools on large datasets (up to several hundred patients), comparing their outputs, and selecting suitable parameters for measuring IPN degree. In this

paper, we describe the concept, design, analysis tools and performance of CINQS. We also present analysis results of 45 plaques of 23 patients.

II. Concepts of Cinqs

CINQS requires side-by-side simultaneously acquired contrast and B-mode image sequences. This choice was made because the plaque motion is a serious issue in IPN analysis, and this motion can be obtained more accurately from B-mode images than from contrast images. It was designed for the side-by-side carotid contrast images (see fig. 2) of the Philips iU22 system but it could be easily extended for other ultrasound systems which provide such side-by-side images.

The features of CINQS are listed below:

1. *Specialized IPN analysis tools for carotid CEUS image sequences*: Currently available contrast quantification tools (e.g. QLAB and VueBox) generally provide only TIC analysis for a ROI (without motion compensation suitable for plaques). In addition to TIC perfusion analysis, CINQS includes motion compensation tools tailored for plaques; time integrated parametric images of plaque perfusion such as maximum intensity projection (MIP), and analogously, minimum, mean, and standard deviation intensity projection images over time; detection and tracking of individual contrast spots within a plaque ROI to detect microvasculature paths; and segmentation of individual contrast spots based on statistical models of intensity distributions, and their time integration to find neovascularization area.
2. *Saving and retrieving of objects and analyses*: Objects (ROIs of plaque, lumen and background, or motion compensation points) and complete analyses (e.g. a MIP including ROI, motion compensation points and all analysis settings) are saved separately into XML files and can be retrieved separately as well. Objects can be reused and assigned to multiple IPN analysis tools. Retrieving previously defined objects for every patient allows systematic comparison of different IPN analysis tools over patient datasets. Furthermore, this allows comparing different versions of IPN analysis algorithms and optimizing their parameters for the same objects. CINQS also allows retrieving complete analyses without displaying the previously defined objects. This allows observers to redefine objects with previous analysis settings (e.g. frame interval, motion compensation pattern) while being blinded to the previous objects, for measuring intra-observer and inter-observer variability. In currently available contrast quantification tools, objects such as ROIs generally cannot be shared between different analyses: for each analysis, a user has to draw a new ROI. That makes it hard to perform exact comparisons of methods. To compare intraobserver or interobserver variability of different methods, the same set of ROIs defined by observer(s) should be applied to each of the methods. CINQS uses an independent database for DICOM files. A local copy of DICOM files are obtained before analysis. Objects and analyses are also saved to this database.
3. *User-friendly operation*: CINQS hosts an extensive toolbox of freely selectable analysis tools in a graphical user interface (GUI), which makes it very versatile and

flexible in use and requires no scripting or programming for the user. On the other hand, a very structured use of these tools is desired to perform patient studies. To provide a structured interface for the clinical users, the different complex analyses are offered as a so-called *wizard* structure: a checklist-like interface that provides different required steps in a predefined order, with associated help and suggestions for each step. This enforces the clinical users to use the analysis tools in a repeatable fashion throughout a study.

4. *Extendable with new analysis tools*: CINQS has a modular design and this allows integrating new analysis tools without restructuring software.

In addition to the features listed above, CINQS allows exporting output parameters, graphs, images, and clips. Numerical output parameters and graphs can be exported as an Excel file with specific time, date and version number. This allows comparing parameters of different versions of analysis algorithms in a systematic way and importing the results into a statistical software package such as SPSS (SPSS Inc., Chicago, IL, USA) for extensive statistical analyses and tests. Screenshots of CEUS clips can be saved as JPEG format. Video clips with or without overlaid objects can be recorded as AVI format.

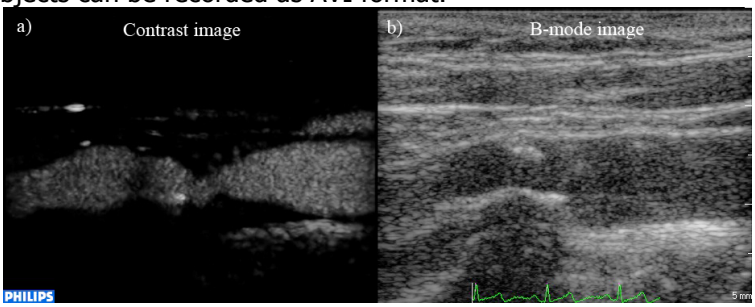

Figure 2: Side-by-side contrast (a) and B-mode (b) image of a carotid artery with plaques

Furthermore, CINQS allows creation of an overlay image (contrast on B-mode, figure 3) for drawing ROIs, which helps to delineate the inner and outer border of plaques more accurately than the duplication of ROI in contrast or B-mode as used in commercial tools (e.g. QLAB and VueBox).

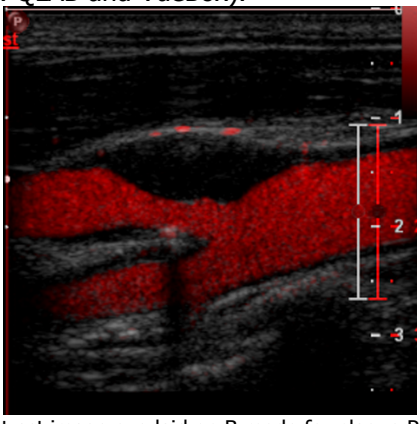

Figure 3: An example of a contrast image overlaid on B-mode for plaque ROI drawing

III. Software Design

CINQS was mainly built in MevisLab (MeVis Medical Solutions AG and Fraunhofer MEVIS, Bremen, Germany), a development environment for medical image processing and visualization. The IPN quantification algorithms were implemented in MATLAB (The Mathworks Inc., Natick, Massachusetts, US), and run through a MeVisLab-MATLAB interface module (MatlabScriptWrapper). The communication between MevisLab modules and the graphical user interface (GUI) was controlled via Python scripts. The GUI (fig. 8, 9) was designed with the internal MevisLab definition language.
CINQS has a modular design as shown in fig. 4. The main modules are GUI, file input/output (I/O), objects and graph management, and analyses.

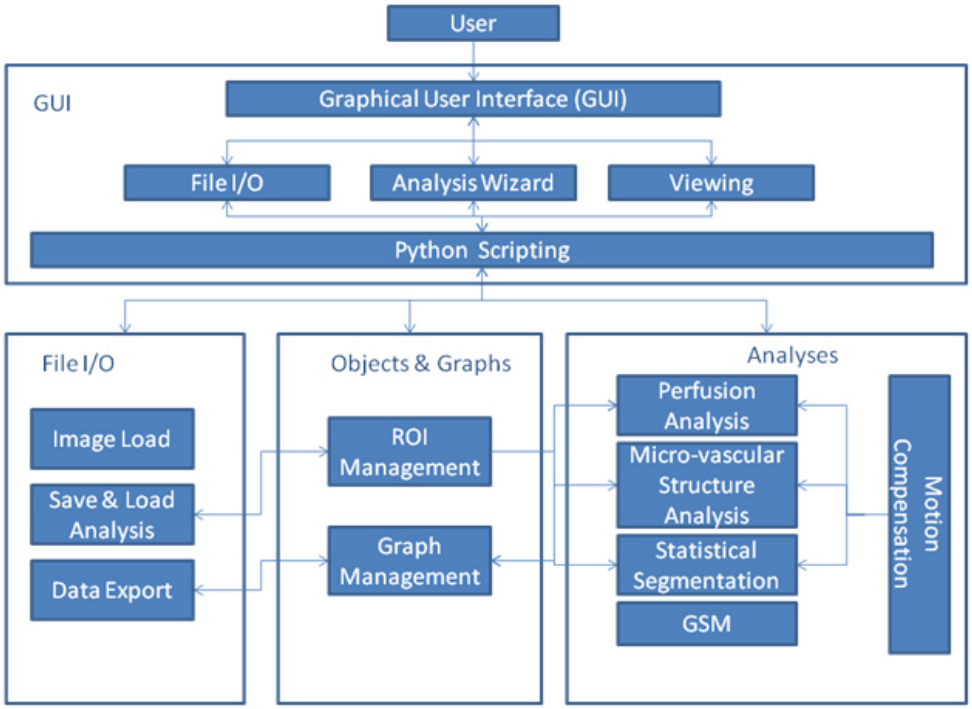

Figure 4: The modules and interaction scheme of CINQS. GUI = Graphical User Interface. I/O = Input/output. ROI = Region of Interest. GSM = Grayscale Median

A brief description of the CINQS framework components is presented here. The File I/O module handles reading and writing of DICOM image files, saving and retrieving objects and analysis files as XML files, and exporting numerical and graph data as EXCEL files. All IPN analysis modules use motion compensation as a prerequisite step. All graphs, drawn objects and their properties are organized by the objects & graphs module. This module also handles the conversion of log-compressed image data into linearly scaled data for graph representation. The GUI

module allows general image and result viewing, user interactions, and guides the user to follow analysis procedures through wizards as described in the following section.

IV. Graphical User Interface

The graphical user interface consists of two main parts, which are the file I/O GUI and the analysis GUI. In the file I/O part, DICOM images, objects lists, and analysis lists can easily be browsed and loaded. DICOM files can also be previewed before loading. When an object or analysis list is loaded the related DICOM images will be automatically loaded. A screenshot of the file I/O GUI is seen in fig 8. The analysis GUI is shown in fig. 9. It contains wizard-like analysis tools, and sections for image and graph viewing, object handling, export, analysis tree, and output parameters. The image viewer (fig. 9E), graph viewer (fig. 9F) and image slider are synchronized with each other. Selecting an image frame will show the corresponding graph point and vice versa. In the analysis tree section (fig. 9G), a log of all user interactions is kept to remind the user of changes in the analysis, e.g. a change in the selected frame interval. To perform an analysis, the user is guided by its specific analysis wizard to perform several interactions: defining the frame interval, drawing ROIs (e.g. for plaque, lumen, background, or adventitia) and assigning meaning to each ROI, placing a marker for tracking of plaque (motion compensation) and running the analysis.

V. Analysis Tools

A. Motion Compensation

Carotid artery walls show considerable motion due to the arterial pulsation, breathing and probe motion. For accurate quantification of IPN, motion compensation is a prerequisite step. CINQS contains two motion compensation methods for plaques, speckle tracking (SPT) and multidimensional dynamic programming (MDP) combined with SPT. Both of them were validated in vitro and in vivo [11-12]. In addition to automated motion compensation, CINQS allows manual indication or correction of tracking points in each frame. This allows users to correct motion in long image sequences if there is any temporary disturbance, such as swallowing or out-of-plane motion.

In SPT, the displacement of plaque is assessed by tracking the positions of small regions of speckle pattern through consecutive frames of an ultrasound image sequence [11]. First, the user chooses a point on the plaque in a B-Mode image of the sequence. A small square region around this point containing the speckle pattern is scanned over a defined search field in each subsequent image to find the position where they best match. The similarity of the template to the image, at each point in the search field, is assessed by calculating their normalized cross correlation (NCC). The point of highest correlation provides the new template position for each subsequent image.

In the second motion compensation method, the results of NCC obtained from as described in SPT for all positions are used as a 3D matrix input to MDP. The optimal plaque displacements in X and Y direction are obtained as a continuous path with MDP as described in detail in [12].

B. Perfusion Analysis

In this analysis, a plaque's perfusion is characterized by analyzing its TIC and maximum intensity projection image (MIP). First, we draw three ROIs subsequently for the plaque, lumen and background. Next, motion compensation is applied to align the plaque ROI over time. After that, the plaque MIP and TIC are derived from the contrast images. From the TIC, we calculate the time average of plaque intensity (PMI: plaque mean intensity), the ratio of PMI and average lumen intensity (PLER: plaque to lumen enhancement ratio), and time average of the percentage of plaque filled with contrast based on average background noise threshold (MPCP: mean plaque contrast percentage). From the MIP image, time integrated IPN surface area (MIPNSA) and IPN to plaque ROI surface area ratio (MIPNSR) based on an adaptive threshold are derived to estimate IPN degree [10]. The adaptive threshold is calculated by taking into account background noise and lumen intensity to adjust for attenuation and gain variations.

To compare our findings, we reproduced the PE parameter explained in the introduction by using the QLAB ROI quantification tool. First, we redrew the plaque ROIs as similar as possible to our analysis. Next, a gamma-variate curve was fitted to the resulting TIC and the PE was obtained. The fit was considered invalid only if the peak occurred at the first or last frame of the interval.

C. Micro-vascular Structure Analysis

In this analysis, we examine spatial structure of IPN. First, the plaque ROI is drawn or chosen from the list of previously drawn ones. Next, motion compensation is applied. After that the micro-vascular structure analysis is performed. The image sequence is divided into 10-frame groups with 80% overlap. In the first frame of each 10-frame group, microbubbles within the plaque ROI are detected by block matching with templates mimicking contrast spots of several radii. The detected spots are tracked over time in the 10-frame groups. Next, the tracked spots are classified into moving contrast spots or stationary artifacts based on their minimal displacement. In the final step, the paths detected several times over time are merged. The number of microvessels (MVN) is calculated as another estimate of IPN degree [13].

D. Statistical Segmentation of Contrast Spots

In this analysis, intensities within the plaque ROI are classified into background, contrast spot, and artifact [14]. First, the plaque ROI is manually drawn/selected and motion compensation is applied. Next, components within the plaque ROI are found from the intensity histogram through an Expectation-Maximization algorithm [15]. The found components are assigned to four initial classes (i.e. background, contrast spot, saturation artifact, and an intermediate class). The final classification is assigned after neighborhood operations. Then, spatiotemporal information is

used to exclude stationary artifacts. In a final step, contrast spots in each frame are integrated over time with a logical-OR operation. Statistical segmentation based IPN surface area (SSIPNSA) and IPN to plaque surface area ratio (SSIPNSR) is calculated as an estimate of IPN degree. Compared with MIP, this method will suppress stationary or saturation artifacts and will be less sensitive to artifacts nearby or within the plaque ROI (fig. 5).

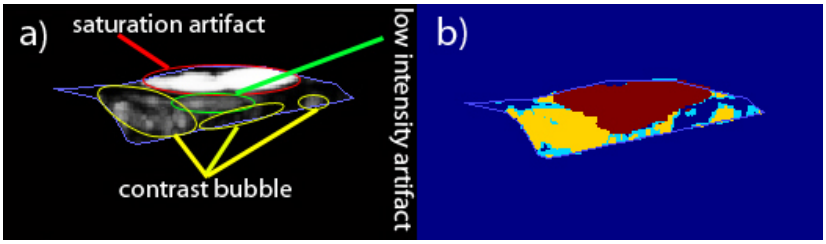

Figure 5: Plaque ROI including artifacts. a) Maximum intensity projection of 130 frames (6.5 seconds) with adaptive threshold. b) Time integrated classes of statistical segmentation (blue = background, yellow = contrast spot class, cyan = intermediate class, red = artifacts)

E. Gray-scale-median Analysis

GSM analysis of B-mode images was adopted from [16]. Plaque echogenicity is measured after gray scale normalization. For a selected image in the sequence, three ROIs are drawn for plaque, lumen and adventitia. The image gray scale values are normalized to the median values of blood and adventitia. After normalization, the median gray scale value for the plaque ROI is determined to estimate plaque echogenicity.

VI. Validation of Outputs and Performance Evaluation

Numerical and graphical outputs of CINQS were validated with synthetic image sequences with known gray values for each pixel. The synthetic image sequences and some motion patterns were generated by using MATLAB. The output results of the CINQS were validated against the pre-calculated numerical results for these synthetic sequences.

All analyses were performed on a computer with Intel(R) Core(TM) 2 Duo CPU (E8600 @ 3.3GHz) and 8GB memory. The performance of CINQS was evaluated based on these computer features and an image sequence of 400 frames (see Table 1).

VII. Statistical Analysis

Recently, 45 plaques of 23 symptomatic patients were analyzed with CINQS [10]. In that study, the derived IPN parameters were compared to the consensus visual score of two experienced physicians (at least 2 years of experience in carotid CEUS analysis) based on a 3-point scale (0: no IPN, 1: mild/moderate IPN, 2: severe IPN). Spearman rank correlation was used for testing the correlation between the visual IPN score and an automated score derived from individual

parameters. The Kruskal-Wallis test was used to compare the output of individual parameters to the visual scoring groups. Receiver operator characteristic (ROC) curve and c-statistic (area under the curve (AUC)) were provided for the two best parameters after dividing our data into no/weak-neovascularization (score 0 and 1) and robust neovascularization (score 2). The optimal operating point (OPT) was obtained by finding the point on the ROC curve with the smallest Euclidian distance to the optimum (100% specificity and sensitivity). The Intra-observer (n=45 plaques) and inter-observer (n=15 plaques) variability were measured using intraclass correlation coefficients (ICC) to assess the reproducibility of IPN parameters. We only analyzed variability in the image analysis, caused by user interactions (e.g. drawing ROIs). The study protocol was approved by the ethical committee at Erasmus Medical Center and all study participants provided informed consent.

VIII. Results

A. Application

Several parameters showed a good correlation with the visual score (correlations (r): MIPNSA r = 0.719, MIPSNSR r = 0.538, MVN r = 0.484, all $p<0.05$). Other parameters showed non-significant correlations with the visual score (correlations: PMI r = 0.227, PLER r = 0.356, MPCP r = 0.151, all $p>0.05$). The PE parameter reported in previous studies [6, 7] also showed non-significant correlation with the visual IPN score in our dataset (r = 0.105). The MIPNSA was able to provide a distinction between the different visual IPN scoring groups ($p<0.05$) (figure 6a). The PMI, PLER and MPCP parameters were not able to provide a clear distinction between the visual scoring groups [10]. In addition to the parameters and results presented in [10], we included here two more parameters: SSIPNSA and SSIPNSR, from the statistical segmentation analysis of contrast spots. These two parameters showed a good correlation with the visual score (correlations: SSIPNSA r =0.698, SSIPNSR r =0.527, both $p<0.05$). The SSIPNSA was also able to provide a clear distinction between the different visual scoring groups ($p<0.05$) (figure 6a). As seen in ROC curve (figure 6b), AUC for MIPNSA and SSIPNSA are 0.93 and 0.92 respectively. Their performance is almost the same.

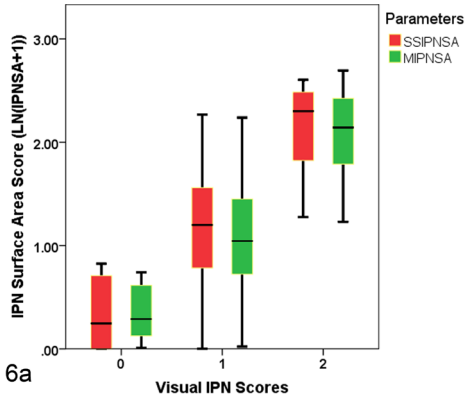

6a

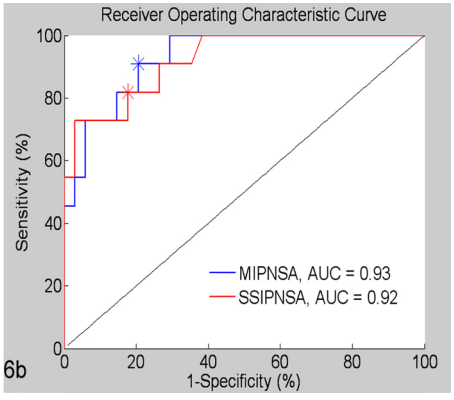

6b

Figure 6: (a) Association of MIPNSA score and SSIPNSA with Visual IPN scoring groups (n=45) ($p<0.001$). (b) Receiver operating characteristic curve for the best two parameters. Blue asterisk shows the OPT for MIPINSA (91% Sensitivity, 80% Specificity). Red asterisk shows the OPT for SSIPNSA (82% Sensitivity, 83% Specificity).

TABLE I
THE PERFORMANCE OF CINQS

Performance	Computation Time
Loading a DICOM clip	a few seconds
User interactions	1-3 minutes
SPT	0.66 minute
MDP combined with SPT	4.33 minute
Perfusion Analysis	1.04 minute
Statistical Segmentation	~ 2 minutes
Micro-vascular Structure Analysis	a few minutes to hours

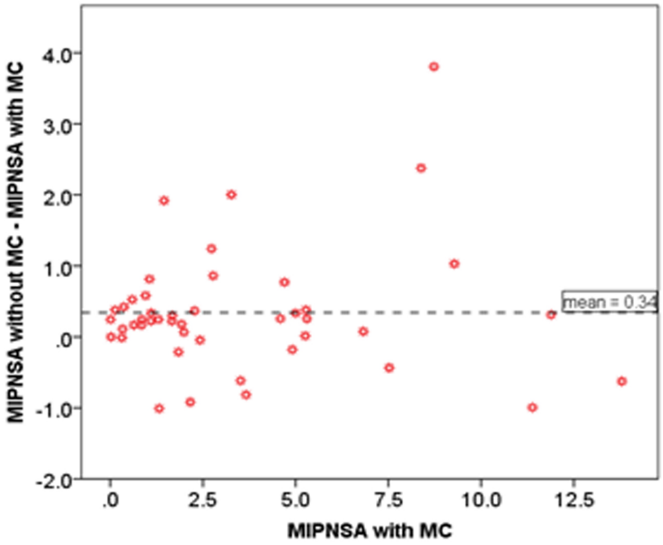

Figure 7: Difference of MIPNSA with and without motion compensation (MC) compared to MIPNSA with MC (units are mm^2).

We selected 8 plaques which had saturation artifacts nearby or within the plaque ROI to verify if SSIPNSA improved the suppression of artifacts. We analyzed them twice, with saturation artifacts included and excluded from the ROI. SSIPNSA was 3.9 ± 3.2 mm2 (mean ± standard deviation) for artifacts included and 3.8 ± 3.2 mm2 for artifacts excluded. MIPNSA was 9 ± 3.3 mm2 for artifacts included and 3.2 ± 2.9 mm2 for artifacts excluded.

Mean difference and standard deviation in calculation of MIPNSA with and without motion compensation was 0.34 ± 0.88 (mm2) for 45 plaques (see fig. 7). The mean and standard deviation of MIPNSA with motion compensation for the dataset was 3.49 ± 3.44 (mm2). In the absence of motion compensation, the found IPN surface area was considerably increased or decreased (>50% for some cases) due to the lumen or artifact infiltration (see fig. 7).

The intra-observer and inter-observer variability for each parameter was presented in our previous study [10]. Intra-observer variability and inter-observer variability for parameters were low. The results showed good agreement in intra-observer (intra class correlation (ICC) range: 0.84-0.98) and inter-observer (ICC range: 0.68-0.96) for all parameters. The parameters which gave the best distinction between visual scores (MIPNSA & SSIPNSA) are reproducible with low intra- and inter-observer variability (ICC > 0.95). One parameter (MVN) showed less reproducibility compared to other parameters (ICC = 0.84 for intra-observer, ICC = 0.68 for inter-observer).

IX. Discussion

CINQS is designed as a special-purpose platform for IPN quantification tools for carotid plaques. CINQS replaces subjective, qualitative and tedious visual assessment with reproducible quantitative IPN parameters. It allows selection of suitable parameters for measuring the degree of IPN by enabling comparison of existing and new IPN parameters with a reference (e.g. visual IPN scoring or histology). The presented analysis tools overcome the limitations of the reported IPN quantification approaches [6-8] and current contrast quantification tools. CINQS could also be used to check changes in neovascularization over time, and to check the outcome of novel therapies on neovascularization.

The parameters are reproducible with low intra-observer and inter-observer variability for user-dependent selections. The image acquisition and bolus injection are standardized in our study [10]. Small variations in this will cause variability in the resulting IPN parameters, but it is beyond the scope of this study to investigate this. For very different image acquisition or bolus injections, the parameters of the IPN quantification algorithms should be re-optimized. These issues could be investigated in further studies.

The software can be run on Windows-compatible computers, from a simple desktop pc up to a sophisticated high-end workstation. CINQS was developed in a modular and extensible way and provides a user-friendly tool for analyzing carotid IPN in CEUS. Using CINQS is quite easy because of its wizard-like design for analysis tools and it requires no specialized knowledge apart from carotid ultrasound image knowledge. To the best of our knowledge, this is the only dedicated software for carotid IPN analysis so far.

The modularity and extensibility of CINQS is based on the modular development framework in MevisLab. MevisLab allows easy integration of external algorithms (e.g. C++ or Matlab code) into a module that can be simply used within the MevisLab framework. To use the new modules within CINQS, some lines need to

be added to the Python script that controls the communication between modules and GUI.

As stated before, TICs of plaque are not similar to the typical TIC curves seen in heart, liver, prostate, or tumor perfusion. Therefore, typical bolus and replenishment kinetics parameters for large organs are not applicable to IPN quantification. The PE parameter derived from the bolus curve models fitted to TICs of plaques gave the lowest correlation with visual IPN scores. In addition to TIC, we used MIP perfusion parameters (MIPNSA, MIPNSR) which estimate vascularization of plaque better than those of TIC.

The motion compensation is an important step in the calculation of MIPNSA of 45 plaques (fig. 7). Leaving out the motion compensation caused on average 10% increase of MIPNSA. This increase of MIPNSA is mainly caused by contrast from lumen or saturation artifacts that infiltrate the plaque ROI. As seen in figure 7, there are also some cases where MIPNSA is decreased. This is caused by some contrast spots that move out of the plaque ROI when no motion compensation is applied. Motion compensation will be especially crucial in case of small plaques, plaques surrounded with saturation artifacts, and adjacency of contrast from the jugular vein to the plaque.

Vavuranakis et al. [17] reported that enhancements in CEUS do not always reflect neovascularization. If there are artifacts within the atherosclerotic plaque ROI, SSIPNSA will suppress artifacts and give more reliable results than MIPNSA. SSIPNSA (3.9±3.2 mm^2 with artifact vs. 3.8±3.2 mm^2 without artifact) gave slightly higher areas but proved to be almost insensitive to artifacts while MIPNSA was sensitive to artifacts (9±3.3 mm^2 with artifacts vs. 3.2±2.9 mm^2 without artifacts).

CINQS was structured for systematic analysis of carotid IPN but its structure may also be useful for microvasculature ROI analysis of other organs such as liver, prostate and myocardium. Especially, CINQS may be useful for other small and relatively poorly perfused structures that are subject to motion. Many tools of CINQS can easily be adopted for analysis of other organs. This will help extend CINQS for other projects.

The use of consensus visual IPN scoring as the ground truth for quantitative IPN parameters is a limitation. Future studies on larger numbers of plaques including histological validation and possibly long term patient follow up are necessary to confirm the present findings. Furthermore, dynamic contrast enhanced MRI of plaques could also be used for comparison to the present findings. However, this was beyond the scope of the present study.

CINQS is limited by the required computation time for running the IPN analysis algorithms. IPN analysis algorithms were written in MATLAB and the code was not optimized for speed. Computation time would decrease if IPN analysis algorithms were written in C or C++. Still, current computation time is satisfactory for clinical applications in datasets of a few hundred patients. For very large patient populations (thousands of patients), speed optimization and integration of CINQS to PACS (Picture Archiving and Communication System) would be desired.

X. CONCLUSION

We have developed and presented a software package, CINQS, for systematic analysis of IPN in CEUS images of carotid plaques. It is well structured, user-friendly and requires minimal user intervention. It enables systematic testing and comparing different IPN analysis tools, and selecting the best parameters for measuring the degree of IPN. This represents an important step towards prediction of plaque vulnerability. As it has a modular design, it is easily extendable with new IPN analyses. It overcomes the limitations of current available contrast quantification tools for IPN quantification. MIPNSA and SSIPNSA showed excellent agreement with visual IPN scores for dichotomized data (no/weak IPN vs. robust IPN).

ACKNOWLEDGEMENTS

This research was supported by the Center for Translational Molecular Medicine (CTMM) and the Netherlands Heart Foundation.

List of abbreviations

CEUS: Contrast Enhanced Ultrasound
CINQS: Carotid Intra-plaque Neovascularization Software
GUI: Graphical User Interface
IPN: Intra-plaque Neovascularization
MIP: Maximum Intensity Projection
MIPNSA: MIP based IPN Surface Area
MIPNSR: MIP based IPN Surface Ratio
MPCP: Mean Plaque Contrast Percentage
MVN: Number of Microvessels
SS: Statistical Segmentation
SSIPNSA: SS based IPN Surface Area
SSIPNSR: SS based IPN Surface Ratio
PE: Plaque Enhancement
PLER: Plaque to Lumen Enhancement Ratio
PMI: Plaque Mean Intensity
ROI: Region Of Interest
TIC: Time Intensity Curve

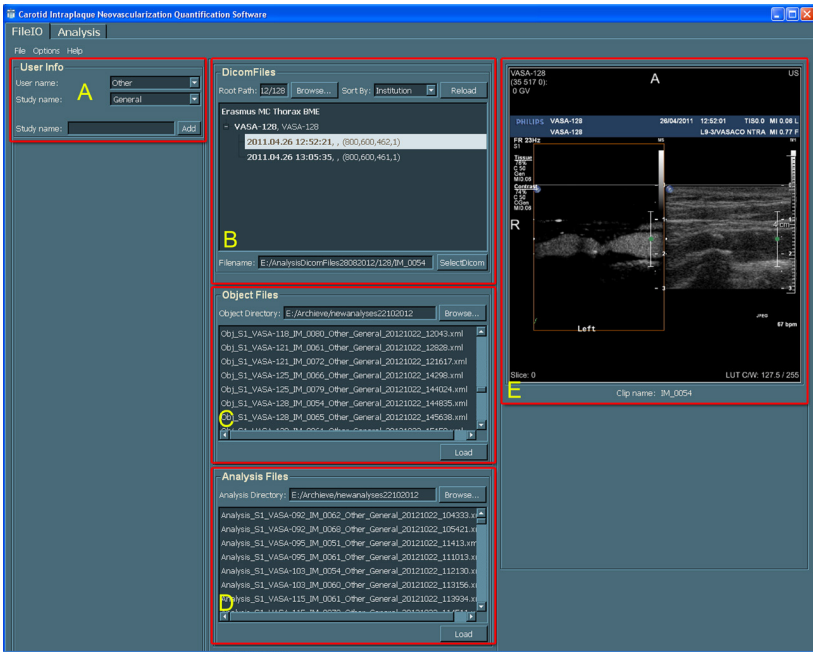

Figure 8: CINQS GUI - file I/O part. A: User info. B: DICOM load panel. C: Object list load panel. D: Analysis list load panel. E: Preview panel.

Figure 9: CINQS GUI - analysis part. A: analysis tools panel structured as a wizard. B: Object list panel. C: Saving object or analysis. D: Export results. E: Viewer panel. F: Graph panel. G: Analysis tree panel. H: Parameter output panel. I: Graph settings.

REFERENCES

[1] W. E. Hellings, W. Peeters, F. L. Moll, S. R. D Piers, J. van Setten , P. J. Van der Spek, J. P. P. M de Vries, K. A. Seldenrijk, P. C. De Bruin, A. Vink, E. Velema, D.P. V. de Kleijn, G. Pasterkamp. "Composition of carotid atherosclerotic plaque is associated with cardiovascular outcome: a prognostic study," Circulation, 121, 1941–1950, 2010.
[2] S. Coli, M. Magnoni, G. Sangiorgi, M. M. Marrocco-Trischitta, G. Melisurgo, A. Mauriello, L. Spagnoli, R. Chiesa, D. Cianflone, A. Maseri. "Contrast-Enhanced Ultrasound Imaging of Intraplaque Neovascularization in Carotid Arteries Correlation With Histology and Plaque Echogenicity," Journal of the American College of Cardiology, 52, 223-230, 2008.
[3] D. Staub, M. B. Patel, A. Tibrewala, D. Ludden, M. Johnson, P. Espinosa, B. Coll, K. A. Jaeger, F. B. Feinstein. "Vasa Vasorum and Plaque Neovascularization on Contrast-Enhanced Carotid Ultrasound Imaging Correlates with Cardiovascular Disease and Past Cardiovascular Events," Stroke, 41, 41-47, 2010.
[4] H. K. Thompson, C. F. Starmer, R. E. Whalen, H. D. Mcintosh. "Indicator Transit Time Considered as a Gamma Variate," Circulation Research, 14, 502-15, 1964.
[5] M. P. J. Kuenen, M. Mischi, H. Wijkstra. "Contrast-Ultrasound Diffusion Imaging for Localization of Prostate Cancer," IEEE Transactions on Medical Imaging, 30, 1493-502, 2011.
[6] P. T. Huang, F. G. Huang, C. P. Zou, H. Y. Sun, X. Q. Tian, Y. Yang, J. F. Tang, P. L. Yang, X. T. Wang. "Contrast-enhanced sonographic characteristics of neovascularization in carotid atherosclerotic plaques," J Clin Ultrasound, 36,346-351, 2008.
[7] L. Xiong, Y. B. Deng, Y. Zhu, Y. N. Liu, X. J. Bi. "Correlation of Carotid Plaque Neovascularization Detected by Using Contrast-enhanced US with Clinical Symptoms," Radiology, 251, 583-589, 2009.
[8] A. Hoogi, D. Adam, A. Hoffman, H. Kerner, S. Reisner, D. Gaitini. "Carotid Plaque Vulnerability: Quantification of Neovascularization on Contrast-Enhanced Ultrasound with Histopathologic Correlation," American Journal of Roentgenology, 196, 431-436, 2011.
[9] G. L. ten Kate, S. C. H. van den Oord, E. J. G. Sijbrands, A. van der Lugt, N. de Jong, J. G. Bosch, A. F. W. van der Steen, A. F. L. Schinkel. "Current status and future developments of contrast-enhanced ultrasound of carotid atherosclerosis," Journal of Vascular Surgery, 57, 539-546, 2013.
[10] Z. Akkus, A. Hoogi, G. Renaud, S. C. H. van den Oord, G.L. ten Kate, A. F. L. Schinkel, N. de Jong, A.F.W. van der Steen, J.G. Bosch. "New Quantification Methods for Carotid Intraplaque Neovascularization using Contrast Enhanced Ultrasound," Ultrasound in Medicine & Biology, vol. 40, pp. 25-36, 2014.
[11] Z. Akkus, J. G. Bosch, G. Renaud, A. Hoogi, G. L. ten Kate, S. van den Oord, A. Schinkel, N. De Jong, A. F. W. Van der Steen. "Motion compensation method for quantification of neovascularization in carotid atherosclerotic plaques with contrast enhanced ultrasound (CEUS)," in Proc. IEEE International Ultrasonics Symposium (IUS), Orlando, 2011, pp.1156-59.
[12] Z. Akkus, A. Hoogi, G. Renaud, G.L. ten Kate, S. C. H. van den Oord, A. F. L. Schinkel, N. de Jong, A.F.W. van der Steen, J.G. Bosch. "Motion Compensation Method using Dynamic Programming for Quantification of Neovascularization in Carotid Atherosclerotic Plaques with Contrast Enhanced Ultrasound (CEUS)," in Proc. SPIE, San Diego, 2012, 8320, 83200C.
[13] A. Hoogi, Z. Akkus, S. C. H. van den Oord, G. L. ten Kate, A. F. L. Schinkel, J. G. Bosch, N. de Jong, D. Adam, A. F. W. van der Steen. "Quantitative analysis of ultrasound contrast flow behavior in carotid plaque neovasculature," Ultrasound in Medicine and Biology, 38, 2072-2083, 2012.
[14] Z. Akkus, G. Vegas-Sánchez-Ferrero, D. D. B. Carvalho, G. Renaud, S. C. H. van den Oord, G. L. ten Kate, A.F. L. Schinkel, N. de Jong, A. F. W. van der Steen, J. G. Bosch. "Statistical segmentation of carotid plaque neovascularization," in Proc. SPIE, Orlando, 2013, 8675, 867506.
[15] A. T. F. Mario, K. J. Anil. "Unsupervised learning of finite mixture models" IEEE Transactions on Pattern Analysis and Machine Intelligence, 24(3), 381–396, 2002.
[16] M. M. Sabetai, T. J. Tegos, A. N. Nicolaides, S. Dhanjil, G. J. Pare, J. M. Stevens. "Reproducibility of computer-quantified carotid plaque echogenicity - Can we overcome the subjectivity?" Stroke, 31, 2189-96, 2000.
[17] M. Vavuranakis, Fragiska S, Dimitrios V et al., "Quantitative analysis of carotid plaque vasa vasorum by CEUS and correlation with histology after endarterectomy" Vasa, vol. 42, pp. 184-195, 2013.

Chapter 7

Lumen Segmentation and Motion Estimation in B-mode and Contrast Enhanced Ultrasound Images of the Carotid Artery in Patients with Atherosclerotic Plaque

In standard B-mode ultrasound (BMUS), segmentation of the lumen of atherosclerotic carotid arteries and studying lumen geometry over time are difficult owing to irregular lumen shapes, noise, artifacts, and echolucent plaques. Contrast enhanced ultrasound (CEUS) improves lumen visualization, but lumen segmentation remains challenging owing to varying intensities, CEUS-specific artifacts and lack of tissue visualization. To overcome these challenges, we propose a novel method using simultaneously acquired BMUS&CEUS image sequences. Initially, the method estimates nonrigid motion (NME) from the image sequences, using intensity-based image registration. The motion-compensated image sequence is then averaged to obtain a single 'epitome' image with improved signal-to-noise ratio. The lumen is segmented from the epitome image through an intensity joint-histogram classification and a graph-based segmentation. NME was validated by comparing displacements with manual annotations in eleven carotids. The average root-mean-square-error (RMSE) was 112±73μm. Segmentation results were validated against manual delineations in the epitome images of two different datasets containing eleven (RMSE 191±43μm) and ten (RMSE 351±176μm) carotids, respectively. From the deformation fields, we derived arterial distensibility with values comparable to the literature. The average errors in all experiments were in the inter-observer variability range. To the best of our knowledge, this is the first study exploiting combined BMUS&CEUS images for atherosclerotic carotid lumen segmentation.

D.D.B. Carvalho*, Z. Akkus*, J.G. Bosch, S. van den Oord, W.J. Niessen, S. Klein. **Global Motion Compensation of B-mode and Contrast Ultrasound images of the carotid artery for lumen segmentation and distensibility assessment.** Submitted. (*shared first author)

1. Introduction

Stroke is a major healthcare problem and one of the main causes of death and long-term disability worldwide [1]. Several studies have demonstrated that patients with carotid atherosclerotic plaques carry an increased risk of cardiovascular events, such as stroke, transient ischaemic attack, myocardial infarction and even death [1,2]. Ultrasound has been widely used as a standard tool for inexpensive and non-invasive diagnosis of carotid atherosclerosis [3]. To assess atherosclerosis (formation of plaques in arterial walls causing narrowing of the lumen), different ultrasound techniques have been used such as standard B-mode ultrasound (BMUS), color Doppler and contrast enhanced ultrasound (CEUS) [4]. For the accurate assessment of the degree of atherosclerosis, delineation of the lumen-intima contour of the carotid artery is an essential step.

So far, carotid lumen segmentation has mostly been done based on standard-BMUS images, as reported in several studies [5-8]. However, carotid lumen segmentation in standard-BMUS images of subjects with atherosclerotic plaques is difficult and can be inaccurate due to irregular lumen shapes, noise in the lumen, artifacts and echolucent plaques, as seen in Fig. 1a. Color Doppler (Fig. 1b) provides information on blood flow in the lumen, which enables the clinician to detect flow reduction, flow abnormalities and occlusion in arteries. While there is no doubt of its usefulness, it is less suitable for vessel lumen segmentation: the border of the color-coded velocity images strongly depends on user-controlled settings of Doppler gain, velocity range and setting of the wall filter, as well as the local direction of flow. Therefore, color may appear far outside the vessel border or may be missing inside the vessel. Especially in regions of disturbed flow (plaques), the color border may be misleading. CEUS (Fig. 1c) is a more useful modality for visualizing the lumen. CEUS suppresses tissue information and provides the luminal shape by detecting ultrasound contrast agent: micrometer-sized gas bubbles which flow within the blood stream. CEUS allows a better delineation of carotid lumen than standard-BMUS [4, 9,10,11]. Compared to color Doppler, CEUS shows the lumen by visualizing the presence of contrast-enhanced blood regardless of flow velocity and direction.

There have been several approaches for detection of the carotid artery contours in standard BMUS, including deformable contours (snakes), Hough transform, dynamic programming, and classification approaches. The principles, performance, advantages and limitations for these approaches have been summarized in recent surveys [12-14]. Several studies have reported that their lumen segmentation methods have limitations in presence of atherosclerotic plaque [15-17].

Carotid artery lumen segmentation in a time series allows one to characterize the lumen diameter across the cardiac cycle, and hence to assess arterial wall stiffness. Several studies have introduced measures related to the stiffness of the arterial wall as a biomarker for cardiovascular disease [18-21]. It has been hypothesized that arterial stiffness parameters indicate early vascular changes that predict the development of major vascular disease. Indices of arterial stiffness that have been proposed include strain [18, 19, 21], stress [19, 21], elastic

modulus or Young's modulus [18, 19, 21], and distensibility coefficient [19-21]. Barth et al. [18] and Van Popele et al. [20] reported that arterial stiffness is strongly associated with atherosclerosis. In another study, men with coronary artery disease were shown to have stiffer arteries than healthy men [22]. Arterial stiffness has been positively associated with risk factors for vascular disease: age, blood pressure, blood cholesterol, and diabetes [23, 24]. Van Popele measured carotid wall motion by means of a vessel wall movement detector system [25]. The displacement of the arterial wall was obtained by tracking the wall position in a selected M-mode line by using the raw ultrasound (RF) signal. The anterior and posterior wall positions were marked on the first time instance of the selected M-mode RF line. Then, the change in phase was calculated between consecutive RF signals to measure the displacement. The algorithm is limited as it utilizes only one M-mode line for measuring vessel wall motion and it requires manual user interactions. An automated method for distensibility measurement in BMUS was presented by Teynor et al. [26]. Their method requires interactive manual corrections for difficult cases with shadow (echo dropouts) or a high level of noise in the BMUS images.

In this study, we present a novel carotid lumen segmentation and motion estimation approach that is suitable for atherosclerotic arteries, less prone to artifacts and more automated than approaches that have appeared in the literature. The method is fully automatic, provided that the image contains just a single branch of the carotid artery. Our method also quantifies carotid lumen geometry over time in subjects with atherosclerotic plaque from simultaneously acquired BMUS and CEUS images. Integrated analysis of BMUS and CEUS provides essential information on the carotid artery lumen contour in patients with atherosclerotic plaques (see Fig. 1). Such information cannot be derived from BMUS or CEUS separately. The combined analysis of BMUS and CEUS, however, presents two additional challenges: CEUS-specific imaging artifacts and lower signal-to-noise ratio (SNR) in BMUS: as low signal power is used to avoid the disruption of ultrasound contrast agents in CEUS, the BMUS images obtained in simultaneous BMUS and CEUS acquisition have lower SNR compared to a standard BMUS image. In order to improve the SNR and suppress noise, we compensate motion in the BMUS and CEUS image sequence and average image intensities pixelwise over the complete sequence. This leads to a single integrated BMUS and CEUS image with improved SNR that we refer to as the 'epitome' image, since it is the best possible presentation of the patient's anatomy. Motion compensation is a prerequisite step for obtaining epitome images, as carotid images contain considerable motion, such as probe movement, patient movement, breathing and pulsation. Previous studies on motion estimation in carotid ultrasound mostly focused on rigid registration of multiple local regions based on block matching [27-30]. We propose to use an accurate nonrigid motion estimation (NME) technique for sequences of complete BMUS and CEUS images.

The constructed epitome image is used as input for an automated lumen segmentation approach. A particular challenge here is the presence of saturation and pseudo-enhancement artifacts [31] in the CEUS image. These artifacts should be suppressed as they could mislead the lumen segmentation. We exploit the joint

information of the integrated BMUS and CEUS image to classify artifacts, lumen, and tissue. Following this classification, we use a robust and efficient graph-based technique for carotid lumen segmentation. Finally, we transform the lumen contours extracted from the epitome image back to each time frame by using the deformation pattern estimated with NME in order to obtain the assessment of carotid artery distensibility.

The accuracy of NME is evaluated by comparing with manually tracked landmarks, and with local rigid registration based on speckle tracking (LRST) [30]. Moreover, we investigate the influence of several important design parameters on the accuracy of the NME. The automated lumen segmentation is evaluated by comparing with manual annotations of the lumen. We also evaluate the accuracy of automatic distensibility measurement by comparing with manual annotations of the carotid wall across time.

Summarizing the main contribution of our study is twofold. First, we provide nonrigid motion compensation for BMUS and CEUS image sequences. Second, using the combined BMUS and CEUS motion-compensated data, we automatically segment the carotid artery lumen, even in the presence of typical artifacts present in both BMUS and CEUS. To the best of our knowledge this is the first study using combined BMUS and CEUS to improve the segmentation of the lumen of the carotid artery in patients with atherosclerotic plaques.

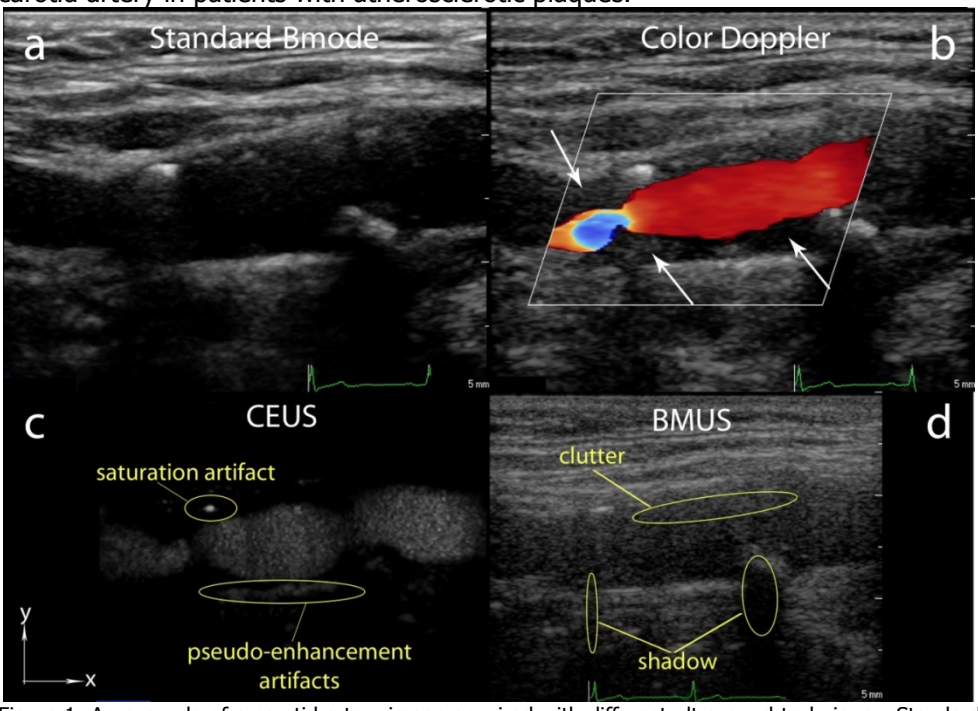

Figure 1: An example of a carotid artery image acquired with different ultrasound techniques. Standard BMUS (a), Color Doppler (arrows show echolucent plaques, blue color shows direction change in the flow) (b), Side-by-side CEUS and B-mode images (c-d). CEUS artifacts are indicated (c). Shadow and clutter in BMUS are indicated (d).

2. Methods

This section is divided in three subsections, describing NME, lumen segmentation and distensibility calculation, respectively. The method steps and their relation are shown in the flowchart in Fig. 2.

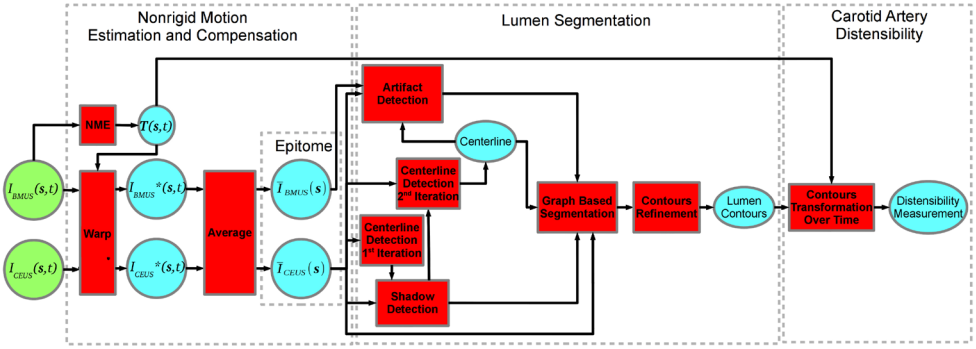

Figure 2: Flowchart of the steps of the method. Inputs (green), operations (red) and outputs (blue). $\boldsymbol{T}(\boldsymbol{s},t)$: Transformation obtained from BMUS with NME. ${I_{BMUS}}^*(\boldsymbol{s},t)$, ${I_{CEUS}}^*(\boldsymbol{s},t)$: Motion compensated BMUS and CEUS respectively. $\bar{I}_{BMUS}(\boldsymbol{s})$, $\bar{I}_{CEUS}(\boldsymbol{s})$: Epitome images.

2.1 Nonrigid Motion Estimation

Owing to the acquisition procedure, the CEUS and BMUS images cover the same field of view and are intrinsically spatially aligned. Figs. 1c and 1d show an example of a typical pair of CEUS and BMUS images. The simultaneous BMUS & CEUS imaging leads to two 2D+time (2D+t) image series, $I_{BMUS}(\boldsymbol{s},t)$ and $I_{CEUS}(\boldsymbol{s},t)$, where $\boldsymbol{s}$ is a spatial coordinate (x,y) and t is the time frame index with $t = 1 \dots \tau$ (τ = number of time frames).

For the nonrigid motion estimation (NME), we adopted the groupwise registration method of Metz et al [32] and optimized it for our purpose. The method estimates the nonrigid deformation of the carotid artery over time from the BMUS image sequence, and subsequently compensates this nonrigid motion in both the BMUS and CEUS image sequences. The method is based on the minimization of the pixel intensity variance over time [32]. The CEUS image sequence violates the constant intensity assumption of the NME method: it exhibits high intensity variations among frames due to slow flow-related contrast concentration changes. Therefore, we use the BMUS image for motion estimation, since it presents only minor intensity variations of anatomical structures over time. We denote the motion-compensated image sequences as:

$${I_{BMUS}}^*(\boldsymbol{s},t) = I_{BMUS}(\boldsymbol{T}(\boldsymbol{s},t),t)$$

$${I_{CEUS}}^*(\boldsymbol{s},t) = I_{CEUS}(\boldsymbol{T}(\boldsymbol{s},t),t)$$

where $\boldsymbol{T}(\boldsymbol{s},t)$ is the transformation field obtained in NME. After motion compensation, the resulting sequences can be averaged over time:

$$\bar{I}_{BMUS}(\boldsymbol{s}) = \frac{1}{\tau}\sum_{t=1}^{\tau} {I_{BMUS}}^{*}(\boldsymbol{s},t)$$

$$\bar{I}_{CEUS}(\boldsymbol{s}) = \frac{1}{\tau}\sum_{t=1}^{\tau} {I_{CEUS}}^{*}(\boldsymbol{s},t)$$

The average images $\bar{I}_{BMUS}(\boldsymbol{s})$ and $\bar{I}_{CEUS}(\boldsymbol{s})$ have improved-SNR and serve as epitome images. In this way, noise is attenuated and the lumen and plaque structures are more clearly depicted, as can be seen in Fig. 3. All further processing of the lumen segmentation is performed on these epitome images. The relations between the transformations and the images are shown in Fig. 2.

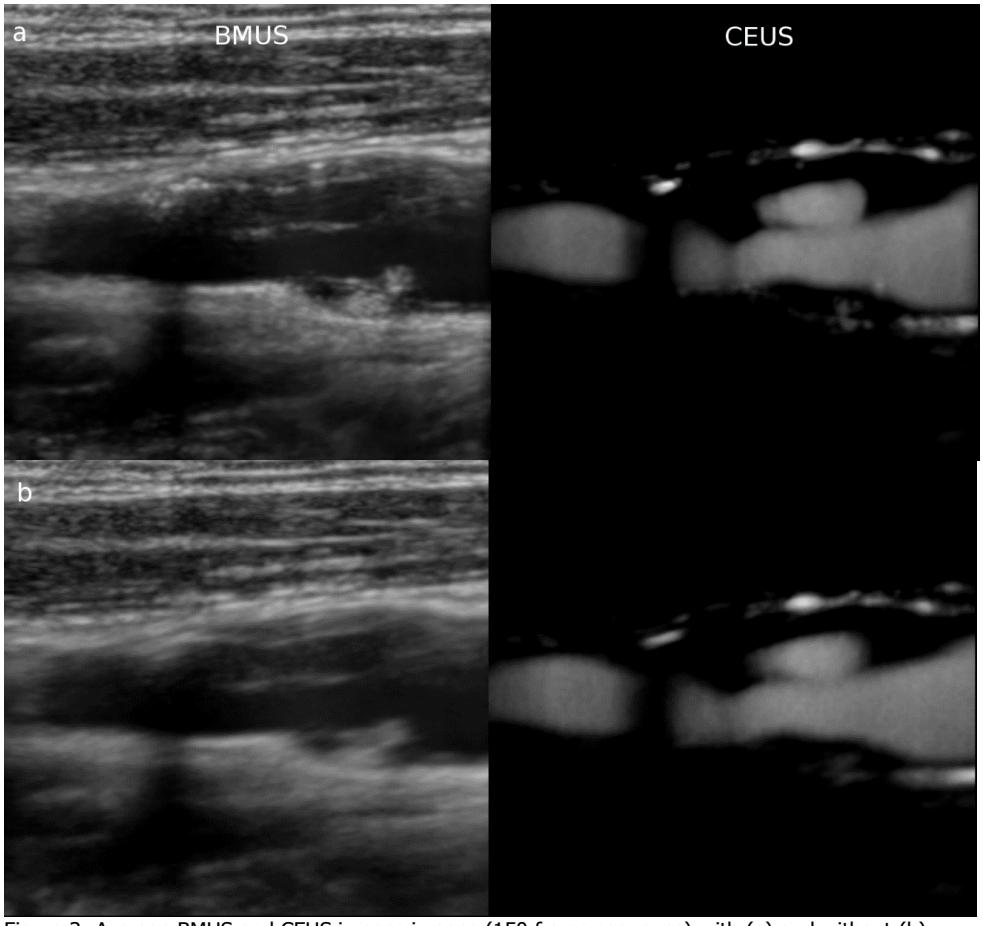

Figure 3: Average BMUS and CEUS images images (150 frame sequence) with (a) and without (b) motion compensation. Average images without motion compensation have a blurry appearance, while the 'epitome' images after motion compensation are sharper.

The groupwise registration method produces a nonrigid motion estimate on the whole image domain, differently from existing techniques for motion estimation in ultrasound [27-29]. The deformations are modeled by a nonrigid 2D+t B-spline transformation, ensuring smoothness (continuous differentiability) both in the spatial and temporal dimensions. An adaptive stochastic gradient descent optimizer [33] is employed to calculate the transformation parameters that minimize a dissimilarity measure based on the variance of the intensities at corresponding spatial locations. In order to improve registration robustness, a multi-resolution strategy is applied: for each resolution, the image is smoothed with a Gaussian filter with spread σ. Important parameters of the method are: 1) the spacing β of the B-spline control points, both spatially (in mm) and temporally (in time frames), 2) the number of resolutions ρ, and 3) the degree of image smoothing σ. In the experiments, a range of settings for these parameters will be evaluated.

2.2 Lumen Segmentation

We perform lumen segmentation of the carotid artery on the epitome images $\bar{I}_{BMUS}(\boldsymbol{s})$ and $\bar{I}_{CEUS}(\boldsymbol{s})$. Our segmentation method consists of five steps: centerline estimation, detection of shadowing, detection of artifacts, graph based segmentation and refinement of lumen contours (see Fig. 2).

2.2.1 Centerline Estimation

We detect the centerline of the carotid artery which appears approximately horizontal (along the *x*-direction) in the image. As a preprocessing, we apply a 2D Gaussian smoothing filter G to $\bar{I}_{CEUS}(\boldsymbol{s})$ using a vertical spread σ_y that is relatively large with respect to the expected vessel size. This filter has the highest response around the centerline of the lumen. The smoothing in horizontal direction, controlled by σ_x, suppresses the influence of small artifacts near the lumen in the CEUS image. After preprocessing, we detect the centerline of the carotid artery in the CEUS image by finding a minimum cost path, using dynamic programming in the *x*-direction [30, 34, 39]. We defined the maximum step size in the cost path as one pixel. The dynamic programming procedure uses negated gray scale values of the blurred CEUS epitome as a cost image $c(\boldsymbol{s})$:

$$c(\boldsymbol{s}) = -G * \bar{I}_{CEUS}(\boldsymbol{s}) + K, \text{ where } K = \max_{\boldsymbol{s}}\left(G * \bar{I}_{CEUS}(\boldsymbol{s})\right).$$

The added constant K ensures that $c(\boldsymbol{s}) > 0$ everywhere.

2.2.2 Detection of Shadowing

After centerline detection, we check for presence of shadowing, which is caused by strong reflection or attenuation, especially from calcifications. Centerline detection and subsequent lumen segmentation will be affected by shadowed regions due to the low signal in those regions. Therefore, shadowed regions should be identified to avoid their influence in obtaining optimal centerline and lumen contours. To detect the shadowed region we compute the mean intensity in a

vertical kernel of height κ_1 around each detected point on the centerline in the CEUS epitome image and fit a linear curve to these intensities. The size of this kernel must be smaller than the expected typical size of the lumen. The points that show an intensity drop of at least 50% in the intensity profile compared to the linear fit are considered to indicate shadow regions. When a shadow region is detected at a certain *x*-coordinate, all points in the cost image $c(\boldsymbol{s})$ with that *x*-coordinate are assigned the same cost value to ensure that this region does no longer affect the centerline extraction. Based on this modified cost image, the centerline is re-estimated.

2.2.3 Detection of Artifacts

In order to obtain an accurate lumen segmentation, the pseudo-enhancement artifacts and saturation artifacts (see Fig. 1c) in the CEUS image need to be detected, as they may mislead the segmentation procedure. The pseudo-enhancement artifacts in the lower part of the CEUS images are caused by nonlinear distortion of the ultrasound signal when it crosses regions with high concentration of contrast, such as the carotid lumen. As these distorted ultrasound signals will be backscattered from the tissue below the lumen, the tissue cancellation will not be perfect in the far wall, and false contrast will appear in the plaque or tissue region right below the lumen. These artifacts appear bright both in the CEUS and BMUS image, while true contrast corresponds to dark BMUS regions.

The upper part of the lumen in the CEUS image is not affected by the pseudo-enhancement artifacts but it may be contaminated with artifacts due to saturation; signals near the maximum intensity level are clipped. These artefacts are easier to detect as they have distinctive, very high contrast intensity levels (and are also bright in BMUS). To detect these different artifacts in CEUS, we construct a joint histogram of the intensities in $\bar{I}_{BMUS}(\boldsymbol{s})$ and $\bar{I}_{CEUS}(\boldsymbol{s})$ and define a joint-intensity classifier. We model the joint histogram by a mixture of 2D Gaussians, corresponding to four classes: $\psi \in \{B, T, L, A\}$ where B = Background, T = Tissue, L = Lumen, A = Artifacts. As seen in Figs. 3 and 4a (schematically depicted joint histogram), lumen is bright in CEUS but dark in BMUS. Tissue is bright in BMUS but dark in CEUS. Background (echolucent tissue) is dark in both BMUS and CEUS. Artifacts are bright in CEUS and their corresponding regions in BMUS are bright as well. Each class ψ is modeled by a 2D Gaussian in the joint histogram, with parameters $\theta_\psi = \{\mu_\psi^c, \sigma_\psi^c, \mu_\psi^b, \sigma_\psi^b\}$ where μ_ψ^c and σ_ψ^c are intensity mean and standard deviation in CEUS, and μ_ψ^b and σ_ψ^b are intensity mean and standard deviation in BMUS. Let Θ denote the collection of all parameters θ_ψ. The initialization of parameters θ_B, θ_T and θ_A is based on the typical appearance of intensities in $\bar{I}_{BMUS}(\boldsymbol{s})$ and $\bar{I}_{CEUS}(\boldsymbol{s})$ as discussed above. For the *L* class, we select the mean and standard deviation of the intensities in a narrow band (size κ_2) around the centerline to initialize θ_L. The Gaussian mixture weights are initialized to a constant value (1/4). These initial parameters are fed into an expectation-maximization algorithm [35, 36] to estimate Θ and find the probability $p(\bar{\boldsymbol{I}}(\boldsymbol{s}) \mid \psi(\boldsymbol{s}), \Theta)$ of each observed pair of intensities $\bar{\boldsymbol{I}}(\boldsymbol{s}) = [\bar{I}_{BMUS}(\boldsymbol{s}), \bar{I}_{CEUS}(\boldsymbol{s})]$ given the pixel belongs to the background, tissue, lumen or artifact class. Since the parts of the lumen below

and above the centerline contain different type of artifacts, classification is performed separately in the upper and lower arterial wall using two different initializations for the artifact class. Saturation artifacts have high mean intensity and low standard deviation, whereas pseudo-enhancement artifacts have intensity similar to contrast intensity in the lumen and high standard deviation. The probability map for the image is shown in Fig. 4b with combined results of two initializations of artifact class for upper and lower parts of the vessel.

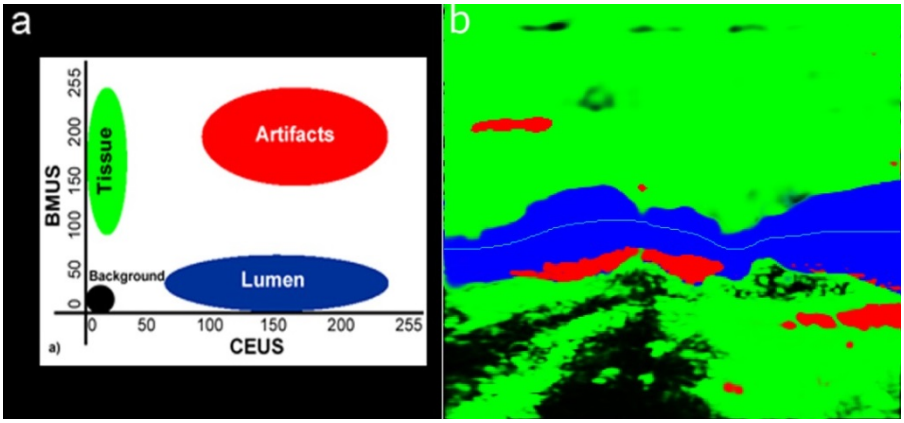

Figure 4: a) Schematic depiction of joint histogram of BMUS and CEUS, b) Probability map obtained through the expectation-maximization algorithm. RGB image channels represent: $p(\bar{\boldsymbol{I}}(\boldsymbol{s}) \mid \psi(\boldsymbol{s}) = B, \Theta)$ = black, $p(\bar{\boldsymbol{I}}(\boldsymbol{s}) \mid \psi(\boldsymbol{s}) = T, \Theta)$ = green, $p(\bar{\boldsymbol{I}}(\boldsymbol{s}) \mid \psi(\boldsymbol{s}) = L, \Theta)$ = blue, $p(\bar{\boldsymbol{I}}(\boldsymbol{s}) \mid \psi(\boldsymbol{s}) = A, \Theta)$ = red.

2.2.4 Graph-based Segmentation

We detect the upper and lower lumen contours with a graph-based minimum cost path approach using dynamic programming (DP). The cost image is based on the epitome $\bar{I}_{CEUS}(\boldsymbol{s})$ and the results from the centerline estimator, the shadow detector, and the artefact segmentation. No restrictions are applied for the start- and endpoint of the minimum cost path.

First, we obtain the *y*-directional gradient of $\bar{I}_{CEUS}(\boldsymbol{s})$ by applying a Gaussian derivative filter (standard deviation 0.3 mm): $\nabla_y \bar{I}_{CEUS}(\boldsymbol{s}) = \nabla_y G * \bar{I}_{CEUS}(\boldsymbol{s})$. The basic cost image $\widetilde{\nabla_y} I_{CEUS}(\boldsymbol{s})$ is defined as the negative gradient image, $\widetilde{\nabla_y} I_{CEUS}(\boldsymbol{s}) = -\nabla_y \bar{I}_{CEUS}(\boldsymbol{s})$, for the upper contour and $\widetilde{\nabla_y} I_{CEUS}(\boldsymbol{s}) = \nabla_y \bar{I}_{CEUS}(\boldsymbol{s})$ for the lower contour. Second, all points in image columns corresponding to shadow regions are assigned the same (arbitrary) cost value to neutralize those regions. Third, saturation and pseudo-enhancement artifacts in the CEUS are suppressed by multiplying $\widetilde{\nabla_y} I_{CEUS}(\boldsymbol{s})$ with the inverse of the posterior probability of the artifact class, $\tilde{p}_A(\boldsymbol{s})$:

$$\tilde{p}_A(\boldsymbol{s}) = 1 - p(\bar{\boldsymbol{I}}(\boldsymbol{s}) | \psi(\boldsymbol{s}) = A, \Theta)$$

Fourth, we apply a curve smoothness penalty, linearly proportional to the step in *y*-direction between adjacent *x*-positions. Fifth, we multiply the cost with a

factor that is linearly proportional to the distance from the centerline to prevent jumps to far layers. The minimum cost path calculation is performed in 'modified' pixel grid coordinates (u, v), where u is the original x-index and v is the y-index relative to the centerline. The cumulative cost C as a function of (u, v) in the dynamic programming framework for detecting the upper and lower lumen contours thus becomes as follows:

$$C(u,v) = \min_{r \in \{-1,0,1\}} C(u-1, v+r) + \widetilde{\nabla_y \bar{I}}_{CEUS}(u,v) \cdot \tilde{p}_A(u,v) \cdot \left(1 + \frac{|r|}{\gamma_1}\right) \cdot \left(1 + \frac{|v|}{\gamma_2}\right)$$

(Equation 1)

The maximum step size of 1 pixel $(\max |r| = 1)$ limits the search space. We introduced two weighting factors γ_1 and γ_2 to control the amount of penalization for the step size $|r|$ and the distance from the centerline $|v|$, respectively.

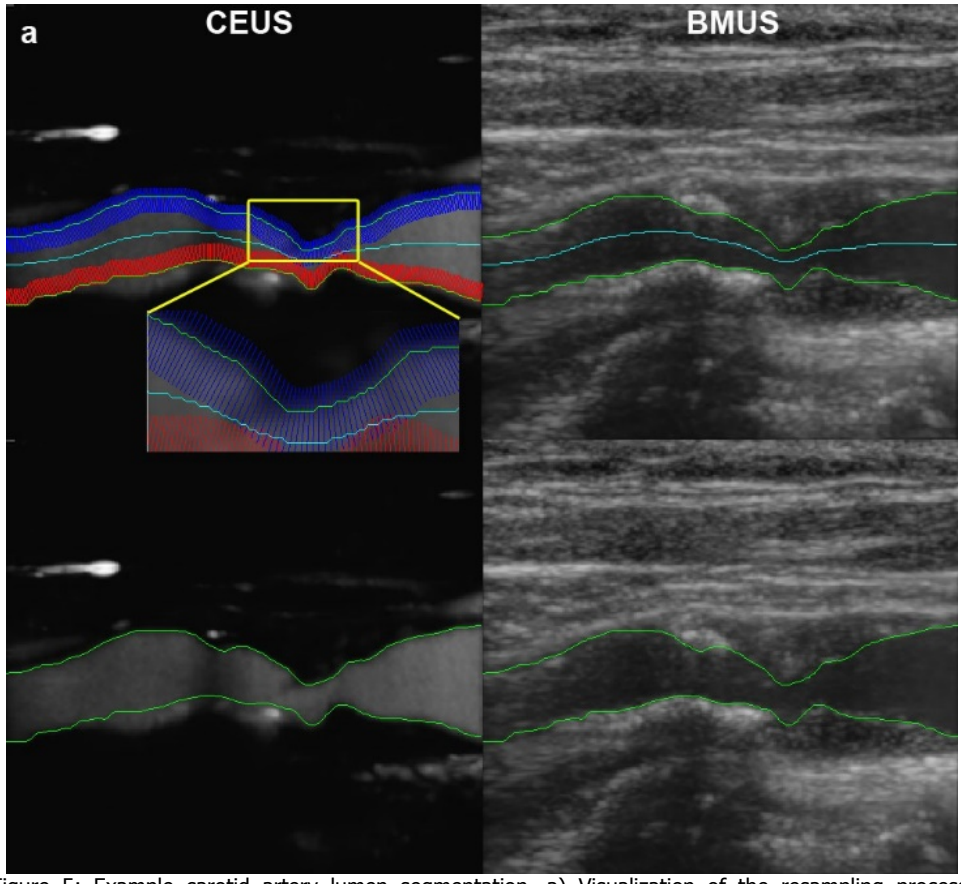

Figure 5: Example carotid artery lumen segmentation. a) Visualization of the resampling process, showing the orthogonal vectors to the contours as red and blue lines for the lower and upper contour respectively. b) Resulting contours estimated with subpixel-precision (one fourth of pixel size, ~ 25µm).

2.2.5 Refinement of Lumen Contours

In the final step of the segmentation algorithm, we resample the image with subpixel precision in a narrow band along the upper and lower contours to follow curves more precisely and obtain smoother contours. In the refinement process, we first follow the local orientation of the contours by fitting a least squares regression line to a neighborhood of each point on the contours and find the vectors orthogonal to the fitted regression line for each contour point. Next, we resample a band of size κ_4 along the orthogonal vectors around each contour point with subpixel-precision (one fourth of pixel size, ~25μm), using cubic spline interpolation. In the resampling process, we chose the length of orthogonal vectors κ_4 as 1mm inward to the lumen for both of the contours. For the outward direction, for the upper contour we chose 0.5mm and for the lower contour 0.1mm. The reason for using a shorter κ_4 in the lower contour outward to lumen is to avoid the influence of imperfectly suppressed pseudo-enhancement artifacts. Based on the resampled image, the lumen contour is re-estimated using Eq. (1), omitting in this case the penalty term for the distance to the centerline. Lastly, the refined contours are transformed back to the original coordinate space. An example of the segmentation is shown in Fig. 5.

2.3 Carotid Artery Distensibility

In order to study the carotid geometry over time, the upper and lower lumen contour points from the epitome images are transformed to each time frame using $\boldsymbol{T}(\boldsymbol{s}, t)$ obtained previously with NME. This allows to compute the distensibility coefficient (*DC*) of the whole section of the carotid artery wall for each cardiac cycle. To measure the radial distensibility, the motion in a direction orthogonal to the lumen centerline should be estimated. For the measurements, a segment of 1 cm length of artery free from plaque along the *x*-dimension is manually selected (see Fig. 6). Plaque regions should be avoided because there exists no proper definition of distensibility in plaque regions. We propose two methods to calculate the distensibility in this region. In the first method (*DC*-Line), the distensibility is calculated for a single line orthogonal to the lumen, located in the center of the 1 cm segment. This method resembles the ground truth manual annotation approach described in Section 4.3. In the second method (*DC*-ROI), all lines inside the 1 cm region of interest are selected, to potentially obtain a more robust measurement by averaging the *DC* over these lines. The local orientation of the centerline is estimated by fitting a least square regression line to a κ_3 neighborhood of each point on the artery centerline. Subsequently, intersection points of each orthogonal vector with the upper and lower lumen contour over time are detected. The R-peaks of ECG signal are extracted from the ECG annotation in the BMUS images. Pulse pressure difference ΔP is calculated by subtracting diastolic pulse pressure from systolic pulse pressure. The systolic diameter SD, diastolic diameter DD, and distensibility coefficient $DC = \left(\frac{2(SD-DD)}{DD}\right)/\Delta P$ [20] are calculated for each cardiac cycle (and averaged over all lines within the 1cm segment in case of the *DC*-ROI approach). The resulting

DC values are averaged over multiple cardiac cycles to obtain a single robust value for the distensibility coefficient of the artery.

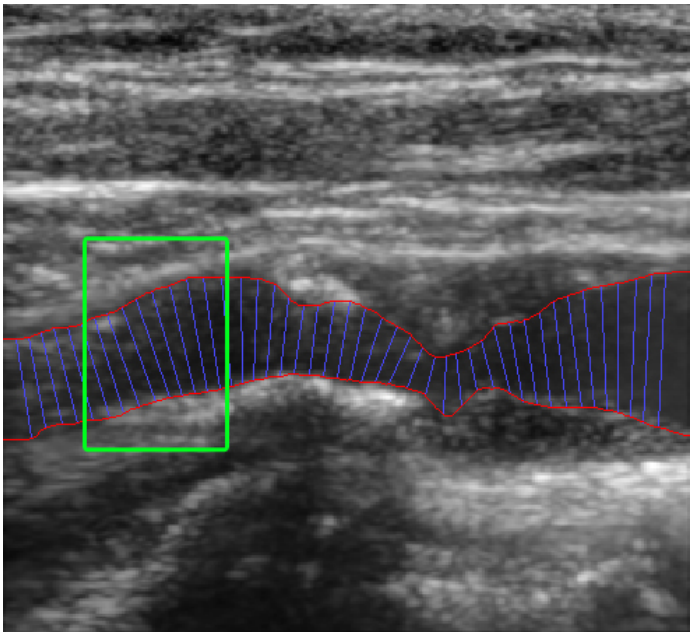

Figure 6: Region of interest (1cm width) for distensibility assessment highlighted in green. The perpendicular lines to the centerline are drawn in blue.

3 Data

3.1 Data Acquisition

Simultaneous, side-by-side CEUS and BMUS images were acquired at ~20Hz frame rate using a Philips iU22 system (Philips Medical Systems, Bothell, USA) with an L9-3 linear probe. Simultaneously acquired CEUS and BMUS are saved and retrieved as a DICOM file for offline post processing. Systolic and diastolic blood pressures were measured for each patient before the ultrasound examination. The standard carotid ultrasound examination and the BMUS&CEUS examination of the carotid arteries were performed. A standardized image acquisition protocol was followed. The protocol was based on the American Society of Echocardiography consensus statement [37]. Pulse pressure of each patient was recorded before examinations. CEUS was performed using intravenous administration of 0.5mL bolus of SonoVue ultrasound contrast agent (Bracco S.p.A., Milan, Italy). For the CEUS examination, power modulation imaging and a mechanical index of 0.06-0.08 were used. For each 0.5mL bolus of SonoVue injection, a 20 seconds image sequence was recorded.

3.2 Patient Population and Study Protocol

All subjects were scanned in the Erasmus MC, University Medical Center Rotterdam in the scope of the PARISk project. The study protocol was approved by the ethical committee at Erasmus MC, and all study participants provided informed consent. The subjects were selected randomly, as a subset from the database of the PARISk project, and were grouped in datasets I and II. The datasets present subjects with different classifications of degree of stenosis [38]. Dataset I consists of 11 carotid arteries with mild to moderate stenosis from 9 patients. The images of this dataset have an average pixel spacing of $95 \pm 24\ \mu m$. This dataset was used in a previous study [30] and this allowed us to compare our NME results to the LRST motion estimation technique presented in that work. A subset of 9 carotid arteries in dataset I was used in a second experiment of NME, and for the evaluation of segmentation and distensibility. We refer to this subset as dataset I'. Two carotid arteries were excluded from dataset I because they were zoomed images and the far walls of the arteries were missing in the field of view. Dataset II consists of 10 carotid arteries with moderate to severe stenosis from 8 patients and the pixel spacing of the images in this dataset is $102 \pm 11\ \mu m$. Dataset II was used to investigate the generalizability of the segmentation. This dataset was not used in any way during development and optimization of the method.

4 Experiments and Validation

4.1 Motion Estimation

4.1.1 Tracking of a Point in the Plaque

First, we evaluated the NME method on the 11 carotid artery images in dataset I, for points in the plaque region. Validation of the motion estimation accuracy was performed by comparing automated to manual tracking. In each image sequence, $\tau = 150$ time frames per carotid were tracked by $J = 3$ observers (GK, SO, ZA). A point on the plaque $\boldsymbol{p}^j(t)$ was selected by an observer j who manually tracked the motion in each time frame. The displacements tracked by each observer on each frame are denoted by: $\boldsymbol{d}^t(t) = \boldsymbol{p}^t(t) - \boldsymbol{p}^t(0)$. We established as the ground truth $\boldsymbol{d}^*(t)$ the average of the displacements for all observers on each time frame: $\boldsymbol{d}^*(t) = \frac{1}{J}\sum_{j=1}^{J} \boldsymbol{d}^j(t)$**.** In order to automatically obtain the displacement of $\boldsymbol{p}^j(0)$ across the subsequent time frames, we apply a composition of the forward and inverse transformation (as explained in [32]): $\tilde{\boldsymbol{T}}(\boldsymbol{s}, t) = \boldsymbol{T}(\boldsymbol{T}^{-1}(\boldsymbol{s}, 0), t)$. We denote the resulting displacements obtained with this transformation as $\boldsymbol{q}^j(t)$, i.e.: $\boldsymbol{q}^j(t) = \tilde{\boldsymbol{T}}(\boldsymbol{p}^j(0), t) - \boldsymbol{p}^j(0)$. This is done to directly compare the displacement pattern between trackings, irrespective of the absolute start position $\boldsymbol{p}^j(0)$, which was slightly different across observers. All automated trackings $\boldsymbol{q}^j(t)$ were compared against the ground truth ($\boldsymbol{d}^*(t)$), and we computed the longitudinal error $e_x^j(t)$, radial error $e_y^j(t)$, and Euclidean error $e_{Euclid}^j(t)$ for each time frame:

$$e_x^j(t) = q_x^j(t) - d_x^*(t),\ e_y^j(t) = q_y^j(t) - d_y^*(t),$$

$$e^{j}_{Euclid}(t) = \sqrt{e^{j}_{x}(t)^2 + e^{j}_{y}(t)^2}$$

We calculated the root mean square error (RMSE) over time for each carotid artery and for each observer j. The errors were averaged over j to obtain a single measure per image sequence:

$$\varepsilon_x = \frac{1}{J}\sum_1^J \sqrt{\frac{1}{\tau}\sum_1^\tau e^{j}_{x}(t)^2},\ \varepsilon_y = \frac{1}{J}\sum_1^J \sqrt{\frac{1}{\tau}\sum_1^\tau e^{j}_{y}(t)^2},\ \varepsilon_{Euclid} = \frac{1}{J}\sum_1^J \sqrt{\frac{1}{\tau}\sum_1^\tau e^{j}_{Euclid}(t)^2}$$

To quantify the interobserver variability, we also computed RMSE for each observer with respect to the ground truth.

The NME method was evaluated with different settings for the B-spline control point spacing β, the number of resolutions ρ (employed in the multi-scale approach used in NME), and the degree of image smoothing σ. For β we investigated a range of 1.25mm to 20mm for the spatial dimension of the grid spacing, and a range of 3 to 12 frames for the temporal dimension. For the number of resolutions, we tested $\rho = 3$ and $\rho = 5$. For the degree of smoothing, we evaluated $\sigma = 0.5$, $\sigma = 1$, and $\sigma = 2$ voxels. In total, 42 different configurations were tested and the optimal configuration was selected. The best configuration was compared with results obtained by each observer and with the LRST method proposed in [32], which is a conventional speckle tracking technique for obtaining a local motion estimate in ultrasound images. A statistical analysis among groups was performed with repeated Anova test using the Octave software for Linux.

4.1.2 Tracking of Points in the Arterial Wall

In this experiment, we evaluated NME on different locations on the wall of the carotid artery. For this purpose, we divided the carotid artery into three segments. A point on the wall in each segment was selected and tracked by two observers (DC, ZA) in 100 frames for the 9 carotid arteries in dataset I′. In these experiments we used the optimal parameters defined in the previous experiment and the same evaluation methodology.

4.2 Lumen Segmentation

Validation of automatic lumen contour extraction was achieved by comparing to manual lumen segmentations of two independent observers (DC, ZA) in the nine carotid arteries of dataset I′ and the ten carotid arteries of dataset II. The evaluation was performed in the epitome images for both datasets, and in five randomly selected time frames $t \in \{11, 18, 37, 74, 135\}$ in the images of dataset I′. The average of the manual segmentations of the two observers was considered as the ground truth. The differences between automated and manual segmentation were expressed as RMSE. The RMSE between two observers was considered as interobserver variability. An alternative definition for interobserver variability would have been to compute the average RMSE between observer and the ground truth, but since the ground truth is based on exactly these two observers, this would give a too optimistic estimate of interobserver variability.

For the artifact detection step, we initialized the parameters of the classes of the Gaussian mixture model based on typical appearance of intensities in BMUS and CEUS images of dataset I′ as follows: $\theta_B = \{\mu_B^c, \sigma_B^c, \mu_B^b, \sigma_B^b\} = \{10, 6, 10, 6\}\}$ (background), $\theta_T = \{10{,}10{,}150{,}30\}$ (tissue). For the artifact class we used different initializations for the upper ($\theta_A = \{200{,}10{,}200{,}10\}$) and lower part ($\theta_A = \{120{,}20{,}150{,}10\}$). The exact initialization values for each class are not critical as the expectation-maximization method uses these values only as a starting point for optimization. We used the following values to the narrow bands: $\kappa_1 = 2\,mm$ (for shadow detection), $\kappa_2 = 1\,mm$ (for initialization of the lumen class in the Gaussian mixture model). κ_1 and κ_2 were selected as a narrow band around the centerline to ensure the selection of pixels inside of the lumen in case of high stenosis. The value of κ_2 is smaller because it is used for initializing the intensity distribution parameters of the lumen class; therefore it is important that only structures that belong to the lumen are selected. For the lumen contour refinement step, we chose $\kappa_3 = 5\,mm$ which is large enough to follow the typically observed local curvature of the initial detected contours. In Equation 1 for the penalty weighting factors we chose $\gamma_1 = 10$, which means 10% additional cost for a step, and $\gamma_2 = 1000$, which means 1% additional cost for each $1mm$ (10 pixels) away from the centerline.

The lumen segmentation results were statistically analyzed using independent t-tests, with SPSS PASW software for Windows (Version 17.0.2, SPSS, Chicago, IL, USA). Significance level was set at $p<0.05$.

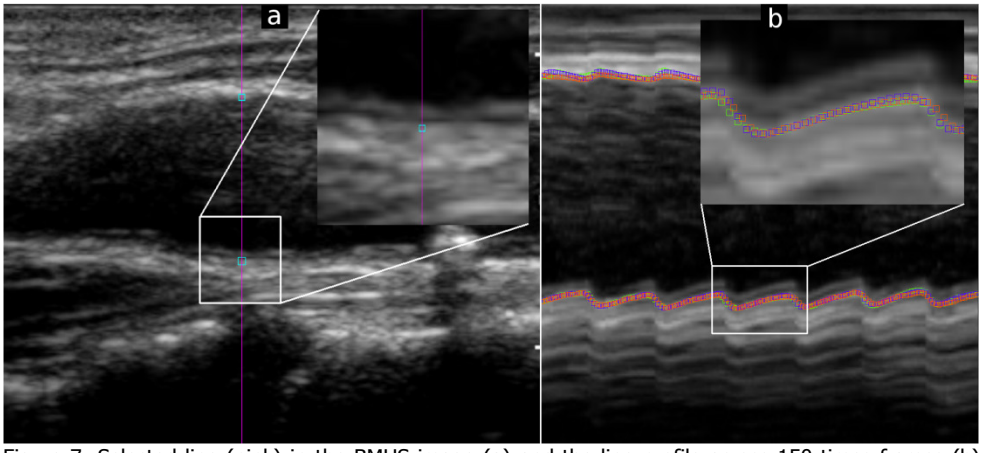

Figure 7: Selected line (pink) in the BMUS image (a) and the line profile across 150 times frames (b). The annotations marked by the observers are represented by green and blue points; the automated tracking is displayed in red.

4.3 Carotid Artery Distensibility

The distensibility measurements for *DC*-Line and *DC*-ROI were evaluated on the nine carotid arteries in dataset I′ by comparing to manual measurements. For the manual *DC* measurement, we selected a line profile (Fig. 7a) approximately orthogonal to the centerline in the BMUS, and extracted it over 150 time frames

(~7 seconds) in order to obtain a virtual representation of M-mode ultrasound (see Fig. 7b). Two observers traced the displacement of one point on the near and far wall of the artery in the virtual M-mode, while also inspecting the positions of the traced points on the BMUS images. Based on these annotations, we calculated *DC* for each cardiac cycle of the image sequence, and averaged the results over all cardiac cycles.

5. Results

5.1 Nonrigid Motion Estimation

The results of the experiment evaluating the displacement of a point in the plaque are shown in Table 1, where the registration errors for NME vs. ground truth, the inter-observer variabilities (observers vs. ground truth), and the errors of the LRST method are reported. Figure 8 shows the results for the entire range of registration parameters used to optimize NME. The lowest registration error was obtained with $\beta = 2.5\,mm \times 2.5\,mm \times 3frames$, $\sigma = 0.5$, and $\rho = 5$. These optimum parameter settings were used for the experiment evaluating the displacements of the three points in the carotid wall, the results of which are shown in Table 2.

The statistical significance was verified with a repeated Anova test considering the results obtained with NME, LRST and the observers annotations. No statistical significance was found among groups ($p>0.05$).

Table 1: Mean ± std. dev. of motion estimation accuracy (ε_x, ε_y and ε_{Euclid}) for NME, the three observers (Obs.) and the LRST method, evaluated in dataset I using a single point in plaque tracked over 150 time frames (all units are in μm).

	NME	Obs. 1	Obs.2	Obs. 3	LRST
ε_x	99±74	74±21	93±82	64±70	87±32
ε_y	47±18	38±13	39±2	37±7	48±11
ε_{Euclid}	112±73	86±27	102±77	76±70	102±29

Table 2: Mean ± std. dev. of motion estimation accuracy ($\varepsilon_x, \varepsilon_y$ and ε_{Euclid}) for NME and two observers (Obs.), evaluated in dataset I′ for three points selected on different sections of the carotid arteries over 100 time frames (all units are in μm).

	NME	Obs. 1 vs. Obs. 2
ε_x	217±112	270±64
ε_y	277±94	99±19
ε_{Euclid}	381±152	290±58

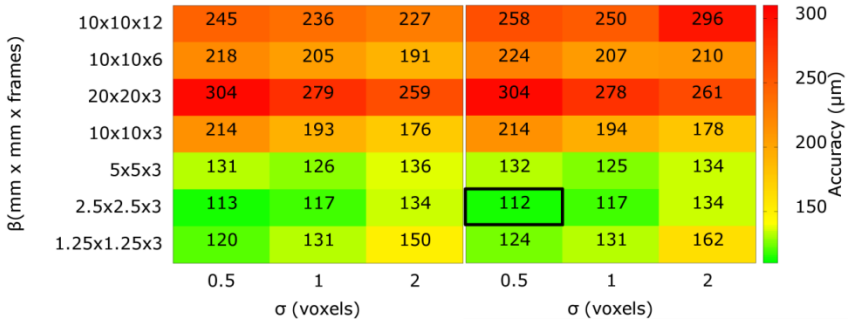

Figure 8: Parameter evaluation for motion estimation. For different number of resolutions ($\rho = 3$ and $\rho = 5$), degrees of smoothing σ, and spacings of the B-spline control points (β), the NME error ε_{Euclid} is shown. The optimum configuration is indicated by the black box.

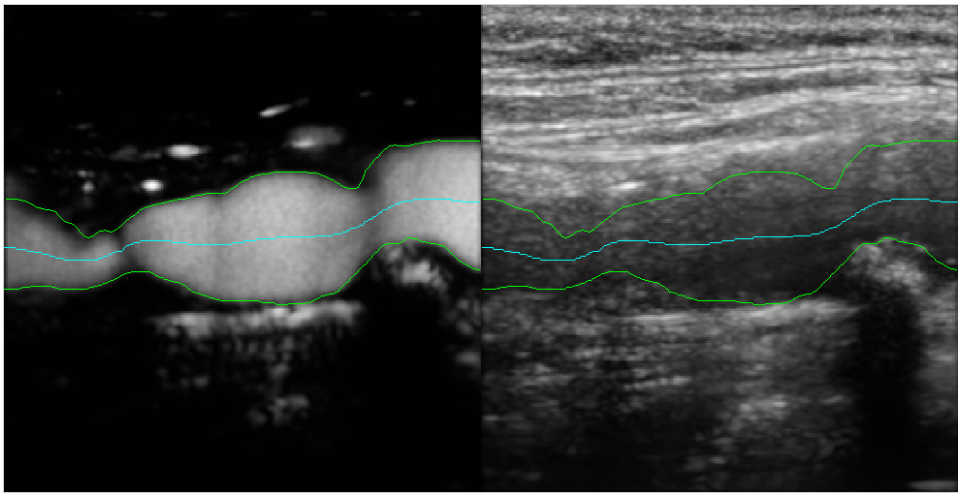

Figure 9: Detection of lumen contours for the image shown in Fig. 1a, containing speckle noise, reverberation artifacts and echolucent plaque in BMUS.

5.2 Lumen Segmentation

Figure 9 shows the carotid artery lumen segmentation results of Fig. 1. Table 3 shows the RMSE between manual segmentations of the two observers, and between automated segmentation and the ground truth in datasets I' and II, both for the epitome images and the randomly selected time-frames. In dataset I', the average RMSE for both upper and lower contours was 191±43μm for the epitome images and 234±36μm for the five randomly selected time-frames respectively. In dataset II, the average RMSE was 351±176μm for the epitome images.

We performed independent t-tests to analyze the differences between the results shown in Table III. For epitome images of dataset I', there is only statistically significant difference between the upper lumen contours and lower lumen contours for interobserver variability (IO) and the error of automated segmentation (AG) ($p<0.05$). For five time-frames of dataset I', there is only significant difference between the AG of the upper lumen contours and the AG of the lower lumen contours ($p<0.05$). In the comparisons of the errors of epitome

images and five time frames of Dataset I′, there is only significant difference for IO and AG of the upper lumen contour ($p < 0.05$). In the comparison of the errors of dataset I and dataset II, there is statistically significant difference for the AG of the upper lumen contour ($p < 0.05$). The other comparisons in each of datasets and between datasets are not significant ($p>0.05$).

Table 3: Mean ± std. dev. RMSE for upper and lower contours in datasets I′ and II. IO = inter-observer variability. AG = Automated vs. ground truth (all units are in μm).

	Upper Lumen Contour		**Lower Lumen Contour**	
	IO	AG	IO	AG
RMSE Dataset I′				
Epitome images	110 ± 50	120 ± 40	220 ± 140	260 ± 70
Five time-frames	190 ± 80	170 ± 60	270 ± 70	290 ± 30
RMSE Dataset II				
Epitome images	226 ± 196	294 ± 100	321 ± 185	408 ± 252

5.3 Distensibility Measurements

Figure 10 shows the carotid artery distensibility measurements based on manual and automated measurements, for dataset I′. In general, the automated distensibility results are conformable to the manual distensibility results. Furthermore, our distensibility coefficient results for 9 carotid arteries (13.1±4.4 [10^{-3}/kPa]) are in the same order as the results reported in the literature (10.5±4.4 [10^{-3}/kPa]) [20]. Whereas *DC*-Line tends to underestimate the distensibility, compared with the manual measurement, *DC*-ROI tends to overestimate.

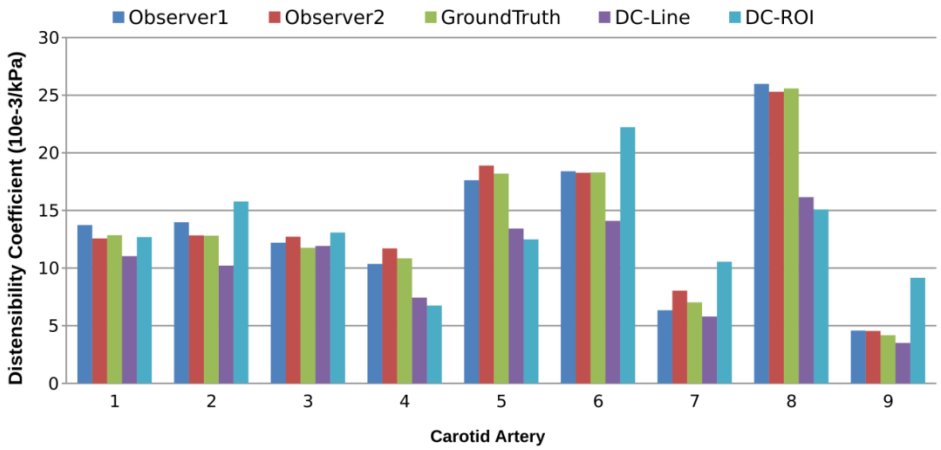

Figure 10: Comparison of carotid artery distensibility based on manual and automated measurements (*DC*-Line and *DC*-ROI)

6. Discussion

We presented a lumen segmentation method which uses the combined information of BMUS and CEUS. First, motion compensation was applied to

construct epitome images, which are used for segmentation. Subsequently, the segmentation and the nonrigid motion estimate are employed to calculate the arterial distensibility. Carotid artery distensibility is an example application of our proposed method. The method provides reliable segmentation of carotid lumen in subjects with atherosclerotic plaques, which can also be a basis for further processing such as segmentation of plaque, assessment of plaque perfusion, and assessment of plaque vulnerability. Since the method requires contrast agent to be injected, we expect that it will be more likely used in the management of early stage disease with visible plaques than in large-scale screening of at risk populations.

The NME method provides results comparable with LRST, which tracks motion locally, whereas NME performs a nonrigid motion compensation of the entire image. The selection of the design parameters of the NME was performed by evaluating the motion of a point that is clearly visible across the whole sequence, situated within the atherosclerotic plaque. In this experiment, the RMSE between NME and the ground truth was around one pixel. Results acquired with NME are comparable with those obtained by observers and with LRST. However, tracking points situated elsewhere in the arterial wall led to larger errors. Both the interobserver variability and the NME vs. ground truth were around 3 pixels. These errors seem mainly due to the lack of clearly visible structures in the arterial wall, complicating the motion estimation, both manually and automatically, especially in the x-direction.

Our method segments accurately the lumen in images that are contaminated with noise in the lumen, artifacts (e.g. clutter or reverberation), and attenuation in the BMUS part and nonlinear propagation artifacts in the CEUS part. As shown in Tab. III, the errors between automated and ground truth segmentations of dataset I and dataset II are in the same order as the error between two observers ($p>0.05$). This means our method is as good as manual delineation of the lumen contours for dataset I′. The error in the lower lumen contour is higher than the error in the upper contour for epitome images of dataset I′ ($p<0.05$). A possible cause for this is the (remaining) influence of the pseudo-enhancement in the lower contour, which makes segmentation more difficult. Therefore, the interobserver variability for the lower contour is also higher than the variability for the upper contour in dataset I′. As seen from Tab. III, the errors between automated and ground truth segmentations in dataset II are in the same order as the error between two observers ($p>0.05$). The errors in the dataset II are in the same order as the errors in the dataset I′ except for the error of automated segmentation for upper lumen contour. Compared to dataset I′, the errors in the lower and upper lumen contours are in the same order in the dataset II. This means that the presence of severe stenosis and heavy shadowing due to calcifications in dataset II make automated segmentation difficult in both upper and lower lumen contours. Comparing the error of automated segmentation to each observer's variability with respect to ground truth is not really fair, since our ground truth is obviously heavily biased towards the two manual observers. As stated before, it has been reported that the lumen segmentation methods using only BMUS have limitations in presence of atherosclerotic plaque [15-17]. The

epitome BMUS and CEUS images obtained through NME allow the DP to better identify the lumen and suppress the noise in atherosclerotic carotids. This provides a clearer separation of the lumen-intima interface, leading to accurate lumen segmentation. To best of our knowledge, our work is the first to use the combination of BMUS and CEUS to segment the lumen, which deals with all the difficulties that have been mentioned in the literature so far for atherosclerotic carotid arteries.

The artefact detection step based on the joint histogram analysis requires a relatively large set of user-defined parameters (Θ). Nevertheless, the exact values are not crucial, since they are used only as initialization parameter for an iterative expectation-maximization approach that further optimizes these joint histogram parameters. The remaining parameters of the lumen segmentation method were defined based on geometrical considerations, taking into account the typical anatomy of the carotid artery, and based on initial trial-and-error experiments on dataset I. The experimental results for dataset II confirm that the method was not "over-tuned" on dataset I.

Our proposed method is also able to measure the carotid artery distensibility coefficient *DC*. Two methods were investigated, *DC*-line and *DC*-ROI. In Fig. 9, it was shown that the *DC*-ROI method overestimated the *DC* in several carotid arteries, especially case 7 and 9. This is due to the difficulty in selecting a ROI that is fully free from plaque around the selected line. Having a partial inclusion of plaque in the ROI will influence the distensibility results as the stiffness of the wall is not well-defined in plaque regions. Distensibility is used as a measure of local vessel stiffness by calculating circumferential stretching, assuming a circular cross section and a fixed radius. This is by definition not the case in a stenosis, and the resulting number cannot be compared to a normal region next to it. The *DC*-Line method yielded results more similar to the inter-observer variability. The observers' distensibility annotations were performed on the virtual M-Mode, which represents a single intensity profile across time. The observers tend to agree more on tracking the brightest layer across the time frames in this visualization than in the 2D+t visualization, which was employed for the manual annotations in the other experiments. It is important to notice that it is not possible to track a point displacement in all directions on the virtual M-Mode.

A distinct advantage of our method is that the operations are performed fully automatic for the whole artery; we just selected a ROI to perform the distensibility evaluation. Temporal evaluation of carotid artery might be useful for other applications such as central pressure estimation. However this is beyond the scope of this study. As a limitation, our data acquisition was not optimized for the purpose of assessment of arterial distensibility, but optimized for plaque perfusion assessment. This may explain some of the erroneous distensibility results for individual subjects. However, we showed that our distensibility results are in the same order as presented in the literature.

Our method is fully automatic for a single carotid branch. We only focused on one branch and excluded carotid arteries with bifurcation and cases with jugular vein presence. As a future work, we would like to include automatic vessel detection in presence of jugular vein and carotid arteries with bifurcation. We have no doubt that the method can work for bifurcated vessels, only the initialization part needs additional attention. Also, we would like to add media-adventitia layer detection, including plaque segmentation.

7 Conclusions

We have performed an accurate lumen segmentation of the carotid artery based on combined BMUS and CEUS images. Our segmentation approach enables the user to detect the lumen-intima border of the artery which can hardly be detected in standard BMUS. The extraction of the motion pattern from the image sequence leads to epitome images that facilitate the lumen segmentation, and furthermore, the assessment of the arterial distensibility. The method is automated, an extensive evaluation was performed, and the results are accurate. Therefore, our method could become a valuable tool for the analysis of atherosclerotic carotid arteries.

Acknowledgements

This research was performed within the framework of CTMM, the Center for Translational Molecular Medicine (www.ctmm.nl), project PARISk (grant 01C-202), and supported by the Netherlands Heart Foundation. We wish to thank Dr G. Luit ten Kate for performing the patient scans.

References:

[1] Naghavi, M., et al., *From vulnerable plaque to vulnerable patient - A call for new definitions and risk assessment strategies: Part I.* Circulation, 2003. **108**(14): p. 1664-1672.
[2] Spagnoli, L.G., et al., *Extracranial thrombotically active carotid plaque as a risk factor for ischemic stroke.* Jama-Journal of the American Medical Association, 2004. **292**(15): p. 1845-1852.
[3] ten Kate G. L. et al, *Noninvasive imaging of the vulnerable atherosclerotic plaque*, Current problems in cardiology, **35**(11), pp. 556–591, 2010.
[4] van den Oord, S.C.H., et al., *Assessment of subclinical atherosclerosis and intraplaque neovascularization using quantitative contrast-enhanced ultrasound in patients with familial hypercholesterolemia.* Atherosclerosis, 2013. **231**(1): p. 107-113.
[5] Delsanto, S., et al., *Characterization of a Completely User-Independent Algorithm for Carotid Artery Segmentation in 2-D Ultrasound Images.* Instrumentation and Measurement, IEEE Transactions on, 2007. **56**(4): p. 1265-1274.
[6] Destrempes, F., et al., *Segmentation in Ultrasonic B-Mode Images of Healthy Carotid Arteries Using Mixtures of Nakagami Distributions and Stochastic Optimization.* Medical Imaging, IEEE Transactions on, 2009. **28**(2): p. 215-229.
[7] Loizou, C.P., et al., *Manual and automated media and intima thickness measurements of the common carotid artery.* Ultrasonics, Ferroelectrics and Frequency Control, IEEE Transactions on, 2009. **56**(5): p. 983-994.
[8] Mao, F., et al., *Segmentation of carotid artery in ultrasound images: Method development and evaluation technique.* Medical Physics, 2000. **27**(8): p. 1961-1970.
[9] Sirlin, C.B., et al., *Contrast-enhanced B-mode US angiography in the assessment of experimental in vivo and in vitro atherosclerotic disease.* Academic Radiology, 2001. **8**(2): p. 162-172.
[10] Kono, Y., et al., *Carotid Arteries: Contrast-enhanced US Angiography—Preliminary Clinical Experience.* Radiology, 2004. **230**(2): p. 561-568.
[11] G. L. ten Kate,et al., "Usefulness of contrast-enhanced ultrasound for detection of carotid plaque ulceration in patients with symptomatic carotid atherosclerosis," The American journal of cardiology, vol. **112(**2), pp. 292–298, 2013.
[12] Noble, J.A. and D. Boukerroui, *Ultrasound image segmentation: a survey.* Medical Imaging, IEEE Transactions on, 2006. **25**(8): p. 987-1010.
[13] Molinari, F., G. Zeng, and J.S. Suri, *A state of the art review on intima–media thickness (IMT) measurement and wall segmentation techniques for carotid ultrasound.* Computer Methods and Programs in Biomedicine, 2010. **100**(3): p. 201-221.
[14] Naik, V., R.S. Gamad, and P.P. Bansod, *Carotid Artery Segmentation in Ultrasound Images and Measurement of Intima-Media Thickness.* BioMed Research International, 2013. **2013**: p. 10.
[15] Gustavsson, T., et al. *A dynamic programming procedure for automated ultrasonic measurement of the carotid artery*. in *Computers in* Cardiology 1994. **1994**. pp.297,300
[16] Xu, X., et al., *Ultrasound intima–media segmentation using Hough transform and dual snake model.* Computerized Medical Imaging and Graphics, 2012. **36**(3): p. 248-258.
[17] Destrempes, F., et al., *Segmentation of Plaques in Sequences of Ultrasonic B-Mode Images of Carotid Arteries Based on Motion Estimation and a Bayesian Model.* Biomedical Engineering, IEEE Transactions on, 2011. **58**(8): p. 2202-2211.
[18] Barth, J.D., et al., *Quantitative Ultrasound Pulsation Study in Human Carotid-Artery Disease.* Arteriosclerosis, 1988. **8**(6): p. 778-781.
[19] Selzer, R.H., et al., *Improved common carotid elasticity and intima-media thickness measurements from computer analysis of sequential ultrasound frames.* Atherosclerosis, 2001. **154**(1): p. 185-193.
[20] van Popele, N.M., et al., *Association Between Arterial Stiffness and Atherosclerosis: The Rotterdam Study.* Stroke, 2001. **32**(2): p. 454-460.
[21] Godia, E.C., et al., *Carotid Artery Distensibility: A Reliability Study.* Journal of Ultrasound in Medicine, 2007. **26**(9): p. 1157-1165.
[22] Stefanadis, C., et al., *Distensibility of the ascending aorta: comparison of invasive and non-invasive techniques in healthy men and in men with coronary artery disease.* European Heart Journal, 1990. **11**(11): p. 990-996.
[23] Riley, W.A., et al., *Decreased arterial elasticity associated with cardiovascular disease risk factors in the young. Bogalusa Heart Study.* Arteriosclerosis, Thrombosis, and Vascular Biology, 1986. **6**(4): p. 378-86.

[24] Reneman, R.S., et al., *Flow velocity patterns in and distensibility of the carotid artery bulb in subjects of various ages.* Circulation, 1985. **71**(3): p. 500-9.
[25] Hoeks, A.P.G., et al., *Assessment of the distensibility of superficial arteries.* Ultrasound in Medicine & Biology, 1990. **16**(2): p. 121-128.
[26] Teynor, A., et al., *An automated, interactive analysis system for ultrasound sequences of the common carotid artery.* Ultrasound in Medicine & Biology, 2012. **38**(8): p. 1440-1450.
[27] Golemati, S., et al., *Carotid artery wall motion estimated from B-mode ultrasound using region tracking and block matching.* Ultrasound in Medicine and Biology, 2003. **29**(3): p. 387-399.
[28] Chan, K.L., *2 Approaches to motion analysis of the ultrasound image sequence of carotid atheromatous plaque.* Ultrasonics, 1993. **31**(2): p. 117-123.
[29] Akkus, Z., *Dynamic assessment of carotid plaque motion.* Ultrasound, 2010. **18**(3): p. 140-147.
[30] Akkus, Z., et al., *Motion Compensation Method using Dynamic Programming for Quantification of Neovascularization in Carotid Atherosclerotic Plaques with Contrast Enhanced Ultrasound (CEUS).* SPIE Medical Imaging 2012: Ultrasonic Imaging, Tomography, and Therapy. **2012**. pp. 83200C-83200C.
[31] ten Kate, G.L., et al., *Far-Wall Pseudoenhancement during Contrast-Enhanced Ultrasound of the Carotid Arteries: Clinical Description and in Vitro Reproduction.* Ultrasound in Medicine and Biology, 2012. **38**(4): p. 593-600.
[32] Metz, C.T., et al.,s *Nonrigid registration of dynamic medical imaging data using nD+t B-splines and a groupwise optimization approach.* Medical Image Analysis, 2011. **15**(2): p. 238-249.
[33] Klein, S., et al., *Adaptive Stochastic Gradient Descent Optimisation for Image Registration.* International Journal of Computer Vision, 2009. **81**(3): p. 227-239.
[34] Nevo, S.T., et al., *Automated tracking of the mitral valve annulus motion in apical echocardiographic images using multidimensional dynamic programming.* Ultrasound in Medicine and Biology, 2007. **33**(9): p. 1389-1399.
[35] Akkus, Z., et al., *Statistical segmentation of carotid plaque neovascularization.* In *SPIE Medical Imaging*. International Society for Optics and Photonics. **2013**. p. 867506-867506.
[36] Moon, T.K., *The expectation-maximization algorithm.* IEEE Signal Processing Magazine, 1996. **13**(6): p. 47--60.
[37] Stein, J.H., et al., *Use of Carotid Ultrasound to Identify Subclinical Vascular Disease and Evaluate Cardiovascular Disease Risk: A Consensus Statement from the American Society of Echocardiography Carotid Intima-Media Thickness Task Force Endorsed by the Society for Vascular Medicine.* Journal of the American Society of Echocardiography, 2008. **21**(2): p. 93-111.
[38] C. Warlow, *Mrc european carotid surgery trial: interim results for symptomatic patients with severe (70-99%) or with mild (0-29%) carotid stenosis*, The Lancet, 1991, **337**, no. 8752, pp. 1235–1243.
[39] G. Zahnd, M. Orkisz, A. Sérusclat, P. Moulin, and D. Vray, "Simultaneous extraction of carotid artery intima-media interfaces in ultrasound images: assessment of wall thickness temporal variation during the cardiac cycle," International journal of computer assisted radiology and surgery, pp. 1–14, 2013.

Chapter 8

Fully Automated Carotid Plaque Segmentation in Combined Contrast Enhanced and B-mode Ultrasound

Carotid plaque segmentation in B-mode Ultrasound (BMUS) and Contrast-Enhanced Ultrasound (CEUS) is crucial to assess plaque morphology and composition, which are linked to plaque vulnerability. Segmentation in BMUS is challenging due to noise, artifacts, and echolucent plaques. CEUS allows a better delineation of the lumen but contains artifacts and lacks tissue information. We present a method which exploits the combined information from simultaneously acquired BMUS&CEUS images. Our method consists of nonrigid motion estimation, vessel detection, lumen-intima segmentation, and media-adventitia segmentation. The evaluation was performed in training (n=20 carotids) and test (n=28) datasets by comparing to manually obtained ground-truth. The average root-mean-square errors in the training and test datasets were comparable for media-adventitia (411±224μm and 393±239μm) as well as for lumen-intima (362±192μm and 388±200μm), and were comparable to inter-observer variability. To the best of our knowledge, this is the first method to perform fully automatic carotid plaque segmentation using combined BMUS&CEUS.

Z. Akkus*, D.D.B. Carvalho*, S. Klein, S C.H. van den Oord, A. F.L. Schinkel, N. de Jong, A.F.W. van der Steen, J.G. Bosch**. Fully Automatic Segmentation and Deformation Estimation of Atherosclerotic Carotid Plaques in Combined B-mode and Contrast Ultrasound Images.** Submitted. (*shared first author)

1) Introduction

Cerebrovascular disease ranks as the third world leading cause of death[1]. The carotid arteries are two vessels located at both sides of the neck. They are responsible for providing blood to the brain and muscles of the face. Each carotid starts as a common carotid artery (CCA) which forks into two branches: internal carotid artery (ICA) and external carotid artery (ECA). The incidence of ischemic strokes is highly associated with the rupture of atherosclerotic plaques in the carotid artery [2]. Rupture can cause severe vessel obstruction due to distal propagation of a thrombus[3]. The formation of an atherosclerotic plaque occurs due to atherosclerosis, which is a process of inflammation in the arterial wall. For assessing the risk of rupture, current clinical practice is heavily relying on the degree of stenosis. However, there is an increasing awareness that not the size of the plaque, but its composition is related to risk of rupture. For example, intra-plaque neovascularization (IPN) has been linked to plaque vulnerability in several histopathological studies [4-6]. Ultrasound has been widely used as a standard tool for inexpensive and non-invasive diagnosis of carotid plaque morphology and composition. Different ultrasound techniques have been used such as standard B-mode ultrasound (BMUS), color Doppler and contrast enhanced ultrasound (CEUS) [7]. For the accurate assessment of the degree of stenosis and plaque composition, objective and reproducible segmentation of carotid plaques from ultrasound images is a crucial step.

So far, carotid plaque segmentation has mainly been performed on standard BMUS images [8-10]. However, in standard BMUS images this is difficult and can be inaccurate due to noise in the lumen, artifacts, lumen irregularity and echolucent plaques. Color Doppler provides an approximate view of blood flow in the lumen, but its accuracy is dependent on user-controlled settings (e.g. Doppler gain, wall filter, and velocity range) and local direction of flow. This may overestimate or underestimate the lumen, and thus color Doppler is not a suitable imaging technique for plaque segmentation. CEUS allows a better delineation of the carotid lumen than standard BMUS [7, 11, 12]. CEUS provides visualization of the vessel lumen regardless of flow velocity and direction by the use of ultrasound contrast agents. However, CEUS contains specific artifacts and contains no tissue information [13] which make the plaque segmentation difficult.

Some studies have addressed carotid plaque segmentation in longitudinal vessel cross sections visualized with standard BMUS [8-10]. Loizou et al. [8] presented a method based on gray scale normalization, speckle reduction filtering, and snake segmentation. The method compares the accuracy of four snake techniques on 80 patients. The method is automatic and uses color Doppler images to avoid the difficulties in echolucent plaque detection in BMUS and for extracting the initial snake contour. Several limitations of the study were reported: 1) Overlapping of color flow with wall or plaque tissue, 2) lack of information for low velocity regions, 3) convergence of snake to false local minima, and 4) exclusion of echolucent and calcified plaques. Loizou et al. [9] presented another plaque

segmentation method based on snake segmentation. The plaque is segmented in different time frames, according to a manual initialization in the first time frame. Destrempes et al. [10] presented a plaque segmentation method which models the intensities of vessel lumen, plaque and adventitial wall with a mixture of three Nakagami distributions. The mixture parameters were first estimated with an Expectation-Maximization algorithm, and this yielded the likelihood of a Bayesian segmentation model. They also obtained the motion fields in the image sequence using an optical flow technique and used it as a prior of the Bayesian model which includes a local geometrical smoothness constraint. The method was tested on 93 sequences of 33 patients (in total 8988 images). The method is semi-automatic since it requires manual segmentation of plaque in the first frame.

Due to the noise, artifacts, and echolucent plaques, the fully automatic segmentation of plaques in BMUS images remains a challenge. Two specific types of plaques (I and V according to the classification of Nicolaides et al. [14]) are particularly challenging. Type I plaques are uniformly echolucent, making it very difficult to differentiate their intensity from the lumen. Type V plaques present with calcified caps that cause shadows.

CEUS allows delineation of the vessel lumen, but it also enables the detection of IPN. The ultrasound contrast agent enters the plaque neovasculature and is seen as intermittently appearing bright spots. For assessment of IPN from CEUS images, a first step is the delineation of the plaque region of interest (ROI). In several studies, manual delineation has been used, which is subjective and tedious [15-18]. As tissue information is absent in CEUS images, automatic plaque segmentation is extremely difficult. Some studies have addressed plaque segmentation in CEUS images [19-21]. Hoogi et al. [19] segments the lumen with an active contour method and fits a parabola to the arterial wall, enabling the plaque segmentation in a single frame. A limitation of the method is the fact that media-adventitia is not segmented but estimated by a parabola. The method of Molinari et al. [20] performs automatic segmentation of the plaque and characterization of its tissue in BMUS enhanced with ultrasound contrast agent. The plaque is segmented by a k-means classification algorithm and subsequent application of a deformable model. They reported that using contrast enhanced BMUS overcomes the difficulties in segmenting echolucent plaques in standard BMUS. However, the method was evaluated only on 5 echolucent plaques. Zhang et al. [21] proposed a method in CEUS images using spatio-temporal analysis and snakes. The method uses the spatial correlation of time intensity curves to detect initial contours of plaques, and then deforms them to refined contours with a gradient vector flow snake. The method requires a user defined ROI around the plaque in the CEUS image to simplify the segmentation process. In another study, Zhang et al. [22] presented interactive plaque segmentation in CEUS. A mean image with improved signal-to-noise ratio (SNR) is obtained by time averaging of the image sequence, and interactive plaque segmentation is performed in the temporal mean image. The user needs to indicate points on the plaque border and

B-spline interpolation of the discrete points is used to get a smooth closed curve. No motion compensation is performed and the segmentation is fully manual.

Several algorithms have been described that segment intima-media thickness (IMT) in asymptomatic carotids in BMUS. Since they do not consider the presence of atherosclerotic plaques in the carotids, they are not applicable to plaque segmentation. Liang et al. [23] presented a method to detect arterial boundaries in a user-selected ROI through multiscale dynamic programming (DP). The cost function is constructed from a weighted sum of features and geometrical characteristics extracted from a manually segmented training set. The method does not segment IMT in the presence of plaque. The method of Cheng and Jiang [24] uses a Dual Dynamic Programming (DDP) approach to detect the intima and adventitia layers of the common carotid wall. The method is semi-automatic and requires the manual selection of a ROI containing the layers. Destrempes et al. [25] presented a method which segments the IMT through Expectation Maximization (EM) in a manually selected ROI. The EM is initialized using three Nakagami distributions to represent the intima-media layers, the lumen and the adventitia. The method was evaluated on healthy common carotids. The work of Teynor [26] uses the DDP method of [27] in conjunction with manual user interactions to track the systolic and diastolic IMT of asymptomatic carotids in a manually defined ROI. Zhou et al. [27] presented a method that merges different techniques to segment the intima-media layer and presents a novel DP approach, the dual line detection (DLD). An edge map is created from the output of two edge detectors in different scales. The DLD is applied on local segments of this edge map. In the end, the calculated contours are employed as an input for a snake segmentation model.

Some studies have also investigated automatic carotid vessel detection in BMUS, which could be used as a first step to automate plaque segmentation. The work of Molinari et al. [28] tracks the adventitia layer by using geometric feature extraction, line fitting, and line classification of the CCA. The method is sensitive to inhomogeneities in the lumen intensities. The work of Rocha et al. [29] employs DP to automatically extract the lumen axis of the CCA. The proposed methods are limited to the common carotid artery and thus multibranch carotid artery detection still remains a challenge.

Previous studies either worked on only BMUS or CEUS, and therefore they were prone to difficulties associated with these imaging modalities. This limits their performance. BMUS and CEUS present complementary information. In this study, we exploit the combined information from simultaneously acquired BMUS&CEUS images to overcome the difficulties of plaque segmentation in previous studies. An example of side-by-side simultaneously acquired BMUS and CEUS image and a schematic depiction of arterial wall layers are shown in Figure 1. The advantage of this combination is that CEUS shows a better delineation of the lumen, where BMUS provides the visualization of tissues. Since CEUS does not contain any information about the tissues, the combination with BMUS is necessary to

accurately segment the plaque. We proposed a novel and fully automatic carotid plaque segmentation method which overcomes the difficulties of the separate use of BMUS and CEUS.

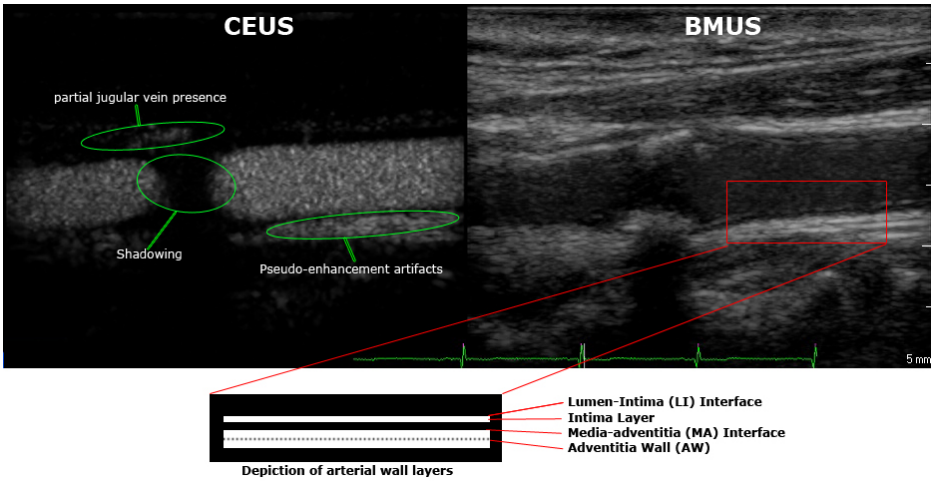

Figure 1: Simultaneously acquired BMUS&CEUS image with typical artifacts and schematic depiction of arterial wall layers

2) Materials and Methods

In our study, we use simultaneously acquired side-by-side BMUS and CEUS image sequences. The simultaneous BMUS & CEUS imaging leads to two 2D+time (2D+t) image series, $I_{BMUS}(\boldsymbol{s},t)$ and $I_{CEUS}(\boldsymbol{s},t)$, where $\boldsymbol{s}$ is a spatial coordinate (x,y) and t is the time frame index with $t = 1 \dots \tau$ (τ = number of time frames). Our proposed segmentation method for carotid plaques consists of three main steps: nonrigid motion estimation and compensation, automated vessel detection, and plaque segmentation. A flowchart of the method is shown in Figure 2.

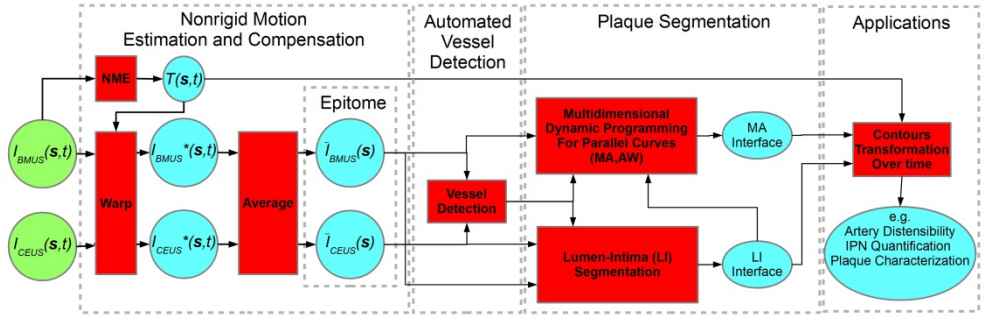

Figure 2: Flowchart of the steps of the method. Inputs (green), operations (red) and outputs (blue). $\boldsymbol{T}(\boldsymbol{s},t)$: Transformation obtained from BMUS with nonrigid motion estimation (NME). $I_{BMUS}{}^{*}(\boldsymbol{s},t)$, $I_{CEUS}{}^{*}(\boldsymbol{s},t)$: Motion compensated BMUS and CEUS respectively. $\bar{I}_{BMUS}(\boldsymbol{s})$, $\bar{I}_{CEUS}(\boldsymbol{s})$: Epitome images. $\boldsymbol{s}$: Spatial position (x,y) within the image. t: Time frame index. MA: Media-Adventitia; LI: Lumen-Intima. AW: Adventitia Wall.

2.1) Nonrigid motion estimation and compensation

In a previous work [30], we proposed a nonrigid motion compensation method for simultaneously acquired BMUS&CEUS image sequences. As the first step of our plaque segmentation method we obtain single BMUS and CEUS 'epitome' images ($\bar{I}_{BMUS}(\boldsymbol{s})$, $\bar{I}_{CEUS}(\boldsymbol{s})$) with improved SNR by averaging image intensities of each pixel over time in the motion compensated BMUS&CEUS image sequences ($I_{BMUS}{}^{*}(\boldsymbol{s},t)$, $I_{CEUS}{}^{*}(\boldsymbol{s},t)$). In the proposed motion compensation method, we estimate the nonrigid deformation ($\boldsymbol{T}(\boldsymbol{s},t)$) of the carotid over time from the BMUS image sequence and subsequently compensate the motion in both the BMUS and CEUS image sequences. The method performs a groupwise registration of the entire 2D+t dataset. It produces a nonrigid motion estimate on the complete image, differently from existing local motion estimation techniques in ultrasound [31-34]. The deformations are modeled by a nonrigid 2D+t B-spline transformation, ensuring smoothness both in the spatial and temporal dimensions. An adaptive stochastic gradient descent optimizer [35] is employed to calculate the transformation parameters that minimize a dissimilarity measure based on the variance of the intensities at corresponding spatial locations. The nonrigid motion compensation method is described and evaluated in detail in [30]. All further processing is performed on the epitome images $\bar{I}_{BMUS}(\boldsymbol{s})$ and $\bar{I}_{CEUS}(\boldsymbol{s})$.

2.2) Automated vessel detection

Prior to plaque segmentation, we perform automated detection of vessels in the BMUS and CEUS epitome images. CEUS images provide only perfusion information of vessels, which avoids the confusion of vessel-like anatomical structures in the BMUS images. However, CEUS presents artifacts which might cause false detection. We assume that there is at least one vessel in the image plane as images are acquired for the carotid examination. We further assume the proximal part of the carotid (CCA) is on the right side of the image, according to the standardized scanning protocol. The bifurcation may or may not be within the field of view, and the jugular vein may or may not be visible. Figure 3 illustrates the possible scenarios. To identify the arteries of interest (CCA, ICA, ECA), we propose a four-stage algorithm, consisting of: a) Rough lumen identification b) Morphological operations c) Vessel profile scanning d) Heuristic classification of vessel candidates.

a) Rough lumen identification: We apply an intensity based classification in the BMUS and CEUS epitome images to identify true lumen and circumvent artifacts as described in detail in our previous study [36]. Based on typical intensity distribution of classes (background, tissue, lumen and artifacts) in the joint histogram of BMUS and CEUS epitomes, we initialize these classes and feed them into an Expectation-Maximization (EM) algorithm. This results in a fuzzy segmentation, indicating for each pixel the probability that it is located in a lumen.

b) Morphological processing: In this step, morphological opening using a disk-shaped structuring element with radius 1 mm is applied to remove noise or small objects such as remaining artifacts in the probabilistic lumen segmentation obtained in the previous step. We assume that, after this aggressive morphological opening, any isolated artifacts have been eliminated from the probabilistic lumen segmentation. Next, we convert this probabilistic segmentation to a binary image by using Otsu's global image threshold. Subsequently, we extract the edges from the binary image using a Canny edge detector.

c) Vessel profile scanning: In this step, we vertically scan the edge map at each x position (i.e. column), from top to bottom, and record each pair of edge points. Assuming that these pairs of edge points represent the boundaries of a vessel, we calculate the center points and connect them to each other from column to column (left to right) based on the closest Euclidean distance. To compensate for missed regions due to acoustic shadowing or out-of-plane artifacts, we use linear interpolation between detected center points for empty regions.

d) Heuristic classification of vessel candidates: We classify the detected candidates in a heuristic manner. In the most extreme case, a maximum of 3 vessels (jugular, internal and external carotid artery as seen in Fig. 3d) can be seen in the field of view of 3 or 4 cm depth in the standard carotid B-mode ultrasound. The possible combinations of detected vessels are listed below:

   1) If there is only one vessel detected (see Fig. 3a), it is considered to be the carotid artery.

   2) If two vessels are detected, this may be a jugular vein and a carotid artery (see Fig. 3b) or a bifurcated artery (see Fig. 3c). To discriminate between these two cases, we analyze the detected center point sets for the two vessels. If they do not have a "common center points region", i.e., a part where the centerlines merge, or if this region is smaller than 5 mm length, we consider these two vessels are separate vessels (jugular and carotid). In this case, the top-most one is the jugular vein and the bottom one is the carotid artery. If the common center points region (see Fig. 3c) is at least 5 mm length, we consider it as a carotid bifurcation. In this case, the x-position where the centerline undergoes the largest vertical shift indicates the bifurcation point. The upper branch is the ICA.

   3) If three vessels are detected (see Fig. 3d), we consider the top-most as the jugular vein and both others as a bifurcated artery which consists of internal and external carotid branches.

Having identified the arteries of interest, based on the procedure above, we proceed with vessel wall segmentation. In the case of a single branch carotid

artery detection (see Fig. 3a and 3b), we segment the lumen-intima (LI) and media-adventitia (MA) interfaces of the near wall (upper wall) and far wall (lower wall) of the artery as described in the following sections. In the case of a bifurcated carotid artery detection (see Fig 3c and 3d), we segment the LI and MA interfaces of the near wall, the far wall, and the bifurcation region (see Fig. 3c) of the artery.

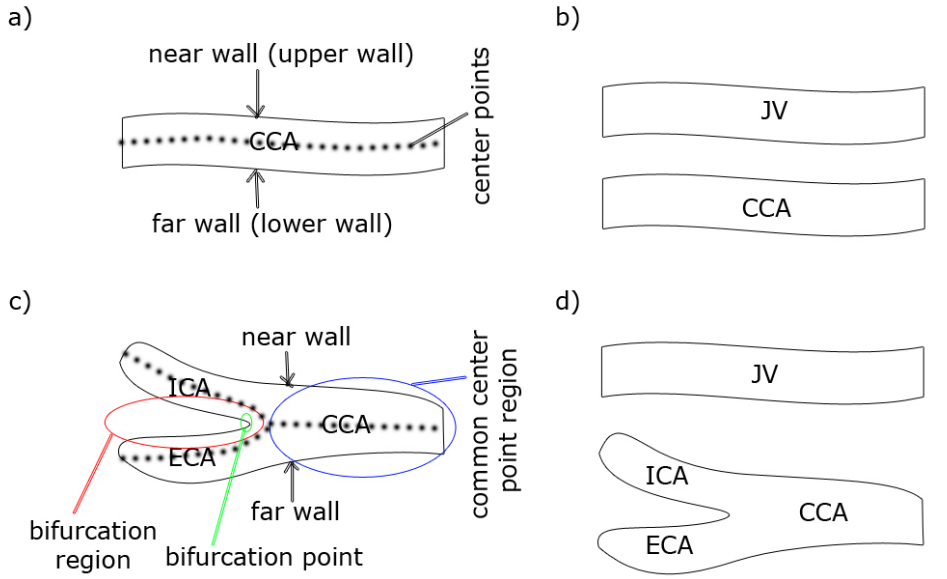

Figure 3: Depiction of possible scenarios of the vessel geometry visible in the carotid ultrasound images. Common carotid artery (CCA) only (a); Jugular vein (JV) and CCA (b); Bifurcated carotid artery (c); JV and bifurcated carotid artery (d)

2.3) Plaque segmentation

To detect the carotid plaques, we sequentially segment LI and MA interfaces of the upper and lower carotid walls and apply the Mannheim consensus [37] for delimitation of the plaque. The Mannheim consensus established the metrics to identify the plaque: "Plaque is defined as a focal structure that encroaches into the arterial lumen by at least 0.5 mm or 50% of the surrounding IMT value or demonstrates a thickness > 1.5 mm as measured from the media-adventitia interface to the intima-lumen interface". In the following sections, we briefly describe LI interface segmentation adopted from our previous work [36] and MA interface segmentation using multidimensional dynamic programming (MDP) for parallel curves. The MA interface segmentation is the main focus of this study.

The LI and MA interfaces obtained in the epitome images can be warped back to each time frame using the transformation $\boldsymbol{T}(\boldsymbol{s}, t)$ resulting from the nonrigid motion estimation described in section 2.1. This allows following plaques over time and possible applications such as arterial distensibility, IPN quantification, and plaque characterization.

2.3.1) Lumen-intima interface segmentation

We perform LI interface segmentation of the carotid artery on the epitome images $\bar{I}_{BMUS}(\boldsymbol{s})$ and $\bar{I}_{CEUS}(\boldsymbol{s})$. Our LI segmentation method which is explained in detail in [36] consists of five steps: centerline estimation, detection of shadowing, detection of artifacts, graph based segmentation and refinement of lumen contours. For segmenting of a single-branch carotid artery we perform the following steps.

First, we estimate the centerline of the carotid artery by applying a 2D Gaussian smoothing filter to the CEUS epitome image and finding a minimum cost path, using dynamic programming in the x-direction [34, 38]. Second, we detect the shadow regions by fitting a linear curve to the mean intensity profile of a band around the centerline and neutralize these regions by assigning the same cost value. We then redetect the centerline. Third, we detect the CEUS-specific pseudo-enhancement artifacts [13] and saturation artifacts [18], by using a joint intensity classifier for BMUS&CEUS epitomes and suppress them in the CEUS epitome. Fourth, we detect the upper and lower LI interfaces in the CEUS epitome using dynamic programming. Fifth, we refine the upper and lower LI interfaces by resampling the neighborhood of the interfaces with subpixel precision and applying dynamic programming.

In the case of a carotid bifurcation, we detect two separate centerlines for ICA and ECA. We use the bifurcation point that was obtained in the vessel detection step (section 2.2). Left of that point, we mask the quadrant to the lower left side of the bifurcation point and detect the centerline for the upper branch (ICA) plus the common carotid as explained above for a single-branch artery. Then we mask the upper left quadrant and detect the second centerline (ECA+CCA). Subsequently, we detect the shadow regions and artifacts as explained above for a single-branch carotid artery. Lastly, we detect the upper LI interface of the bifurcated artery from the ICA+CCA centerline and the lower LI interface from the ECA+CCA centerline. For the LI interfaces of the bifurcation region, we detect the upper LI interface in the region between ICA centerline and bifurcation line, and the lower LI interface in the region between bifurcation line and ECA centerline (see Fig. 3c).

2.3.2) Media-adventitia interface segmentation

As tissue information is suppressed in CEUS images, it is not possible to segment the media-adventitia (MA) interface from CEUS images. We therefore

segment the MA interface from the simultaneously acquired BMUS epitome image, using multidimensional dynamic programming (MDP) for detection of parallel curves [24, 27]. The layers of the arterial wall in a BMUS image are shown in Fig. 1. As seen in Fig. 1, the MA interface is the transition from the media layer to the adventitia wall, characterized by a strong outward (from lumen) intensity gradient. The adventitia wall is seen in the BMUS image as the brightest part of the vessel wall. We define the centerline of this structure as the adventitia wall (AW) position. The MA interface runs in parallel with the AW and they are assumed to possess the following characteristics:

a) Intra-curve smoothness: Both the MA interface and AW should be a smooth curve.
b) Inter-curve smoothness: the MA interface and AW should be nearly parallel with a specific distance.
c) Intima-media (IM) distance: The distance between MA and LI interface is between 0.3mm and 1.5mm [37, 39] in a vessel wall free from plaques and will increase in case of plaques.

2.3.2.1) Multidimensional dynamic programming for parallel curves

The objective of MDP for parallel curves is finding two curves that minimize a certain cost function. Let $\bar{I}_{BMUS}(\boldsymbol{s})$ be of size $X \times Y$. The MA interface and the adventitia wall (AW) run from left to right (in the *x*-dimension) and are described by two coordinates y_{MA} and y_{AW} at each *x*-position, with $1 \leq y_1, y_2 \leq Y$. We find the optimal interfaces by minimizing a dedicated cost function composed of appearance and geometry related terms. The appearance terms stimulate that the MA curve traverses high outward gradient locations and that the AW curve passes through bright regions. The geometry terms favour solutions that satisfy the three above mentioned characteristics.

The appearance cost of the MA interface (C_{MA}) is calculated by applying a Gaussian derivative filter with standard deviation of 0.3 mm, which gives the *y*-directional gradient of the BMUS epitome image $\widetilde{\nabla_y} I_{BMUS}(\boldsymbol{s}) = \pm \nabla_y G * \bar{I}_{BMUS}(\boldsymbol{s})$, where the sign is chosen such that gradients pointing outward from the lumen centerline are positive. The cost of the MA interface passing through coordinate $\boldsymbol{s}$ is then defined as $C_{MA}(\boldsymbol{s}) = 1 - \widetilde{\nabla_y} I_{BMUS}(\boldsymbol{s}) / \max_{\boldsymbol{s}} \widetilde{\nabla_y} I_{BMUS}(\boldsymbol{s})$. The cost representing the AW wall is defined as $C_{AW} = 1 - \bar{I}_{BMUS}(\boldsymbol{s}) / \max_{\boldsymbol{s}} \bar{I}_{BMUS}(\boldsymbol{s})$. For both C_{MA} and C_{AW}, 0 is the optimal cost. The combined appearance cost is calculated by taking the average: $C(x, y_1, y_2) = \big(C_{MA}(x, y_1) + C_{AW}(x, y_2)\big)/2$.

MDP is defined by minimizing a cumulative cost function ($\hat{C}$), which combines the appearance costs with several geometry-related terms:

$$\hat{C}(x, y_1, y_2) = \min_{\delta_1, \delta_2 \in \{-1,0,1\}} [\, \hat{C}(x-1, y_1 - \delta_1, y_2 - \delta_2) + C(x, y_1, y_2) \cdot (1+\alpha_1)^{\delta_1} \cdot (1+\alpha_1)^{\delta_2} \cdot (1 + \alpha_2 \cdot |(y_1 - y_2) - (\delta_1 - \delta_2)|) + \alpha_3 \cdot P\big(x, y_1 - y_{LI}(x)\big) \,] \quad (Eq.1)$$

subject to $d_{min} \le (y_2 - y_1) \cdot R \le d_{max}$ and $2 \le x \le N$

where δ_1 and δ_2 are the step sizes (in pixel units) in y_1 and y_2 directions, α_1 and α_2 are weights for intra-curve smoothness and inter-curve smoothness respectively, P is an IMT penalty term, $y_{LI}(x)$ is the lumen-intima position, α_3 is a weighting factor for the IMT penalty term, d_{min} and d_{max} are the minimal and maximal distance (in *mm*) between MA interface and AW, R is pixel spacing in *mm*. The MDP procedure for detection of parallel curves subject to the constraint $d_{min} \le (y_2 - y_1) \cdot R \le d_{max}$ is illustrated in Fig. 4.

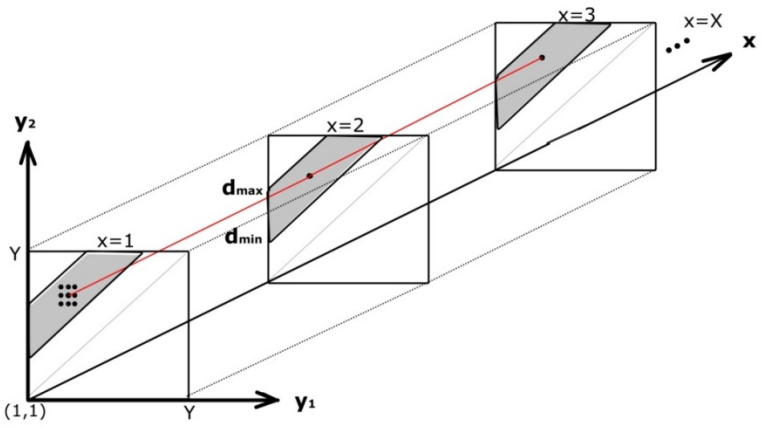

Figure 4: An illustration of multidimensional dynamic programming for a given image of size $X \times Y$ to detect parallel curves subject to the constraint $d_{min} \le (y_2 - y_1) \cdot R \le d_{max}$ (gray region). y_2 and y_2 represent the positions of the two curves, as function of the *x*-coordinate. The 3×3 dots indicate the search space $\delta_1, \delta_2 \in \{-1,0,1\}$.

The minimum and maximum allowed distance (d_{min} and d_{max}) between MA interface and AW are considered to be 0.3 mm and 1.5 mm, respectively, based on adventitial wall thickness measurements reported in previous studies [39, 40]. The IMT penalty term $P\big(x, y_1 - y_{LI}(x)\big)$ encodes prior information on the expected distance between MA and LI, $y_1 - y_{LI}(x)$, taking into account the possible presence of plaque at position *x*. The IMT penalty function is defined as a

combination of two sigmoid functions and an uncertainty region as seen in Eq. 2 and Figure 5.

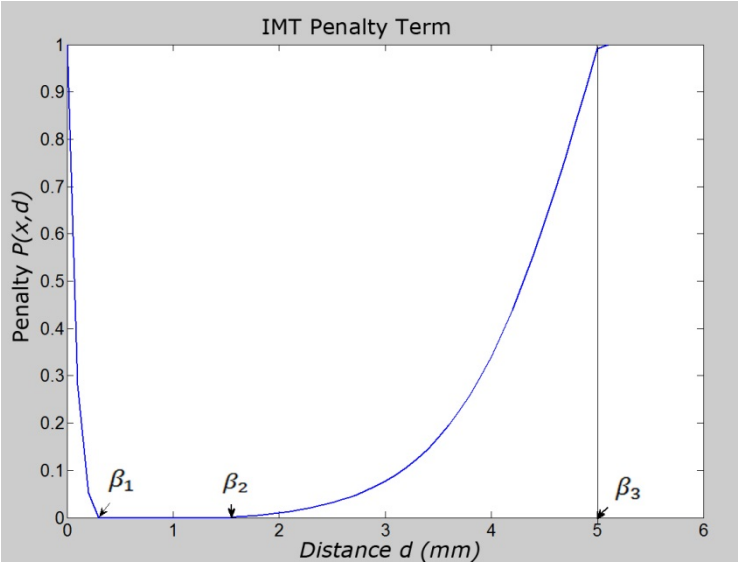

Figure 5: An example of an IMT penalty term P for healthy section of artery (β_1=0.3mm, β_2=1.5mm, β_3=5mm).

$$P(x,d) = \begin{cases} 1 - \tanh\left(\frac{c \cdot d}{\beta_1}\right) & d \in [0, \beta_1] \\ 0 & d \in (\beta_1, \beta_2) \\ 1 - \tanh\left(\frac{c \cdot (\beta_3(x) - d)}{\beta_3(x) - \beta_2(x)}\right) & d \in [\beta_2, \beta_3] \\ 1 & d \in (\beta_3, +\infty] \end{cases}$$

(Eq.2)

where $\beta_1 = 0.3\ mm$ (minimum expected IMT); $\beta_2(x)$ is maximum expected IMT at position x;

$\beta_3(x) = \beta_2(x) + 3.5\ mm; c = e^1$ (constant which supplies $tanh(c) \sim = 1$); and:

$$\beta_2(x) = 1.5\ mm + p(x) \cdot (D_{max} - D(x)) \cdot \gamma$$

(Eq. 3)

where $p(x) \in \{0,1\}$ indicates the presence of plaque at position *x*, D_{max} is a representative lumen diameter (80th percentile of all lumen diameters along the

artery), $D(x)$ is the local lumen diameter at position x (clipped to D_{max}), and $\gamma = 1.5$ is a factor for outward growing of plaques.

The constant $\beta_1 = 0.3\,mm$ was chosen based on minimum IMT values presented in the literature [39, 40]. The point β_2 determines the length of the zero-penalty region, which represents the range of IMT values over which we assume no prior knowledge. Minimum β_2 was chosen $1.5\,mm$ as the maximum expected IMT for a healthy carotid based on presented values in the literature [37, 39, 40]. The point β_2 is shifted based on local features indicating the presence of plaque, $p(x)$, as shown in Eq. 3. As features, we consider the shape of the LI interface and the degree of lumen stenosis. We propose two configurations of the method to estimate $p(x)$, which both are evaluated in the experiments. Configuration 1 uses only the shape of the LI interface. Configuration 2 uses both the shape of the LI interface and the stenosis degree. These configurations will be explained in detail in the next subsections. In case $p(x)$=1, point β_2 is shifted by an amount based on the estimated degree of stenosis ($D_{max} - D(x)$), multiplied by a factor $\gamma = 1.5$ to accommodate a 50% outward growth of the plaque. After β_2 mm, we apply an exponentially increasing penalty reaching its maximum at β_3, reflecting the prior knowledge that IMT values this high are less likely.

The reason for choosing β_3 as 3.5mm further than β_2 was to provide a safety margin to avoid any hard penalty in case of misidentification. The reason for choosing D_{max} as the 80th percentile of the lumen diameter distribution was to avoid misidentification of presence of plaque for vessels which do not have uniform lumen diameter distribution along the vessel (e.g. the ones which have the carotid bulb and one branch of bifurcation in the image plane). We chose the value of γ based on the maximum plaque development outward from the lumen (50%) observed in our data.

2.3.2.2) Configuration 1

For a healthy carotid artery, the LI interface is expected to be sufficiently smooth to be represented reasonably well by a third-order polynomial fit. Plaque regions on the other hand are represented by an "inward bump" of the LI interface. To detect these bumps, we fit a third-order polynomial curve to the LI interface. After the first fit, we discard the contour points at the lumen side of the fit and fit another third-order polynomial curve to the remaining points. This is repeated three times to converge to an estimate of what the 'healthy' LI interface would look like. Based on the Mannheim consensus [37] for plaque, if the distance between the fit and the actual LI interface is larger than 0.5mm for an image column x, that position is considered as a possible plaque region ($p(x) = 1$). The remaining positions are considered as healthy sections of the artery ($p(x) = 0$).

2.3.2.3) Configuration 2

In this configuration, we include lumen stenosis as a second feature to detect the presence of plaques, next to the detection of inward bumps as in Configuration 1. Regions with lumen diameter $D(x) < (D_{max} - 0.5\,mm)$ are considered as a sign of presence of plaque, again based on the Mannheim consensus [37]. The plaque indicator variable $p(x)$ is computed by a logical OR operation on the assessments based on inward bump detection and lumen stenosis estimation.

3 Data and Experiments

3.1 Data acquisition

Simultaneous, side-by-side CEUS and BMUS images were acquired at ~20Hz frame rate using a Philips iU22 system (Philips Medical Systems, Bothell, USA) with an L9-3 linear probe. The standard carotid ultrasound examination and the BMUS&CEUS examination of the carotid arteries were performed. A standardized image acquisition protocol was followed based on the American Society of Echocardiography consensus statement [41]. CEUS clips were recorded with the dual display mode for simultaneous B-mode ultrasound and CEUS. CEUS was performed using intravenous administration of 0.5mL bolus of SonoVue ultrasound contrast agent (Bracco S.p.A., Milan, Italy). For the CEUS examination, power modulation imaging and a mechanical index of 0.06-0.08 were used. For each 0.5mL of SonoVue bolus injection, we recorded a 20 seconds image sequence. Both carotid arteries were examined, focusing on the presence of plaques. If plaques were present, the largest plaque area was identified visually in the longitudinal axis of the carotid artery and recorded.

3.2 Patient population and study protocol

The study population consisted of 23 symptomatic patients with carotid atherosclerotic disease who had had a stroke, transient ischemic attack or ischemic ocular event and 7 asymptomatic patients. Symptomatic patients had moderate to severe carotid stenosis (≥70%). A total of 46 carotid arteries in 23 symptomatic patients and a total of 9 carotid arteries in 7 asymptomatic patients were included in the study. We included in total 55 carotid arteries in our study. Seven carotid arteries were excluded due to poor image quality or acoustic shadowing over > 50% of image width. Image quality for the whole dataset was assessed in advance with consensus of two observers. We used 20 carotid arteries as a training set to tune our parameters. The remaining 28 carotid arteries were included as a test set to evaluate performance of our segmentation method. Since the study was aimed at the CCA, we had a total of only 7 bifurcated arteries (3 in training dataset, 4 in test dataset) in the entire dataset. The study protocol was approved by the ethical

committee at Erasmus MC, University Medical Center, and all study participants provided informed consent.

3.3) Evaluation

The performance of automated vessel detection (Section 2.2) was evaluated on the training and test dataset by comparing with the consensus visual score of two observers (D, Z).

Validation of LI and MA interfaces was achieved by comparing the automated segmentation result with a manual reference standard. The reference standard (ground truth) was obtained as the average of manual annotations of two independent observers (D, Z). Root mean square error (RMSE) was calculated between the automated results and the ground truth in training and test dataset including and excluding shadow regions. First, we evaluated the weights of intra-curve smoothness (α_1) and inter-curve smoothness (α_2) for a range of values ($\alpha_1, \alpha_2 \in \{0, 0.05, 0.1, 0.15, 0.2, 0.25\}$) on the training set by comparing to ground truth. The optimum values of α_1 and α_2 were obtained separately for upper and lower contours. Next, the weighting factor for the IMT penalty term was evaluated for a range of values $\alpha_3 \in \{0.25, 0.5, 1, 2, 4\}$. These evaluations were done both for Configuration 1 and 2. After that, the method with optimum values of α_1, α_2 and α_3 and optimum configuration was evaluated on the test set. In all experiments, cases which had RMSE >1mm were considered as failures and excluded when computing the mean RMSE over subjects.

The area between the automatically detected LI and MA interfaces, the automated intima-media (IM) area A, was compared to the ground truth IM area G in the training and test datasets. A Dice Index ($DI = 2 * (A \cap G)/(|A| + |G|)$) was calculated to measure the overlap between *A* and *G*.

The results were statistically analyzed using SPSS PASW software for Windows (Version 17.0.2, SPSS, Chicago, IL, USA). To test the association between automated segmentation results and manual reference standard, Pearson correlation (r) was used.

4) Results

The success rate of automated vessel detection was 96% (46 cases out of 48) compared to the consensus score of two observers. The automated detection failed in two cases where the jugular vein was only partially present above the carotid artery.

Table 1 shows the results of the evaluation of intra-curve (α_1) and inter-curve (α_2) smoothness in the training dataset, both for Configuration 1 and 2. The best settings for α_1 and α_2 were highlighted with bold red border lines for each configuration. As seen in Table 1, the intra-curve smoothness has more influence

on the results than the inter-curve smoothness and the average RMSE is optimal without inter-curve smoothness for the lower wall. Table 2 shows the results for evaluation of the weighting factor α_3 for the IMT penalty term. On average, $\alpha_3 = 1$ is the best setting for the IMT penalty term. No substantial difference between Configuration 1 and 2 is observed.

In the training dataset, there was one failure (RMSE > 1mm) for the lower MA interface of an artery, and no failures for the LI interface. In the test dataset, there were four lower and three upper MA interface failures for Configuration 1, three upper and three lower MA interface failures for configuration 2, and one failure for LI interface. The best settings of α_1 and α_2 shown in Table 1 for each configuration, and $\alpha_3 = 1$ were used for the RMSE calculations of MA interface in Table 3 and 5. The average RMSE between automated segmentation results and the ground truth, and inter-observer variability are shown in Table 3 for the MA interface of upper and lower contours in the training dataset and test dataset. As it is hard to obtain the ground truth for shadowed regions, Table 3 also shows the results when excluding shadowed regions. The average RMSE between automated segmentation and the ground truth over subjects in the training and test datasets for MA interface were 411±224 μm and 393±239 μm, respectively. The average RMSE between automated segmentation and the ground truth over subjects in the training and test datasets for LI interface were 362±192 μm and 388±200 μm, respectively. Table 4 shows the average RMSE between automated results and the ground truth for the LI interface in the training and test dataset. In general, average RMSE between automated MA and LI interface segmentation and manual ground truth is almost double of inter-observer variability apart from the results for the upper LI interface (see Table 3 and 4). Table 5 shows the results for the MA interface using Configuration 1 with the best settings and LI interface of bifurcation region. The RMSE of segmentation results of LI and MA interface for the lower wall of the bifurcation region, including shadow regions, are almost three times larger than the inter-observer variability.

Figure 6 shows the comparison of the automated IM area with ground truth IM area in the training and test datasets. In the training dataset, automated IM area was found to be significantly correlated to manual ground truth IM area for upper ($r=0.92$, $p<0.01$) and lower ($r=0.74$, $p<0.01$) wall. In the test dataset, automated IM area was found to be significantly correlated to manual ground truth for upper ($r=0.73$, $p<0.01$) and lower ($r=0.71$, $p<0.01$) wall. For IM area overlap between automated and ground truth, average Dice index (DI) was 68% for upper wall and 70% for lower wall in the training dataset, and was 71% for upper wall and 68% for lower wall in the test dataset.

An example of MA and LI segmentation is shown in Figure 7 for a single-branch artery and in Figure 8 for a bifurcated artery.

Table 1: The average root-mean-square-error for media-adventitia interface segmentation for a range of intra-curve (α_1) smoothness and inter-curve (α_2) smoothness

RMSE (μm)			Configuration1						Configuration2					
			Inter-curve smoothness (α_2)						Inter-curve smoothness (α_2)					
			0	0.05	0.1	0.15	0.2	0.25	0	0.05	0.1	0.15	0.2	0.25
Upper	Intra-curve smoothness (α_1)	0	583	502	505	502	502	500	737	734	737	729	733	731
		0.05	435	446	435	439	437	440	655	640	649	623	621	622
		0.1	482	480	486	478	479	465	549	487	485	488	462	452
		0.15	520	522	521	508	483	480	504	502	499	467	471	474
		0.2	554	550	541	538	513	515	534	530	517	499	496	499
		0.25	566	576	577	575	555	554	549	563	558	535	531	532
Lower	Intra-curve smoothness (α_1)	0	542	537	538	541	540	539	546	542	544	549	546	544
		0.05	457	453	447	451	448	450	457	452	446	451	447	449
		0.1	460	455	458	458	458	458	456	454	456	456	456	456
		0.15	388	393	395	395	413	414	390	395	397	397	416	417
		0.2	395	395	401	399	400	402	398	399	400	402	404	405
		0.25	404	411	416	418	421	423	407	415	421	421	424	427

Table 2: Average RMSE between automated segmentation and ground truth for given factors (α_3) of the IMT penalty curve, using cost function of configuration1

Automated vs. Ground Truth					
RMSE (μm)	weighting factor (α_3)				
	0.25	0.5	1	2	4
Upper	627	604	435	446	473
Lower	440	385	388	392	450
Mean	534	495	411	419	462

Table 3: Average RMSE between automated segmentation (A) and ground truth (G) for MA interface in the training and test datasets. IO: Interobserver variability. Z: Observer 1; D: Observer 2

MA Interface	Config.	RMSE	include shadow		exclude shadow	
		(μm)	Upper	Lower	Upper	Lower
Training Dataset	1	A vs. G	435±174	388±274	372±116	354±259
	2	A vs. G	452±145	390±276	399±91	356±262
	IO	Z vs. D	242±123	253±192	219±112	174±27
Test Dataset	1	A vs. G	396±202	390±276	371±181	427±189
	2	A vs. G	446±215	430±192	429±215	427±190
	IO	Z vs. D	210±105	258±163	204±103	242±154

Table 4: Average RMSE between automated segmentation (A) and ground truth (G) for LI interface in the training and test datasets. IO: Interobserver variability. Z: Observer 1; D: Observer 2

LI Interface	RMSE	include shadow		exclude shadow	
	(μm)	Upper	Lower	Upper	Lower
Training Dataset	A vs. G	338±187	386±197	280±126	338±187
	Z vs. D	275±114	239±115	249±105	338±188
Test Dataset	A vs. G	327±182	449±218	298±155	469±255
	Z vs. D	250±187	266±119	239±179	247±97

Table 5: Average RMSE between automated segmentation (A) and ground truth (G) for MA and LI interface of bifurcation region. Z: Observer 1; D: Observer 2

Bifurcated Arteries (n=7)					
	RMSE	include shadow		exclude shadow	
	(μm)	Upper	Lower	Upper	Lower
MA	A vs. G	386±208	606±233	378±211	437±162
	Z vs. D	250±164	233±129	227±148	211±109
LI	A vs. G	369±315	613±385	337±331	338±79
	Z vs. D	445±342	187±106	256±160	149±73

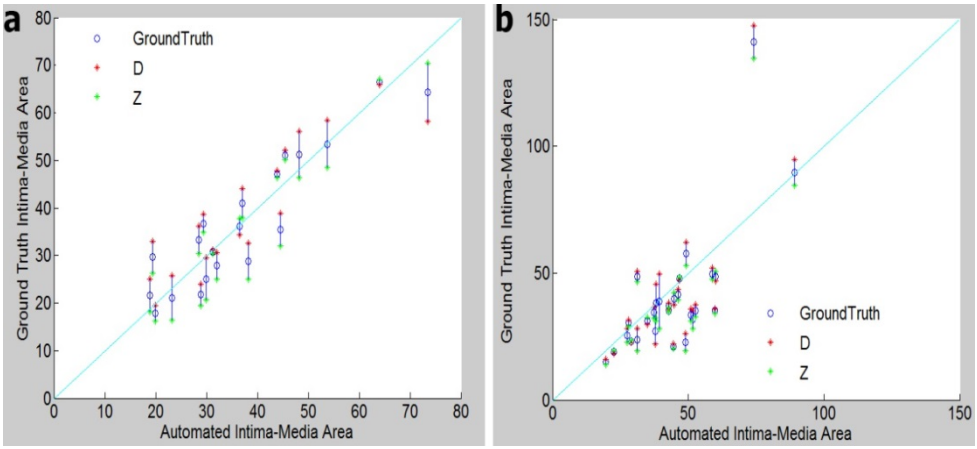

Figure 6: Comparison of automated intima-media area with ground-truth intima media area (blue circles) for training dataset (a) and test dataset (b). Intima-media area for each observer is shown as red (D) and green (Z) asterisk.

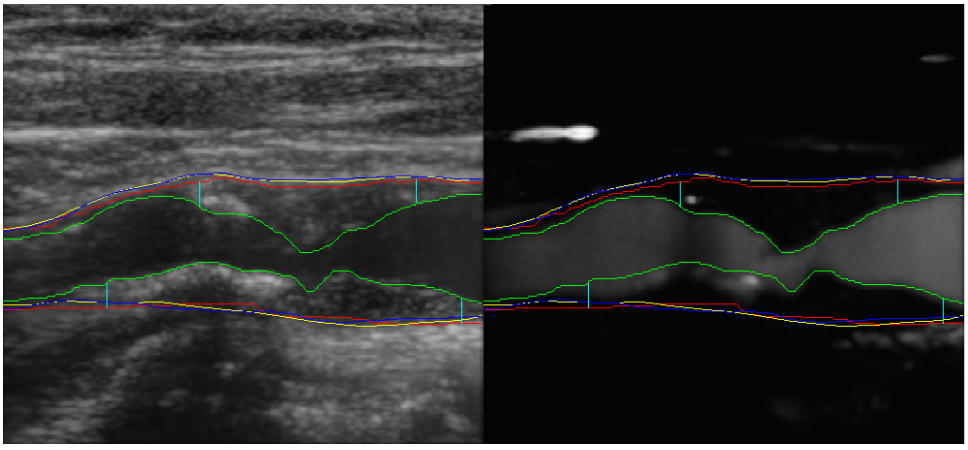

Figure 7: An example of automated MA (red line) and LI (green line) interface segmentations in the BMUS (left) and CEUS (right) epitomes. Manual segmentations of MA interface by two observers are shown in blue (D) and yellow (Z). The left and right borders of plaques are shown with light blue vertical lines based on Mannheim consensus (IMT>1.5mm).

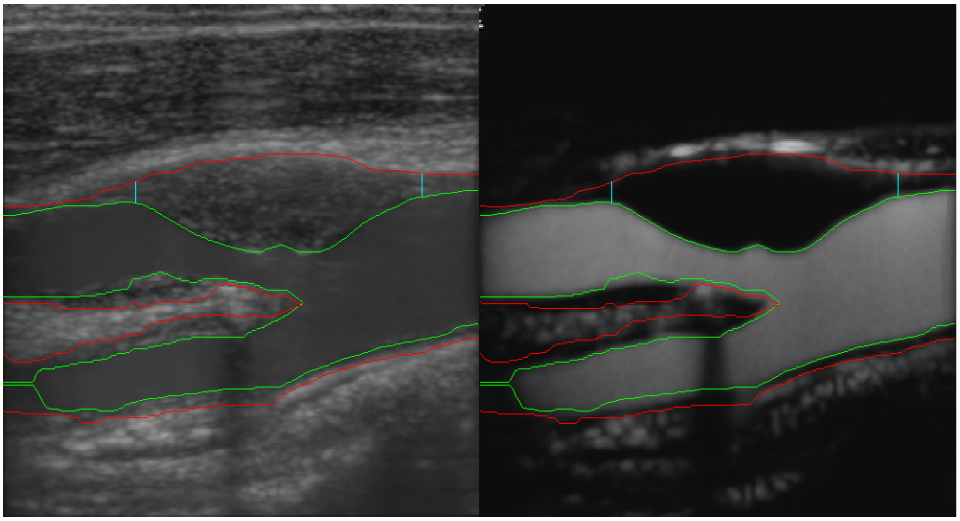

Figure 8: An example of automated MA (red line) and LI (green line) interfaces segmentation for a bifurcated artery in BMUS (left) and CEUS (right) epitomes. Light blue vertical lines indicate the left and right border of plaque based on Mannheim consensus (IMT>1.5mm).

5) Discussion

We presented a carotid plaque segmentation method in simultaneously acquired BMUS and CEUS image sequences. The method is fully automatic and robust to noise, artifacts and echolucent plaques. In the literature, segmentation of arterial layers in carotid arteries without plaques in BMUS is well established. However, the accurate segmentation of arterial layers in carotid arteries with plaques presents many additional challenges. Therefore, IMT segmentation techniques are not applicable to carotid arteries with plaques. In the case of echolucent plaques, which present the same intensity values as the lumen, it is impossible to make a clear delineation. These limitations were discussed in the work of Loizou et al. [8].

The combination of BMUS and CEUS allows the detection of artifacts and the segmentation of echolucent plaques. CEUS provides a clear definition of the arterial lumen. Despite the advantages brought by the combination of these modalities, the BMUS in simultaneous BMUS and CEUS possesses lower SNR compared to standard BMUS. This occurs due to the fact that a lower transmit signal power is used to avoid the disruption of the contrast agents in CEUS. To handle this issue, we employ nonrigid motion estimation and compensation to obtain an epitome image with improved SNR. As stated before, the methods of Hoogi et al. [19] and Zhang et.al. [21, 22] estimated adventitia wall position in CEUS based on the estimated original lumen position and thus outward growing of plaques with respect to the lumen was ignored. This might lead to over- or under-estimation of plaque region and affect further IPN assessment. In our method, we overcome this difficulty by segmenting the media-adventitia interface from the

BMUS image. Another advantage of our method compared to other studies [9, 10, 22] is that it does not require any user interaction. Furthermore, our method allows automatic multiple branch carotid detection while previous studies [25, 28, 29] are limited to one branch (CCA) detection.

Our automatic vessel detection only failed in two cases out of 48, due to shadowing and partial appearance of the jugular vein on top of the carotid artery. These two vessels were detected as a bifurcated artery, since the geometry was very close to that. As seen in Table 1, 3, and 4, the results for Configuration 1 and 2 are quite similar in both our training and test dataset. That means that including the lumen stenosis to define presence of plaque (configuration 2) does not give a noticeable improvement. As seen in Table 1, inter-curve smoothness does not have as much influence on the results as intra-curve smoothness. For evaluation of the weighting of the IMT penalty term, the weight $\alpha_3 = 1$ is shown to be optimal in the center of the given range of α_3 values as seen in Table 2. The average RMSE increases with increase or decrease of the value of α_3. The errors for MA interface detection in the training and test datasets are in the same order, about 400μm (~ 4 pixels), and they are almost the double of the inter-observer variability (see Table 3). This might be partly explained by a systematic error between automated and manual segmentation as seen in Fig. 7. The automated method and manual observers seem to pick slightly different layers. The exclusion of shadow regions does not improve the results. The errors for the LI interface in the training and test datasets are in the same order and similar to the inter-observer variability after exclusion of shadow regions (see Table 4). As seen in Table 5, the segmentation results of MA and LI after exclusion of shadow regions in the bifurcation region are comparable with the segmentation results of MA and LI for the near and far wall of the CCA in Table 3 and 4. The average RMSE of MA and LI for the lower wall (far wall), including shadow regions, are almost 3 times higher than the interobserver variability. This is because of the shadow regions especially in the beginning and the end of bifurcation regions which introduce larger errors as there is no wall information in those regions.

As seen in Figure 6a and 6b, comparison of automated IM area with manual ground truth IM area is scattered around the identity line ($y = x$) for the training and test datasets apart from a few outliers in the test dataset. We found significant correlation between automated IM area and manual ground truth IM area ($p<0.01$). We found the DI for area overlap similar to the study of Loizou et al. [8] for 4 snake methods ($DI \epsilon \{67.6\%, 67.7\%, 69.3\%, 66.6\%\}$) and the study of Destrempes et al. [10] ($DI = 74.6\%$). Compared to plaque segmentation in CEUS, the accuracy of our method is in the same order as the method of Zhang et al. [21] that presented a mean distance error of 0.40±0.08 mm for the plaque segmentation in CEUS. Our method was evaluated in the training and test datasets separately. In all the datasets the accuracy is almost in the same order, testifying the method's generalizability. One should keep in mind that the used image data and ground truth in these studies can be very different, so a detailed comparison

of results is not possible. Since our method is fully automated and reaches very similar results to earlier methods, we consider our method successful and accurate.

As a limitation, the BMUS image obtained in simultaneous BMUS&CEUS has low SNR as lower signal power is used to avoid the disruption of the contrast agents in CEUS. To improve the SNR, we obtained the BMUS epitome image by performing temporal averaging. However, this might not be enough for some image sequences due to extensive noise and lack of tissue signal. Improvement on the BMUS image quality in simultaneous acquisition would enhance the performance of our method. For example, using plane wave ultrasound imaging instead of conventional linear line scan could provide an improved SNR BMUS.

6) Conclusion

In conclusion, our method performs accurate and fully automatic plaque segmentation with multibranch vessel detection. Using simultaneous BMUS&CEUS provides clear advantages in segmentation of carotid plaques rather than the sole use of BMUS or CEUS. The use of the combined imaging modalities allows the suppression of noise, detection and suppression of artifacts, wall information for plaque segmentation in CEUS images, and detection of echolucent plaques in BMUS images. This plaque segmentation method is a crucial step for objective and automatic assessment of plaque composition such as IPN quantification. As far as we know, this is the first study exploiting combined information from BMUS&CEUS to automatically segment carotid plaques.

Acknowledgements

This research was performed within the framework of CTMM, the Center for Translational Molecular Medicine (www.ctmm.nl), project PARISk (grant 01C-202), and supported by the Netherlands Heart Foundation. We wish to thank Dr G. Luit ten Kate for performing the patient scans.

References:

[1] R. Lozano, M. Naghavi, K. Foreman, S. Lim, K. Shibuya, V. Aboyans, J. Abraham, T. Adair, R. Aggarwal, S. Y. Ahn, and others, "Global and regional mortality from 235 causes of death for 20 age groups in 1990 and 2010: a systematic analysis for the Global Burden of Disease Study 2010," *The Lancet,* vol. 380, pp. 2095-2128, 2013.

[2] S. Carr, A. Farb, W. H. Pearce, R. Virmani, and J. S. T. Yao, "Atherosclerotic plaque rupture in symptomatic carotid artery stenosis," *Journal of Vascular Surgery,* vol. 23, pp. 755-766.

[3] J. Golledge, R. M. Greenhalgh, and A. H. Davies, "The symptomatic carotid plaque," *Stroke,* vol. 31, pp. 774-781, 2000.

[4] J. A. Schaar, J. E. Muller, E. Falk, R. Virmani, V. Fuster, P. W. Serruys, A. Colombo, C. Stefanadis, S. W. Cassells, P. R. Moreno, A. Maseri, and A. F. W. van der Steen, "Terminology for high-risk and vulnerable coronary artery plaques - Report of a meeting on the vulnerable plaque, June 17 and 18, 2003, Santorini, Greece," *European Heart Journal,* vol. 25, pp. 1077-1082, Jun 2004.

[5] W. E. Hellings, W. Peeters, F. L. Moll, S. R. D. Piers, J. van Setten, P. J. Van der Spek, J. P. P. M. de Vries, K. A. Seldenrijk, P. C. De Bruin, A. Vink, E. Velema, D. P. V. de Kleijn, and G. Pasterkamp, "Composition of Carotid Atherosclerotic Plaque Is Associated With Cardiovascular Outcome A Prognostic Study," *Circulation,* vol. 121, pp. 1941-U111, May 4 2010.

[6] F. Shah, P. Balan, M. Weinberg, V. Reddy, R. Neems, M. Feinstein, J. Dainauskas, P. Meyer, M. Goldin, and S. B. Feinstein, "Contrast-enhanced ultrasound imaging of atherosclerotic carotid plaque neovascularization: a new surrogate marker of atherosclerosis?," *Vascular Medicine,* vol. 12, pp. 291-297, 2007 2007.

[7] S. C. H. van den Oord, Z. Akkus, J. E. Roeters van Lennep, J. G. Bosch, A. F. W. van der Steen, E. J. G. Sijbrands, and A. F. L. Schinkel, "Assessment of subclinical atherosclerosis and intraplaque neovascularization using quantitative contrast-enhanced ultrasound in patients with familial hypercholesterolemia," *Atherosclerosis,* vol. 231, pp. 107-113, 2013.

[8] C. P. Loizou, C. S. Pattichis, M. Pantziaris, and A. Nicolaides, "An integrated system for the segmentation of atherosclerotic carotid plaque," *Information Technology in Biomedicine, IEEE Transactions on,* vol. 11, pp. 661-667, 2007.

[9] C. Loizou, S. Petroudi, C. Pattichis, M. Pantziaris, T. Kasparis, and A. Nicolaides, "Segmentation of atherosclerotic carotid plaque in ultrasound video," in *Engineering in Medicine and Biology Society (EMBC), 2012 Annual International Conference of the IEEE*, ed, 2012, pp. 53-56.

[10] F. Destrempes, J. Meunier, M. F. Giroux, G. Soulez, and G. Cloutier, "Segmentation of Plaques in Sequences of Ultrasonic B-Mode Images of Carotid Arteries Based on Motion Estimation and a Bayesian Model," *Biomedical Engineering, IEEE Transactions on,* vol. 58, pp. 2202-2211, 2011.

[11] C. B. Sirlin, Y. Z. Lee, M. S. Girard, T. M. Peterson, G. C. Steinbach, K. G. Baker, and R. F. Mattrey, "Contrast-enhanced B-mode US angiography in the assessment of experimental in vivo and in vitro atherosclerotic disease," *Academic Radiology,* vol. 8, pp. 162-172, 2001.

[12] Y. Kono, S. P. Pinnell, C. B. Sirlin, S. R. Sparks, B. Georgy, W. Wong, and R. F. Mattrey, "Carotid Arteries: Contrast-enhanced US Angiography—Preliminary Clinical Experience," *Radiology,* vol. 230, pp. 561-568, 2004.

[13] G. L. ten Kate, G. G. J. Renaud, Z. Akkus, S. C. H. van den Oord, F. J. ten Cate, V. Shamdasani, R. R. Entrekin, E. J. G. Sijbrands, N. de Jong, J. G. Bosch, A. F. L. Schinkel, and A. F. W. van der Steen, "Far-Wall Pseudoenhancement during Contrast-Enhanced Ultrasound of the Carotid Arteries: Clinical Description and in Vitro Reproduction," *Ultrasound in Medicine and Biology,* vol. 38, pp. 593-600, Apr 2012.

[14] A. N. Nicolaides, S. K. Kakkos, M. Griffin, M. Sabetai, S. Dhanjil, D. J. Thomas, G. Geroulakos, N. Georgiou, S. Francis, E. Ioannidou, and others, "Effect of image normalization on carotid plaque classification and the risk of ipsilateral hemispheric ischemic events: results from the asymptomatic carotid stenosis and risk of stroke study," *Vascular,* vol. 13, pp. 211-221, 2005.

[15] P. T. Huang, F. G. Huang, C. P. Zou, H. Y. Sun, X. Q. Tian, Y. Yang, J. F. Tang, P. L. Yang, and X. T. Wang, "Contrast-enhanced sonographic characteristics of neovascularization in carotid atherosclerotic plaques," *Journal of Clinical Ultrasound,* vol. 36, pp. 346-351, Jul-Aug 2008.

[16] A. Hoogi, Z. Akkus, S. C. H. van den Oord, G. L. ten Kate, A. F. L. Schinkel, J. G. Bosch, N. de Jong, D. Adam, and A. F. W. van der Steen, "Quantitative Analysis of Ultrasound Contrast Flow Behavior in Carotid Plaque Neovasculature," *Ultrasound in Medicine and Biology,* vol. 38, pp. 2072-2083, Dec 2012.

[17] L. Xiong, Y. B. Deng, Y. Zhu, Y. N. Liu, and X. J. Bi, "Correlation of Carotid Plaque Neovascularization Detected by Using Contrast-enhanced US with Clinical Symptoms," *Radiology,* vol. 251, pp. 583-589, May 2009.

[18] Z. Akkus, A. Hoogi, G. Renaud, S. C. H. van den Oord, G. L. ten Kate, A. F. L. Schinkel, D. Adam, N. de Jong, A. F. W. van der Steen, and J. G. Bosch, "New Quantification Methods for Carotid Intra-plaque Neovascularization Using Contrast-Enhanced Ultrasound," *Ultrasound in Medicine & Biology,* vol. 40, pp. 25-36, 2014.

[19] A. Hoogi, D. Adam, A. Hoffman, H. Kerner, S. Reisner, and D. Gaitini, "Carotid Plaque Vulnerability: Quantification of Neovascularization on Contrast-Enhanced Ultrasound With Histopathologic Correlation," *American Journal of Roentgenology,* vol. 196, pp. 431-436, 2011.

[20] F. Molinari, W. Liboni, E. Pavanelli, P. Giustetto, S. Badalamenti, and J. S. Suri, "Accurate and automatic carotid plaque characterization in contrast enhanced 2-D ultrasound images," in *Engineering in Medicine and Biology Society, 2007. EMBS 2007. 29th Annual International Conference of the IEEE*, ed, 2007, pp. 335-338.

[21] Z. Qi, Y. Lijing, L. Chaolun, and W. Wenping, "Contrast-enhanced ultrasound image segmentation of atherosclerotic plaques using spatial-temporal analysis and snakes," in *Systems and Informatics (ICSAI), 2012 International Conference on*, 2012, pp. 1901-1905.

[22] Q. Zhang, C. Li, H. Han, L. Yang, Y. Wang, and W. Wang, "Computer-aided quantification of contrast agent spatial distribution within atherosclerotic plaque in contrast-enhanced ultrasound image sequences," *Biomedical Signal Processing and Control,* vol. 13, pp. 50-61, 2014.

[23] Q. Liang, I. Wendelhag, J. Wikstrand, and T. Gustavsson, "A multiscale dynamic programming procedure for boundary detection in ultrasonic artery images," *Medical Imaging, IEEE Transactions on,* vol. 19, pp. 127-142, 2000.

[24] D.-C. Cheng and X. Jiang, "Detections of arterial wall in sonographic artery images using dual dynamic programming," *Information Technology in Biomedicine, IEEE Transactions on,* vol. 12, pp. 792-799, 2008.

[25] F. Destrempes, J. Meunier, M. F. Giroux, G. Soulez, and G. Cloutier, "Segmentation in Ultrasonic <emphasis emphasistype="italic">B</emphasis>-Mode Images of Healthy Carotid Arteries Using Mixtures of Nakagami Distributions and Stochastic Optimization," *Medical Imaging, IEEE Transactions on,* vol. 28, pp. 215-229, 2009.

[26] A. Teynor, S. Caviezel, J. Dratva, N. Künzli, and A. Schmidt-Trucksäss, "An Automated, Interactive Analysis System for Ultrasound Sequences of the Common Carotid Artery," *Ultrasound in Medicine & Biology,* vol. 38, pp. 1440-1450, 2012.

[27] Y. Zhou, X. Cheng, X. Xu, and E. Song, "Dynamic programming in parallel boundary detection with application to ultrasound intima-media segmentation," *Medical Image Analysis,* vol. 17, pp. 892-906, 2013.

[28] F. Molinari, G. Zeng, and J. S. Suri, "An Integrated Approach to Computer-Based Automated Tracing and Its Validation for 200 Common Carotid Arterial Wall Ultrasound Images: A New Technique," *Journal of Ultrasound in Medicine,* vol. 29, pp. 399-418, March 1, 2010 2010.

[29] R. Rocha, J. Silva, and A. Campilho, "Automatic detection of the carotid lumen axis in B-mode ultrasound images," *Computer Methods and Programs in Biomedicine*.

[30] D. D. Carvalho, Z. Akkus, J. G. Bosch, S. C. van den Oord, W. J. Niessen, and S. Klein, "Nonrigid motion compensation in B-mode and contrast enhanced ultrasound image sequences of the carotid artery," in *SPIE Medical Imaging*, ed, 2014, pp. 90340N-90340N.

[31] K. L. Chan, "2 APPROACHES TO MOTION ANALYSIS OF THE ULTRASOUND IMAGE SEQUENCE OF CAROTID ATHEROMATOUS PLAQUE," *Ultrasonics,* vol. 31, pp. 117-123, 1993 1993.

[32] S. Golemati, A. Sassano, M. J. Lever, A. A. Bharath, S. Dhanjil, and A. N. Nicolaides, "Carotid artery wall motion estimated from B-mode ultrasound using region tracking and block matching," *Ultrasound in Medicine and Biology,* vol. 29, pp. 387-399, 2003 2003.

[33] Z. Akkus, "Dynamic assessment of carotid plaque motion " *Ultrasound,* vol. 18, pp. 140-147, 2010 2010.

[34] Z. Akkus, A. Hoogi, G. Renaud, G. L. ten Kate, S. C. H. van den Oord, A. F. L. Schinkel, N. de Jong, A. F. W. van der Steen, and J. G. Bosch, "Motion Compensation Method using Dynamic Programming for Quantification of Neovascularization in Carotid Atherosclerotic Plaques with Contrast Enhanced Ultrasound (CEUS)," *Medical Imaging 2012: Ultrasonic Imaging, Tomography, and Therapy,* vol. 8320, 2012.

[35] S. Klein, J. W. Pluim, M. Staring, and M. Viergever, "Adaptive Stochastic Gradient Descent Optimisation for Image Registration," *International Journal of Computer Vision,* vol. 81, pp. 227-239, 2009/03/01 2009.

[36] Z. Akkus, D. D. Carvalho, S. Klein, S. C. van den Oord, A. F. Schinkel, N. de Jong, A. F. van der Steen, and J. G. Bosch, "Atherosclerotic carotid lumen segmentation in combined B-mode and contrast enhanced ultrasound images," in Proc. *SPIE Medical Imaging*, 2014, pp. 903445-903445.

[37] P. J. Touboul, M. G. Hennerici, S. Meairs, H. Adams, P. Amarenco, N. Bornstein, L. Csiba, M. Desvarieux, S. Ebrahim, M. Fatar, R. Hernandez Hernandez, M. Jaff, S. Kownator, P. Prati, T. Rundek, M. Sitzer, U. Schminke, J. C. Tardif, A. Taylor, E. Vicaut, K. S. Woo, F. Zannad, and M. Zureik, "Mannheim Carotid Intima-Media Thickness Consensus (2004–2006)," *Cerebrovascular Diseases,* vol. 23, pp. 75-80, 2007.

[38] S. T. Nevo, M. Van Stralen, A. M. Vossepoel, J. H. C. Reiber, N. de Jong, A. F. W. van der Steen, and J. G. Bosch, "Automated tracking of the mitral valve annulus motion in apical echocardiographic images using multidimensional dynamic programming," *Ultrasound in Medicine and Biology,* vol. 33, pp. 1389-1399, Sep 2007.

[39] M. R. Skilton, L. Boussel, F. Bonnet, S. Bernard, P. C. Douek, P. Moulin, and A. Serusclat, "Carotid intima-media and adventitial thickening: comparison of new and established ultrasound and magnetic resonance imaging techniques," *Atherosclerosis,* vol. 215, pp. 405-10, 2011.

[40] D. H. O'Leary and M. L. Bots, "Imaging of atherosclerosis: carotid intima–media thickness," *European Heart Journal,* June 11, 2010 2010.

[41] J. H. Stein, C. E. Korcarz, R. T. Hurst, E. Lonn, C. B. Kendall, E. R. Mohler, S. S. Najjar, C. M. Rembold, and W. S. Post, "Use of Carotid Ultrasound to Identify Subclinical Vascular Disease and Evaluate Cardiovascular Disease Risk: A Consensus Statement from the American Society of Echocardiography Carotid Intima-Media Thickness Task Force Endorsed by the Society for Vascular Medicine," *Journal of the American Society of Echocardiography,* vol. 21, pp. 93-111, 2008.

Chapter 9

Assessment of Subclinical Atherosclerosis and Intraplaque Neovascularization using Quantitative Contrast-Enhanced Ultrasound in Patients with Familial Hypercholesterolemia

Objective Patients with heterozygous familial hypercholesterolemia (FH) are at severely increased risk of developing atherosclerosis at relatively young age. The aim of this study was to assess the prevalence of subclinical atherosclerosis and intraplaque neovascularization (IPN) in patients with FH, using contrast-enhanced ultrasound (CEUS) of the carotid arteries.
Methods The study population consisted of 69 consecutive asymptomatic patients with FH (48% women, mean age 55 ± 8 years). All patients underwent carotid ultrasound to evaluate the presence and severity of carotid atherosclerosis, and CEUS to assess IPN. IPN was assessed in near wall plaques using a semi-quantitative grading scale and semi-automated quantification software.
Results Carotid plaque was present in 62 patients (90%). A total of 49 patients had plaques that were eligible for the assessment of IPN: 7 patients (14%) had no IPN, 39 (80%) had mild to moderate IPN and 3 (6%) had severe IPN. Semi-automated quantification software showed no statistical significant difference in the amount of IPN between patients >50 years and patients ≤50 years and between patients with a defective low-density lipoprotein receptor (LDLR) mutation and patients with a negative LDLR mutation. Plaques with irregular or ulcerated surface had significantly more IPN than plaques with a smooth surface ($p<0.05$).
Conclusion Carotid ultrasound demonstrated atherosclerotic plaque in 90% of asymptomatic patients with FH without known atherosclerosis. IPN assessed with CEUS, was present in 86% of these patients. Irregular and ulcerated plaques exhibited significantly more IPN than plaques with a smooth surface.

S. C.H. van den Oord, Z. Akkus, G. Renaud, E. J.G. Sijbrands, F. J. ten Cate, A. van der Lugt, J. G. Bosch, N. de Jong, A. F.W. van der Steen, A. F.L. Schinkel. **Assessment of Subclinical Atherosclerosis and Intraplaque Neovascularization using Quantitative Contrast-Enhanced Ultrasound in Patients with Familial Hypercholesterolemia Atherosclerosis.** Atherosclerosis, 231(1):107-13, 2013

INTRODUCTION

Heterozygous familial hypercholesterolemia (FH) is the most prevalent autosomal dominant inherited disorder of the lipoprotein metabolism, resulting in increased LDL cholesterol levels. Patients with FH are at severely increased risk of developing atherosclerosis at relatively young age. The introduction of statin treatment has partly reduced the risk of myocardial infarction and stroke in patients with FH [1–4]. Still, patients with FH receiving long term statin treatment may have a substantial amount of subclinical atherosclerosis [5]. There is a large variation in the extent and severity of atherosclerotic disease, and therefore presymptomatic evaluation of atherosclerosis may be especially useful in patients with FH.

Carotid ultrasound is a widely available, low-cost and free from ionizing radiation imaging modality for the evaluation of (subclinical) atherosclerosis. Previous studies have demonstrated that ultrasound assessment of carotid intima-media thickness and plaque provides valuable information for monitoring the response to treatment and for risk-stratification in patients with FH [6,7]. Contrast-enhanced ultrasound (CEUS) is an advanced form of ultrasound imaging using a microbubble contrast agent to provide improved detection of plaques and can be used to visualize intraplaque neovascularization (IPN) [8–10]. Recent data indicate that IPN is a marker of plaque instability. A recent pathology study of unstable carotid lesions demonstrated that IPN and intraplaque haemorrhage are predictors of rupture of atherosclerotic plaques [11]. This confirms the suggestion that these histological characteristics are considered to be components of the vulnerable atherosclerotic plaque [12]. Information on IPN in patients with FH is at present not available, but may be relevant for a better understanding of the pathophysiology of atherosclerosis, development of new treatment approaches, and risk stratification. The aim of this study was therefore to assess the prevalence of subclinical atherosclerosis and IPN in a consecutive group of patients with FH. Carotid ultrasound was used to evaluate the presence and severity of carotid atherosclerosis, and CEUS was used to assess IPN.

METHODS

Patient population and study protocol

The study population consisted of 69 asymptomatic patients with heterozygous FH. Inclusion criteria were: heterozygous FH, and age ≥18 years. Exclusion criteria were: known atherosclerosis, contra-indications for the use of ultrasound contrast agent, such as unstable angina, acute cardiac failure, acute endocarditis, known right-to-left shunts and known allergy to microbubble contrast agents. FH was diagnosed according to the criteria of van Aalst-Cohen [13], which can be summarized as either the presence of a documented LDL-receptor mutation, or an LDL-cholesterol level above the 95th percentile for gender and age in combination with the presence of typical tendon xanthomas in the patient or in a first degree relative, or an LDL-cholesterol level above the 95th percentile for gender and age in a first degree relative or proven coronary artery disease in the patient or in a first degree relative under the age of 60. Genetic screening for the presence of

mutations in the low-density lipoprotein receptor (LDLR) gene, apolipoprotein B (APOB) gene and proprotein convertase subtilisin/kexin gene was routinely performed for all patients. Carotid ultrasound and CEUS were performed to investigate the prevalence of subclinical atherosclerosis and the density of IPN. The study protocol was approved by the local ethical committee and all patients provided informed consent. A single carotid ultrasound and CEUS examination takes approximately 30 minutes.

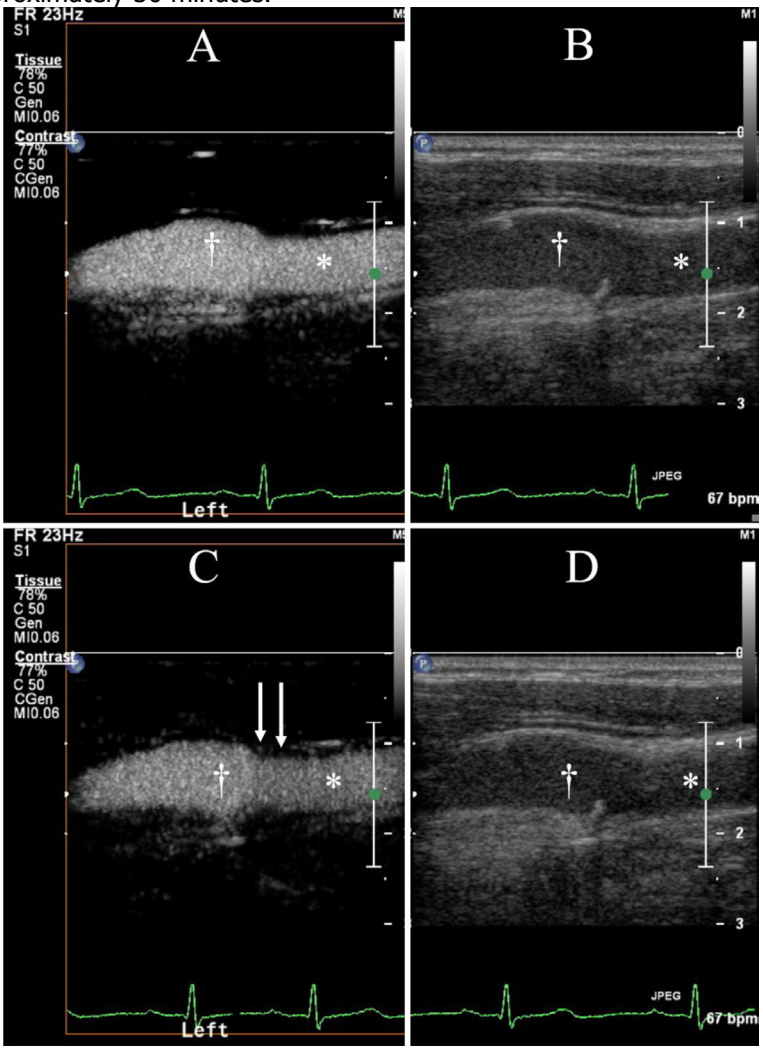

Figure 1: Example of side-by-side contrast enhanced ultrasound (CEUS) examination. * = common carotid artery, † = carotid bulb. Panel A: CEUS clip of the left carotid artery shortly after contrast injection. Panel B: corresponding B-mode clip of the left carotid artery recorded simultaneously with the CEUS clip. Panel C: A CEUS clip of the same carotid artery recorded a few seconds following contrast administration. The arrows indicate contrast-enhancement in a small atherosclerotic plaque in the carotid bulb. Panel D: corresponding B-mode clip of the left carotid artery recorded simultaneously with the CEUS clip.

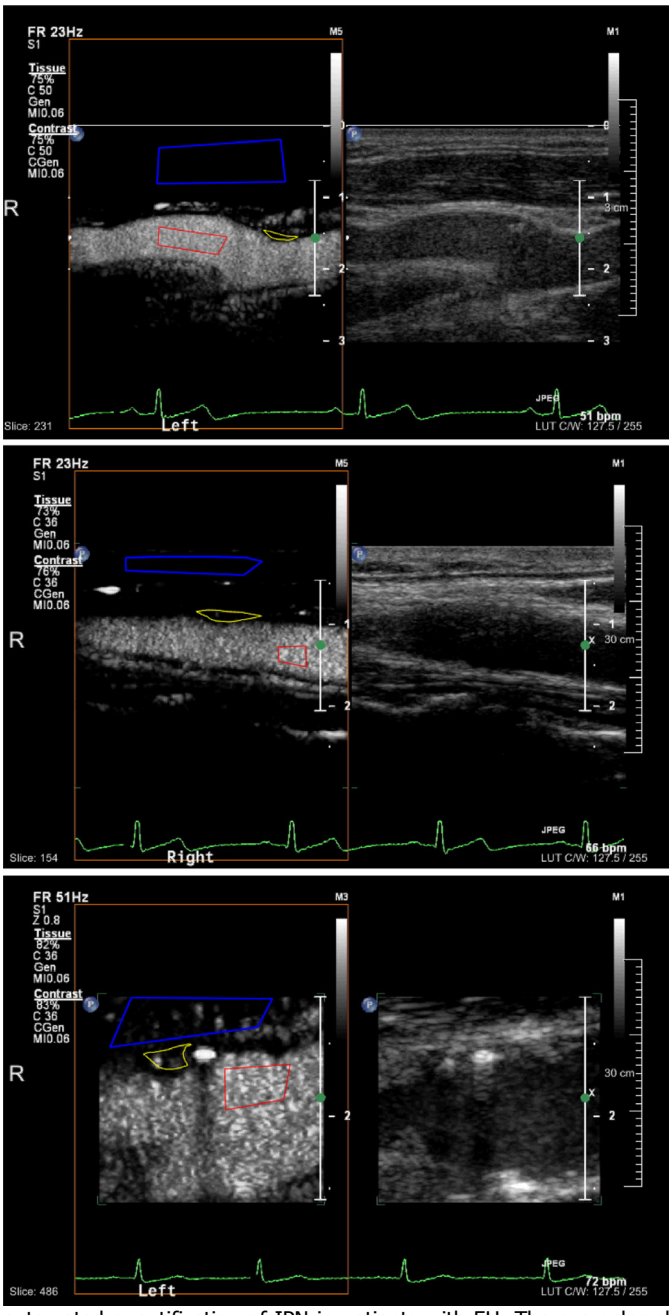

Figure 2: Semi-automated quantification of IPN in patients with FH. The examples shown are from 3 different patients with FH. Side-by-side contrast-enhanced ultrasound clips were used to quantify the amount of contrast enhancement in the atherosclerotic plaques. Yellow regions of interest: atherosclerotic plaque. Red regions of interest: lumen, used to adjust for lumen intensity. Blue regions of interest: background, used to adjust for background intensity. Supplemental files A-C contain movie files of these examples.

Carotid ultrasound acquisition

Carotid ultrasound including color Doppler, and CEUS were performed with a Philips iU-22 ultrasound system (Philips Medical Systems, Bothell, USA), equipped with a L9-3 transducer. For standard carotid ultrasound a frequency of 7 MHz was used. Image acquisition was performed using a scanning protocol according to the American Society of Echocardiography consensus [14]. In short, both left and right carotid arteries were examined with the patient in a supine position with the head turned at a 45° angle to the contralateral side. The left and the right common carotid artery (CCA), carotid bifurcation (BIF), internal carotid artery (ICA), external carotid artery (ECA), and vertebral arteries were imaged with B-mode ultrasound, color Doppler and pulse-wave Doppler. All anatomical sites were examined from different angles of view. Gain and imaging depth were adjusted per patient to obtain optimal ultrasound images. Each side was extensively evaluated for the presence of plaques.

CEUS was performed using intravenous administration of SonoVue™ contrast agent (Bracco S.p.A., Milan, Italy). For CEUS a frequency of 3.5 MHz was used. The contrast mode of the ultrasound system, using amplitude modulation, a minimum frame-rate of 13/second and a mechanical index of 0.06, was used to optimize the CEUS examination. CEUS clips were recorded with a dual display mode for simultaneous B-mode ultrasound and CEUS view. The ultrasound contrast agent was injected in boluses of 0.5 ml. Each contrast agent bolus was followed by a saline flush using 2.0 ml NaCl 0.9% solution. Bolus injections were repeated when necessary to a maximum dose of 9.6 ml, depending on the number of CEUS cineclips that were required for complete imaging of the carotid arteries. Both carotid arteries were examined, focusing on the presence of plaques. If plaques were present, the plaque was visualized in the longitudinal axis of the carotid artery. The longitudinal image plane with visually the largest plaque area was used to record cineclips. Still frames and cineclips with a maximum of 20 seconds were digitally stored.

Carotid ultrasound analysis

Carotid ultrasound studies were reviewed offline. Carotid plaque screening was performed using the standard carotid ultrasound images, color Doppler, and CEUS. Atherosclerotic plaque was defined as a focal structure encroaching into the lumen by at least 0.5 mm or 50% of the surrounding carotid intima-media thickness, or demonstrates a thickness >1.5 mm as measured from the media-adventitia interface to the intima-lumen interface [15]. The presence of plaque and maximum plaque thickness was recorded for each carotid segment. All analyses were performed at the near wall of the carotid artery. For intima-media thickness measurements this will give less reproducible results [16] but since the plaque thickness as defined above is at minimum the double of the resolution of the ultrasound this will not be the case for the current plaque measurements. Maximum plaque thickness was measured perpendicular to the longitudinal axis of the carotid artery. The carotid segments were defined as CCA, BIF, ICA and ECA. Additionally for each segment with signs of atherosclerosis the presence of

calcification, wall irregularities and/or ulceration were recorded. Plaque ulceration was defined as a disruption in the plaque-lumen border ≥1×1mm.

IPN was assessed using CEUS clips. To minimize the contribution of pseudo-enhancement to the assessment of IPN, only near wall plaques were used. Clips without atherosclerotic plaques or with plaques that could have been affected by pseudo-enhancement were not eligible for the assessment of IPN. Pseudo-enhancement is an artifact that is mainly seen in the far-wall of the carotid artery and mimicks contrast-enhancement which may lead to overestimation of IPN [17,18]. In general that means that plaques below contrast pools (e.g. the carotid lumen or jugular lumen) were excluded from assessment of IPN. The amount of IPN was assessed using a semi-quantitative grading scale and semi-automated quantification software. For each carotid artery with ≥1 atherosclerotic plaque on the near wall of the carotid artery, the clip with visually the highest amount of contrast enhancement was selected for analysis (Figure 1). In patients with bilateral plaques, the thicker plaque was selected for patient based analysis. Visual assessment of IPN was performed using a 3 point grading scale as 0= no IPN, 1= mild to moderate IPN and 2= severe IPN. Semi-automated quantification of IPN was performed using dedicated software (Figure 2 and supplemental files A & B). The software was based on a simple and user-friendly user interface created using MevisLab (MeVis Medical Solutions AG and Fraunhofer MEVIS, Bremen, Germany). DICOM files of side-by-side B-Mode and contrast mode ultrasound clips were imported in the software to assess different plaque perfusion features after selection of the time-frame. Several plaque perfusion features were calculated after motion compensation of regions of interest. The calculations were based on maximum intensity projection images and time intensity curves. Features that were calculated included IPN surface area in mm^2 (IPN-SA), IPN surface area ratio in % (IPN-SA ratio), mean percentage of the plaque filled with contrast over time (MPCP), the plaque mean intensity (PMI), and plaque area. Details of the quantification features have been described previously [19].

Statistical analysis

Statistical analysis was performed using SPSS 20.0 for Windows (SPSS, Chicago, USA). Continuous variables are presented as mean (SD) or median [Inter-quartile range]. Categorical variables are expressed as number (percentage). Mann-Whitney U test was performed to compare the output of the semi-automated software in selected patient groups. Spearman's rank correlation coefficients were calculated to test for correlations between IPN features and continuous variables. A p value <0.05 was considered to indicate a statistically significant difference.

RESULTS

Patient characteristics

The clinical characteristics of the study population are summarized in Table 1. Sixty-six patients (96%) received statin treatment for a mean duration of 11 ± 8 years. Due to side effects of the statin medication, 28 patients (41%) did not receive a maximum dose or no statin at all. In 63 patients (91%) results of the

genetic screening for the presence of mutations in the LDLR gene were available. A total of 27 patients (39%) had LDLR-negative mutations. A total of 19 patients (28%) had LDLR-defective or APOB mutations which in general lead to a milder phenotype (Table 2). The remaining 17 patients (25%) had unidentified mutations.

Table 1: Patient characteristics (n=69)

Male gender	36 (52%)
Age, years	55 ± 8
Current or former smoker	30 (43%)
Hypertension	11 (16%)
Diabetes mellitus	2 (3%)
Body mass index (kg/m2)	26 ± 4
Identified genetic mutation causing FH	46 (67%)
Tendon xanthomas	18 (26%)
Arcus cornealis	19 (28%)
Highest total cholesterol without therapy, mmol/L	8.6± 2.1
Current total cholesterol, mmol/L	5.6 ± 1.9
LDL, mmol/L	3.7 ± 1.7
HDL, mmol/L	1.5 ± 0.4
Triglycerides, mmol/L	1.3 ± 0.7
Statin use	66 (96%)
Ezetimibe use	38 (57%)
Age of first statin use, years	44 ± 10
Duration of statin use, years	11 ± 8

Data are presented as number of patients (percentage) or as mean ± standard deviation.

Carotid ultrasound results

Using the standard ultrasound clips, carotid plaque was detected in 157 of 552 carotid segments (28%). The mean plaque thickness was 2.4 ± 0.8mm. A total of 96 carotid segments (61%) with plaque exhibited signs of calcification. An irregular plaque surface was present in 46 carotid segments with plaque (29%). Fourteen of the carotid segments with atherosclerotic plaques (9%) had an ulcerated plaque surface. In 89 carotid arteries (64%) ≥1 atherosclerotic plaque was detected.

CEUS results

A total of 68 carotid arteries (49%) were eligible for the assessment of IPN. The remaining 70 carotid arteries (51%) had plaques that were affected by the pseudo-enhancement artifact (n=19, 14%) or had no atherosclerotic plaque (n=51, 37%). Visual assessment showed no IPN in 7 carotid arteries (10%), mild to moderate IPN in 58 carotid arteries (85%) and severe IPN in 3 carotid arteries (4%).The output of the semi-automated IPN quantification software is summarized in Table 2. The median number of frames used for IPN quantification was 255 (IQR=148). The selected time-frames had a median duration of 11 seconds (IQR=7). Plaques with an irregular or ulcerated surface (n=18, 27%) had a

significantly higher visual IPN score ($p<0.05$) and had significantly more IPN as assessed by semi-automated quantitative software ($p<0.05$) (Figure 3).

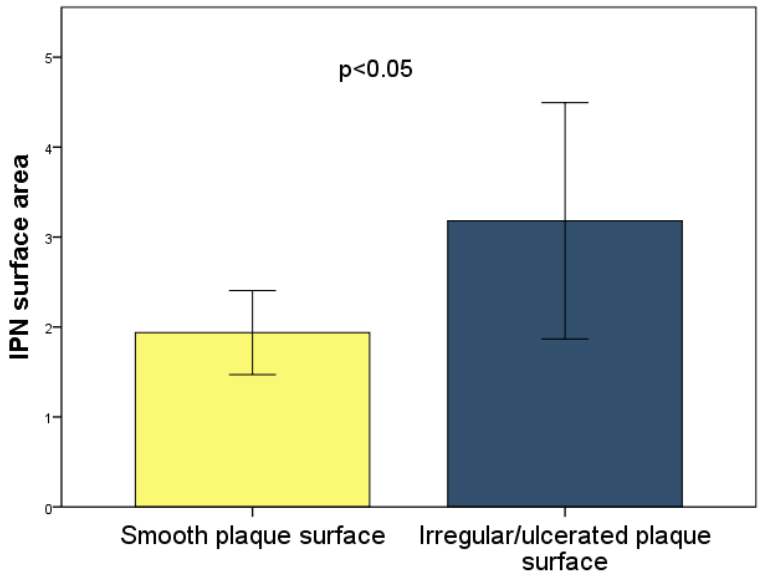

Figure 3: IPN in plaques with a smooth surface compared to plaques with an irregular/ulcerated surface. Semi-automated quantification software calculated the surface area enhanced during CEUS examinations. Plaques with an irregular or ulcerated surface had significantly more IPN than plaques with a smooth surface ($p<0.05$).

Table 2: Quantitative assessment of intraplaque neovascularization (n=68 carotid arteries)

IPN features	Median	IQR	Range
IPN -SA (mm^2)	1.9	2.1	11.1
IPN -SA ratio (%)	48	55	98
MPCP (%)	26	40	97
PMI	3.0	4.9	20.0
Plaque area (mm^2)	4.0	3.9	29.1

IPN-SA = Intraplaque neovascularization surface area, IQR = Inter quartile range, MPCP = Percentage of the plaque filled with contrast over time, PMI = Plaque mean intensity.

Patient-based carotid ultrasound and CEUS results

A total of 62 patients (90%) exhibited carotid atherosclerotic plaque. In these patients the median number of carotid segments involved was 2 (IQR: 1-4). In 49 patients (71%) the plaques were eligible for the assessment of IPN. Of these, a total of 19 patients (39%) had bilateral plaques, 30 patients (61%) had unilateral plaques. Visual assessment showed no IPN in 7 patients (14%), mild to moderate IPN in 39 patients (80%) and severe IPN in 3 patients (6%).The quantitative evaluation of IPN is summarized in Table 3. No statistically significant differences in

the amount of IPN were detected between patients aged ≤50 years and patients aged >50 years (p=0.072). In addition, correlations between IPN features and patients age were not statistically significant (p>0.14). Comparison of the amount of IPN between patients with and without LDLR rest function (i.e. the residual capacity of the genetically mutated LDLR to bind LDL) showed no statistically significant difference between the groups. The current total cholesterol levels and the highest total cholesterol level without medical therapy showed no statistically significant correlations with the IPN features (p>0.5)

Table 3 : Quantitative assessment of intraplaque neovascularization (n=49 patients)

IPN features	Median	IQR	Range
IPN -SA (mm^2)	2.0	2.3	11.1
IPN -SA ratio (%)	45	57	98
MPCP (%)	22	41	97
PMI	2.6	5.0	20.0
Plaque area (mm^2)	4.3	4.1	29.2

IPN-SA = Intraplaque neovascularization surface area, IQR = Inter quartile range, MPCP = Percentage of the plaque filled with contrast over time, PMI = Plaque mean intensity.

DISCUSSION

In the present study the prevalence of subclinical atherosclerosis and IPN was assessed using standard ultrasound and CEUS in a consecutive group of patients with FH. All patients were asymptomatic and had no known atherosclerosis. Carotid plaque was present in 90% of these patients despite the entire study population receiving long-term statin treatment. The majority of the patients (86%) had ≥1 plaques with IPN. Semi-automated quantification software was used to precisely assess the amount of contrast-enhancement in the plaques. Atherosclerotic plaques with an irregular or ulcerated surface had significantly more IPN than plaques with a smooth surface (p<0.05).

Limited data is available on the prevalence of carotid atherosclerosis in asymptomatic patients with FH and information on IPN in these patients is currently lacking. It has become clear that IPN is a marker of the instable or vulnerable atherosclerotic plaque [11,20]. The intraplaque neovessels are probably formed to meet the increased metabolic demands of the developing atherosclerotic plaque. However, due to their poor structural integrity the intraplaque neovessels may serve a pathologic role [21]. These microvessels are immature thin-walled vessels that may leak lipids, glucose and red blood cells which attracts macrophages and may lead to progression into a more advanced plaque type [22]. Plaques with a high IPN density are consequently at an increased risk of intraplaque hemorrhage and plaque rupture which may lead to cerebrovascular events [23]. Information on IPN may be particularly relevant in patients with FH, for a better understanding of the pathophysiology and progression of atherosclerosis, development of new treatment approaches, and risk stratification.

Previous studies have reported on the prevalence of plaque and IPN in patients without FH. Staub et al. [24] used CEUS to study the prevalence of IPN in 159 patients (61% men, age 64 ± 11 years) who underwent carotid ultrasound for a

clinical indication. Established cardiovascular disease was documented in 61% of the patients. Standard ultrasound and CEUS demonstrated ≥1 plaques in 111 (76%) patients; the maximum plaque thickness was 2.8 ± 0.8 mm. CEUS demonstrated IPN in 54% of the patients. Patients with IPN more frequently had a history of cardiovascular disease as compared to patients without IPN [24]. Xiong et al. [25] studied IPN with CEUS in 104 patients (80% men, age 64 ± 9 years) who underwent carotid ultrasound for a clinical indication and had ≥1 plaque thicker than 2.0 mm. A relatively large proportion (34%) of the patients were symptomatic (i.e. had a previous transient ischemic attack and/or stroke). Per inclusion criterion, all patients had a carotid plaque. IPN was present in 80% of the symptomatic patients, and in 30% of the asymptomatic patients. The authors concluded that symptomatic patients had more intense contrast enhancement in the plaque than asymptomatic patients suggesting that CEUS may be used for plaque risk stratification [25].

In comparison to these 2 previous studies, the present study included asymptomatic patients with heterozygous FH, without known atherosclerosis. The patients had no clinical indication for carotid ultrasound, and were asked to participate in this research project. The current study included a higher proportion of women (48%) than in the previous studies [24,25]. Additionally, the mean age of our patients was substantially lower (55 ± 8 years), and nearly all patients received statin therapy (96%). Despite this, the mean plaque thickness was comparable with the previously reported findings. The patients with FH more frequently exhibited IPN as compared with the 2 previous reports. This finding suggests that patients with FH exhibit more vascularized atheroslerotic plaques, which may be of the vulnerable plaque type. This is supported by the fact that irregular and ulcerated plaques exhibited more IPN. In this study dedicated quantification software was used to accurately assess the amount of IPN. Previously, Xiong et al. [25] used a semi-automated quantitative scoring system for IPN, but that method lacked a motion compensation tool to adjust for pulsatility of the carotid artery and motion due to breathing of the patient [25]. The semi-automated quantification software used in this study was equiped with motion compensation tools and provided multiple features on contrast-enhancement of the atherosclerotic plaques. This allows a more accurate evaluation of IPN, and may be used to monitor changes in IPN density over time or following treatment.

The current findings are in accordance with clinical observations that patients with FH are at severely increased risk of developing symptomatic atherosclerosis at relatively young age. Statin treatment significantly reduces morbidity and mortality in these patients. The benificial effect of statin therapy is perhaps not only caused by the inhibition of cholesterol synthesis in the liver, but may also have a stabilizing effect on atherosclerotic plaques. In animal models of atherosclerosis, statin treatment has been shown to inhibit IPN [26]: 14 pigs were randomized to a normal diet (n=5), a high cholesterol (HC) diet (n= 5) or a HC diet with simvastatin (n=4). After 12 weeks, the animals were sacrificed and micro-CT demonstrated an increased density of vasa vasorum in coronary specimens of animals on a HC diet whereas animals on a HC diet and statin therapy had a lower

density of vasa-vasorum. A recent study in 28 patients (82% male, mean age 55 ± 6 years) with coronary and/or carotid atherosclerosis has reported a similar effect of statin treatment [27]. Dynamic contrast-enhanced magnetic resonance imaging of the carotid arteries demonstrated a significant reduction of adventitial vasa vasorum signal after one year of statin treatment. Efforts to develop novel treatment strategies to reduce progression of atherosclerosis and inhibit IPN may have substantial clinical benefits.

This study has limitations. First, the study population was relatively small. Further studies are needed to confirm the findings in larger populations. Second, no age and gender matched control subjects were available to compare the amount of IPN between patients with FH and patients without FH. Future studies should aim to investigate whether there are difference in the amount of IPN in patients with FH and patients without FH. Third, in the comparison between age groups, the cut-off value of 50 year was chosen arbitrary without scientific arguments. A different cut-off value to divide the patients in age groups could possibly lead to different results. Fourth, prospective follow-up studies are needed to evaluate the prognostic implications of carotid plaque and carotid IPN in patients with FH. Finally, this study did not investigate the prevalence and density of adventitial microvascularization. Future studies should aim to investigate this topic in patients with FH.

CONCLUSION

Carotid ultrasound demonstrated atherosclerotic plaque in 90% of asymptomatic patients with FH without known atherosclerosis. IPN assessed with CEUS, was present in 86% of these patients. Irregular and ulcerated plaques exhibited significantly more IPN than plaques with a smooth surface.

FUNDING SOURCES

This research was supported by the Center for Translational Molecular Medicine and the Netherlands Heart Foundation (PARISk).

ABBREVIATIONS

CEUS	Contrast-enhanced ultrasound
CIMT	Carotid intima-media thickness
FH	Familial hypercholesterolemia
IPN	Intraplaque neovascularization

REFERENCES

1. Mortality in treated heterozygous familial hypercholesterolaemia: implications for clinical management. Scientific Steering Committee on behalf of the Simon Broome Register Group. *Atherosclerosis*. 1999;142:105–112.
2. Versmissen J, Oosterveer DM, Yazdanpanah M, Defesche JC, Basart DC, Liem AH, Heeringa J, Witteman JC, Lansberg PJ, Kastelein JJ, Sijbrands EJ. Efficacy of statins in familial hypercholesterolaemia: a long term cohort study. *BMJ*. 2008;337:a2423.
3. Huxley RR, Hawkins MH, Humphries SE, Karpe F, Neil HA. Risk of fatal stroke in patients with treated familial hypercholesterolemia: a prospective registry study. *Stroke*. 2003;34:22–25.
4. Soljanlahti S, Autti T, Lauerma K, Raininko R, Keto P, Turtola H, Vuorio AF. Familial hypercholesterolemia patients treated with statins at no increased risk for intracranial vascular lesions despite increased cholesterol burden and extracranial atherosclerosis. *Stroke*. 2005;36:1572–1574.
5. Neefjes LA, Ten Kate GJ, Rossi A, Galema-Boers AJ, Langendonk JG, Weustink AC, Moelker A, Nieman K, Mollet NR, Krestin GP, Sijbrands EJ, de Feyter PJ. CT coronary plaque burden in asymptomatic patients with familial hypercholesterolaemia. *Heart*. 2011;97:1151–1157.
6. Kastelein JJ, Akdim F, Stroes ES, Zwinderman AH, Bots ML, Stalenhoef AFH, Visseren FL, Sijbrands EJ, Trip MD, Stein EA, Gaudet D, Duivenvoorden R, Veltri EP, Marais AD, de Groot E. Simvastatin with or without ezetimibe in familial hypercholesterolemia. *N Engl J Med.* 2008;358:1431–1443.
7. Caballero P, Alonso R, Rosado P, Mata N, Fernández-Friera L, Jiménez-Borreguero LJ, Badimon L, Mata P. Detection of subclinical atherosclerosis in familial hypercholesterolemia using non-invasive imaging modalities. *Atherosclerosis*. 2012;222:468–472.
8. Feinstein SB. Contrast ultrasound imaging of the carotid artery vasa vasorum and atherosclerotic plaque neovascularization. *J Am Coll Cardiol*. 2006;48:236–243.
9. Staub D, Schinkel AF, Coll B, Coli S, van der Steen AF, Reed JD, Krueger C, Thomenius KE, Adam D, Sijbrands EJ, ten Cate FJ, Feinstein SB. Contrast-enhanced ultrasound imaging of the vasa vasorum: from early atherosclerosis to the identification of unstable plaques. *JACC Cardiovasc Imaging*. 2010;3:761–771.
10. Ten Kate GL, van den Oord SC, Sijbrands EJ, van der Lugt A, de Jong N, Bosch JG, van der Steen AF, Schinkel AF. Current status and future developments of contrast-enhanced ultrasound of carotid atherosclerosis. *J Vasc Surg.* 2013;57:539–546.
11. Hellings WE, Peeters W, Moll FL, Piers SR, van Setten J, Van der Spek PJ, de Vries JP, Seldenrijk KA, De Bruin PC, Vink A, Velema E, de Kleijn DP, Pasterkamp G. Composition of carotid atherosclerotic plaque is associated with cardiovascular outcome: a prognostic study. *Circulation*. 2010;121:1941–1950.
12. Schaar JA, Muller JE, Falk E, Virmani R, Fuster V, Serruys PW, Colombo A, Stefanadis C, Ward Casscells S, Moreno PR, Maseri A, van der Steen AF. Terminology for high-risk and vulnerable coronary artery plaques. Report of a meeting on the vulnerable plaque, June 17 and 18, 2003, Santorini, Greece. *Eur Heart J*. 2004;25:1077–1082.
13. Van Aalst-Cohen ES, Jansen AC, Tanck MW, Defesche JC, Trip MD, Lansberg PJ, Stalenhoef AF, Kastelein JJ. Diagnosing familial hypercholesterolaemia: the relevance of genetic testing. *Eur Heart J.* 2006;27:2240–2246.
14. Stein JH, Korcarz CE, Hurst RT, Lonn E, Kendall CB, Mohler ER, Najjar SS, Rembold CM, Post WS. Use of carotid ultrasound to identify subclinical vascular disease and evaluate cardiovascular disease risk: a consensus statement from the American Society of Echocardiography Carotid Intima-Media Thickness Task Force. Endorsed by the Society for Vascular Medicine. *J Am Soc Echocardiogr*. 2008;21:93–111; quiz 189–190.
15. Touboul PJ, Hennerici MG, Meairs S, Adams H, Amarenco P, Bornstein N, Csiba L, Desvarieux M, Ebrahim S, Hernandez Hernandez R, Jaff M, Kownator S, Naqvi T, Prati P, Rundek T, Sitzer M, Schminke U, Tardif JC, Taylor A, Vicaut E, Woo KS. Mannheim carotid intima-media thickness and plaque consensus (2004-2006-2011). An update on behalf of the advisory board of the 3rd, 4th and 5th watching the risk symposia, at the 13th, 15th and 20th European stroke conferences, mannheim, Germany, 2004, brussels, belgium, 2006, and hamburg, Germany, 2011. *Cerebrovasc Dis.* 2012;34:290–296.

16. Montauban van Swijndregt AD, The SH, Gussenhoven EJ, Lancée CT, Rijsterborgh H, de Groot E, van der Steen AF, Bom N, Ackerstaff RG. An in vitro evaluation of the line pattern of the near and far walls of carotid arteries using B-mode ultrasound. *Ultrasound Med Biol*. 1996;22:1007–1015.
17. Ten Kate GL, Renaud GG, Akkus Z, van den Oord SC, ten Cate FJ, Shamdasani V, Entrekin RR, Sijbrands EJ, de Jong N, Bosch JG, Schinkel AF, van der Steen AFW. Far-wall pseudoenhancement during contrast-enhanced ultrasound of the carotid arteries: clinical description and in vitro reproduction. *Ultrasound Med Biol*. 2012;38:593–600.
18. Thapar A, Shalhoub J, Averkiou M, Mannaris C, Davies AH, Leen EL. Dose-dependent artifact in the far wall of the carotid artery at dynamic contrast-enhanced US. *Radiology*. 2012;262:672–679.
19. Akkus Z, Vegas Sanchez Ferrero G, Renaud G, van den Oord SCH, Schinkel AF, de Jong N, et al. New Quantification Methods for Carotid Intraplaque Neovascularization in Contrast Enhanced Ultrasound. Proc IEEE Ultrasonics Symposium 2013 2013;In Press.
20. Ten Kate GL, Sijbrands EJ, Staub D, Coll B, ten Cate FJ, Feinstein SB, Schinkel AF. Noninvasive imaging of the vulnerable atherosclerotic plaque. *Curr Probl Cardiol*. 2010;35:556–591.
21. Moreno PR, Purushothaman M, Purushothaman KR. Plaque neovascularization: defense mechanisms, betrayal, or a war in progress. *Ann N Y Acad Sci*. 2012;1254:7–17.
22. Dunmore BJ, McCarthy MJ, Naylor AR, Brindle NP. Carotid plaque instability and ischemic symptoms are linked to immaturity of microvessels within plaques. *J Vasc Surg*. 2007;45:155–159.
23. Virmani R, Kolodgie FD, Burke AP, Finn AV, Gold HK, Tulenko TN, Wrenn SP, Narula J. Atherosclerotic plaque progression and vulnerability to rupture: angiogenesis as a source of intraplaque hemorrhage. *Arterioscler Thromb Vasc Biol*. 2005;25:2054–2061.
24. Staub D, Patel MB, Tibrewala A, Ludden D, Johnson M, Espinosa P, et al. Vasa vasorum and plaque neovascularization on contrast-enhanced carotid ultrasound imaging correlates with cardiovascular disease and past cardiovascular events. Stroke 2010;41:41–7.
25. Xiong L, Deng YB, Zhu Y, Liu Y-N, Bi XJ. Correlation of carotid plaque neovascularization detected by using contrast-enhanced US with clinical symptoms. *Radiology*. 2009;251:583–589.
26. Wilson SH, Herrmann J, Lerman LO, Holmes DR Jr, Napoli C, Ritman EL, Lerman A. Simvastatin preserves the structure of coronary adventitial vasa vasorum in experimental hypercholesterolemia independent of lipid lowering. *Circulation*. 2002;105:415–418.
27. Dong L, Kerwin WS, Chen H, Chu B, Underhill HR, Neradilek MB, Hatsukami TS, Yuan C, Zhao XQ. Carotid artery atherosclerosis: effect of intensive lipid therapy on the vasa vasorum--evaluation by using dynamic contrast-enhanced MR imaging. *Radiology*. 2011;260:224–231.

Chapter 10

Discussion and Conclusion

10. Discussion and Conclusion

10.1 Challenges

Several histo-pathological studies have presented intraplaque neovascularization (IPN) as an important biomarker for progressive atherosclerotic disease and plaque vulnerability [1, 2]. As IPN can be detected by contrast enhanced ultrasound (CEUS), quantitative imaging biomarkers based on CEUS may allow early prediction of plaque at risk of rupture and thus prevention of future cardiovascular events such as stroke. So far, subjective and tedious visual IPN scoring on CEUS clips has been used to assess IPN, as quantification tools for IPN are scarce.

Currently available commercial tools for contrast quantification, e.g. QLAB ROI quantification tool (Philips Medical Systems, Bothell, USA) and VueBox (Bracco Suisse SA, Geneva, Switzerland), are not suitable for quantitative analysis of IPN. These commercial quantification tools have been developed mainly for time intensity curve analysis (TIC) of large organs such as heart, liver and prostate, not for plaques. Some IPN quantification approaches [3-6] have been reported but they suffer from a number of limitations. In some studies [3, 4], plaque enhancement was analyzed by use of a TIC. However, it may be questioned whether common TIC analysis as applied in large well-perfused organs is applicable to quantification of microvessels in plaques. Plaques are very small and intermittently perfused. Therefore, the perfusion characteristics of plaques are quite different from those of large organs. For these reasons, it is hard to obtain bolus kinetic parameters from TIC for plaque. Furthermore, the previously reported IPN methods used no or imperfect motion compensation. Plaques are also moving substantially due to pulsation, breathing, or patient motion. In addition, plaques are directly adjacent to the lumen and saturation artifacts can be present close by. Therefore, an accurate motion compensation of the plaque is essential for reliable IPN quantification. Especially, it is vital for TIC analysis to prevent contamination of the plaque region of interest (ROI) by contrast from the lumen and artifacts. As another limitation, the ROI for plaques needs to be delineated manually in all reported IPN methods and commercial tools. However, this is a tedious work for a physician and will cause subjectivity in IPN analysis.

Many previous studies performed TIC analysis on carotid plaques located on the far wall. However, it is not possible to reliably analyze atherosclerotic plaques that are located on the far wall because of the so-called pseudo-enhancement artifact [7, 8]. The contrast enhancement in the far wall plaques will show a similar pattern as the lumen and perfusion will be erroneously detected or overestimated due to this artifact.

10.2 Summary

In this thesis work, we avoided the known limitations of IPN quantification methods reported in previous studies. We developed specialized IPN analysis tools for carotid CEUS image sequences: motion compensation tools tailored for plaques (***Chapter 2 and 7***), detection and tracking of individual contrast spots within a plaque ROI to detect microvasculature paths (***Chapter 3***), motion compensated TIC perfusion analysis, time integrated parametric images of plaque perfusion such as maximum intensity projection (MIP) (***Chapter 4***), segmentation of individual contrast spots based on statistical models of intensity distributions (***Chapter 5***), and their time integration to quantify the area of neovascularization. From these perfusion and structure analyses, several quantification parameters were derived to estimate the degree of IPN of carotid plaques. The proposed IPN analyses were tested on several patient datasets. The derived parameters were compared to visual scores of IPN. The purpose of this study was to find the parameters which match significantly to the visual consensus scores, to replace subjective visual scoring and provide an objective quantitative IPN assessment in CEUS. Furthermore, we developed a customized software package called Carotid Intraplaque Neovascularization Software (CINQS) intended for clinical researchers, which includes all developed IPN quantification tools (***Chapter 6***). We also developed a novel carotid lumen and plaque segmentation method in combined B-mode ultrasound (BMUS) and CEUS images to fully automate IPN quantification (***Chapter 7-8***). In ***Chapter 9***, we describe a clinical study, assessment of IPN in patients with familial hypercholesterolemia, using the CINQS (Chapter 6) and quantification tools described in Chapters 3-5.

10.3 Discussion of Contribution

10.3.1 Motion compensation (Rigid+Nonrigid)

Carotid images exhibit considerable motion such as breathing, pulsation, probe or patient motion. For accurate quantification of IPN, motion compensation is a prerequisite step. In this thesis work, we developed rigid and nonrigid motion compensation methods tailored for carotid plaques. In **Chapter 2,** we introduced a rigid registration of a local region based on block matching [9] to follow the plaque ROI. However, this technique is sensitive to sudden disturbances and has the tendency to lose tracking when there are artifacts, out-of-plane motion, reduced or noisy correlation values. To improve the performance of block matching techniques and avoid sudden disturbances, we combined this technique with multidimensional dynamic programming (MDP) in **Chapter 2** [10]. MDP and block matching results were evaluated in-vitro by a phantom and in-vivo by comparing to manual tracking of three experts for multibeat image sequences of 11 plaques. The MDP results showed that the method is sufficiently accurate and successful for in-vivo application. MDP combined with block matching decreased the failure rate of tracking plaques by a factor of 4 compared to block matching. Yet, our rigid

technique only compensates for translational movements but not for rotation and deformation, and also gives only a local motion estimate. To estimate and compensate the complex motion in the complete BMUS and CEUS images, we proposed a nonrigid motion estimation method in **Chapter 7** [11]. This method generates a detailed nonrigid deformation field for the complete BMUS and CEUS images. This not only enables us to track the plaques but also to improve image quality by time averaging of the registered image sequences. This provides "epitome" images of improved quality that provides the basis for automated segmentation. The nonrigid motion compensation was validated by comparing displacements with manual annotations of two independent observers in 11 carotid arteries. The nonrigid motion compensation results are comparable with interobserver variability and local results of MDP. Motion compensation is used as a preprocessing step for all developed IPN quantification methods.

10.3.2 New IPN quantification methods

We developed several specialized IPN quantification methods for carotid plaques in this thesis work. In ***Chapter 4*** [12], we first investigated plaque perfusion with classical TIC analysis, and derived parameters from motion compensated TIC of plaques**.** Furthermore, we identified the perfused regions within the plaque by time integrated parametric images such as MIP. The results of TIC and MIP were verified with a synthetic image sequence with a known motion pattern and known intensities. From the MIP image, we obtained absolute and relative IPN area by applying an intensity threshold. However, if there are artifacts within the plaque ROI, the MIP image will include them as well. This will cause overestimation of IPN area. To avoid this, we analyzed the structure of the microvasculature network and applied statistical contrast spot segmentation methods. In ***Chapter 3*** [13], we obtained microvascular network paths by detection and tracking of individual contrast spots. We also discriminated between stationary and moving objects based on their displacement over time. However, microvessels that cross the imaging plane almost perpendicularly might be considered as stationary objects or artifacts and this would lead to underestimation of IPN. The results of this method were validated with manual tracking and visual classification of contrast spots and the success rate of the method for classification of artifacts and vessels was 75%. We developed a statistical contrast spot segmentation method (***Chapter 5***) [14] that classifies intensities within the plaque ROI into 4 classes: background, intermediate, contrast spot and artifact class. Classifying intensities in each time frame and applying spatiotemporal analysis handles several issues raised by other methods and allows accurate quantification of IPN. This method was shown to be more robust to artifacts. The results of this method were validated with manual segmentation of contrast spots in 10 plaques and an average Dice similarity index of 0.73 was obtained.

10.3.3 Fully automated carotid lumen and plaque segmentation

Carotid plaque segmentation in B-mode Ultrasound (BMUS) and CEUS is crucial to assess plaque morphology and composition, which are linked to plaque vulnerability. Segmentation in BMUS is challenging due to noise, artifacts, and echolucent plaques. CEUS allows a better delineation of the lumen but contains artifacts and lacks tissue information. We developed a method which exploits the combined information from simultaneously acquired BMUS&CEUS images to overcome the difficulties of the separate use of BMUS and CEUS. First, we obtain the epitome images by taking the average of registered BMUS and CEUS images over time to improve the signal-to-noise ratio (SNR) (***Chapter 7***). Second, we segment the lumen-intima (LI) interface (inner layer of plaques) from the CEUS epitome, using the joint intensity histogram of BMUS and CEUS epitomes and graph based segmentation (***Chapter 7***). Third, we segment the media-adventitia (MA) interface from the BMUS epitome by using multidimensional dynamic programming for parallel curves (***Chapter 8***). The results of the automated lumen (n=19 carotids) and plaque segmentations (n=48) were compared to manual segmentations of two independent observers in the epitome images. The differences between automated segmentation results and manual ground truth were comparable with interobserver variability of manual ground truth. Our method also allows studying the geometry of the artery over time by transforming the detected LI and MA interfaces from the epitome images to each time frame, since we obtained the deformation field of each time frame by nonrigid motion estimation. Furthermore, our segmentation method allows several applications such as fully automated IPN quantification, arterial distensibility, and plaque characterization. To the best of our knowledge, this is the first method segmenting carotid lumen and plaques in combined BMUS and CEUS images.

10.3.4 Dedicated software package for carotid plaque neovascularization

As explained above, currently available commercial tools for contrast quantification are not suitable for quantitative analysis of carotid IPN due to substantial motion of the carotid artery, artifacts, and intermittent perfusion of plaques. TICs of atherosclerotic plaques are characterized by a number of short peaks corresponding to the passage of single (or clusters of) contrast bubbles and do not resemble the typical massive bolus passage or flash/replenishment curves seen in the lumen of an artery or in the perfusion pattern of large organs or tumors. Therefore, we developed a dedicated software package that includes all the developed carotid IPN quantification tools, called Carotid Intraplaque Neovascularization Quantification Software (CINQS) (***Chapter 6***) [15]. Numerical and graphical outputs of CINQS were tested on synthetic image sequences with known gray values for each pixel and validated against the pre-calculated numerical results for these sequences. CINQS is designed as a special-purpose platform for IPN quantification tools for carotid plaques. CINQS replaces subjective, qualitative and tedious visual IPN assessment with reproducible quantitative IPN parameters. It allows selection of suitable parameters for measuring the degree of IPN by enabling comparison of existing and new IPN parameters with a reference (e.g. visual IPN scoring or histology). CINQS was

developed in a modular and extensible way and provides a user-friendly tool for analyzing carotid IPN in CEUS. CINQS could also be used to check changes in neovascularization over time, and to check the outcome of novel therapies on neovascularization. To the best of our knowledge, this is the first software package dedicated to carotid IPN quantification.

In ***Chapter 9***, a clinical study, assessment of IPN in patients with familial hypercholesterolemia (FH), using the CINQS is presented. CINQS is used to precisely assess the amount of contrast enhancement in atherosclerotic plaques. It was shown that plaques with an irregular or ulcerated surface had significantly more IPN than plaques with a smooth surface.

10.4 Limitations of Current Study

10.4.1 2D imaging and out-of-plane motion

The main limitation of this study is formed by the use of 2D imaging. In all studies, we used single longitudinal cross sections of the carotid artery. This limits the detection of IPN to this cross section. Slice thickness of the Philips linear array L9-3 probe used in this study is about 2 mm. This indicates that detection of IPN is limited to a narrow volume slice plane. Only microvessels in the plane or crossing the plane are detected. This makes it hard to quantify true IPN degree; the detected IPN degree is assumed to be proportional to the true IPN degree of the whole plaque, but from histological studies it is known that distribution of microvessels in plaques is highly inhomogeneous [1].

Out-of-plane motion caused by 2D imaging is another limitation of this study. Out-of plane motion will interfere with the tracking of microbubbles and image registration. It is not possible to compensate out-of-plane motion, as the in-plane information is lost. Therefore, out-of-plane motion should be small with respect to the slice thickness to assure reliable compensation of in-plane motion and accurate IPN quantification.

10.4.2 Pseudo-enhancement artifacts (far wall plaques)

In this study, we only analyzed far-wall plaques. Several studies have analyzed far wall plaques to assess IPN [3, 4, 6]. However, it is not reliable to analyze far wall plaques due to the pseudo-enhancement artifact [7, 8]. Current multi-pulse contrast detection techniques rely on linear propagation of the transmitted ultrasound signal. However, an acoustic wave will be distorted when it crosses highly concentrated contrast regions (e.g. lumen) and thus scattering from tissue will not be perfectly canceled behind these regions. In the contrast image, a response will appear that is similar to the contrast response in the lumen. This is often misinterpreted as neovasculature [3, 4, 6] . There may be no actual perfusion present, or it may be overestimated. In any case, no reliable quantification is possible in the far wall. We therefore did not analyze far wall plaques in our study. This limitation of CEUS might be overcome by development

of new pulse sequences [16]. If the artifact can be prevented, the analyses described in this thesis can be applied to far wall plaques as well.

10.4.3 Low perfusion of plaque neovascularization

The detection of neovessels in plaque by CEUS is strongly dependent on the actual number of microbubbles that can be expected in these tiny vessels. We will supply a very rough calculation of the chance of the appearance of such bubbles. CEUS was performed after intravenous administration of a $0.5mL$ bolus of SonoVue ultrasound contrast agent (Bracco, Milan, Italy). The bubble concentration for SonoVue is up to $0.5\ x\ 10^9\ bubbles/mL$ [17]. The bolus passes the lungs and the left ventricle and is assumed to be passing into the main arteries in about 10 heartbeats. This means the whole bolus is diluted in about 1L of blood, and the arterial concentration would be maximally 250 bubbles/μL (assuming all bubbles survive). A microvessel with a diameter of $100\mu m$ and a length of $2mm$ would hold about 5 bubbles in this optimal scenario. If the blood velocity of such a vessel is 1mm/s, about 25 bubbles would pass during a 10-second ultrasound recording. This shows that for microvessels with diameters < $100\mu m$ the chance of detecting bubbles is actually small and it can be questioned which part of the microvasculature will be detected with CEUS. Further studies are needed to investigate dose dependent perfusion of IPN, since this is a principal limitation of CEUS perfusion imaging of plaques.

Increasing the bubble concentration is only possible to a certain limit. CEUS examination was performed for multiple sites of right and left carotid arteries. The used cumulative dose per patient was kept below $10mL$ in our study. Using single bolus injections with a higher concentration might increase the chance of IPN perfusion but this will also reduce the number of examination sites or multiple recording of the same site.

10.4.4 Histological validation

In our studies, we compared automated IPN scores to visual IPN scores in CEUS. This is a valid comparison, since we are aiming at replacing the subjective visual scoring. However, we still need to validate whether our automated parameters reflect the true number of microvessels or the perfusion of the plaques. For this, histological assessment of plaques would be the ground truth. To confirm our present findings, we performed a limited histological study. A total of 27 specimens of carotid artery plaques were available after atherectomy and included for histological assessment for the presence of IPN. An IPN hot-spot analysis was performed on histological cross sections of each plaque by two independent observers. The microvessels are generally concentrated in certain regions of the plaque (hot spots), and the number of microvessels was counted in these spots to quantify the degree of IPN. This process was explained in detail in the thesis work of Van den Oord [23]. Unfortunately, we did not find any substantial correlation with our quantitative CEUS imaging parameters. However,

there are good reasons why an existing correspondence would not result in a correlation in our study setup. There are limitations both in quantitative CEUS analysis (as explained above) as well as in the histological IPN estimations. In CEUS, we only analyzed the near wall part of plaques in a longitudinal cross section. In the histological assessment, the vessels were counted only in three hot spots on the transversal cross sections of the plaque specimen. This indicates that the site of the imaging plane might not cut a hot spot at all (see Figure 1). An IPN density assessment in the whole histological specimen would provide a more representative measure of IPN degree. However, such an analysis requires much more work than the hot spot analysis and was practically infeasible.

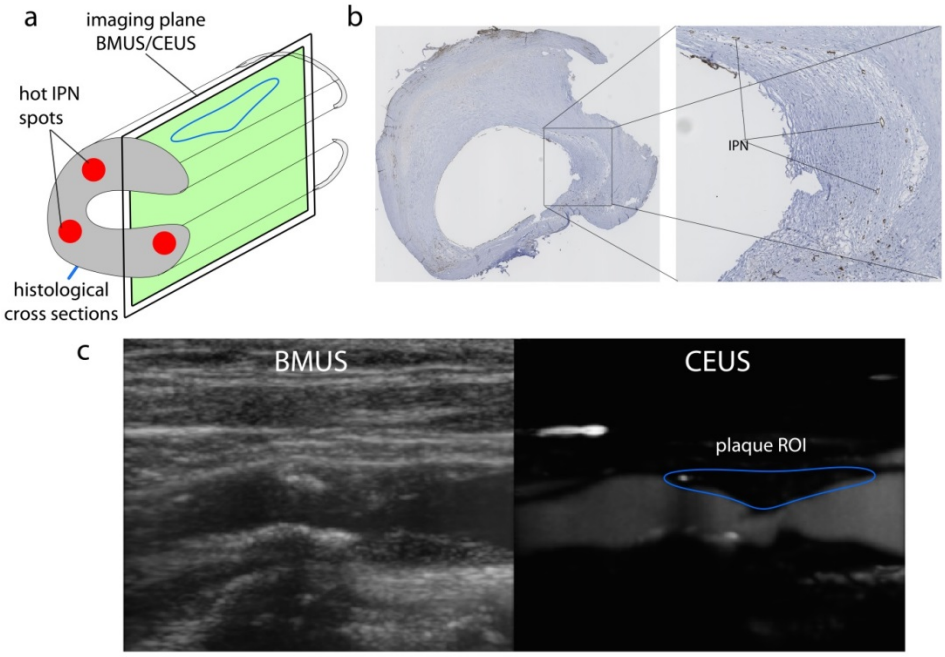

Figure 1: Relation between histological and CEUS assessment of IPN a) Schematic depiction of a cross-section of histological atherosclerotic plaque specimen (gray) in relation to the ultrasound BMUS/CEUS imaging plane (green). Red circles represent IPN hot spots. b) An example slice of histological plaque specimen with CD34 staining shows IPN. c) An example of simultaneously acquired BMUS and CEUS image.

Predictive value of parameters

The ultimate goal of our study and of the PARISk CTMM project is to provide imaging biomarkers that can be used for early prediction of plaque vulnerability. We have shown that our quantitative parameters can replace visual IPN scoring of CEUS imaging in an objective and reproducible manner. However, to determine their predictive value for cerebrovascular events, the derived quantitative parameters should be evaluated in a long-term patient follow-up study

to verify that they are predictive for cerebrovascular events and outperform visual IPN scoring.

10.5 Future perspectives

10.5.1 Molecular imaging with targeted contrast agents

Molecular imaging approaches aim at detecting biological processes such as endothelial activation, macrophage infiltration and angiogenesis. Developments in targeted contrast agents present a future for molecular CEUS imaging of IPN. Targeted contrast agents have been used in several animal studies to identify cellular receptors linked to angiogenesis in tumors and atherosclerotic plaques, e.g. vascular endothelial growth factor receptor 2 (VEGFR2) [18-20]. BR55 (a VEGFR2-targeted microbubble, Bracco Suisse, Geneva, Switzerland) is the first targeted ultrasound contrast agent used in clinical trials. The first human study has been performed for the ability of BR55 to identify prostate cancers on the basis of their increased VEGFR2 expression (ref: ClinicalTrials.gov identifier: NCT01253213). Molecular CEUS imaging of IPN may allow early diagnosis and treatment of atherosclerosis. The IPN quantification tools developed in this thesis are also suitable for targeted contrast ultrasound imaging. They may just need to be optimized for this purpose. Our microvascular structure analysis (***Chapter 3***) tool was optimized for a targeted contrast study [21] to distinguish bound contrast agents from free-floating bubbles.

10.5.2 3D +time CEUS imaging

As 2D CEUS imaging is limited to a narrow volume slice, volumetric information will improve the accuracy of IPN detection. Extension of carotid contrast 2D CEUS imaging to 3D + time CEUS imaging will allow reconstruction of the complete microvasculature network. This will give a more reliable and accurate estimate of IPN degree of the whole plaque. Out of plane motion will no longer be an issue and comparison to histology will become more feasible. Our rigid and nonrigid motion compensation and IPN quantification tools could be readily adapted for 3D CEUS imaging.

10.5.3 Ultrafast plane wave imaging

Unlike standard B-mode imaging that generates one image line per transmission, ultrafast plane wave imaging can generate one complete image per plane wave transmission. It can achieve a frame rate of 10.000 frames per second, while standard B-mode ultrasound allows 25-50 frames per second. However, each plane wave generates a low quality image compared to a standard B-mode image. To improve the quality of plane wave imaging, coherent plane wave compounding is used by transmitting plane waves under different angles and summing the results. This allows a similar image quality as standard B-mode but at a much higher frame rate (~1kHz). Ultrafast plane wave imaging can be used for contrast

detection as well. It could give similar image quality as standard CEUS at a much higher frame rate with coherent plane wave compounding, while reducing the peak acoustic pressure and bubble disruption. Ultrafast plane wave imaging could also improve the low-SNR BMUS images that we obtain in the standard side-by-side, simultaneous, BMUS and CEUS acquisition. Improved-SNR BMUS and CEUS images could also improve the plaque segmentation performance. Furthermore, plane wave imaging can be used to assess minute deformations of the carotid artery and plaque tissue [22] and thus offers interesting elastographic possibilities: it could assess the tissue elastic properties of the carotid artery and plaque.

Conclusion

In this thesis work, we developed several image analysis tools and a dedicated software package, CINQS, for CEUS carotid imaging. Our quantitative imaging parameters, which provide objective and reproducible results, might replace subjective and tedious visual IPN scoring. CINQS enables systematic testing and comparing of different IPN analysis tools, and selecting the best parameters for measuring the degree of IPN. This represents an important step towards prediction of plaque vulnerability. Future studies are needed to confirm that our quantitative parameters outperform visual IPN scoring in the prediction of cerebrovascular events or the presence of IPN in histology.

References:

[1] W. E. Hellings, W. Peeters, F. L. Moll, S. R. D. Piers, J. van Setten, P. J. Van der Spek, J. P. P. M. de Vries, K. A. Seldenrijk, P. C. De Bruin, A. Vink, E. Velema, D. P. V. de Kleijn, and G. Pasterkamp, "Composition of Carotid Atherosclerotic Plaque Is Associated With Cardiovascular Outcome A Prognostic Study," *Circulation,* vol. 121, pp. 1941-U111, May 4 2010.

[2] J. B. Michel, R. Virmani, E. Arbustini, and G. Pasterkamp, "Intraplaque haemorrhages as the trigger of plaque vulnerability," *European heart journal,* vol. 32, pp. 1977-85, 1985a, 1985b, 1985c, 2011.

[3] P. T. Huang, F. G. Huang, C. P. Zou, H. Y. Sun, X. Q. Tian, Y. Yang, J. F. Tang, P. L. Yang, and X. T. Wang, "Contrast-enhanced sonographic characteristics of neovascularization in carotid atherosclerotic plaques," *Journal of Clinical Ultrasound,* vol. 36, pp. 346-351, Jul-Aug 2008.

[4] L. Xiong, Y. B. Deng, Y. Zhu, Y. N. Liu, and X. J. Bi, "Correlation of Carotid Plaque Neovascularization Detected by Using Contrast-enhanced US with Clinical Symptoms," *Radiology,* vol. 251, pp. 583-589, May 2009.

[5] A. Hoogi, D. Adam, A. Hoffman, H. Kerner, S. Reisner, and D. Gaitini, "Carotid Plaque Vulnerability: Quantification of Neovascularization on Contrast-Enhanced Ultrasound With Histopathologic Correlation," *American Journal of Roentgenology,* vol. 196, pp. 431-436, 2011.

[6] T. G. Papaioannou, M. Vavuranakis, A. Androulakis, G. Lazaros, I. Kakadiaris, I. Vlaseros, M. Naghavi, I. Kallikazaros, and C. Stefanadis, "In-vivo imaging of carotid plaque neoangiogenesis with contrast-enhanced harmonic ultrasound," *International Journal of Cardiology,* vol. 134, pp. e110-e112, 2009.

[7] G. L. ten Kate, G. G. J. Renaud, Z. Akkus, S. C. H. van den Oord, F. J. ten Cate, V. Shamdasani, R. R. Entrekin, E. J. G. Sijbrands, N. de Jong, J. G. Bosch, A. F. L. Schinkel, and A. F. W. van der Steen, "Far-Wall Pseudoenhancement during Contrast-Enhanced Ultrasound of the Carotid Arteries: Clinical Description and in Vitro Reproduction," *Ultrasound in Medicine and Biology,* vol. 38, pp. 593-600, Apr 2012.

[8] A. Thapar, J. Shalhoub, M. Averkiou, C. Mannaris, A. H. Davies, and E. L. S. Leen, "Dose-Dependent Artifact in the Far Wall of the Carotid Artery at Dynamic Contrast-enhanced US," *Radiology,* vol. 262, pp. 672-679, February 1, 2012 2012.

[9] Z. Akkus, J. G. Bosch, G. Renaud, A. Hoogi, G. L. ten Kate, S. van den Oord, A. Schinkel, N. De Jong, and A. F. W. Van der Steen, "Motion compensation method for quantification of neovascularization in carotid atherosclerotic plaques with contrast enhanced ultrasound (CEUS)," in *Ultrasonics Symposium (IUS), 2011 IEEE International*, 2011, pp. 1156-1159.

[10] Z. Akkus, A. Hoogi, G. Renaud, G. L. ten Kate, S. C. H. van den Oord, A. F. L. Schinkel, N. de Jong, A. F. W. van der Steen, and J. G. Bosch, "Motion Compensation Method using Dynamic Programming for Quantification of Neovascularization in Carotid Atherosclerotic Plaques with Contrast Enhanced Ultrasound (CEUS)," *Medical Imaging 2012: Ultrasonic Imaging, Tomography, and Therapy,* vol. 8320, 2012.

[11] A. Z. Carvalho D D B, Bosch J G, van der Oord S C H, Niessen J W, Klein S, "Nonrigid registration of B-mode and contrast ultrasound images of carotid artery," *SPIE medical imaging, in press* 2014.

[12] Z. Akkus, A. Hoogi, G. Renaud, S. C. H. van den Oord, G. L. ten Kate, A. F. L. Schinkel, D. Adam, N. de Jong, A. F. W. van der Steen, and J. G. Bosch, "New Quantification Methods for Carotid Intra-plaque Neovascularization Using Contrast-Enhanced Ultrasound," *Ultrasound in Medicine & Biology,* vol. 40, pp. 25-36, 2014.

[13] A. Hoogi, Z. Akkus, S. C. H. van den Oord, G. L. ten Kate, A. F. L. Schinkel, J. G. Bosch, N. de Jong, D. Adam, and A. F. W. van der Steen, "Quantitative Analysis of Ultrasound Contrast Flow Behavior in Carotid Plaque Neovasculature," *Ultrasound in Medicine and Biology,* vol. 38, pp. 2072-2083, Dec 2012.

[14] Z. Akkus, J. G. Bosch, G. V. Sánchez-Ferrero, D. D. B. Carvalho, G. Renaud, S. C. H. van den Oord, G. L. ten Kate, A. F. L. Schinkel, N. de Jong, and A. F. W. van der Steen, "Statistical segmentation of carotid plaque neovascularization," pp. 867506-867506, 2013.

[15] Z. Akkus, G. van Burken, S. C. H. van den Oord, A. F. I. Schinkel, N. De Jong, F. W. van der steen, and J. G. Bosch, "Carotid Intraplaque Neovascularization Quantification Software (CINQS)," *Biomedical and Health Informatics, IEEE Journal of,* vol. PP, pp. 1-1, 2014.

[16] G. Renaud, J. G. Bosch, G. L. ten Kate, V. Shamdasani, R. Entrekin, N. de Jong, and A. F. W. van der Steen, "Counter-propagating wave interaction for contrast-enhanced ultrasound imaging," *Physics in Medicine and Biology,* vol. 57, pp. L9-L18, Nov 7 2012.

[17] M. Schneider, "SonoVue, a new ultrasound contrast agent," *European Radiology,* vol. 9, pp. S347-S348, 1999/11/01 1999.

[18] J. Bzyl, W. Lederle, A. Rix, C. Grouls, I. Tardy, S. Pochon, M. Siepmann, T. Penzkofer, M. Schneider, F. Kiessling, and M. Palmowski, "Molecular and functional ultrasound imaging in differently aggressive breast cancer xenografts using two novel ultrasound contrast agents (BR55 and BR38)," *European Radiology,* vol. 21, pp. 1988-1995, 2011/09/01 2011.

[19] S. Pochon, I. Tardy, P. Bussat, T. Bettinger, J. Brochot, M. von Wronski, L. Passantino, and M. Schneider, "BR55: A Lipopeptide-Based VEGFR2-Targeted Ultrasound Contrast Agent for Molecular Imaging of Angiogenesis," *Investigative Radiology,* vol. 45, pp. 89-95 10.1097/RLI.0b013e3181c5927c, 2010.

[20] I. Tardy, S. Pochon, M. Theraulaz, P. Emmel, L. Passantino, F. Tranquart, and M. Schneider, "Ultrasound Molecular Imaging of VEGFR2 in a Rat Prostate Tumor Model Using BR55," *Investigative Radiology,* vol. 45, pp. 573-578 10.1097/RLI.0b013e3181ee8b83, 2010.

[21] Z. A. V. Daeichin, I. Skachkov, K. Kooiman, A. Needles, J. Sluimer, M.J.A.P. Daemen, A. F.W. van der Steen, N. de Jong, J.G. Bosch, "Quantification of bound microbubbles in ultrasound molecular imaging," *IEEE Transactions on Ultrasonics, Ferroelectrics and Frequency Control,* 2014.

[22] S. Korukonda, R. Nayak, N. Carson, G. Schifitto, V. Dogra, and M. M. Doyley, "Noninvasive vascular elastography using plane-wave and sparse-array imaging," *IEEE Trans Ultrason Ferroelectr Freq Control,* vol. 60, pp. 332-42, 2013.

[1] W. E. Hellings, W. Peeters, F. L. Moll, S. R. D. Piers, J. van Setten, P. J. Van der Spek, J. P. P. M. de Vries, K. A. Seldenrijk, P. C. De Bruin, A. Vink, E. Velema, D. P. V. de Kleijn, and G. Pasterkamp, "Composition of Carotid Atherosclerotic Plaque Is Associated With Cardiovascular Outcome A Prognostic Study," *Circulation,* vol. 121, pp. 1941, May 4 2010.

[2] J. B. Michel, R. Virmani, E. Arbustini, and G. Pasterkamp, "Intraplaque haemorrhages as the trigger of plaque vulnerability," *European heart journal,* vol. 32, pp. 1977-85, 1985a, 1985b, 1985c, 2011.

[3] P. T. Huang, F. G. Huang, C. P. Zou, H. Y. Sun, X. Q. Tian, Y. Yang, J. F. Tang, P. L. Yang, and X. T. Wang, "Contrast-enhanced sonographic characteristics of neovascularization in carotid atherosclerotic plaques," *Journal of Clinical Ultrasound,* vol. 36, pp. 346-351, 2008.

[4] L. Xiong, Y. B. Deng, Y. Zhu, Y. N. Liu, and X. J. Bi, "Correlation of Carotid Plaque Neovascularization Detected by Using Contrast-enhanced US with Clinical Symptoms," *Radiology,* vol. 251, pp. 583-589, May 2009.

[5] A. Hoogi, D. Adam, A. Hoffman, H. Kerner, S. Reisner, and D. Gaitini, "Carotid Plaque Vulnerability: Quantification of Neovascularization on Contrast-Enhanced Ultrasound With Histopathologic Correlation," *American Journal of Roentgenology,* vol. 196, pp. 431-436, 2011.

[6] T. G. Papaioannou, M. Vavuranakis, A. Androulakis, G. Lazaros, I. Kakadiaris, I. Vlaseros, M. Naghavi, I. Kallikazaros, and C. Stefanadis, "In-vivo imaging of carotid plaque neoangiogenesis with contrast-enhanced harmonic ultrasound," *International Journal of Cardiology,* vol. 134, pp. e110-e112, 2009.

[7] G. L. ten Kate, G. G. J. Renaud, Z. Akkus, S. C. H. van den Oord, F. J. ten Cate, V. Shamdasani, R. R. Entrekin, E. J. G. Sijbrands, N. de Jong, J. G. Bosch, A. F. L. Schinkel, and A. F. W. van der Steen, "Far-Wall Pseudoenhancement during Contrast-Enhanced Ultrasound of the Carotid Arteries: Clinical Description and in Vitro Reproduction," *Ultrasound in Medicine and Biology,* vol. 38, pp. 593-600, Apr 2012.

[8] A. Thapar, J. Shalhoub, M. Averkiou, C. Mannaris, A. H. Davies, and E. L. S. Leen, "Dose-Dependent Artifact in the Far Wall of the Carotid Artery at Dynamic Contrast-enhanced US," *Radiology,* vol. 262, pp. 672-679, February 1, 2012 2012.

[9] Z. Akkus, J. G. Bosch, G. Renaud, A. Hoogi, G. L. ten Kate, S. van den Oord, A. Schinkel, N. De Jong, and A. F. W. Van der Steen, "Motion compensation method for quantification of neovascularization in carotid atherosclerotic plaques with contrast enhanced ultrasound (CEUS)," in *Ultrasonics Symposium (IUS), 2011 IEEE International*, 2011, pp. 1156-1159.

[10] Z. Akkus, A. Hoogi, G. Renaud, G. L. ten Kate, S. C. H. van den Oord, A. F. L. Schinkel, N. de Jong, A. F. W. van der Steen, and J. G. Bosch, "Motion Compensation Method using Dynamic Programming for Quantification of Neovascularization in Carotid Atherosclerotic Plaques with Contrast Enhanced Ultrasound (CEUS)," *Medical Imaging 2012: Ultrasonic Imaging, Tomography, and Therapy,* vol. 8320, 2012.

[11] Carvalho D D B, Akkus Z Bosch J G, van der Oord S C H, Niessen J W, Klein S, "Nonrigid registration of B-mode and contrast ultrasound images of carotid artery," *SPIE medical imaging, in press* 2014.

[12] Z. Akkus, A. Hoogi, G. Renaud, S. C. H. van den Oord, G. L. ten Kate, A. F. L. Schinkel, D. Adam, N. de Jong, A. F. W. van der Steen, and J. G. Bosch, "New Quantification Methods for Carotid Intra-plaque Neovascularization Using Contrast-Enhanced Ultrasound," *Ultrasound in Medicine & Biology,* vol. 40, pp. 25-36, 2014.

[13] A. Hoogi, Z. Akkus, S. C. H. van den Oord, G. L. ten Kate, A. F. L. Schinkel, J. G. Bosch, N. de Jong, D. Adam, and A. F. W. van der Steen, "Quantitative Analysis of Ultrasound Contrast Flow Behavior in Carotid Plaque Neovasculature," *Ultrasound in Medicine and Biology,* vol. 38, pp. 2072-2083, Dec 2012.

[14] Z. Akkus, J. G. Bosch, G. V. Sánchez-Ferrero, D. D. B. Carvalho, G. Renaud, S. C. H. van den Oord, G. L. ten Kate, A. F. L. Schinkel, N. de Jong, and A. F. W. van der Steen, "Statistical segmentation of carotid plaque neovascularization," pp. 867506-867506, 2013.

[15] Z. Akkus, G. van Burken, S. C. H. van den Oord, A. F. I. Schinkel, N. De Jong, F. W. van der steen, and J. G. Bosch, "Carotid Intraplaque Neovascularization Quantification Software (CINQS)," *Biomedical and Health Informatics, IEEE Journal of,* vol. PP, pp. 1-1, 2014.

[16] G. Renaud, J. G. Bosch, G. L. ten Kate, V. Shamdasani, R. Entrekin, N. de Jong, and A. F. W. van der Steen, "Counter-propagating wave interaction for contrast-enhanced ultrasound imaging," *Physics in Medicine and Biology,* vol. 57, pp. L9-L18, Nov 7 2012.

[17] M. Schneider, "SonoVue, a new ultrasound contrast agent," *European Radiology,* vol. 9, pp. S347-S348, 1999/11/01 1999.

[18] J. Bzyl, W. Lederle, A. Rix, C. Grouls, I. Tardy, S. Pochon, M. Siepmann, T. Penzkofer, M. Schneider, F. Kiessling, and M. Palmowski, "Molecular and functional ultrasound imaging in differently aggressive breast cancer xenografts using two novel ultrasound contrast agents (BR55 and BR38)," *European Radiology,* vol. 21, pp. 1988-1995, 2011.

[19] S. Pochon, I. Tardy, P. Bussat, T. Bettinger, J. Brochot, M. von Wronski, L. Passantino, and M. Schneider, "BR55: A Lipopeptide-Based VEGFR2-Targeted Ultrasound Contrast Agent for Molecular Imaging of Angiogenesis," *Investigative Radiology,* vol. 45, pp. 89-95, 2010.

[20] I. Tardy, S. Pochon, M. Theraulaz, P. Emmel, L. Passantino, F. Tranquart, and M. Schneider, "Ultrasound Molecular Imaging of VEGFR2 in a Rat Prostate Tumor Model Using BR55," *Investigative Radiology,* vol. 45, pp. 573-578 10.1097/RLI.0b013e3181ee8b83, 2010.

[21] V. Daeichin, Z. Akkus, I. Skachkov, K. Kooiman, A. Needles, J. Sluimer, M.J.A.P. Daemen, A. F.W. van der Steen, N. de Jong, J.G. Bosch, "Quantification of bound microbubbles in ultrasound molecular imaging," *IEEE Transactions on Ultrasonics, Ferroelectrics and Frequency Control,* 2014.

[22] S. Korukonda, R. Nayak, N. Carson, G. Schifitto, V. Dogra, and M. M. Doyley, "Noninvasive vascular elastography using plane-wave and sparse-array imaging," *IEEE Trans Ultrason Ferroelectr Freq Control,* vol. 60, pp. 332-42, 2013.

[23] S. C. H. van den Oord. Clinical evaluation of contrast-enhanced carotid ultrasound imaging". PhD Thesis. Erasmus MC, Rotterdam, the Netherlands.

Summary

Intraplaque neovascularization (IPN) has been presented as an important biomarker for progressive atherosclerotic disease and plaque vulnerability in several pathological studies. Therefore, quantification of IPN may allow early prediction of plaque at risk of rupture and thus prevention of future cardiovascular events such as stroke. Contrast enhanced ultrasound (CEUS) enables us to detect and visualize IPN by use of ultrasound contrast agents. So, the degree of IPN can potentially be measured by quantitative imaging biomarkers derived from CEUS. Since quantification tools for IPN are scarce, so far mainly visual IPN scoring on CEUS clips has been used to assess IPN, which is subjective and tedious.

Currently available commercial tools for contrast quantification, e.g. QLAB region of interest (ROI) quantification tool (Philips Medical Systems, Bothell, USA) and VueBox (Bracco Suisse SA, Geneva, Switzerland), are not suitable for quantitative analysis of IPN. These commercial quantification tools have been developed mainly for time intensity curve analysis (TIC) of large organs such as heart, liver and prostate, not for plaques. Plaques are very small and intermittently perfused. Therefore, the perfusion characteristics of plaques are quite different from those of large organs and TIC analysis as applied in large well-perfused organs is not applicable. Some IPN quantification approaches have been reported but they suffer from a number of limitations such as imaging artifacts and no or imperfect motion compensation. In this thesis work, we avoided the known limitations of IPN quantification methods reported in previous studies and developed and evaluated specialized IPN analysis tools for carotid CEUS image sequences.

Chapter 1 gives an overview of diagnostic ultrasonography, contrast enhanced ultrasound, contrast detection techniques, and ultrasound image analysis. The scope and outline of the thesis are also described in more detail.

Carotid images exhibit considerable motion such as breathing, pulsation, probe or patient motion. For accurate quantification of IPN, motion compensation is a prerequisite step. In **Chapter 2**, we present a motion compensation tool tailored for plaques. A rigid motion compensation of a local region based on block matching combined with multidimensional dynamic programming is introduced to follow the plaque ROI over time. It is shown that the method is sufficiently accurate and successful for in-vivo application. However, our rigid technique only compensates for translational movements but not for rotation and deformation, and also gives only a local motion estimate.

In **Chapter 3**, we present an IPN quantification method which detects and tracks individual contrast spots to reconstruct microvascular network paths. This

method allows distinguishing between stationary and moving objects based on their displacement over time. However, microvessels that cross the imaging plane almost perpendicularly might be considered as stationary objects or artifacts and this would lead to underestimation of IPN.

In **Chapter 4**, we investigate plaque perfusion with motion compensated TIC analysis and time integrated parametric images such as maximum intensity projection (MIP). Also, several quantitative parameters, derived from TIC and MIP, are studied to replace qualitative visual IPN scores. However, if there are artifacts within the plaque ROI, the MIP image will include them as well. This will cause overestimation of IPN area. To prevent this, we analyze the structure of the microvasculature network in Chapter 3 and apply statistical contrast spot segmentation methods in Chapter 5.

We introduce a statistical contrast spot segmentation method in **Chapter 5**. This method classifies intensities within the plaque ROI into 4 classes: background, intermediate, contrast spot and artifact class. Classifying intensities in each time frame and applying spatiotemporal analysis handles several issues raised by other methods and allows accurate quantification of IPN. It is shown that the method is more robust to artifacts in chapter 6.

In **Chapter 6,** we present a dedicated software package that includes all the developed carotid IPN quantification tools, called Carotid Intraplaque Neovascularization Quantification Software (CINQS). CINQS is designed as a special-purpose platform for IPN quantification tools for carotid plaques. CINQS was developed in a modular and extensible way and provides a user-friendly tool for analyzing carotid IPN in CEUS. CINQS could also be used to check changes in neovascularization over time, and to check the outcome of novel therapies on neovascularization. To the best of our knowledge, this is the first software package dedicated to carotid IPN quantification.

In **Chapter 7**, we present a nonrigid motion estimation method to estimate and compensate the complex motion in the complete B-mode ultrasound (BMUS) and CEUS images. This method exploits the combined information from simultaneously acquired BMUS&CEUS images to overcome the difficulties of the separate use of BMUS and CEUS. The method generates a detailed nonrigid deformation field for the complete BMUS and CEUS images. This not only allows us to track the plaques but also to improve image quality by time averaging of the registered image sequences. This provides "epitome" images of improved quality that we employ for an accurate segmentation of the lumen-intima (LI) interface in subjects with atherosclerotic arteries, using the joint intensity histogram of BMUS and CEUS epitomes and graph based segmentation.

Carotid plaque segmentation in BMUS and CEUS images is crucial to assess plaque morphology and composition, which are linked to plaque vulnerability. In

Chapter 8, we present a novel and fully automatic plaque segmentation technique in simultaneously acquired BMUS and CEUS images. The LI interface is segmented as described in Chapter 7. The media-adventitia (MA) interface from the BMUS epitome is segmented by using multidimensional dynamic programming for parallel curves. Our plaque segmentation method allows several applications such as fully automated IPN quantification, arterial distensibility, and plaque characterization. To the best of our knowledge, this is the first method segmenting carotid plaques in combined BMUS and CEUS images.

In **Chapter 9**, we describe a clinical study, assessment of IPN in patients with familial hypercholesterolemia, using the software described in Chapter 6 and quantification tools described in Chapters 3-5. It was shown that irregular and ulcerated plaques exhibited significantly more IPN than plaques with a smooth surface.

In **Chapter 10**, we discuss the merits of the developed IPN analysis tools and provide the future perspectives and conclusions of this thesis work.

Samenvatting

Intra-plaque neovascularisatie (IPN) wordt in verschillende pathologische studies genoemd als een belangrijke biomarker voor progressieve atherosclerose en kwetsbaarheid van plaques. Daarom kan kwantificering van IPN een vroege voorspelling van het risico van scheuring van de plaque in de halsslagaders (carotiden) mogelijk maken, en daarmee de preventie van toekomstige cardiovasculaire gebeurtenissen zoals een beroerte. Contrastechografie (CEUS) stelt ons in staat om IPN te detecteren en te visualiseren door middel van het gebruik van echografische contrastmiddelen. De mate van IPN kan daarom potentieel worden gemeten met behulp van kwantitatieve imaging biomarkers afgeleid van CEUS. Omdat kwantificeringshulpmiddelen voor IPN schaars zijn, is tot nu toe vooral visuele IPN scoring op CEUS clips gebruikt, hetgeen subjectief en lastig te beoordelen is.

Momenteel beschikbare commerciële tools voor kwantificering van contrast, zoals QLAB Region of Interest (ROI) (Philips Medical Systems, Bothell, USA) en VueBox (Bracco Suisse SA, Genève, Zwitserland), zijn niet geschikt voor kwantitatieve analyse van IPN. Deze commerciële kwantificeringshulpmiddelen zijn voornamelijk ontwikkeld voor analyse van tijd-intensiteitscurves (TIC) van grote organen zoals hart, lever en prostaat, en niet van plaques. Plaques zijn zeer klein en intermitterend doorbloed. Daarom zijn de perfusiekenmerken van plaques nogal verschillend van die van grote organen en TIC-analyse zoals toegepast in grote, goed doorbloede organen is niet toepasbaar. Een aantal IPN kwantificeringsbenaderingen is beschreven, maar deze vertonen serieuze beperkingen zoals gevoeligheid voor beeldvormingsartefacten en geen of onvolmaakte bewegingscompensatie. In dit proefschrift hebben wij de bekende beperkingen van IPN kwantificeringsmethoden zoals gemeld in eerdere studies aangepakt en gespecialiseerde IPN analysetools voor CEUS beeldseries van de carotis ontwikkeld en geëvalueerd.

Hoofdstuk 1 geeft een overzicht van diagnostische echografie, contrast-echografie, contrast-detectietechnieken, en beeldverwerking voor ultrageluidsbeelden. De reikwijdte en opzet van het proefschrift worden in meer detail beschreven.

ultrageluidsopnamen van de carotis vertonen aanzienlijke bewegingartefacten ten gevolge van ademhaling, hartslag, beweging van de transducer of beweging van de patiënt. Voor een nauwkeurige kwantificering van IPN is bewegingscompensatie een vereiste stap. In **hoofdstuk 2** presenteren we een bewegingscompensatiemethodiek speciaal voor plaques. Om de plaque ROI in de tijd te volgen gebruiken we een rigide bewegingscompensatie op basis van *block matching* gecombineerd met *multidimensional dynamic programming*. We

tonen aan dat deze werkwijze voldoende nauwkeurig en succesvol is voor *in vivo* toepassing. Echter, onze rigide techniek compenseert alleen voor translatiebewegingen maar niet voor rotatie en vervorming, en geeft ook slechts een lokale bewegingsschatting.

In **hoofdstuk 3** presenteren we een IPN-kwantificatiemethode die individuele contrastpunten detecteert en volgt om microvasculaire netwerken te reconstrueren. Deze methode maakt onderscheid tussen stilstaande en bewegende objecten op basis van hun verplaatsing in de tijd. Het is echter mogelijk dat de bloedvaatjes die het beeldvlak bijna loodrecht kruisen beschouwd worden als stilstaande objecten of artefacten, hetgeen zou leiden tot een onderschatting van IPN.

In **hoofdstuk 4** onderzoeken we plaque perfusie met bewegingsgecompenseerde TIC analyse en parametrische beelden verkregen door integratie over de tijd zoals maximale intensiteitsprojectie (MIP). Ook verschillende kwantitatieve parameters, afgeleid van TIC en MIP, worden bestudeerd om kwalitatieve visuele IPN scores te vervangen. Echter, als er artefacten binnen de plaque ROI voorkomen zal de MIP deze omvatten. Dit zal overschatting van het IPN oppervlak veroorzaken. Om dit te voorkomen, analyseren we de structuur van het microvasculatuurnetwerk zoals beschreven in hoofdstuk 3 en gebruiken we de statistische contrastsegmentatie methoden van hoofdstuk 5.

We introduceren een statistische contrastsegmentatiemethode in **hoofdstuk 5**. Deze methode classificeert intensiteiten binnen de plaque ROI in 4 klassen: contrast, achtergrond, tussenliggende klasse en artefact klasse. Het classificeren van intensiteiten over de gehele tijdreeks en het toepassen van een spatiotemporele analyse verhelpt de beperkingen van andere methoden en maakt nauwkeurige kwantificering van IPN mogelijk. We tonen in hoofdstuk 6 aan dat deze methode robuuster omgaat met artefacten.

In **Hoofdstuk 6** presenteren we een speciaal software-pakket dat alle ontwikkelde carotis IPN kwantificeringstools omvat, genaamd Carotis Intra-plaque Neovascularisatie Quantification Software (CINQS). CINQS is ontworpen als een special-purpose platform voor IPN kwantificeringshulpmiddelen voor plaques. CINQS werd ontwikkeld als een modulaire, uitbreidbare en gebruiksvriendelijke tool voor het analyseren van de halsslagader IPN in CEUS. CINQS kan ook worden gebruikt om veranderingen in neovascularisatie over de tijd te volgen en het effect van nieuwe therapieën op neovascularisatie te beoordelen. Voor zover ons bekend is dit de eerste software-pakket speciaal voor IPN kwantificatie in de carotis.

In **hoofdstuk 7** presenteren we een *nonrigid motion estimation* methode om de complexe beweging in de volledige B-mode echografie (BMUS) en CEUS beeldreeksen te bepalen en te compenseren. Deze methode maakt gebruik van de gecombineerde informatie van gelijktijdig opgenomen BMUS & CEUS beeldreeksen om de beperkingen van het afzonderlijk gebruik van BMUS en CEUS te overwinnen. De methode genereert een gedetailleerd nonrigid vervormingsveld

voor de volledige BMUS en CEUS beeldreeksen. Hierdoor kunnen we niet alleen de beweging van de plaques volgen, maar ook de beeldkwaliteit verbeteren door een tijdmiddeling van de geregistreerde beeldreeksen. Dit zorgt voor "epitoom" beelden van betere kwaliteit die we gebruiken voor een nauwkeurige segmentatie van de lumen-intima-overgang (LI) bij patiënten met atherosclerotische slagaders, met behulp van het gecombineerde intensiteitshistogram van BMUS en CEUS *epitomes* en een graaf-gebaseerde segmentatie.

Carotis plaquesegmentatie in BMUS en CEUS beelden is cruciaal voor het beoordelen van plaque morfologie en samenstelling, die een indicatie vormen voor de kwetsbaarheid van plaque. In **hoofdstuk 8** presenteren we een nieuwe en volledig automatische plaquesegmentatietechniek voor gelijktijdig opgenomen BMUS en CEUS beeldreeksen. De LI-overgang wordt gesegmenteerd zoals beschreven in hoofdstuk 7. De media-adventitia (MA)-overgang van de BMUS epitoom wordt gesegmenteerd met behulp van multidimensional dynamic programming voor parallelle curves. Onze plaque segmentatiemethode is geschikt voor verschillende toepassingen zoals volautomatische IPN kwantificering, arteriële distensibiliteit, en plaque karakterisering. Voor zover ons bekend is dit de eerste methode voor het segmenteren van plaques in gecombineerde BMUS en CEUS afbeeldingen.

In **hoofdstuk 9** beschrijven we een klinische studie, de beoordeling van IPN bij patiënten met familiaire hypercholesterolemie, met behulp van de software beschreven in hoofdstuk 6 en de kwantificerings gereedschappen beschreven in de hoofdstukken 3-5 . We hebben aangetoond dat onregelmatige en opengebrokenplaques significant meer IPN vertoonden dan plaques met een glad oppervlak.

In **hoofdstuk 10** bespreken we de verdiensten van de ontwikkelde IPN analyse-instrumenten en de toekomstperspectieven en conclusies van dit proefschrift.

Acknowledgements

I have had great four years in my PhD with biomedical engineering group (BME) in Erasmus MC, Rotterdam. I find myself fortunate to be in this great research group. Actually I had never planned to be in Netherlands until I had a visa issue in UK. First, I got a job offer in Sheffield university hospitals, UK after having my master's degree. However, I could not start the job due to an issue with work permit. That pushed me to search for alternatives. I found two available positions related to atherosclerotic plaque in Erasmus MC and applied to both of them. One of the positions was in biomedical imaging group and the other was in biomedical engineering group. First, biomedical imaging group invited me for an interview but I was not offered that job. Perhaps that was for a reason. A week after that, I was also invited by biomedical engineering group for an interview. After my first disappointment with biomedical imaging group, I was a-bit hesitating to go Erasmus MC again. But, I arranged a same day return flight from London to Amsterdam. This time, I had an interview at 23rd floor, 2 floors upper than biomedical imaging group. I had my interview with Ton van der Steen, Nico de Jong and Hans Bosch. Few days later, I received the job offer and accepted it. The position in BME group was more suitable and interesting for me. I believe this was meant to happen and I had to spend four years with BME family. First of all, I would like to thank Ton van der Steen, Nico de Jong, and Hans Bosch for giving me a chance to be at the right place. Without that opportunity, this thesis and all success with it would not be achieved.

During my four years research in BME, I had an inspiring, motivating, and hardworking supervisor, Hans Bosch. Specially, I am so grateful for your supervision. Thanks for always having time for me, your original ideas, and your useful comments. Every chapter of this thesis work would not be realized without you. Especially, I also would like to thank Gerard for his great technical support.

I would also like to thank all my colleagues for creating a friendly research environment in BME. When I started in BME, there was only Guillaume, French guy who started a month before me as a post doc in our project, in my trench. He is a modest, friendly and well organized scientist. I had great discussions with him in our project during my PhD. He helped me a lot in the beginning of my PhD. I was always scared to touch his smelly cheeses with bare hands but he was a great fellow. Thanks Guillaume for your assistance, discussions and reviewing my papers. I wish you long life happiness with Ross in Paris. Verya is my Iranian trench mate who is a climbing freak. Glad that he never had a serious injury after his climbing adventures. Even though I have never convinced him to join us for football, he is a great fellow. Thanks for your friendly conversations on several topics. We had a guest for 6 months for the cooperation in my project from Technion, Assaf Hoogi. Thanks Assaf for productive cooperation, friendly

conversations and joining me lunch outside. I enjoyed all my time together with you. You are a genuine fellow. In the last months of my PhD, I also shared my trench with Jacobo who is a great fellow. Thank you for your company and supportive remarks. Specially, I would like to thank my Russian colleague, Ilya. I really appreciated your company for coffee, hanging out, friendly conversations, dinners, and barbecues. You have a very good heart and are a true friend. Wish you huge success and happiness in your future with all my heart. Thanks Tom for inviting us to your birthday parties. I enjoyed being among your friends and family. I wish you long life happiness with Anke. I also would like to thank all other past and present colleagues: Alex, Ying, Deep, David, Krista, Marcia, Tom van Roi, Klazina, Rik, Muthu, Tianshi, Pieter, Ali, Merih, Harm, Jelle, Lambert, Gonzalo and so on.

I especially would like to thank our clinical partners, Luit ten Kate, Stijn van den Oord and Arend Schinkel. I really appreciated working with you during my PhD project. All of you have countless contribution in my research. Thank you for data acquisition, assisting and supporting me in my work, constructive and useful comments in reviewing my papers. Specially, thanks to Stijn van den Oord for his feedbacks during the development of our clinical software.

I also would like to thank to Fritz, Robert and Hans Verdoes for their technical support. Thanks to Mieke, Gracia and Rita for their valuable help in dealing with our administrative issues.

During the four years of my PhD, I had a great collaboration with Diego and Stefan from biomedical imaging group and we published several papers together. I would like to thank to Diego and Stefan for their collaboration, reviewing my papers, and their constructive comments.

I also would like to thank my Turkish friend, Burak, and his parents, Ahmet and Hacce, in Rotterdam, who never left me alone during my PhD. Thanks Burak for your company and always supportig me when I needed you. Thanks to his parents always welcoming me to their house and preparing delicious Turkish dishes to make me feel at home. I also would like to thank my parents and siblings for their love and support. Without your support, I would not have this courage to go further in my career.

Publications

Abstracts:

1. J.G. Bosch, Z. Akkus, A. Hoogi, G. Renaud, S. C.H. van den Oord, A. F.L. Schinkel, D. Adam, N. de Jong, A. F.W. van der Steen. **Quantification of neovascularization in carotid artery plaques**. Contrast Conference 2013, Rotterdam, Netherlands

Posters:

1. Z. Akkus/S. van den Oord, J.G Bosch, G. Renaud, G.L. ten Kate,A. Schinkel, N. de Jong, A.F.W. van der Steen**. Automated quantification of carotid intraplaque neovascularization using contrast-enhanced ultrasound.** 18th European Symposium on Contrast Ultrasound imaging, Rotterdam, 2013. (***The Best Poster Award)
2. S.C.H. Van Den Oord, G.L. Ten Kate, Z. Akkus, G. Renaud, E.J.G. Sijbrands, F.J. Ten Cate, N. De Jong, J.G. Bosch, A.F.W. Van Der Steen, A.F.L. Schinkel. **Incremental value of contrast enhanced ultrasound (CEUS) for detection of carotid atherosclerosis.** Conference of EuroEcho-imaging, 2011.
3. S. van den Oord, Z. Akkus, J.G Bosch, G. Renaud, G.L. ten Kate,A. Schinkel, N. de Jong, A.F.W. van der Steen. **Semi-automated quantification of intraplaque neovascularization using contrast-enhanced ultrasound of the carotid arteries.** Conference of EuroEcho-imaging 2012
4. Z. Akkus, D.D.B Carvalho, S. Klein, S C.H. van den Oord, A. F.L. Schinkel, N. de Jong, A.F.W. van der Steen, J.G. Bosch. **Atherosclerotic Carotid Lumen Segmentation in Combined B-mode and Contrast Enhanced Ultrasound Images.** SPIE medical imaging 2014. (*** **Honorable Mention Poster Award**)
5. Z. Akkus, J.G Bosch, G. Renaud, A. Hoogi, G.L. ten Kate, S. van den Oord,A. Schinkel, N. de Jong, A.F.W. van der Steen. **Non-targeted Imaging of Plaque Vasa Vasorum: Plaque Neovascularization-Ultrasound Image Analysis.** CTMM-ParisK project meetings, 2011-2014.

Conference proceedings:

1. Z. Akkus, J.G Bosch, G. Renaud, A. Hoogi, G.L. ten Kate, S. van den Oord,A. Schinkel, N. de Jong, A.F.W. van der Steen. **Motion Compensation Method for Quantification of Neovascularization in Carotid Atherosclerotic Plaques with Contrast Enhanced Ultrasound (CEUS).** Proc. IEEE Int Ultrasonics Symposium 2011.

2. Z. Akkus, A. Hoogi, G. Renaud, G.L. ten Kate, S. van den Oord,A. Schinkel, N. de Jong, A.F.W. van der Steen, J.G Bosch. **Motion Compensation Method using Dynamic Programming for Quantification of Neovascularization in Carotid Atherosclerotic Plaques with Contrast Enhanced Ultrasound (CEUS).** Proc. SPIE medical imaging 2012, 8320, 83200C.

3. Hoogi, J.G Bosch, Z. Akkus, G. Renaud, G.L. ten Kate, S. van den Oord,A. Schinkel, N. de Jong, A. Dan, A.F.W. van der Steen. **Quantitative analysis of flow behavior of carotid plaque neovasculature.** Proc. IEEE Int Ultrasonics Symposium 2011.

4. Z. Akkus, A. Hoogi, J.G Bosch, G. Renaud, G.L. ten Kate, S. van den Oord,A. Schinkel, D. Adam, N. de Jong, A.F.W. van der Steen. **Analysis of Neovascularization of Atherosclerotic Carotid Plaques in Contrast Enhanced Ultrasound.** Proc. IEEE Int. Ultrasonics Symposium 2012.

5. D.D.B. Carvalho, S. Klein, Z. Akkus, G. L. ten Kate, H. Tang, M. Selwaness, A.F.L. Schinkel, J.G. Bosch, A van der Lugt and W.J. Niessen, **Registration of Free-hand Ultrasound and MRI of Carotid Arteries Through Combination of Point-based and Intensity-based Algorithms**. Workshop on Biomedical Image Registration (WBIR) 2012.

6. Z. Akkus, J. G. Bosch, G.V. S. Ferrero, Diego D. B. Carvalho, G. Renaud, S. C. H. van den Oord, G. L. ten Kate, A. F. L. Schinkel, N. Jong, A. F. W. van der Steen. **Statistical segmentation of carotid plaque neovascularization.** Proc. SPIE medical imaging 2013, 8675, 867506.

7. Z. Akkus, G.V.S. Ferrero, G. Renaud, S.C.H. van den Oord, A.F.L. Schinkel, N. de Jong, A.F.W. van der Steen, J.G. Bosch. **New Quantification Methods for Carotid Intraplaque Neovascularization in Contrast Enhanced Ultrasound (CEUS).** Proc. IEEE Ultrasonics sypmposium 2013. (***The Best Student Paper Competition Award)

8. V. Daichin, Z. Akkus, A Hoogi et al. **Quantification of targeted microbubbles in contrast enhanced ultrasound.** Proc. IEEE Ultrasonics sypmposium 2013.

9. Z. Akkus, D.D.B Carvalho, S. Klein, S C.H. van den Oord, A. F.L. Schinkel, N. de Jong, A.F.W. van der Steen, J.G. Bosch. **Atherosclerotic Carotid Lumen Segmentation in Combined B-mode and Contrast Enhanced Ultrasound Images.** Proc. SPIE medical imaging 2014, 9034, 903445.

10. D.D.B Carvalho, Z. Akkus, J.G. Bosch, S C.H. van den Oord, W.J. Niessen, N. de Jong, A.F.W. van der Steen , S. Klein. **Nonrigid Motion Compensation in B-mode and Contrast Enhanced Ultrasound Image Sequences of the Carotid Artery.** Proc. SPIE medical imaging 2014, 9034, 90340N.

11. Z. Akkus, D.D.B Carvalho, S. Klein, S C.H. van den Oord, A. F.L. Schinkel, N. de Jong, A.F.W. van der Steen, J.G. Bosch. **Fully Automated Carotid Plaque Segmentation in Combined B-mode and Contrast Enhanced Ultrasound.** Proc. IEEE int. Ultrasonics Symposium 2014.

Peer-reviewed papers:

1. G.L. ten Kate, G. Renaud, Z. Akkus, S.C.H. van den Oord, F.J. ten Cate, V. Shamdasani, R. Entrekin, E.J.G. Sijbrands, N. de Jong, J.G.Bosch, A.F.L. Schinkel, A.F.W. van der Steen. **Far Wall Pseudoenhancement During Contrast Enhanced Ultrasound of the Carotid Arteries: Clinical Description and in Vitro Reproduction.** Ultrasound Med Biol., 38(4):593-600, 2012.
2. A. Hoogi, Z. Akkus, S. van den Oord, G.L. ten Kate, A. Schinkel, J.G Bosch, N. de Jong, A. Dan, A.F.W. van der Steen**. Quantitative analysis of ultrasound contrast flow behavior in Carotid Plaque Neovasculature.** Ultrasound Med. Biol., 38(12):2072-2083, 2012.
3. Z. Akkus, A. Hoogi, G. Renaud, S. C.H. van den Oord, G. L. ten Kate, A. F.L. Schinkel, D. Adam, N. de Jong, A. F.W. van der Steen, J. G. Bosch. **New Quantification Methods for Carotid Intraplaque Neovascularization using Contrast Enhanced Ultrasound.** Ultrasound Medicine and Biology, 40(1):25-36, 2013
4. S. C.H. van den Oord, Z. Akkus, G. Renaud, E. J.G. Sijbrands, F. J. ten Cate, A. van der Lugt, J. G. Bosch, N. de Jong, A. F.W. van der Steen, A. F.L. Schinkel. **Assessment of Subclinical Atherosclerosis and Intraplaque Neovascularization using Quantitative Contrast-Enhanced Ultrasound in Patients with Familial Hypercholesterolemia Atherosclerosis.** Atherosclerosis, 231(1):107-13, 2013
5. Z. Akkus, G. van Burken, S. C.H. van den Oord, A. F.L. Schinkel, N. de Jong, A. F.W. van der Steen, J. G. Bosch. **Carotid Intraplaque Neovascularization Software (CINQS).** IEEE Journal of Biomedical and Health Informatics, 99,1-7, 2014
6. D.D.B. Carvalho*, Z. Akkus*, J.G. Bosch, S. van den Oord, W.J. Niessen, S. Klein. **Global Motion Compensation of B-mode and Contrast Ultrasound images of the carotid artery for lumen segmentation and distensibility assessment.** Submitted. (*shared first author)
7. Z. Akkus*, D.D.B. Carvalho*, S. Klein, S C.H. van den Oord, A. F.L. Schinkel, N. de Jong, A.F.W. van der Steen, J.G. Bosch**. Fully Automatic Segmentation and Deformation Estimation of Atherosclerotic Carotid Plaques in Combined B-mode and Contrast Ultrasound Images.** Submitted. (*shared first author)
8. Z. Akkus, K. V. Ramnarine**. Dynamic Assesment of Carotid Plaque Motion**. Ultrasound, 2010, vol 18, 140-147.
9. D.D.B. Carvalho, S. Klein, Z. Akkus, G. L. ten Kate, A.F.L. Schinkel, J.G. Bosch, A van der Lugt and W.J. Niessen, **Estimating 3D lumen centerlines of carotid arteries in free-hand acquisition ultrasound**, Int J Comput Assist Radiol Surg., 7(2):207-15, 2012.
10. S. C.H. van den Oord, G. L. ten Kate, Z. Akkus, G. Renaud, E. J.G. Sijbrands, F. J. ten Cate, A. van der Lugt, J. G. Bosch, N. de Jong, A. F.W. van der

Steen, A. F.L. Schinkel. **Assessment of subclinical atherosclerosis using contrast-enhanced ultrasound** Eur Heart J Cardiovasc Imaging, 14, 56-61, 2012.

11. D.D.B. Carvalho, S. Klein, Z. Akkus, A. van Dijk, H. Tang, M. Selwaness, A.F.L. Schinkel, J.G. Bosch, A van der Lugt and W.J. Niessen, **Automated Joint Intensity-and-Point Based Registration of Free-hand B-Mode Ultrasound and MRI of the Carotid Artery**. Med Phys., 41(5):052904, 2014.
12. S. C.H. van den Oord, Z. Akkus, J. G. Bosch, A. Hoogi, G. L. ten Kate, G. Renaud, E. J.G. Sijbrands, H. J. Verhagen, A. van der Lugt, D. Adam, N. de Jong, A. F.W. van der Steen, A. F.L. Schinkel. **Quantitative Contrast-Enhanced Ultrasound of Intraplaque Neovascularization in Patients with Carotid Atherosclerosis.** Ultraschall Med., 2014 (Epub)
13. S. C.H. van den Oord, J. van der Burg, Z. Akkus, E. J.G. Sijbrands, J. G. Bosch, R. T. van Domburg, A. F.W. van der Steen, A. F.L. Schinkel. **Impact of Gender on the Density of Intraplaque Neovascularization: A Quantitative Contrast-Enhanced Ultrasound Study.** Atherosclerosis, 233(2):461-6, 2013.
14. S. C.H. van den Oord, Z. Akkus, G. Renaud, J. G. Bosch, N. de Jong, A. F.W. van der Steen, E. J.G. Sijbrands, A. F.L. Schinkel. **Assessment of carotid atherosclerosis, intraplaque neovascularization, and plaque ulceration using quantitative contrast-enhanced ultrasound in asymptomatic patients with diabetes mellitus.** Eur Heart J Cardiovasc Imaging, 2014 (Epub)
15. V. Daeichin, Z. Akkus, I. Skachkov, K. Kooiman, A. Needles, J. Sluimer, B. Janssen, M.J.A.P. Daemen, A. F.W. van der Steen, N. de Jong, J.G. Bosch. **Quantification of bound microbubbles in ultrasound molecular imaging.** Submitted. Special issues IEEE, 2014.

Curriculum Vitae

Zeynettin akkus was born in Batman on November 8, 1982. He obtained his BSc degree in electronics and communication from Marmara University in Istanbul, Turkey. He received his master's degree (MSc) in medical imaging, from medical engineering department of school of health and technology (KTH, the royal institute of technology, Stockholm, Sweden), in 2009. He worked as a visiting researcher in ultrasound research group, department of medical physics (University Hospitals of Leicester, Royal Infirmary), in 2009. He has been working as a junior researcher (PhD student) in biomedical engineering department (Erasmus Medical Center, Rotterdam, Netherlands) since February 2010. His research interests are biomedical image and signal processing, angiogenesis imaging and quantification, computer aided surgical interventions, and photoacoustic imaging. He received the Best Paper Award in 2013 (IEEE Ultrasonics Symposium), the Best Poster Award in 2013 (18th European symposium on Ultrasound Contrast Imaging) and Honorable Mention Poster Award in SPIE medical imaging 2014.

PhD portfolio

PhD Student: Zeynettin Akkus
PhD period: 2010-2014
Department: Biomedical Engineering, Thoraxcenter, Erasmus MC
Research school: COEUR
Promoter: Prof. dr. ir. A.F.W. van der Steen
Supervisor: Assoc. Prof. J.G. Bosch

Activity	Location	Year	ECTS
General academic skills			
Biomedical English writing and communication (Erasmus MC) Rotterdam	Rotterdam	2013	4.0
In-depth courses			
Advanced morphological filtering	Groningen	2010	4.0
C++ programming	Rotterdam	2011	2.0
Cardiovascular imaging and diagnostics (COEUR)	Rotterdam	2012	1.5
Graph algorithmic techniques for biomedical image segmentation (SPIE)	San Diego	2012	0.35
Basic introduction course on SPSS	Rotterdam	2012	0.6
Measuring features (ASCI)	Delft	2012	4.0
Knowledge driven image segmentation (ASCI)	Leiden	2012	4.0
Seminars and workshops			
Vascular imaging: Atherosclerosis and biomechanics	Rotterdam	2010	0.4
Imaging for mouse phenotyping	Rotterdam	2011	0.4
The translational imaging (from mouse to man)(AMIE)	Rotterdam	2013	1.4
International conferences			
IEEE international ultrasonics symposium, oral presentation	Orlando	2011	2.0
IEEE international ultrasonics symposium, oral presentation	Dresden	2012	2.0
IEEE international ultrasonics symposium, oral presentation *(the best student paper award)*	Prague	2013	2.0

IEEE international ultrasonics symposium, oral presentation	Chicago	2014	2.0
SPIE medical imaging, oral presentation	San Diego	2012	2.0
SPIE medical imaging, oral presentation	Orlando	2013	2.0
SPIE medical imaging, poster presentation, *(honorable mention poster award)*	San Diego	2014	2.0
16th European symposium on ultrasound contrast imaging	Rotterdam	2011	1.0
17th European symposium on ultrasound contrast imaging	Rotterdam	2012	1.0
18th European symposium on ultrasound contrast imaging *(the best poster award)*	Rotterdam	2013	2.0
19th European symposium on ultrasound contrast imaging	Rotterdam	2014	1.0

Other presentations

Ultrasound symposium (NVMU), invited speaker	Twente	2014	2.0

Total	**43.60**